Enhancing the therapeutic efficacy of poly(ADP-ribose) polymerase (PARP) inhibitors in prostate cancer

Nicholas Paul Bullock

Doctor of Philosophy

March 2022

Summary

Despite developments in recent years, outcomes remain poor for men with castrate resistant prostate cancer (CRPC). Inhibitors of poly(ADP-ribose) polymerase (PARPi), which plays a key role in the DNA damage response (DDR), are effective in men with CRPC and pre-existing aberrations in genes encoding proteins involved in homologous recombination (HR) repair of double strand DNA breaks (DSBs). However, responses are limited in patients that lack such aberrations, indicating a need to improve the efficacy of PARPi in this cohort.

Experiments in this thesis show that whilst HR-proficient CRPC cells are insensitive to PARPi, treatment leads to DNA damage and activation of CHK1, the downstream effector of another key DDR protein, ataxia telangiectasia and Rad-3 related (ATR). ATR inhibition (ATRi) reverses CHK1 activation and is synergistic with PARPi in vitro in HR-proficient CRPC cells. Furthermore, combined PARPi and ATRi significantly reduces growth and vascularity of PC-3 subcutaneous xenograft tumours compared with vehicle or monotherapy, as well as the prevalence of invasive carcinoma in a genetically modified mouse model (GEMM) of p53 and PTEN deficient localised prostate cancer. Likewise, combination therapy also reduces proliferation of tumour cells within a novel ex vivo model of neuroendocrine CRPC.

The role of PARP1, the predominant PARP isoform, was also explored through use of transgenic mouse models. Genetic depletion of PARP1 within prostatic epithelial cells did not alter the phenotype of glands within the normal adult mouse prostate or tumours in the aforementioned GEMM of p53 and PTEN deficient localised prostate cancer. On the contrary, siRNA mediated depletion of *PARP1* reduces proliferation of CRPC cells in vitro, with simultaneous *PARP2* depletion having no additional benefit, suggesting selective PARP1 inhibition may reduce off target toxicity whilst maintaining efficacy.

Collectively, these results demonstrate that combined PARP and ATR inhibition is effective against HR-proficient prostate cancer and support its ongoing investigation in this setting.

Acknowledgements

I would firstly like to thank my supervisor, Dr Helen Pearson, for her enthusiasm and support of this project from its inception through to completion, together with her patience in teaching me the fundamental principles of laboratory research. I would also like to thank Professor Howard Kynaston for his support, wisdom and mentorship throughout this research and my wider urological training, as well as Professors John Staffurth and Richard Clarkson for their valuable contributions to the supervisory team over the past three years.

I am also indebted to my colleagues and friends in the Pearson Group, including Daniel Turnham and Manisha Dass, as well as others in the European Cancer Stem Cell Research Institute that have taught me all the techniques necessary to complete this work. I am particularly grateful for their patience in helping me transition from clinician to clinician scientist, and for always answering my questions, no matter how big or small. I would also like to thank the T2 Facility team, Asif Jeelani, Elaine Taylor, Sharyn Hailer, Mike Quirk and Paul Chapman for their invaluable assistance with the transgenic components of this thesis, as well as Kate Mason and Sarah Martin for her help with the in vivo preclinical trials.

I would like to thank The Urology Foundation and John Black Charitable Foundation, together with their trustees and fundraisers, for supporting my TUF Research Scholarship and enabling me to pursue this project and develop my career as an academic urologist. I am also grateful to my clinical colleagues in the University Hospital of Wales and Morriston Hospital for their understanding and support throughout the research period, as well as for their limitless hard work during what has been a very challenging time for the medical profession.

I would finally like to thank my wife Steph for her unwavering support in all of my academic and clinical endeavours, together with my son Oliver for bringing so much joy to our lives and providing a welcomed escape when the going has been tough.

COVID-19 Impact Statement

The research for this thesis was undertaken during a three year Out of Programme for Research (OOPR) period during my Specialty Training in Urology between August 2018 and July 2021. Progress towards completion of my original aims and objectives was on track until the onset of the COVID-19 pandemic. However, on 17th of March 2020 Cardiff University instructed that all non-essential research should cease and that staff and students should work from home. This was accompanied by instructions that all non-essential breeding of transgenic mice should also cease, with immediate separation of breeding pairs. With the potential impact of the first wave unknown and expected to be severe, junior doctors working in the Department of Urology at the University Hospital of Wales, for whom I was already working to provide out of hours emergency cover, were reallocated to COVID-19 medical teams. In response, I applied for an Interruption of Study and returned to full time clinical practice to support my colleagues. Together with the Clinical Director, I designed and implemented an emergency Registrar level rota to provide cover for essential clinical activities. I remained on this rota until the first wave had subsided and junior doctors returned to the team.

Despite recommencing research activity in June 2020, ongoing restrictions meant that the European Cancer Stem Cell Research Institute in which this work was undertaken remained closed until August 2020, after which I and other members of the group were allowed to return and recommence experiments in a morning/afternoon shift pattern. Further changes to university policy enabled return to full day laboratory activity from December 2020 onwards, although we were still subject to social distancing measures that restricted the number of staff/students in each laboratory bay/area. Collectively my return to clinical work, along with these significant and lengthy restrictions on laboratory activity, had a major impact on productivity and hence my ability to achieve the original project aims. However, given the fixed nature of my OOPR and date of return to clinical training in August 2021, I opted not to extend my research period despite the formal Interruption of Study. Nevertheless, regular meetings with my supervisors and internal assessor as the situation evolved enabled me to modify my aims and objectives so as to render them achievable within the framework of restrictions and remaining time. This did however mean that a number of planned experiments, particularly those involving the transgenic models, were unfortunately no longer possible. Despite these detrimental effects, I am grateful that I had the opportunity to return to clinical practice and support my colleagues during what has been, and continues to be, an incredibly challenging period for the National Health Service. Similarly, I appreciate that others have experienced much greater hardship both in their working and personal lives, and I wish to pay tribute to all those that have suffered as a consequence of this terrible disease.

Abbreviations

ADT	androgen deprivation therapy
AP	anterior prostate lobe
AR	androgen receptor
ARE	androgen response element
AS	active surveillance
ATM	ataxia telangiectasia mutated
ATR	ataxia telangiectasia and Rad-3 related
ATRi	ATR inhibitor
ATRIP	ATR interacting protein
BER	base excision repair
BMI	body mass index
BOO	bladder outlet obstruction
BRCA	breast cancer susceptibility protein
Cas9	CRISPR-associated protein 9
cDNA	complementary DNA
CHK1	checkpoint kinase 1
CHK2	checkpoint kinase 2
CK	cytokeratin
Cre	Cre recombinase
CRISPR	clustered regularly interspaced short palindromic repeats
CRPC	castrate resistant prostate cancer
CZ	central zone
DDR	DNA damage response
DHT	dihydrotestosterone
DP	dorsal prostate lobe
DRE	digital rectal examination
DSB	double strand DNA break
EBRT	external beam radiotherapy
EMT	epithelial to mesenchymal transition
gDNA	genomic DNA
H&E	Haematoxylin and eosin
HR	homologous recombination
LH	luteinising hormone

LHRH	lutenising hormone releasing hormone
LP	lateral prostate lobe
MMR	mismatch repair
NER	nucleotide excision repair
NHEJ	non-homologous end joining
NICE	National Institute for Health and Care Excellence
PAP	prostate-specific alkaline phosphatase
PARP	poly-ADP ribose polymerase
PARPi	PARP inhibitor
PDE	patient derived explant
PDX	patient derived xenograft
PI3K	phosphoinositide-3-kinase
PIN	prostatic intraepithelial neoplasia
PTEN	phosphatase and tensin homolog
PZ	peripheral zone
RP	radical prostatectomy
SSB	single strand DNA break
SV	seminal vesicle
TGF-beta	transforming growth factor beta
TNBC	triple negative breast cancer
TURP	transurethral resection of prostate
TZ	transition zone
VP	ventral prostate lobe
WW	watchful waiting

Table of Contents

1 Introduction

1.1 The human prostate gland

1.1.1 Anatomy and histology

1.1.1.1 History and nomenclature

The human prostate is a walnut sized exocrine gland that lies in the extraperitoneal space between the pelvic diaphragm and peritoneal cavity. Its gross anatomy was appreciated as long ago as the mid-16th century, as noted in the works and drawings of Andreas Vesalius. Several decades later at the turn of the 20th century, through use of serial sections of the foetal prostate, Lowsley identified five distinct groups of prostatic ducts originating from the urogenital sinus (UGS) and designated them as the middle, posterior, ventral and two lateral lobes (Lowsley, 1912). However, in the adult prostate these lobes are fused and cannot be easily defined, therefore prompting considerable debate concerning the nomenclature used to describe the anatomical structure of the prostate in the years that followed. In the present day, the most commonly utilised description is that published by McNeal in the latter half of the 20th century, which divides the prostate into four main regions, termed 'zones', which are anatomically separate and histologically distinct (McNeal, 1968, McNeal, 1981).

1.1.1.2 Gross anatomy

The prostate gland is situated inferior to the bladder, superior to the perineal membrane, posterior to the pubic symphysis and anterior to the rectum (Cox et al., 2019). It is conical in shape, as shown in ***Figure 1.1***, with its base in continuity with the bladder superiorly and its apex fusing with the striated external urethral sphincter inferiorly. The prostate is supported by the puboprostatic ligaments anteriorly and the external urethral sphincter and perineal membrane inferiorly. It is enclosed by a capsule, comprising of collagen, elastin and smooth muscle, which separates it from the surrounding periprostatic fat, and is covered by three distinct layers of fascia; the anterior and anterolateral fascia which are in continuity with the capsule and contain the deep dorsal vein of the penis and its tributaries, and the rectovesical (Denonvilliers) fascia, which is located between the posterior aspect of the prostate and the anterior rectal wall. The gland itself surrounds the proximal urethra as it exits the bladder, termed the prostatic urethra. The left and right seminal vesicles, which lie superior to the posterior aspect of the prostate beneath the base of the bladder, are joined by their corresponding vas deferens to form the ejaculatory ducts, which in turn enter the prostate at the verumontanum, immediately proximal to the external urethral sphincter.

The prostate derives it arterial blood supply predominantly from the inferior vesical artery, a branch of the internal iliac artery (Cox et al., 2019). In turn this gives rise to two main branches, the first of which is the urethral artery, that enters the prostatovesical junction posterolaterally and travels inwards perpendicular to the urethra at approximately 5 o'clock and 7 o'clock before turning caudally and parallel to the urethra. This is of clinical relevance as it is the main arterial supply to the adenoma of benign prostatic hyperplasia and thus a common source of bleeding during transurethral resection of the prostate (TURP). The second of these branches is termed the capsular artery, which runs posterolateral to the prostate and supplies the glandular tissue.

Venous drainage of the prostate begins with the deep dorsal vein of the penis, which passes anterosuperior to the perineal membrane and divides into three main branches; superficial, left and right, which in turn drain into the internal iliac vein (Cox et al., 2019). Lymphatic drainage is predominantly via the obturator and internal iliac nodes, as well as through communications with external iliac, presacral and para-aortic nodes. The nerve supply to the prostate is mainly autonomic via the pelvic plexus, which derives parasympathetic fibres from the sacral levels (S2-S4) and sympathetic fibres from the thoracolumbar levels (L1-L2).

1.1.1.3 Microscopic anatomy and histology

McNeal's description divides the gland into four regions, as shown in ***Figure 1.1A***, each with differing cellular composition, histological features and propensity for benign or malignant change. The anterior fibromuscular stroma accounts for approximately 5% of prostate volume and is devoid of glandular components. The periurethral transition zone (TZ) surrounds the prostatic urethra and accounts for approximately 5-10% of the total prostatic glandular tissue (Aaron et al., 2016). Whilst the percentage of adenocarcinomas arising in the TZ is around 25% (McNeal et al., 1988), this is the predominant site of nodular adenoma development, termed benign prostatic hyperplasia (BPH). As the adenoma increases in size it causes compression of the urethra and distortion of the bladder outlet, leading to bladder outlet obstruction (BOO) and a sequelae of associated clinical features (Foo, 2017). The peripheral zone (PZ) constitutes approximately 70% of the total prostatic glandular tissue and makes up the posterior and lateral aspects of the gland. Furthermore, the PZ also contains the proximal urethral segment which contains a cylindrical sleeve of smooth muscle, termed the internal urethral sphincter. The PZ can be easily palpated on digital rectal examination and is the site in which 70% of adenocarcinomas arise (McNeal et al., 1988). Finally, the central zone (CZ) is the region that surrounds the ejaculatory ducts. The CZ comprises approximately 25% of total prostatic glandular tissue and, unlike the PZ in which glandular acini are predominantly round or oval, acini in the CZ are

polyhedral in cross section and often larger and more irregular (Aaron et al., 2016). Furthermore, unlike both the TZ and PZ, the CZ has a low incidence of disease, with fewer than 10% of adenocarcinomas arising from this region (McNeal et al., 1988).

Prostate cell types are defined by their shape, location, cell surface markers and gene expression profiles. Microscopically the gland is composed of glandular epithelial acini embedded in a fibromuscular stromal network, which account for approximately 70% and 30% of the total prostate volume respectively, as shown in ***Figure 1.1B***. The stroma contains predominantly interstitial fibroblasts, immune cells, endothelial cells and smooth muscle cells whist the epithelium is arranged into a bilayer comprising of an outer basal layer (comprising approximately 10% of the epithelial population) and an inner layer of tall columnar secretory luminal cells (comprising approximately 90% of the epithelial population), as demonstrated in ***Figure 1.1C*** (McNeal, 1988, Packer and Maitland, 2016). Additionally, a rare population of neuroendocrine cells (comprising around 1% of the epithelial population) that express synaptophysin and chromogranin A and secrete a number of neuropeptides such as serotonin and somatostatin are found among the basal layer and often display dendritic like processes that extend inwards to contact the glandular lumen (Abrahamsson, 1999, Toivanen and Shen, 2017).

Each of the cell types of the prostatic epithelium have been well studied and described. The secretory luminal cells are tall columnar epithelial cells characterised by expression of low molecular weight cytokeratins (CK) 8 and 18, Androgen Receptor (AR) and secretory proteins such as prostate specific antigen (PSA) and prostate-specific alkaline phosphatase (PAP) (Verhagen et al., 1992, Wang et al., 2001). The basal cell layer lies between the secretory epithelial cell layer and a basement membrane composed of extracellular matrix. Basal cells are cuboidal epithelial cells characterised by high expression of CK5, CK14 and the transcription factor p63, with low or typically undetectable levels of AR expression (Toivanen and Shen, 2017). In contrast to luminal cells, which are androgen dependent and undergo apoptosis following androgen withdrawal, these cells are largely unaffected by castration (Xie et al., 2017). In addition to luminal and basal cells, there is also a population of 'intermediate' epithelial cells that co-express markers specific to each, as well as additional proteins such as CK19 (Hudson et al., 2001, Toivanen and Shen, 2017). However, there is debate within the literature as to whether these intermediate cells constitute a functionally distinct cell type or simply represent a transition between basal and luminal states (Hudson et al., 2001, Wang et al., 2001, Toivanen and Shen, 2017).

Further to luminal, basal and neuroendocrine cells, contemporary research also supports the existence of another cell type within the prostatic epithelium, prostate stem cells. Through use of a range of approaches such as lineage tracing, label-retention and tissue reconstitution, a subpopulation of progenitor cells possessing the key stem cell properties of multipotency and self-renewal have been identified (Li and Shen, 2019). Candidate human prostate stem cell populations, which can be identified through their expression of specific stem cell markers such as integrin $\alpha_2\beta_1$ and CD133, initially appeared to be located within the basal epithelial compartment, where they constitute approximately 1% of all basal cells (Collins et al., 2001, Richardson et al., 2004). Furthermore, through use of mitochondrial DNA mutations a surrogate lineage tracing marker, multipotent basal stem cells have been located to discrete niches in the juxta-urethral ducts, which in turn generate bipotent basal progenitor cells that are then dispersed throughout the entirety of the prostate glandular network via directed epithelial migration streams (Moad et al., 2017). However, the exact origin and nature of prostate stem cells remains the subject of debate within the literature, with advances in three-dimensional organoid culture also identifying the existence of a subset of bipotent luminal progenitor cells in both mouse and human prostate (Chua et al., 2014, Karthaus et al., 2014).

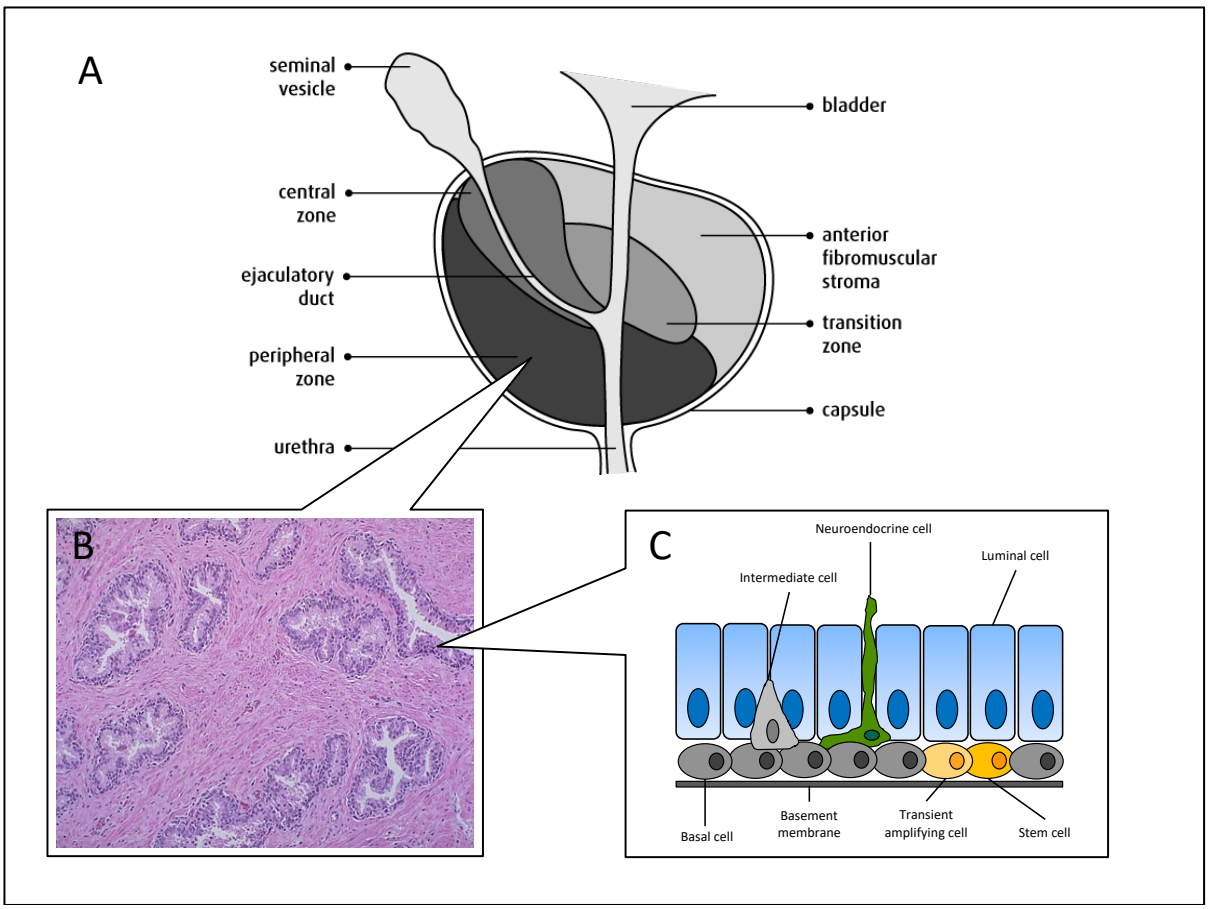

Figure 1.1: *Gross and microscopic anatomy of the human prostate.* A: Schematic sagittal section of the prostate demonstrating key anatomical structures and McNeal Zones, adapted from The Canadian Cancer Society, 2019. B: Haematoxylin and eosin section of normal prostate tissue at low power demonstrating the appearance of normal glands interspersed within fibromuscular stroma, courtesy of the WebPath Internet Pathology Laboratory, University of Utah, 2019 (with permission). C: Schematic diagram demonstrating the cellular composition and arrangement of the prostatic epithelium, including the proposed location of stem and transient amplifying cells. Adapted from (Packer and Maitland, 2016).

1.1.2 Physiology and function of the normal human prostate

1.1.2.1 Prostatic fluid production and secretion

The different components of the prostate gland have a number of physiological roles. The main function of the stroma is to provide a hospitable microenvironment to support the structure and function of the epithelium and thereby maintain normal tissue homeostasis (Verze et al., 2016). Of the many roles of the epithelium, the most significant is the production of prostatic fluid which constitutes approximately one-third of ejaculate volume (Roberts and Jarvi, 2009). Prostatic fluid comprises a range of proteins and other factors that contribute to semen liquefaction and sperm motility, including kallikrein-related peptidases (KLKs), citrate and zinc (Verze et al., 2016). Prostate Specific Antigen (PSA) is one of a family of 15 KLKs and is of particular physiological and clinical importance. It is secreted into the prostatic ducts as an inactive proenzyme (proPSA), which is

subsequently activated through cleavage of seven N-terminal amino acids by other enzymes such as trypsin, KLK2, LKL4 and KLK5 (Paju et al., 2000). Once active, PSA acts to cleave semenogelin I and II in the seminal coagulum so as to facilitate liquefaction of the semen and release of motile spermatozoa to enable their passage through the female reproductive tract (Lilja, 1985). In normal conditions, the majority of PSA that enters the circulation is rapidly bound by protease inhibitors, whilst a small fraction is inactivated by proteolysis and remains as free PSA (Balk et al., 2003). Both are detectable in the serum and increase when the architecture of the gland is disrupted, such as occurs in prostate cancer. The role of serum PSA in the diagnosis and risk stratification of prostate cancer is discussed in more depth in Section 1.3.

1.1.2.2 Androgen metabolism

Androgens are sex hormones that are responsible for a diverse range of physiological processes, including differentiation and maturation of the male reproductive organs, as well as prostate gland function and homeostasis. The predominant circulating androgen is testosterone, which is produced by the Leydig cells of the testes in response to stimulation by luteinising hormone (LH), which is in turn released from the anterior pituitary gland following stimulation by LH-releasing hormone (LHRH) from the hypothalamus; a feedback loop known collectively as the hypothalamic-pituitary-gonadal axis (Amory and Bremner, 2003). Although testosterone constitutes 90% of circulating androgens, the majority is bound to serum proteins such as sex hormone binding globulin and albumin, leaving only 1-2% in the free unbound state (Hammond et al., 2003, Dehm and Tindall, 2006). The remaining 10% of circulating androgens, which include dehydroepiandosterone and androstenediol, are produced by cells of the adrenal cortex and subsequently converted to testosterone in peripheral tissues (Dehm and Tindall, 2006).

Testosterone is highly lipophilic and therefore passes easily across cell membranes and into the cytoplasm. Within the prostatic epithelial cells, this is then converted to its more potent form, dihydrotestosterone (DHT) by the cytochrome P450 enzymes 5-alpha-reductase Type I and II (Verze et al., 2016). Both testosterone and DHT exert their actions through binding to the AR, a member of the nuclear receptor transcription factor superfamily, with DHT having a significantly higher binding affinity. Following binding, the resulting complex translocates to the nucleus where it dimerises and binds to androgen response elements (ARE) in the promoter and enhancer regions of target genes which, together with the recruitment of coactivator and coregulatory proteins, regulate gene expression (Dehm and Tindall, 2006). AR signalling is known to control expression of a number of genes in a wide range of tissues. In the prostate it regulates expression of target genes within both

the stromal and epithelial compartments, including that those that encode PSA and the AR itself, collectively resulting in maintenance of gland homeostasis (Lamont and Tindall, 2010, Fujita and Nonomura, 2019). Androgen signalling is also fundamental to the development, progression and treatment of prostate cancer, as discussed in Section 1.3.

1.2 The murine prostate gland

1.2.1 Gross anatomy

An appreciation of the key differences between the gross and microscopic anatomy of the mouse and human prostate is necessary for the use of murine models in prostate cancer research. Whilst both species possess male accessory organs that are androgen sensitive and form lobular glands composed of distinctly differentiated epithelial cells, unlike in the human, the mouse prostate is divided into anatomically distinct lobes: the anterior prostate lobes (AP), the ventral prostate lobes (VP), the dorsal prostate lobes (DP) and the lateral prostate lobes (LP). The DP and LP are often grouped together and termed the DLP, as shown in ***Figure 1.2*** (Shappell et al., 2004). Each lobe is invested by a thin mesothelial lined capsule and composed of a series of branching blind ending ducts. The glandular components are separated from the capsule by a loose fibroadipose connective tissue comprising vessels, nerves and ganglia. The ducts themselves are in surrounded by a thin fibromuscular tunica that is composed of a small number of spindle cells interspersed in collagen (Shappell et al., 2004).

1.2.2 Microscopic anatomy and histology

The distinct lobes of the mouse prostate differ from one another in terms of their histology and biochemistry, as demonstrated in ***Figure 1.2***. The DP is lined by a simple columnar epithelium that is occasionally stratified, with cells possessing lightly eosinophilic granular cytoplasm and central-basally located small nuclei. The extent of infolding lies between that seen in the AP and flatter luminal borders of the LP and VP, with homogenous eosinophilic secretions often seen within the lumen (Shappell et al., 2004). The LP is lined by a cuboidal to low columnar epithelium, with clear to slightly granular cytoplasm and small basally located nuclei. The histological features of the collective DLP have been described as the most homologous to the human PZ, which is the most common site of origin of prostate cancers as discussed previously (Price, 1963, McNeal et al., 1988). However, on the basis of differences in embryonal development and the lack of evidence for a direct relationship between the specific mouse lobes and specific zones in the human prostate, it was the consensus of the Bar Harbor Pathology Panel that no one lobe of the mouse prostate is more relevant to human prostate cancer than any other (Shappell et al., 2004). The AP is adjacent to the seminal vesicles and

demonstrates a more papillary and cribriform histological pattern in comparison with the other lobes, comprising cuboidal to columnar epithelial cells containing central nuclei and eosinophilic granular cytoplasm. The lumen also contains abundant, mildly eosinophilic secretions. Finally, the cells of the VP contain small basally located nuclei and are arranged into ducts with flat luminal edges and only focal infolding.

On a cellular level, whilst each lobe of the mouse prostate is composed of distinct cell populations similar to those seen in humans, including secretory luminal epithelial cells, basal epithelial cells and neuroendocrine cells, the proportions of each cell type differ, and the basal layer is not continuous. Likewise, although there are some apparent cytological differences, the same antibodies can be used in both species for identification of basal and luminal markers (Shappell et al., 2004).

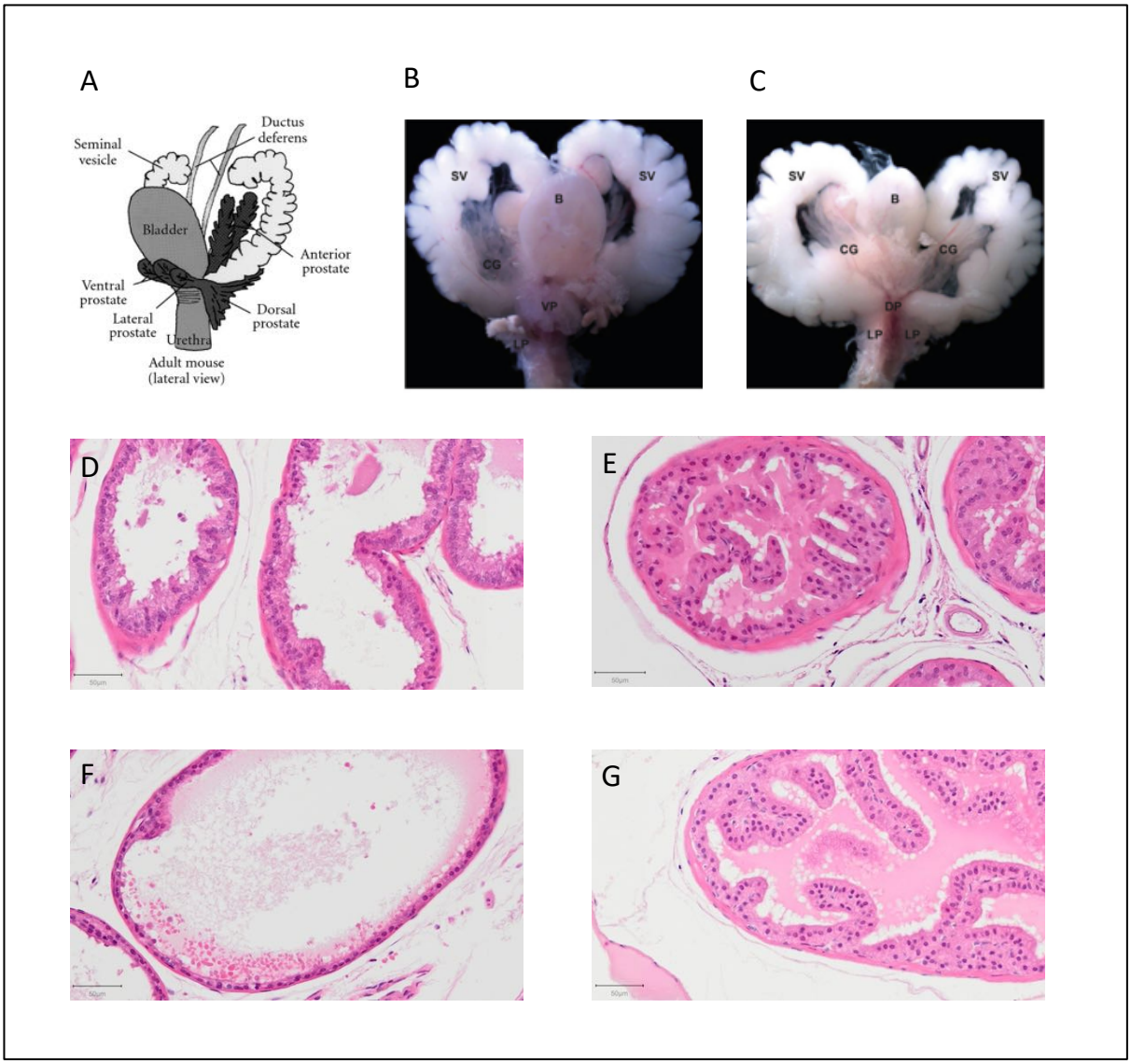

Figure 1.2: *Gross and microscopic anatomy of the murine prostate gland.* A: Schematic diagram of the murine prostate demonstrating the lobes and their anatomical relationships to other organs of the urogenital tract, adapted from (Abate-Shen and Shen, 2000). B: High resolution photograph of the ventral view of the mouse urogenital tract. Adapted from (Knoblaugh et al., 2018). SV; seminal vesicle, B: bladder, CG; coagulative gland / anterior prostate, VP; ventral prostate. C: High resolution photograph of the dorsal view of the mouse urogenital tract, adapted from (Knoblaugh et al., 2018). LP; lateral prostate, DP; dorsal prostate. D-G: High power H&E microscopy images of VP (D), DP (E), LP (F) and AP (G) of an adult mouse. Scale bars 50 µm.

1.3 Prostate cancer

1.3.1 Epidemiology

1.3.1.1 Worldwide perspective

Prostate cancer is the second most common cancer in men and the fifth leading cause of cancer related death worldwide, with an estimated 1414000 new cases and 375000 deaths in 2020 based on the GLOBOCAN dataset produced by the International Agency for Research on Cancer (Gandaglia et al., 2021). Incidence varies across regions and populations, with age standardised rates being highest in Northern Europe (83 per 100 000) and lowest in South-Central Asia (6.3 per 100 000).

1.3.1.2 UK incidence

Prostate cancer is the most common cancer in men in the UK, with approximately 52300 new cases each year (Cancer Research UK, 2018). Incidence has gradually increased across almost all age groups since the early 1990's, with a 48% rise in age standardised incidence rate between 1993-1995 and 2016-2018 (Cancer Research UK, 2018). This trend is thought to be the result of more widespread use of PSA testing following its introduction in the late 1980's, together with increasing rates of incidental detection following Transurethral Resection of Prostate (Brewster et al., 2000, Cancer Research UK, 2018) Incidence also increases with advancing age, as shown in ***Figure 1.3***, with the overall current lifetime risk of developing the disease estimated to be 1 in 6 (18%) for men born after 1960 (Cancer Research UK, 2018). Furthermore, the combination of an ageing population, the introduction of more sensitive diagnostic techniques and a trend towards increasing use of PSA screening, has led to the prediction that there will be 69% more cases diagnosed in 2030 than in 2007 (Mistry et al., 2011).

1.3.1.3 UK mortality

Prostate cancer is the second most common cause of cancer death in the UK, accounting for 11900 deaths each year (Cancer Research UK, 2018). Similar to incidence, mortality rate is closely linked to age, with highest rates seen in those men over 90 years, as shown in ***Figure 1.4***. However, mortality from prostate cancer has decreased over time, with the age standardised five and ten year survival rates increasing from 36.6% and 27.8% respectively in 1971-72 to 85% and 84% respectively in 2010-11 (Quaresma et al., 2015). Furthermore, mortality has decreased a further 10% in the last decade (Cancer Research UK, 2018), which is likely a result of increased early detection of low-risk disease due to increased PSA screening and more sensitive diagnostic techniques, combined with an improvement in both radical and palliative treatment options for men with all stages of the disease (Kvåle et al., 2007, Berg et al., 2017).

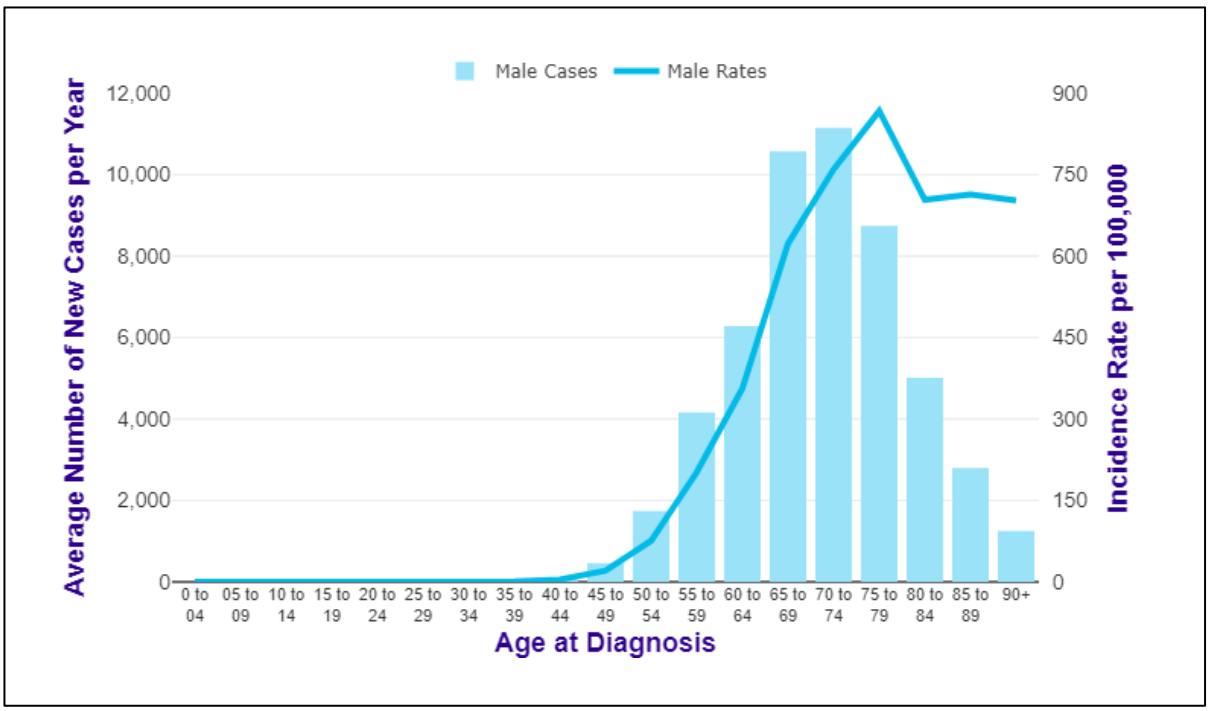

***Figure 1.3**: Prostate cancer incidence.* Number of new prostate cancer cases per year and age specific incidence rates per 100 000 men in the United Kingdom between 2016-18. Adapted from (Cancer Research UK, 2018).

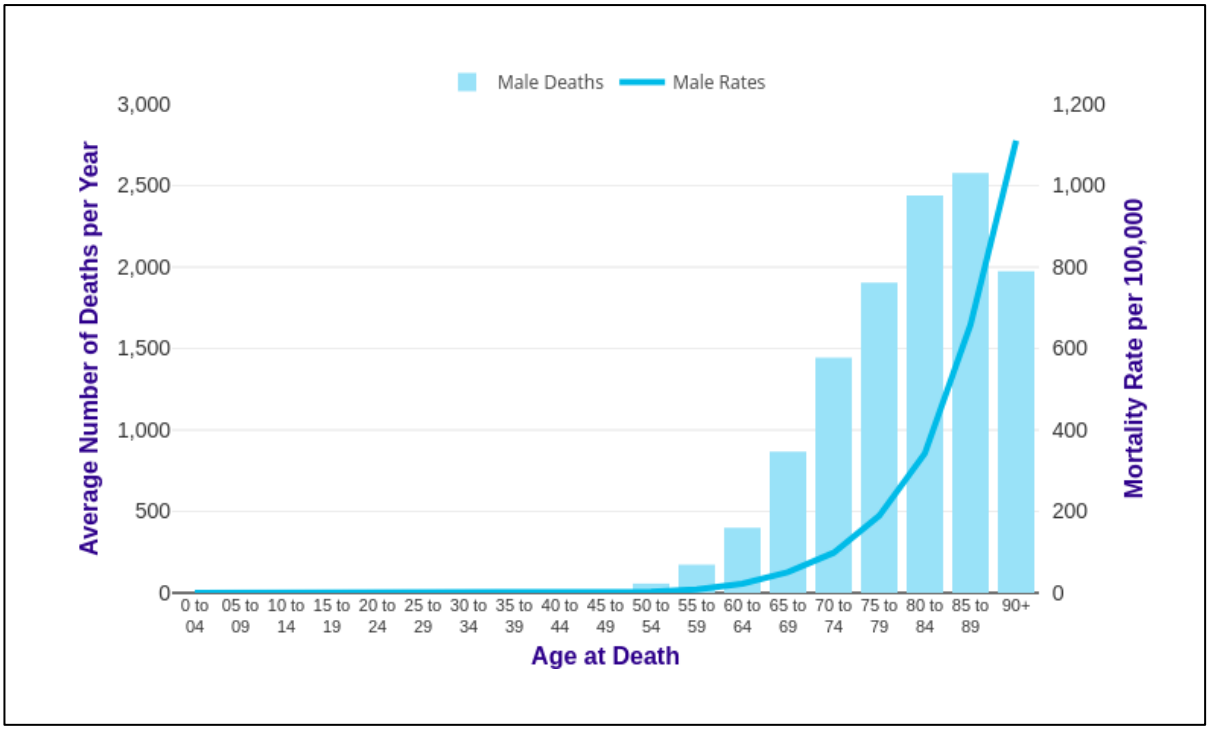

***Figure 1.4:** Prostate cancer mortality.* Number of prostate cancer deaths per year and age specific mortality rates per 100 000 men in the United Kingdom between 2016-18. Adapted from (Cancer Research UK, 2018).

1.3.1.4 Risk factors for prostate cancer development

1.3.1.4.1 Age

Despite considerable research, the aetiology of prostate cancer remains less well characterised than several other common cancers. Increasing age is the most significant risk factor, with very few cases diagnosed in White men under 50 with no family history or in Black men or those with a family history under 40 years of age (Rawla, 2019). However, several post mortem studies have sought to infer the prevalence of latent prostate cancer within the general population. Although there are some methodological differences, these series have shown that prevalence increases steadily with advancing age from the third decade onwards, with up to 86.6% of men aged 81-95 demonstrating foci of adenocarcinoma on histological assessment (Breslow et al., 1977, Sánchez-Chapado et al., 2003, Soos et al., 2005). These findings reflect the heterogeneity of the disease and support the notion that a significant proportion of men have indolent disease that never becomes clinically apparent and go on to die from causes other than prostate cancer.

1.3.1.4.2 Race

There is marked variation in the incidence of prostate cancer across both geographical regions and within differing populations in the same country. However, given that the rates of latent prostate cancer appear similar across countries (Breslow et al., 1977), it is probable that differing genetic and environmental factors may account for progression of these latent cancers to clinically significant disease. For example, in the USA between 2011-15 the lowest incidence of clinical prostate cancer was observed in the American Indian/Alaska population (age adjusted rate of 54.8 per 100 000), followed by White (105.7 per 100 000) and Black (178.3 per 100 000) (National Cancer Institute: Surveillance Epidemiology and End Results Programme, 2018). Mortality rate was also highest in the Black population, in whom it was 2.2 times greater than that of White Americans (National Cancer Institute: Surveillance Epidemiology and End Results Programme, 2018). The exact reasons for this disparity are not known, but it has been postulated that both genetic predisposition and socioeconomic factors pertaining to receipt of lower quality healthcare and reduced PSA testing within the Black community may be responsible (Wu and Modlin, 2012).

1.3.1.4.3 Family history

Reports of familial clustering of prostate cancer was first described in the mid-20th century and have since been supported by a number of studies demonstrating prostate cancer affecting a first degree relative to be an independent risk factor for prostate cancer development (Lichtenstein et al., 2000, Brandt et al., 2010). A meta-analysis of such studies was undertaken by Kicinski et al. in 2011 which

demonstrated that prostate cancer in a first degree relative confers a 2.5 fold increased risk, which was further increased if that relative was diagnosed before 65 years of age (2.87 fold), if a brother was affected (3.14 fold) or if two or more first degree relatives were affected (4.39 fold) (Kiciński et al., 2011). Contemporary studies have subsequently demonstrated that whilst approximately 20% of men with prostate cancer report a positive family history (Rawla, 2019), the proportion of disease risk variability in the population resulting from genetic factors (termed heritability) is greater than 50%; higher than for that for almost all other cancers (Mucci et al., 2016).

A number of gene linkage studies undertaken in patients with familial prostate cancer and their relatives have identified prostate cancer susceptibility genes. These include the hereditary prostate cancer-1 (*HPC1*) gene on chromosome 1q25, which encodes the enzyme ribonuclease L (RNASEL) that plays a role in innate immune defence mechanisms (Rökman et al., 2002, Chen et al., 2003) and the *ELAC2* gene on chromosome 17p11 which encodes the zinc phosphodiesterase ELAC protein 2 that is thought to contribute to prostate cancer development through activation of the TGF-beta signalling pathway (Tavtigian et al., 2001, Noda et al., 2006). However, developments in technology in recent years have enabled genome wide association studies to become the gold standard for identification of links between germline variants and complex diseases such as prostate cancer. Such studies have identified more than 160 common loci associated with prostate cancer susceptibility, indicating a multigenic or polygenic model of prostate tumorigenesis (Schumacher et al., 2018, Farashi et al., 2019). The proposed clinical application of these findings, and the ongoing work of large collaborative endeavours such as the Prostate Cancer Association Group to Investigate Cancer Associated Alterations in the Genome (PRACTICAL) is far reaching, ranging from risk stratification for population based screening through to enabling treatments to be tailored to patients specific genetic variants (Benafif et al., 2018).

A subset of hereditary prostate cancer has been well described in men carrying germline mutations in two genes: *BRCA1* (17q21), which encodes the breast cancer type 1 susceptibility protein, and *BRCA2* (13q12), which encodes the breast cancer type 2 susceptibility protein, both of which are tumour suppressor genes involved in the repair of DNA damage. Studies have shown that germline loss of function mutations in *BRCA1* and *BRCA2* confer an increased risk of developing prostate cancer of 3.75 and 8.6 fold respectively, rendering the latter the highest currently known inherited genetic risk factor for prostate cancer (Kote-Jarai et al., 2011, Leongamornlert et al., 2012). Furthermore, germline *BRCA1/2* mutations are associated with higher Gleason grade and stage at diagnosis, including lymph node involvement and distant metastases, as well as worse prognosis (Castro et al., 2013, Castro et

al., 2015). The frequency of germline and somatic *BRCA1/2* mutations in localised and metastatic prostate cancer, along with their clinical significance, is discussed in Section 1.6.

1.3.1.4.4 Lifestyle factors

Observational studies have demonstrated an increase in prostate cancer diagnosis among immigrant populations that have moved from developing countries in which there is a low risk of prostate cancer to industrialised, 'Westernised' regions in which the risk is much greater, implicating environmental factors such as diet and lifestyle (Hsing et al., 2000, Chu et al., 2011). Indeed, men of the same ethnic group raised in different environments demonstrate a risk of prostate cancer similar to that of their county of residence rather than country of origin (Kolonel et al., 2004). As such, the influence of a number of lifestyle factors on prostate cancer development and progression have been investigated.

1.3.1.4.4.1 Obesity

Although the results of studies relating to obesity have been inconsistent, meta-analyses have demonstrated that an elevated Body Mass Index (BMI) confers a small but statistically significant association with increased prostate cancer incidence (MacInnis and English, 2006, Allott et al., 2013). Furthermore, higher stage disease and increased rates of both biochemical recurrence after radical treatment and prostate cancer specific mortality have been reported in the obese patients, indicating that obesity is associated with a more aggressive disease phenotype and poorer clinical outcomes (MacInnis and English, 2006, Cao and Ma, 2011, Parker et al., 2013a). The causal mechanisms underpinning such observations remain unclear but may relate to delayed diagnosis as a result of technical difficulties in accurate digital rectal examination combined with the phenomenon of decreasing serum PSA as BMI increases secondary to increased plasma volume (Banez et al., 2007). Similarly, the poorer outcomes after treatment may be partly attributable to the higher positive margin rate seen in obese men following radical prostatectomy (Freedland et al., 2004), as well as greater variation in prostate location between radiotherapy fractions (Millender et al., 2004).

1.3.1.4.4.2 Alcohol

The association between alcohol and prostate cancer has also been investigated, with studies reporting conflicting results. For example, whilst a large meta-analysis of 235 studies failed to identify an association with risk of development of prostate cancer (Bagnardi et al., 2001), a subsequent large prospective study, the Prostate Cancer Prevention Trial, demonstrated that heavy alcohol consumption (defined as $\geq$ 50 g per day) and regular heavy drinking (defined as $\geq$ 4 drinks daily on $\geq$ 5 days per week) were associated with increased risk of high grade prostate cancer, with relative risks

of 2.01 (95% CI 1.33-3.05) and 2.17 (95% CI 1.42-3.39) respectively (Gong et al., 2009). Conversely, a more recent prospective cohort study, the Health Professionals Follow-Up Study, reported opposing results, with alcohol drinkers found to have a lower risk of developing lethal prostate cancer (hazard ratio of 0.84, 95% CI 0.71-0.99) (Downer et al., 2019). Furthermore, consumption of 15 - 30 g per day of total alcohol after diagnosis was associated with a lower risk of death (hazard ration 0.71, 95% CI 0.5-1.0). Given these conflicting results, further high-quality observational studies are therefore necessary so as to better establish the role that alcohol plays, if any, in the development and progression of prostate cancer.

1.3.1.4.4.3 Smoking

Whilst tobacco smoking is associated with increased risk of developing a number of malignant diseases such as lung, bladder and head and neck cancer, its role in the development and progression of prostate cancer remains a matter of debate. Several cohort studies have failed to demonstrate a significant impact of smoking on risk, whilst a number of case control studies have described either increased risk or an association with higher grade disease in those patients that smoke (Giovannucci et al., 2007, Rohrmann et al., 2007, Butler et al., 2009, Murphy et al., 2013, Ho et al., 2014, Tang et al., 2017). Although some of these differences may be attributable to variation in methodology or selection bias, there seems to be a clear difference in association between smoking status and prostate cancer risk between racial groups. For example, in a study of 1085 patients with prostate cancer, African American men that smoked heavily had both an increased risk of diagnosis (odds ratio of 2.6) and high-grade disease (odds ratio 1.9) whereas no such association was identified in European American men that also smoked heavily (Murphy et al., 2013). On the contrary, the results of studies exploring the association between smoking and risk of both recurrence following treatment and cancer-related mortality are more consistent. Two large meta-analyses have demonstrated that smoking at the time of diagnosis is linked to an increased risk of death from prostate cancer, along with higher risk of biochemical recurrence and development of metastases after radical treatment (Islami et al., 2014, Foerster et al., 2018). Interestingly, the risk of cancer specific mortality appears to return to that of those who have never smoked following 10 years of cessation, thereby advocating early counselling in men newly diagnosed with prostate cancer (Kenfield et al., 2011).

1.3.1.4.4.4 Diet

A number of dietary factors and their influence on prostate cancer development and progression have been investigated. Full discussion of the literature relating to each individual factor is beyond the scope of this thesis, however, in brief, milk, dairy, calcium, high doses of zinc, saturated fats, grilled

meats and heterocyclic amines have been associated with increased risk, whilst tomatoes, carotenoids, cruciferous vegetables, vitamin E, selenium, fish, soy, isoflavones and polyphenols may confer a protective effect (Chan et al., 2005). However, the quality of such evidence is low, with few randomised trials.

1.3.1.4.5 Hormones

Given that testosterone and DHT play fundamental roles in prostate growth and homeostasis, as well as early observations that surgical castration leads to regression of advanced prostate cancer (Huggins and Hodges, 1941), the role of androgens in the development of prostate cancer has been extensively investigated. A number early in vitro and in vivo studies using established cell lines and animal models supported this hypothesis, with androgen stimulation shown to promote cancer proliferation and growth whilst withdrawal leading to apoptosis and tumour regression (Kyprianou et al., 1990, Bladou et al., 1996, Webber et al., 1996). However, despite these observations, clinical studies exploring the association between serum androgen concentration and prostate cancer have reported contradictory outcomes. The largest pooled analysis of epidemiological studies was undertaken by the Endogenous Hormones and Prostate Cancer Collaborative Group in 2008, which included 3886 men with prostate cancer and 6438 controls, and failed to demonstrate any association between risk of prostate cancer and serum testosterone or DHT concentration (Endogenous Hormones and Prostate Cancer Collaborative Group, 2008). Furthermore, the use of testosterone supplementation in patients with hypogonadism has not been demonstrated to increase the risk of prostate cancer (Fernández-Balsells et al., 2010). Nevertheless, two randomised clinical trials of 5-alpha reductase enzyme inhibitors, finasteride and dutasteride, which prevent conversion of testosterone to DHT, demonstrated reduced incidence of prostate cancer in the treatment groups (Thompson et al., 2003, Andriole et al., 2010). Interestingly the reduction in incidence was only seen for low-grade prostate cancer, with an absolute increase in incidence of high-grade tumours observed in those treated (Theoret et al., 2011). As a consequence, 5-alpha reductase inhibitors are not currently licenced for prostate cancer prevention.

1.3.2 Detection and diagnosis

The clinical spectrum of prostate cancer ranges from low-grade localised disease that is detected via screening in an otherwise asymptomatic patient through to symptomatic, high-grade locally advanced or metastatic disease that is associated with significant morbidity and mortality. In England 14% of men have metastatic disease at the time of diagnosis, whilst 42% have high risk localised or locally advanced disease and the remaining 39% and 6% have intermediate or low risk localised disease respectively (National Prostate Cancer Audit, 2021). These figures vary worldwide, largely as a result of differences in screening practices, with only 6% of patients in the US, in which PSA based screening

is commonplace, presenting with metastatic disease (National Cancer Institute: Surveillance Epidemiology and End Results Programme, 2018). Although diagnostic pathways differ from centre to centre, the current approach generally involves a man in whom there is a clinical suspicion of prostate cancer, based on either an elevated PSA or abnormal feeling prostate on digital rectal examination (DRE), undergoing a combination of both multiparametric magnetic resonance imaging (mpMRI) of the prostate and needle biopsy via either the transrectal or transperineal route. On the contrary, patients with more advanced disease may present in a plethora of ways, such as with obstructive renal failure or metastatic spinal cord compression. As a result, the diagnostic evaluation of patients with advanced disease warrants a differing, patient specific approach based upon the individual case in question. As such, this section only relates to the diagnosis of patients in whom there is a clinical suspicion of localised prostate cancer.

1.3.2.1 Digital rectal examination

As approximately 70% of tumours develop in the peripheral zone of the prostate, larger tumours in this region may be palpable on DRE (McNeal et al., 1988). However, many tumours are not clinically palpable either due to their small size or anatomical location within the prostate, such as those that are in the anterior region of the gland. A study comparing PSA and DRE in 6630 male volunteers prior to the introduction of more contemporary diagnostic techniques found that only 18% of cancers were identified on DRE alone, regardless of PSA (Richie et al., 1993). The diagnostic sensitivity of an abnormal DRE was increased when combined with serum PSA, with a similar study conducted in 22513 volunteers reporting the positive predictive value to range from 5% in men with a PSA of 0 - 1 ng/ml to 30% in men with a PSA of 2.6 - 4.0 ng/ml (Carvalhal et al., 1999). Furthermore, additional studies have demonstrated that tumours detected by DRE are associated with adverse pathological features such as higher Gleason grade, therefore suggesting that whilst DRE alone should not be considered a screening test for prostate cancer in an asymptomatic patient, those found to have an abnormal DRE should undergo further diagnostic evaluation (Okotie et al., 2007, Gosselaar et al., 2008).

1.3.2.2 Prostate specific antigen

As discussed in Section 1.1.2, PSA is produced by prostate epithelial cells and plays an important role in the liquefaction of semen. In diseases of the prostate that disrupt tissue architecture such as prostate cancer, PSA is secreted into the circulation and can be detected using laboratory assays. However, whilst serum PSA testing has revolutionised the detection of prostate cancer (Stamey et al., 1987), the fact that it is organ- and not tumour-specific means that PSA levels are also increased in other prostatic conditions such as prostatitis and benign prostatic enlargement. As such, pooled analyses have demonstrated an elevated PSA of above 4 ng/ml to have a sensitivity of 21% and 51%

for the diagnosis of any and high-grade prostate cancer respectively, with a specificity of 91% (Wolf et al., 2010). Nevertheless, the higher the PSA, the more likely a diagnosis of prostate cancer, with increasing levels correlating with increased chance of locally advanced or metastatic disease. For example, in one study of 187 men, the positive predictive value of a PSA greater than 30 ng/ml was 95.7%, rising to 98.5% for values greater than 50 ng/ml (Gerstenbluth et al., 2002). On the contrary, men with a low PSA may also have prostate cancer. For example, of the 2950 men in the placebo group of the Prostate Cancer Prevention Trial that had a PSA of less than 4.0 ng/ml throughout the seven year follow up period, 15.2% were found to have prostate cancer at the end of study biopsy, with 1.6% having high-grade disease (Thompson et al., 2004).

Whilst PSA is a valuable tool in the detection and diagnosis of prostate cancer in asymptomatic men, it is not capable of differentiating between clinically significant and insignificant disease. For this reason, the use of PSA in screening for prostate cancer remains controversial and has been the focus of several large clinical studies. A systematic review and meta-analysis of five randomised controlled trials including 721718 participants, including those in the Cluster Randomised Trial of PSA Screening for Prostate Cancer (CAP) undertaken in the UK, was performed by Ilic et al. in 2018. Whilst PSA screening was found to increase detection of prostate cancer of any stage (incidence rate ratio (IRR) 1.23, 95% CI 1.03-1.48), it had no effect on all-cause mortality (incidence rate ratio (IRR) 0.99, 95% CI 0.98-1.01) and little or no effect on prostate cancer specific mortality (IRR 0.96, 95% CI 0.85-1.08) (Ilic et al., 2018). However, several of these studies were considered to be low quality, with European Randomised Study of Screening in Prostate Cancer (ERSPC) heralded as the only trial at low risk of bias. In this study men between 50 - 74 years from eight European countries were randomised to PSA screening versus no screening, with those found to have a PSA ≥ 3.0 ng/ml being offered a standard transrectal biopsy (Schröder et al., 2014). In this study, screening resulted in an increase in detection of prostate cancer of any stage, with a relative risk reduction in prostate cancer specific mortality of 21% over 13 years of follow up. Despite this the number needed to be screened to avert one death from prostate cancer was 781, meaning a large number of men would be exposed to the risks of biopsy, as well as the issues associated with overdiagnosis and overtreatment of clinically insignificant disease, in order to save one life. Consequentially, widespread screening for prostate cancer is not undertaken in the UK.

However, there is emerging evidence to support use of PSA screening programmes specifically within those men with increased risk of prostate cancer development, such as those with mutations in DNA damage repair genes. For example, the IMPACT study explored the use PSA screening within men

harbouring germline *BRCA1* and *BRCA2* gene mutations. After three years of screening, men harbouring a *BRCA2* mutation were found to have a higher incidence of prostate cancer (19.4 versus 12.0 cases per 1000 person years), a younger age at diagnosis (61 versus 64 years) and a higher proportion of clinically significant tumours (77% versus 40%), thereby supporting the use of selective screening in this cohort (Page et al., 2019).

1.3.2.3 Multiparametric magnetic resonance imaging

mpMRI is a variant of magnetic resonance imaging that combines anatomic T2 weighted sequences with two functional sequences, diffusion weighted imaging (DWI) and dynamic contrast enhanced imaging (DCE). These sequences are then evaluated using a standardised approach termed the Prostate Imaging-Reporting and Data System (PI-RADS) and allocated a score reflecting the likelihood of clinically significant cancer, ranging from 1 (very low) to 5 (very high) (Barentsz et al., 2016, Weinreb et al., 2016). Studies correlating mpMRI with radical prostatectomy specimens have demonstrated that it carries a high level of sensitivity for the detection of larger tumours of Gleason grade 3+4=7 and above, but is relatively poor at identifying those of Gleason grade 3+3=6 that are less than 0.5 cc (Bratan et al., 2013, Le et al., 2015). More recently the PROMIS trial explored the diagnostic efficacy of mpMRI compared with conventional transrectal ultrasound (TRUS) guided prostate biopsy in 576 men with suspected prostate cancer, using transperineal template biopsy as the reference standard. Whilst the authors reported mpMRI to have a 93% sensitivity and 41% specificity for detection of clinically significant cancer (defined as Gleason 4+3=7 or higher, or maximum cancer core length of 6mm or more), sensitivity fell to 87% when the definition of clinically significant cancer was changed to Gleason of 3+4=7 or more or core length greater than 4mm (Ahmed et al., 2017). Subsequent analysis has estimated that between 11 - 28 out of 100 patients with a low-risk mpMRI actually have an underlying diagnosis of clinically significant cancer, therefore mandating that these patients must be counselled thoroughly prior to declining subsequent biopsy on account of the MRI findings alone (National Institute for Health and Care Excellence, 2021).

A further application of mpMRI is its use in guiding prostate biopsy via either cognitive fusion (whereby the practitioner uses the mpMRI images in conjunction with real-time TRUS to locate the lesion), MRI-ultrasound fusion (whereby specialist software merges the MRI images with real-time TRUS images) and in-bore biopsy (in which a biopsy is taken using real-time MRI guidance). Several studies have shown that in comparison to standard systematic TRUS guided biopsy, MRI guided biopsy strategies result in increased diagnosis of clinically significant cancers, with a reduction in the number of clinically insignificant cancers (Siddiqui et al., 2013, Siddiqui et al., 2015, Gayet et al., 2016). These findings were

confirmed in the recently published randomised multicentre non-inferiority PRECISION trial of mpMRI guided biopsy versus standard TRUS biopsy in 500 biopsy naïve men with elevated PSA, abnormal DRE or both. In the MRI guided biopsy group, those with a PI-RADS score of 3 or greater underwent targeted biopsy. Diagnosis of clinically significant cancer, defined as Gleason 3+4=7, was higher in those men that underwent targeted biopsy (38% versus 26%) whilst diagnosis of insignificant cancer was lower (9% versus 22%) (Kasivisvanathan et al., 2018).

Despite this evidence, only 87% and 67% of men in England and Wales underwent pre-biopsy mpMRI in respectively in 2017-18 (National Prostate Cancer Audit, 2018). However, in their recently updated guideline on the diagnosis and management of prostate cancer, the National Institute for Health and Care Excellence (NICE) now recommended that patients with suspected localised prostate cancer are offered mpMRI as the first-line investigation, and that mpMRI influenced prostate biopsy be offered to all patients with a Likert score (an alternative to PI-RADS) of 3 or more (National Institute for Health and Care Excellence, 2021).

1.3.2.4 Prostate biopsy

Acquisition of tissue for histology is essential for the diagnosis and risk stratification of patients with prostate cancer. Given the anatomical location of the prostate and that the majority of tumours arise within the PZ, ultrasound guided prostate biopsy via the transrectal route has long been the standard of care throughout the world. However, comparison studies with radical prostatectomy specimens have demonstrated that transrectal ultrasound (TRUS) guided biopsy is relatively poor at estimating both tumour location and grade (Schulte et al., 2008, Sinnott et al., 2012), with a meta-analysis performed by Cohen et al. in 2008 demonstrating Gleason grade of tumours to was increased in 30% of patients that underwent radical prostatectomy following histological examination of the radical specimen (Cohen et al., 2008). Furthermore, in the aforementioned PROMIS trial, TRUS biopsy had a sensitivity of only 48% for the diagnosis of clinically significant cancer when compared with transperineal template biopsy (Ahmed et al., 2017).

Given the limitations of conventional TRUS biopsy, a number of alternative approaches have been explored. These include transperineal template biopsy, in which needle biopsies are taken systematically through the perineum using real-time image guidance. This technique has been shown to be superior to TRUS biopsy in terms of establishing both tumour location and grade (Barzell et al., 2012, Hu et al., 2012). Furthermore, transperineal biopsy provides improved anterior sampling, with prostate cancer detected in 24 (26%) of 92 patients with at least two prior negative TRUS in one

reported series, of which 83.3% were in the anterior gland (Mabjeesh et al., 2012). However, whilst studies have also shown a reduction in major complications compared with TRUS biopsy, transperineal biopsy is more time consuming and complex, often requiring regional or general anaesthesia (Guo et al., 2015). As a consequence, only 17% and 7% of men underwent biopsies via this approach in England and Wales respectively in 2017-18, with the technique largely reserved for patients in whom the initial TRUS biopsy is negative but there remains a high suspicion of prostate cancer (National Prostate Cancer Audit, 2018).

1.3.3 Classification: grading and staging

Prostate cancer can be classified in several ways. In general terms it can be classified as localised (contained within the gland), locally advanced (extending beyond the gland) and metastatic (disease that has disseminated to other sites, most commonly lymph nodes and bones). More detailed classification is based on the grade and stage of disease, as discussed below.

1.3.3.1 Gleason grade

Whilst most malignant diseases are graded according to the appearance of individual cancer cells on microscopy, grading of prostate cancer is based upon the architectural pattern of the tumour at low magnification. This approach was first described by the American Pathologist, Donald F Gleason in 1966 and is hence termed the Gleason grade (Gleason, 1966). Prostate adenocarcinomas are classified according to the shape and differentiation of glands, allocating a score from 1 (small, uniform well differentiated glands) through to 5 (occasional glands or sheets comprising of poorly differentiated/anaplastic cells), with the cytological features of individual cells bearing no importance, as shown in ***Figure 1.5***. Since grades 1 and 2 are seldom ever seen on needle biopsy, contemporary practice involves grading tumours from 3 to 5 only. In recognition of the heterogeneity and multifocal nature of the disease, two scores are allocated per specimen; the primary Gleason score (the most prevalent pattern) and secondary Gleason score (the second most prevalent pattern), which are then combined to give a total score.

The original scoring system described by Gleason in 1966 has been updated following conferences of the International Society of Urological Pathology (ISUP) in 2005 and 2014 (Epstein et al., 2005, Epstein et al., 2016a). Following the latter, a new five 'grade group' system has been introduced in order to address issues with the conventional Gleason grading system, with groups ranging from 1 (Gleason 6) through to 5 (Gleason 9 or 10) (Epstein et al., 2016b). One important aspect of this new approach is separation of Gleason 7 disease into grade group 2 (Gleason 3+4=7) and grade group 3 (Gleason 4+3=7) on account of their markedly different natural history and prognosis (McNeal et al., 1990,

Epstein et al., 1993). Collectively both the Gleason grade and ISUP grade group play an important role in both risk stratification and treatment decision making in patients with prostate cancer.

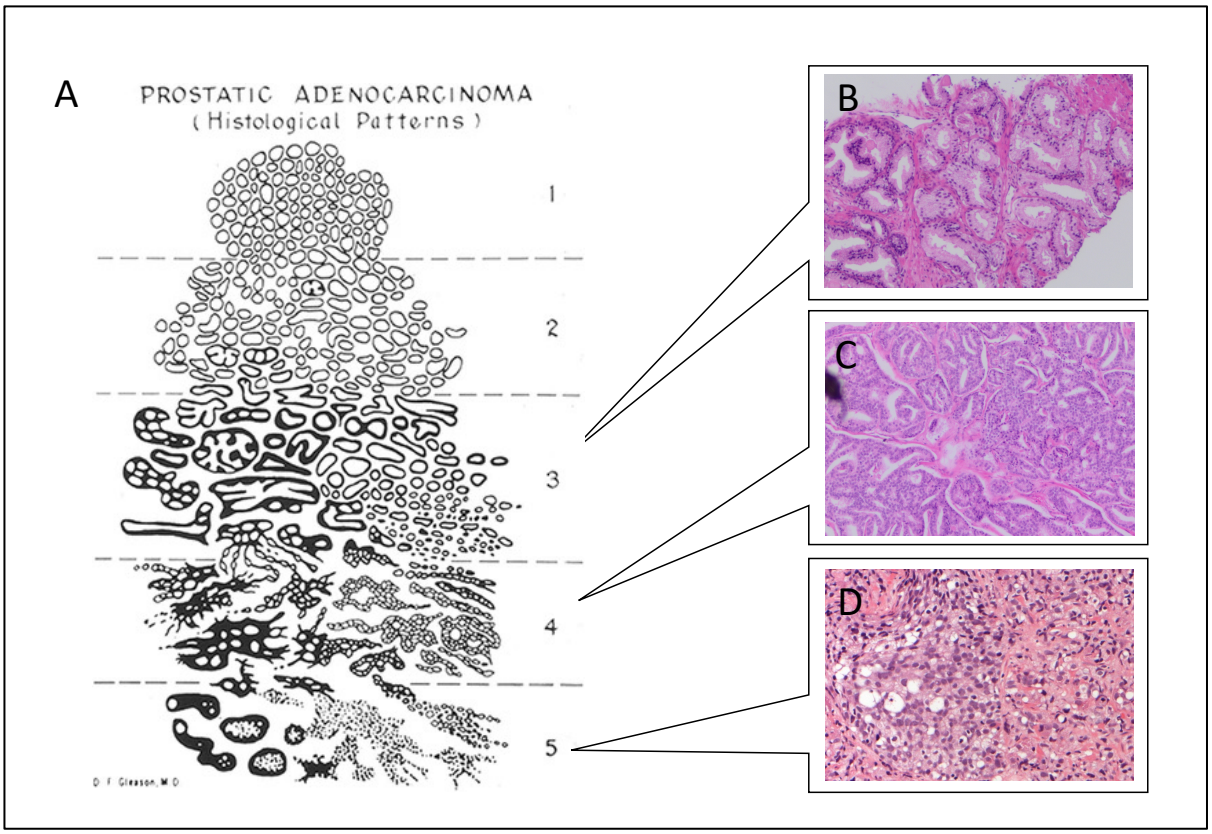

Figure 1.5: *Gleason grading of prostate adenocarcinoma.* A: Original diagram of Gleason patterns 1 – 5 as illustrated and published by Gleason in 1966, adapted from (Gleason, 1966). B-D: H&E stained sections of human prostate cancer at low power demonstrating Gleason pattern 3 (B), Gleason pattern 4 (C) and Gleason pattern 5 (D). All images courtesy of Dr Hywel Thomas, Consultant Urological Pathologist, University Hospital of Wales, Cardiff.

1.3.3.2 Stage

As with several other solid malignancies, adenocarcinoma of the prostate is staged using a specific variant of the Union for International Cancer Control (UICC) Tumour, Node, Metastases (TNM) system, as illustrated in ***Table 1.1***. The T stage (T) denotes the local extent of the tumour and ranges from T1 (incidental prostate cancer detected following TURP or needle biopsy) through to T4 (invading adjacent structures such as bladder neck and rectum). Node status (N) refers to metastases involving regional lymph nodes (N1) whilst metastases status (M) refers to the presence of distant metastases, most commonly non-regional lymph nodes (M1a) and bone (M1b). Each component may be determined using a range of diagnostic modalities. For example, the T stage may be determined clinically via digital rectal examination (termed the clinical stage, denoted as cT), via appearances on

MRI, or on evaluation of the radical prostatectomy specimen if the patient undergoes surgery (termed the pathologic stage, denoted as pT).

Table 1.1: *Union for International Cancer Control (UICC) TNM staging of prostate cancer (Version 8).* Adapted from (Brierley et al., 2017). TURP; transurethral resection of prostate.

Primary tumour (T)		
Tx	Primary tumour cannot be assessed	
T0	No evidence of primary tumour	
T1	Clinically inapparent tumour not palpable or visible on imaging	
	T1a	*Incidental histological finding in 5% or less of tissue resected at TURP*
	T1b	*Incidental histological finding in more than 5% of tissue resected at TURP*
	T1c	*Tumour identified by needle biopsy*
T2	Tumour confined within the prostate	
	T2a	*Tumour involves one half of one lobe or less*
	T2b	*Tumour involves more than half of one lobe*
	T2c	*Tumour involves both lobes*
T3	Tumour extends through the prostate capsule	
	T3a	*Extraprostatic extension including microscopic bladder neck involvement*
	T3b	*Tumour invades the seminal vesicles*
T4		Tumour invades adjacent structures other than seminal vesicles
Regional lymph nodes (N)		
NX	Regional lymph nodes cannot be assessed	
N0	No regional lymph node metastases	
N1	Regional lymph node metastases	
Distant metastases (M)		
M0	No distant metastases	
M1	Distant metastases	
	M1a	*Non-regional lymph node(s)*
	M1b	*Bone(s)*
	M1c	*Other site(s)*

1.3.4 Prognostic factors and risk stratification

Treatment decision making in men with newly diagnosed prostate cancer requires careful consideration of its natural history combined with the risk of progression to disseminated and potentially fatal disease. Despite improvement in diagnostic techniques and an increase in our understanding of the pathobiology of the disease, Gleason grade has stood the test of time and

remains one of the most powerful prognostic indicators in newly diagnosed prostate cancer (Mellinger et al., 1967, Epstein et al., 1996, Albertsen et al., 1998, Barry et al., 2001, Egevad et al., 2002). Gleason 3+3=6 disease has a predominantly indolent natural history, with most patients able to safely embark on a surveillance based management strategy with avoidance of the risks of radical treatment. However, surveillance cohorts in whom there has been long term follow up demonstrate that a small population of patients with Gleason 3+3=6 disease do develop progression and/or metastases, although the absolute numbers are small and the biological mechanisms underpinning them unclear (Klotz et al., 2015). Increasing Gleason grade is associated with increasing risk of prostate cancer specific mortality. For example, in one retrospective study of 767 men with localised prostate cancer that were managed conservatively, prostate cancer specific mortality rate over 20 years follow up was 65 per 1000 person-years for those with Gleason 7 disease and 121 per 1000 person-years for those with Gleason 8-10 disease (Albertsen et al., 2005). Furthermore, increasing Gleason grade is also associated with higher rates of biochemical recurrence following radical treatments (Khan et al., 2003).

In 1998, D'Amico and colleagues described a three-group risk classification system combining the individual prognostic powers of PSA, Gleason grade and tumour stage to predict biochemical recurrence following radical prostatectomy or radiotherapy with curative intent in men with non-metastatic prostate cancer (D'amico et al., 1998). Risk groups were defined as low, intermediate and high, as outlined in ***Table 1.2***. As with Gleason grade, this system has stood the test of time and undergone validation using large prospectively collected datasets and has proved predictive of not only recurrence but also prostate cancer specific mortality (Boorjian et al., 2008). As such it remained an integral part of clinical practice in the UK for many years. More recently a new five-tiered system has been published, termed Cambridge Prognostic Groups (***Table 1.3***), which has been shown to possess superior discrimination compared to the three-tiered D'Amico system in predicting prostate cancer mortality across different age and treatment groups (Gnanapragasam et al., 2018). As such this system has been recommended for use by cancer multidisciplinary teams in the UK in the most recent amendment of guidance published by NICE (National Institute for Health and Care Excellence, 2021).

Unsurprisingly, outcomes for men presenting with metastatic prostate cancer are poorer than for those presenting with localised or locally advanced disease. The control arm of the Systemic Therapy in Advancing or Metastatic Prostate Cancer: Evaluation of Drug Efficacy (STAMPEDE) trial of men presenting with advanced and metastatic prostate cancer has provided insight into the natural history in the contemporary treatment era. An analysis of the cohort of patients with newly diagnosed M1 disease treated with androgen deprivation therapy (ADT) demonstrated a median overall survival of

42 months, with survival time influenced by performance status, age, Gleason grade and distribution of metastases (James et al., 2015). Interestingly, median failure-free survival, which indicates the time to development of castrate resistant prostate cancer (CRPC), was only 11 months, indicating that most patients spend the majority of their remaining life in a state of castration resistant relapse (James et al., 2015).

Unlike in men with localised or locally advanced disease, prognostication in the metastatic patient group has been less well studied. In an analysis of patients with newly diagnosed metastatic prostate cancer using the Southwest Oncology Group trial cohort, lower metastatic burden, absence of bone pain, lower Gleason score and lower PSA were all found to be independent predictors of increased survival (Tangen et al., 2003). However, whilst 98% of patients that died in the first 5 years of follow up were correctly predicted using the statistical model, only 13% of those that lived beyond 10 years were correctly predicted. These factors must therefore be taken into consideration when counselling men with newly diagnosed metastatic disease prior to instigation of treatment.

Table 1.2: *D'Amico risk stratification of prostate cancer, as described in 1998 (D'amico et al., 1998).*

Risk	**PSA (ng/ml)**		**Gleason score**		**Clinical stage**
Low	<10	and	≤6	and	T1a-T2a
Intermediate	10-20	or	7	or	T2b
High	>20	or	8-10	or	≤T2c

Table 1.3: *Cambridge Prognostic Group stratification of prostate cancer, as described in 2018 (Gnanapragasam et al., 2018).*

Group	Criteria
1	Gleason score 6 **and** PSA less than 10 µg/L **and** Stages T1-T2
2	Gleason score 3+4=7 **or** PSA 10–20 µg/L **and** Stages T1-T2
3	Gleason score 3+4=7 **and** PSA 10–20 µg/L **and** stages T1-T2 **or** Gleason 4+3=7 **and** stages T1-T2
4	*One of:* Gleason score 8, PSA more than 20 µg/L, stage T3
5	*Two or more of:* Gleason score 8, PSA more than 20 µg/L, stage T3 **or** Gleason score 9 or 10 **or** Stage T4

1.3.5 Contemporary prostate cancer treatment

1.3.5.1 Treatment of low and intermediate risk localised prostate cancer

Tumours that are confined to the prostate (T1-2) are termed localised prostate cancer. Given the heterogeneity of disease at this end of the spectrum, a diverse array of treatment options are available, ranging from conservative management in the form of active surveillance (AS) through to more invasive radical treatments such as radical prostatectomy (RP) and external beam radiotherapy (EBRT). The decision of which treatment is most suitable for a particular patient is complex and must take several different factors into account including patient preference and fitness, treatment outcomes and side effect profile, and importantly, disease risk category.

1.3.5.1.1 Conservative treatment

Conservative treatment and its associated terminology vary substantially in the published literature and hence definitions have changed over time. Initially termed ‘watchful waiting’ or ‘deferred therapy’ in the pre-PSA era, this referred to avoiding local treatment and instead monitoring patients with

physical examination and nuclear medicine bone scan, with initiation of ADT if there was evidence of disease progression (Chodak and Warren, 2006). However, following introduction of PSA testing, a greater proportion of men are diagnosed with localised disease, leading to a better understanding of the natural history of prostate cancer and a paradigm shift in the use of conservative treatment.

For men with localised disease who would be suitable for other radical treatments on the basis of fitness and estimated life expectancy of greater than 10 years, conservative treatment is now termed 'active surveillance' (AS). This is based on the premise that a number of men will have indolent tumours that are slow growing, with a low risk of progression, metastasis and prostate cancer associated mortality (Albertsen et al., 2005). Whilst protocols differ between institutions, those patients opting for AS generally undergo close PSA surveillance with restaging investigations such as mpMRI and repeat biopsy at set intervals. In the UK this entails PSA testing every 3-4 months in the first year, with repeat DRE at 12 months and mpMRI at 12-18 months, followed by PSA testing and repeat DRE every 6 and 12 months thereafter respectively (National Institute for Health and Care Excellence, 2021). If the patient expresses a preference or if there is evidence of disease progression, as indicated by increasing PSA, increasing clinical or radiological stage or increasing Gleason grade or tumour volume on repeat biopsy, then radical treatment options may be offered. The major advantage is avoidance of unnecessary radical treatment and therefore the associated risks of erectile dysfunction, incontinence or radiotherapy related bowel or bladder complications.

A number of observational studies have reported outcomes in men with localised disease managed with AS. However, direct comparisons are limited due to significant variation in terms of patient selection, follow up and triggers for intervention. In a recently published systematic review of 10 contemporary studies, the proportion of patients discontinuing AS and undergoing delayed curative treatment over 10 years ranged from 40 – 59%, with the 10-year prostate cancer specific survival reported to be between 96 – 100% for patients with both low and intermediate risk disease (Thomsen et al., 2014). To date there have been no formal randomised controlled trials comparing contemporary AS to radical treatment. The closest comparison was that reported in the Prostate Testing for Cancer Treatment (ProtecT) trial of 1643 men with newly diagnosed localised prostate cancer (of whom the majority had low-risk disease) that were randomised to Active Monitoring (AM), RP or EBRT. Whilst the AM arm of the trial comprised a less intensive surveillance strategy than is employed in current AS protocols, 54.8% of men went on to receive radical treatment within 10 years follow up and there was no significant difference in prostate cancer specific mortality when compared with surgery or radiotherapy (1.5 deaths per 1000 person-years versus 0.9 and 0.7 respectively, P=0.48) (Hamdy et

al., 2016). However, higher rates of disease progression and double the rate of metastases were seen in those that underwent AM, thereby supporting the need for comprehensive patient counselling prior to embarking on a surveillance-based management approach.

On the contrary, the term 'Watchful Waiting' is now reserved for those men that are not deemed likely to benefit from radical treatment on account of limited life expectancy, comorbidity and the prolonged natural history of the disease (Bruinsma et al., 2017). This is based on the observation that men with multiple comorbidities are more likely to die from causes other than prostate cancer within 10 years of diagnosis, even in the case of moderate or poorly differentiated disease (Albertsen et al., 2011). Consequently, these patients generally undergo a less intensive, patient specific surveillance approach, with palliative treatment such as ADT instigated when there is evidence of local symptoms or metastases.

1.3.5.1.2 Radical treatment

Radical treatments are those that aim to cure the patient of prostate cancer. The two main radical treatment options for men with localised disease are surgery in the form of RP and radiotherapy in the form of EBRT.

1.3.5.1.2.1 Radical prostatectomy (RP)

RP involves removal of the entire prostate and its capsule, along with the seminal vesicles with or without the regional lymph nodes (pelvic lymphadenectomy). The technique has evolved substantially since its first description in 1905 and is now performed laparoscopically, often using a robotic assisted approach. A small number of randomised trials have compared RP to other modalities in the setting of localised prostate cancer. Whilst the results of early studies such as the Scandinavian Prostate Cancer Group (SPCG-4) and the Prostate Cancer Intervention Versus Observation Trial (PIVOT) comparing RP to observation based approaches were conflicting (Wilt et al., 2017, Bill-Axelson et al., 2018), only 5 of 553 patients in the RP group of the ProtecT trial died from prostate cancer within the 10 years follow up, with no statistically significant difference in cancer-specific mortality between RP, EBRT or AM (Hamdy et al., 2016).

1.3.5.1.2.2 External beam radiotherapy (EBRT)

EBRT involves the use of ionising radiation in the form of X-rays to induce both direct and indirect DNA damage within tumour cells, resulting in cell death (Baskar et al., 2014). Since its introduction, radiotherapy for prostate cancer has evolved substantially on account of developments in technology

and studies addressing technical aspects such as radiation dose and number of fractions. The use and optimal duration of neoadjuvant and adjuvant ADT has also been investigated and is discussed later. Again, the ProtecT trial has been the only randomised controlled trial to directly compare EBRT with other modalities in localised prostate cancer (Hamdy et al., 2016).

A number of other radiation-based treatments are also available for men with localised prostate cancer, some of which are more established (e.g. brachytherapy), and others which are currently undergoing investigation and not in widespread use (e.g. proton beam therapy). A full discussion of these modalities and their evidence base is beyond the scope of this thesis and has been reviewed elsewhere (Vanneste et al., 2016).

1.3.5.1.3 Treatment decision making in low and intermediate risk localised prostate cancer

On account of the current evidence, men diagnosed with low-risk localised prostate cancer in whom radical treatment options are suitable should be empowered to make an informed choice between AS, RP and EBRT, based on full knowledge of the risks and benefits of each (National Institute for Health and Care Excellence, 2021). However, given that conservative management of intermediate risk localised prostate cancer is associated with higher likelihood of adverse outcomes including prostate cancer-specific mortality (Albertsen et al., 2005, Albertsen et al., 2011), these patients should predominantly be offered radical treatment (Mottet et al., 2017, National Institute for Health and Care Excellence, 2019).

1.3.5.1.4 Treatment of high risk localised and locally advanced prostate cancer

Tumours that have breached the capsule of the prostate (>T2) and those with associated pelvic lymph node involvement (N1) are defined as locally advanced (>T2). Given that the D'Amico criteria for high-risk localised disease includes clinical stage of T2c or greater, these patients may also be considered under this heading.

There have been a number of trials exploring the use of EBRT in the setting of high-risk localised and locally advanced prostate cancer. These include the Scandinavian Prostate Cancer Group-7 (SPCG-7) trial, which demonstrated a 17% reduction in 15-year prostate cancer-specific mortality in those men with intermediate or high-risk disease treated with EBRT and ADT compared with ADT alone (Fosså et al., 2016). The Medical Research Council PR07 trial of 1205 patients randomised to either ADT and EBRT or ADT alone validated these findings, with combination therapy resulting in a hazard ratio of 0.46 (CI 0.34 – 0.61) for prostate cancer mortality over a median follow up of 8 years (Mason et al., 2015). Based on these findings, a number of other trials have focussed on the timing and duration of ADT when combined with ERBT. The European Organisation for Research and Treatment of Cancer

(EORTC) trial of 1113 men with locally advanced prostate cancer reported increased 5-year survival for men treated with EBRT combined with long term ADT (3 years) when compared with short term ADT (6 months) (Bolla et al., 2009). A number of trials conducted by the Radiation Therapy Oncology Group (RTOG) sought to further determine the optimal regime of ADT in combination with RT, additionally reporting that 6 months of neoadjuvant ADT reduced the incidence of both PSA and local progression when compared with 3 months or EBRT alone (Denham et al., 2011). As such the current standard of care in the UK is to offer men opting for EBRT six months of neoadjuvant ADT followed by three years of adjuvant ADT (National Institute for Health and Care Excellence, 2021).

Whilst EBRT with ADT is currently regarded as the gold standard treatment for men with locally advanced prostate cancer, surgery may also have an important role as part of a multimodal approach. A number of studies have reported outcomes of RP in this patient group. Although these have not demonstrated a uniformly poor prognosis following surgery, rate of biochemical recurrence was generally high whilst 10-year cancer-specific survival varied significantly between series, ranging between 57-90% for men with clinically T3 disease (Gerber et al., 1997, Ward et al., 2005). Given these results, the use of adjuvant EBRT following RP in those at high risk of residual disease or recurrence, such as those with positive surgical margins, has been explored. Most recently the Radiotherapy and Androgen Deprivation in Combination After Local Surgery (RADICALS) trial, in which 1396 patients at high risk of biochemical recurrence after RP were randomised to either adjuvant radiotherapy or observation plus salvage radiotherapy if biochemical recurrence were to occur, reported equivalent 5-year biochemical progression free survival rates of 85% and 88% respectively (Parker et al., 2020). As such the authors concluded that an observation-based approach with salvage radiotherapy should be the current standard after RP in patients at high risk of biochemical relapse.

Similarly, the use of neoadjuvant and adjuvant ADT combined with RP has also been explored, with one randomised controlled trial reporting increased prostate cancer specific survival in men with lymph node positive disease that were treated with adjuvant ADT (Messing et al., 2006). However, a separate trial of adjuvant Bicalutamide following RP failed to demonstrate a significant increase in survival (McLeod et al., 2006), therefore indicating that the role, if any, of combined RP and ADT remains to be elucidated.

Patients with locally advanced disease or a PSA ≥ 20 ng/ml were excluded from the ProtecT trial and there have been no other high quality randomised trials comparing the various treatment modalities for this patient group. However, one retrospective study utilising Surveillance, Epidemiology and End

Results (SEER)-Medicare data reported 10 year prostate cancer specific-survival of 88.9% for RP with adjuvant EBRT compared with 74.2% for EBRT combined with ADT in men with T3a-b N0 disease (Jang et al., 2018). Therefore, despite EBRT with ADT being the current gold standard for the management of locally advanced disease, further well-designed randomised trials are required to determine the comparative efficacy of a contemporary multimodal approach involving surgery.

1.3.5.1.5 Treatment of metastatic prostate cancer

Following the pioneering work by Huggins and Hodges in 1941, ADT has been the mainstay of treatment for patients with metastatic prostate cancer. Whilst this was initially achieved through surgical castration, the isolation and purification of the decapeptide gonadotropin-releasing hormone (also termed lutenising hormone releasing hormone; LHRH) by Schally and colleagues in 1971 paved the way for the introduction of LHRH agonists as a form of pharmacological castration (Schally et al., 1971). These agents, together with the more recently developed LHRH antagonists such as Degarelix, suppress levels of circulating androgen through their action on the hypothalamic-pituitary-gonadal axis and form the mainstay of treatment for patients with newly diagnosed metastatic disease. A meta-analysis of randomised trials comparing Degarelix with conventional LHRH agonists demonstrated that a greater proportion of patients achieved castrate levels of testosterone within 28 days of commencing treatment with Degarelix (97% versus 45%), whilst both approaches equally maintained castrate levels for 364 days (Sciarra et al., 2016). Whilst immediate ADT in symptomatic patients is standard practice, the timing of treatment in asymptomatic patients is controversial. However, a systematic review conducted by Loblaw et al. in 2007 reported that immediate ADT resulted in a 17% decrease in relative risk of prostate-cancer specific mortality compared with delayed ADT in patients with metastatic disease, thereby suggesting the former to be the more efficacious approach (Loblaw et al., 2007).

Whilst ADT has been the standard of care for newly diagnosed metastatic disease for many years, the aforementioned STAMPEDE trial has, and continues to provide invaluable insight into the management of men with advanced disease. Landmark results include the significant survival benefit of up front docetaxel chemotherapy at the time of starting ADT, which was also reported by another large randomised trial (Sweeney et al., 2015, James et al., 2016), and the benefit of commencing abiraterone at the time of starting ADT (James et al., 2017). These findings have led to a paradigm shift in management in the UK and across the world, with docetaxel now offered up front to men with newly diagnosed metastatic disease in the absence of significant comorbidities (National Institute for Health and Care Excellence, 2021). More recently published findings include an overall survival benefit of prostate EBRT in patients with metastatic prostate cancer and a low metastatic burden; termed

oligometastatic disease (Parker et al., 2018). It is possible that this, when considered with the results of the currently recruiting TRoMbone study examining the benefit of RP and extended pelvic lymphadenectomy in patients with newly diagnosed metastatic disease (Sooriakumaran, 2017), may lead to further significant changes in the management of men with newly diagnosed metastatic prostate cancer.

1.3.5.1.6 Treatment of castrate resistant prostate cancer

ADT is a highly efficacious treatment for recurrent, advanced and metastatic prostate cancer, as reflected in the aforementioned median survival of 42 months in those men with newly diagnosed metastatic disease treated with ADT alone (James et al., 2015). However, despite this initial benefit, prostate cancer cells eventually become resistant to ADT, leading to the development of Castrate Resistant Prostate Cancer (CRPC). A number of mechanisms have been shown to underpin this transformation, including amplification or mutation of the *AR* gene, constitutive AR activation or overexpression, alternative splicing events and intra-tumoral androgen synthesis (Watson et al., 2015). CRPC is clinically defined as evidence of either biochemical or radiological progression despite a serum testosterone level of <50 ng/dL, and may occur both in patients with metastases (termed metastatic CRPC; mCRPC) or without metastases (termed non-metastatic CRPC; nmCRPC) (Saad et al., 2021). Precise characterisation of the epidemiology of CRPC has been hampered by variations in terminology and method of diagnosis that have led to difficulties in defining the patient population. In an effort to address these issues, Kirby and Crawford undertook a systematic review involving 71179 patients with CRPC, which identified that 10 - 20% of patients with prostate cancer develop CRPC within five years of follow up, of which over 84% had bone metastases at the time of diagnosis (Kirby et al., 2011). The survival of patients with CRPC ranged from 9 to 30 months in the 12 included studies, with a sample-weighted survival estimate of 14 months (Kirby et al., 2011). However, whilst advances in diagnosis and treatment of prostate cancer in recent years have continued to alter the landscape of CRPC, median survival remains only 22 months in contemporary clinical trials (James et al., 2015).

Traditionally, the first line treatment for men with CRPC was docetaxel chemotherapy, which leads to a modest improvement in median survival of 2.4 months when compared with the previously utilised regime of mitoxantrone and prednisolone (Tannock et al., 2004). More recently a number of newer agents, including the second-generation antiandrogens abiraterone and enzalutamide, have demonstrated survival benefit in men with CRPC. Abiraterone, which irreversibly blocks the CYP17A1 enzyme involved in the synthesis of androgens in the adrenal cortex, has been shown to increase overall survival by 3.9 months in patients with CRPC that have received chemotherapy and 4.4 months

in those that are chemotherapy naive (De Bono et al., 2011, Ryan et al., 2015). Similarly, the targeted AR inhibitor enzalutamide, which prevents AR translocation to the nucleus along with recruitment of cofactors and AR-DNA binding, has been shown to increase overall survival by 4.8 and 2.2 months in men that had been treated with chemotherapy or were chemotherapy naive respectively (Scher et al., 2012, Beer et al., 2014). On the basis of these studies, NICE currently recommends docetaxel as the first line treatment of option for patients with CRPC and a good performance status, with abiraterone and enzalutamide reserved for those with evidence of progression during or after chemotherapy (National Institute for Health and Care Excellence, 2021).

Despite such notable improvements in the treatment of localised, locally advanced and hormone sensitive metastatic prostate cancer, outcomes remain poor for men that have progressed to CRPC, even with use of these newer therapies. Whilst a number of other novel therapies have been developed, including the bone selective alpha radiation emitter Radium-223, and the autologous active cellular immunotherapy Sipuleucel-T, and others are in various phases of clinical development, these are often experimental, expensive and not widely available (Kantoff et al., 2010, Parker et al., 2013b). As such, there remains an urgent need to identify new, efficacious and cost-effective treatment options for this patient group.

1.4 Pathobiology of prostate cancer

Over the past few decades our understanding of cancer biology has expanded exponentially. Early observations described pathological changes in multiple tissues representing a spectrum from pre-malignant lesions to invasive cancer (Foulds, 1954). Several years later the genetic alterations underpinning such transformation began to be elucidated, with the observation that in malignancies such as colorectal cancer, mutations are acquired sequentially, leading to a predictable and reproducible sequence from adenoma to invasive carcinoma (Fearon and Vogelstein, 1990).

In simple terms, cancer is an acquired genetic disease resulting from multiple dynamic changes to the genome that include gain of function mutations which activate oncogenes and loss of function mutations which inactivate tumour suppressor genes. Collectively these lead to characteristic alterations in cell physiology that result in the phenotype of a cancer cell; termed the 'hallmarks of cancer' by Hanahan and Weinberg (Hanahan and Weinberg, 2000). These hallmarks include self-sufficiency in growth signals, insensitivity to anti-growth signals, tissue invasion and metastases, evasion of apoptosis, sustained angiogenesis and limitless replicative potential, with the later addition

of reprogramming of energy and metabolism and evasion of immune destruction (Hanahan and Weinberg, 2000, Hanahan and Weinberg, 2011).

A linear pathway of prostate cancer initiation and progression from prostatic intraepithelial neoplasia (PIN) to invasive carcinoma has been proposed, as demonstrated in ***Figure 1.6***. However, the relationship between PIN and invasive carcinoma has not been demonstrated conclusively and no single candidate tumour suppressor gene or oncogene has been definitively proven to be necessary for disease progression (Abate-Shen and Shen, 2000, DeMarzo et al., 2003, Gandhi et al., 2018). Furthermore, localised prostate cancer is often multifocal, with studies demonstrating independent foci to be genetically distinct (Bostwick et al., 1998, Macintosh et al., 1998). Given that the prevalence of latent prostate cancer is much greater than that of clinical prostate cancer (Breslow et al., 1977, Sánchez-Chapado et al., 2003, Soos et al., 2005) it is therefore thought that the prostate is the site of multiple concurrent neoplastic transformation events, most of which give rise to indolent disease that does not progress to become clinically significant. In contrast, metastatic prostate cancer has been shown to be clonal in origin (Liu et al., 2009), suggesting that advanced disease arises from the selective advantage of individual clones during progression (Shen and Abate-Shen, 2010).

Whilst the exact genetic and epigenetic changes that lead to progression of indolent prostate cancer to clinically significant disease are not fully understood, recent advances in sequencing technology have enabled us to identify the key genomic changes in both localised and metastatic tumours. Furthermore, the pooling of large genomic datasets in publicly available repositories such as cBioportal, developed by the Centre for Molecular Oncology, Memorial Sloan Kettering Cancer Centre (Cerami et al., 2012, Gao et al., 2013), have increased the validity of these observations. The 20 most common mutations in localised and metastatic prostate cancer, as identified using this resource, are given in ***Figure 1.7***. Whilst few mutations are present in the majority of cancers, alterations in particular signalling cascades such as the PTEN-PI3-Kinase-AKT-mTOR pathway, which is also dysregulated in a number of other cancers, are commonplace and have been implicated in disease progression and androgen independence (Shen and Abate-Shen, 2007, Papa and Pandolfi, 2019, Turnham et al., 2020).

Further to mutations in individual genes, larger chromosomal aberrations such as DNA copy-number alterations (either gain or losses of various chromosomal regions) are common in prostate cancer and appear to be increased in CRPC compared with localised disease (Hieronymus et al., 2014). These include *AR* gene amplification, which was found in 50.6% of the 804 CRPC samples in the

aforementioned pooled analysis using cBioportal, as well as *PTEN* homozygous deletion in 29.2%. Likewise, translocation events such as the fusion of the ETS transcription factor ERG with transmembrane protease serine 2 (TMPRSS2), which leads to the formation of the *TMPRSS2-ERG* fusion gene, are also commonly identified and proposed to be involved in disease progression, with this particular fusion identified in up to 20% of high grade PIN lesions and between 40-70% of invasive carcinomas (Tomlins et al., 2005, Cerveira et al., 2006, Rubin, 2012). Finally, epigenetic alterations such as those in DNA methylation and histone modification, which include the trimethylation of lysine residue 27 of histone H3 by the histone methyltransferase enzyme EZH2, have also been identified and are implicated in both prostate cancer development and progression (Ke et al., 2009).

As our knowledge of the molecular landscape of prostate cancer continues to develop it may reveal potential therapeutic targets and enable stratification of patients according to their likelihood of response. This may be of particular importance in CRPC, where outcomes remain poor. One recent example is the observation that mutations in genes encoding proteins involved in DNA damage repair (DDR) pathways such as *BRCA2* and *ATM* are enriched in CRPC , thereby providing a potential avenue for therapy using DDR inhibitors, as discussed in Section 1.6 (Abeshouse et al., 2015, Robinson et al., 2015, Armenia et al., 2018).

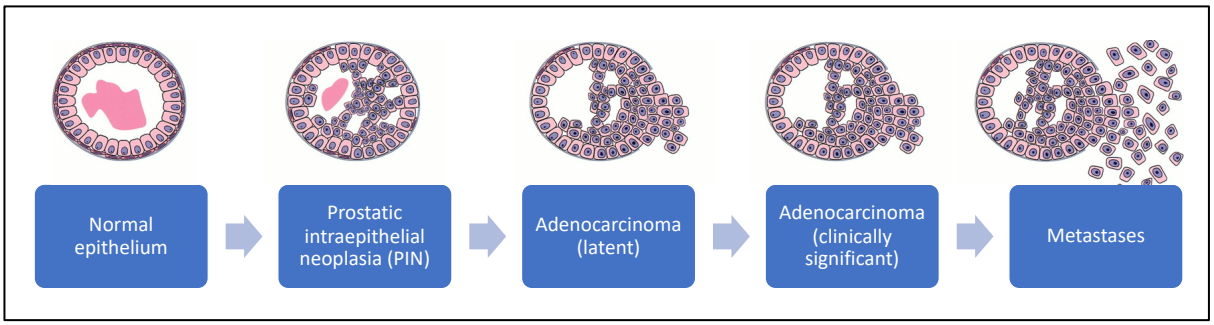

Figure 1.6: *Proposed pathway of human prostate cancer progression.* Adapted from (Shen and Abate-Shen, 2010).

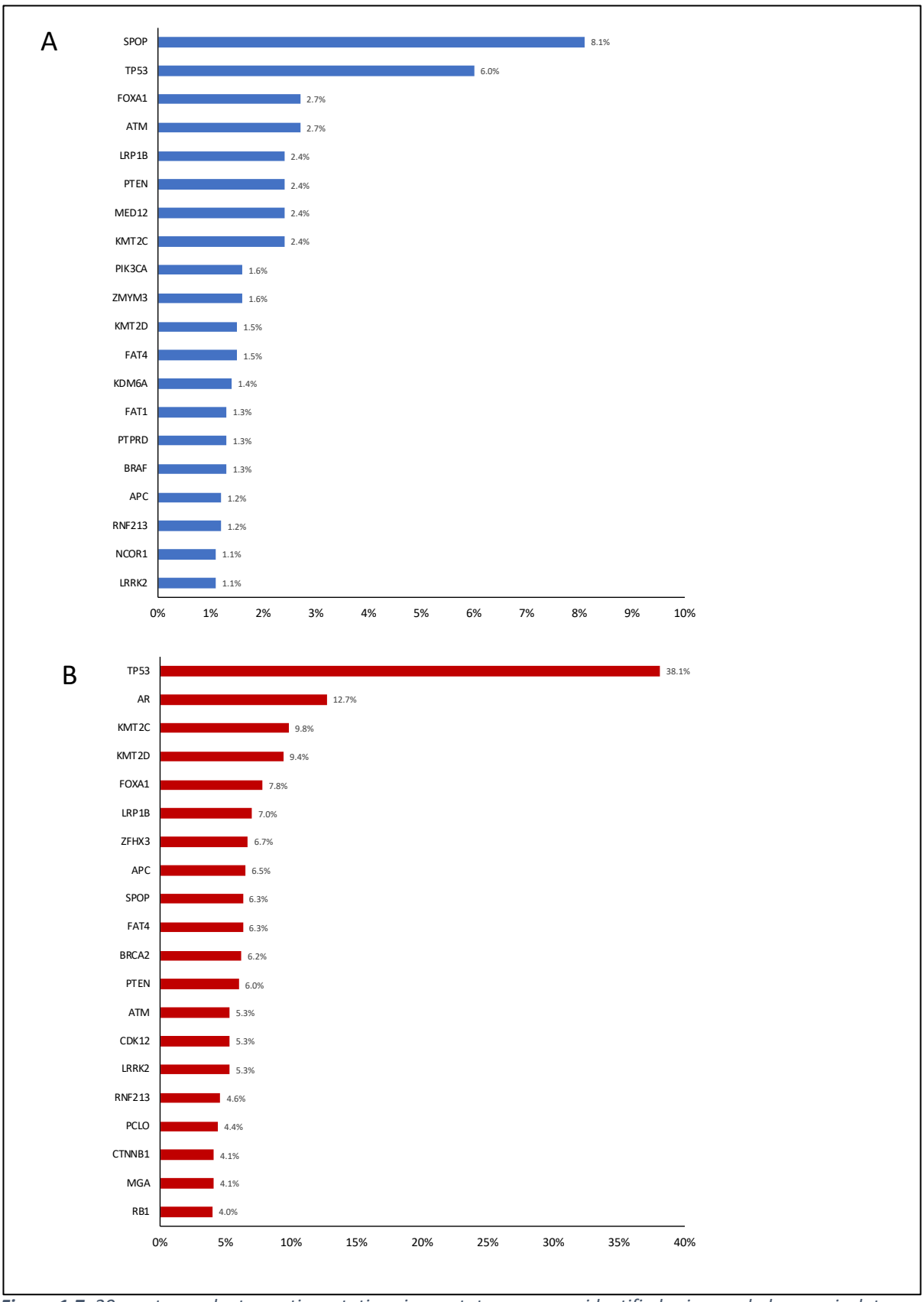

Figure 1.7: *20 most prevalent genetic mutations in prostate cancer, as identified using pooled genomic data from cBioportal.* A: Localised disease, 1357 samples (Barbieri et al., 2012, Baca et al., 2013, Hieronymus et al., 2014, Abeshouse et al., 2015, Fraser et al., 2017, Gerhauser et al., 2018, Ren et al., 2018). B: Metastatic castrate resistant disease, 796 samples (Grasso et al., 2012, Robinson et al., 2015, Kumar et al., 2016, Abida et al., 2019).

1.5 Preclinical models of prostate cancer

Preclinical research has been fundamental to developing our current understanding of prostate cancer pathobiology, as well as to the discovery of potential therapeutic targets and contemporary treatments. These models range in complexity from traditional established cell lines such as LNCaP, DU145 and PC-3 that were developed in the 1970's and 1980's, through to genetically modified mice in which oncogene and tumour suppressor gene function can by selectively altered in a tissue specific manner through use of Cre-Lox recombination technology (Cunningham and You, 2015, Huang et al., 2016). Each of the main preclinical models of prostate cancer are outlined in ***Table 1.4***, along with their advantages and limitations.

Table 1.4: *Overview of the spectrum of preclinical models used in prostate cancer research.* Adapted from (Cunningham and You, 2015, Huang et al., 2016, Rea et al., 2016, Fang and Eglen, 2017, Risbridger et al., 2018).

Model	Overview	Advantages	Limitations
2D culture of established cell lines	Immortalised cell lines established from tumour samples of patients with both localised and advanced disease.	1. Wide range of different cell lines available, each with specific genomic or phenotypic characteristics. 2. Infinite growth potential. 3. Easily cultured and manipulated. 4. Suitable for high throughput screening.	1. Some cell lines lack key features such as AR expression. 2. Lack of heterogeneity. 3. Absence of microenvironment components (immune cells, fibroblasts) or 3D architecture. 4. Poor predictor of clinical responses.
3D culture; spheroids and organoids	Established or primary cells are grown as freely floating cell aggregates or within an extracellular matrix gel, enabling formation of 3D structures termed spheroids. Organoids represent a specific form of spheroid defined as a collection of organ specific cell types that develop from stem cells or progenitors and self-organise in a manner similar to in vivo (Lancaster and Knoblich, 2014) .	1. Retain heterogeneity and in vivo like architecture. 2. Individual cells subject to less mechanical stress than 2D cultures. 3. Clinical data is often available for correlation. 4. Suitable for high throughput screening.	1. Low success rate and difficult to culture for an extended period. 2. Microenvironment not fully recapitulated and no immune influence. 3. Greater cost and complexity than 2D culture.

Patient derived explant culture (PDE)	Tissue obtained from patients directly, or following propagation as xenografts (PDX; discussed below) are cultured ex vivo. A number of approaches have been described, most commonly culture on a gelatin sponge half submerged in media (Risbridger et al., 2018)	1. Retain native tissue architecture and cell-to-cell signalling within the microenvironment. 2. Several proteins, circulating tumour DNA and exosome products can be detected in the media. 3. Enables ex vivo drug testing.	1. Limited viability, with most assays restricted to 48 hours. 2. Patient tissue is not readily available.
Cell line and patient derived xenografts (PDX)	Established cell lines or tumour tissue from a patient sample (PDX) are implanted into an immunodeficient mouse (e.g. athymic nude). Cells can be implanted subcutaneously, beneath the renal capsule or orthotopically into the prostate.	1. PDX models maintain heterogeneity and mutational status. 2. PDX models maintain stromal and tissue architecture of the original tumour. 3. Can be used for in vivo drug testing.	1. Cell line based xenografts do not demonstrate tumour architecture or microenvironment. 2. Time consuming and expensive, low engraftment success with primary prostate tumour specimens. 3. No immune influence.
Genetically Engineered Mouse Models (GEMM)	Specific genes of interest are knocked out either within the whole mouse (whole body knockout) or specific tissues (conditional knockout), or alternatively activated (gain of function). Specific gene manipulation can be achieved using tissue specific promoters, such as *Probasin* and *PSA* to drive expression of Cre-recombinase, which in turn excises genetic material between two *loxP* sequences.	1. Short gestation times. 2. Easy manipulation of gene expression. 3. Allow study of microenvironment and stromal interaction. 4. Immunocompetent. 5. May be used to model all stages of disease, including metastases.	1. Mouse prostate differs anatomically and mice rarely spontaneously develop prostate cancer, suggesting fundamental differences in biology. 2. Rarely metastasise to bone. 3. Limited translation to clinical setting.

1.6 DNA damage response pathways in prostate cancer

1.6.1 Overview of the DNA damage response

Cellular DNA damage events are commonplace, occurring as a result of either endogenous processes occurring during DNA metabolism (e.g. hydrolysis and deamination) or via the action of exogenous physical or chemical agents such as ionising radiation, drugs and toxins (Hoejmakers et al., 2006). In order to maintain genomic integrity and prevent malignant transformation, cells have developed a range of complex mechanisms with which to detect this damage and initiate downstream pathways that culminate in either cell cycle arrest, targeted repair/bypass of the damage or, if the former are not possible, bring about senescence or cell death (O'Connor, 2015). These pathways involve the DNA repair processes themselves, together with the systems responsible for their regulation and integration with the cell cycle, and are collectively known as the DNA damage response (DDR; outlined schematically in ***Figure 1.8*** (Pearl et al., 2015).

Five main DDR pathways have been described. Base excision repair (BER) corrects small base lesions such as modified bases, abasic sites and DNA single strand breaks (SSBs) that arise as a consequence of deamination, oxidation or alkylation caused by chemicals, ionising radiation and spontaneous DNA decay (Krokan and Bjoras, 2013). Nucleotide Excision Repair (NER) acts to remove a number of structurally unrelated DNA lesions, such as 6-4 pyrimidine-pyrimidone photoproducts (induced by ultraviolet radiation), bulky chemical adducts and intrastrand crosslinks (such as those caused by the chemotherapy agent cisplatin). Mismatch Repair (MMR) corrects DNA base-base mismatches that arise during normal DNA metabolism or aberrant DNA processing during replication, recombination and repair (Hoeijmakers, 2009). Homologous Recombination Repair (HR) is one of two major repair mechanisms for DNA double strand breaks (DSBs), highly toxic lesions that are induced by both endogenous and exogenous sources including replication errors, ionising radiation, genotoxic chemicals and collapsed replication forks (Krejci et al., 2012). The process of HR comprises a series of interconnected pathways that, through use of the sister chromatid as a template, culminate in the error free restoration of the original DNA code (Li and Heyer, 2008). Non-homologous end joining (NHEJ) is the other major repair mechanism for DSBs. Unlike HR, NHEJ mechanisms do not utilise a homologous template and therefore occur during all phases of the cell cycle, rather than being restricted to S and G2 phases alone (Davis and Chen, 2013). The lack of template renders classical NHEJ error prone, which in turn can lead to DNA rearrangements that may drive genomic instability and oncogenic transformation (Ceccaldi et al., 2016).

DDR pathways have attracted attention in recent years, with at least 450 proteins implicated, which can be broadly be divided into sensors, transducers, mediators and effectors (O'Connor, 2015, Pearl

et al., 2015). Aberration in several genes that mediate the DDR response have been identified in a number of different cancers, and although some have been well characterised and are directly causal, such as loss of function mutations in the mismatch repair genes *MSH2* and *MLH1* leading to hereditary non-polyposis colorectal cancer (HNPCC) (Hampel et al., 2005), the implications of many underlying defects are only partially understood. As mentioned previously, germline mutations in genes encoding BRCA1 and BRCA2, which are integral to the repair of DSBs via HR, are associated with higher grade prostate cancer at the time of diagnosis, as well as poorer cancer specific survival (Mitra et al., 2008, Gallagher et al., 2010, Castro et al., 2013).

A

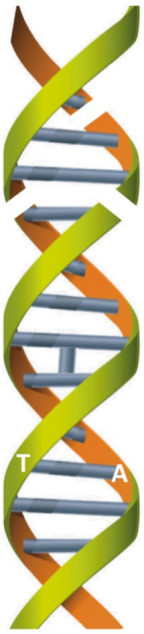

Type of damage	Damaging agents	Repair pathway	Example targets
Single strand breaks (SSBs)	Ionising radiation, Alkylating agents	Base excision repair (BER)	PARP, APE1
Double strand breaks (DSBs)	Ionising radiation, Topoisomerase inhibitors, Nucleoside analogues	Homologous Recombination (HRR) Non-Homologous End Joining (NHEJ)	ATR, ATM
Bulky adducts, Intrastrand crosslinks	UV light Platinum agents	Nucleotide Excision Repair (NER)	ERCC1 XP proteins Polymerases
Nucleotide substitutions, deletions, insertions	Errors during metabolism, replication, recombination and repair	MisMatch Repair (MMR)	MLH, MSH

B

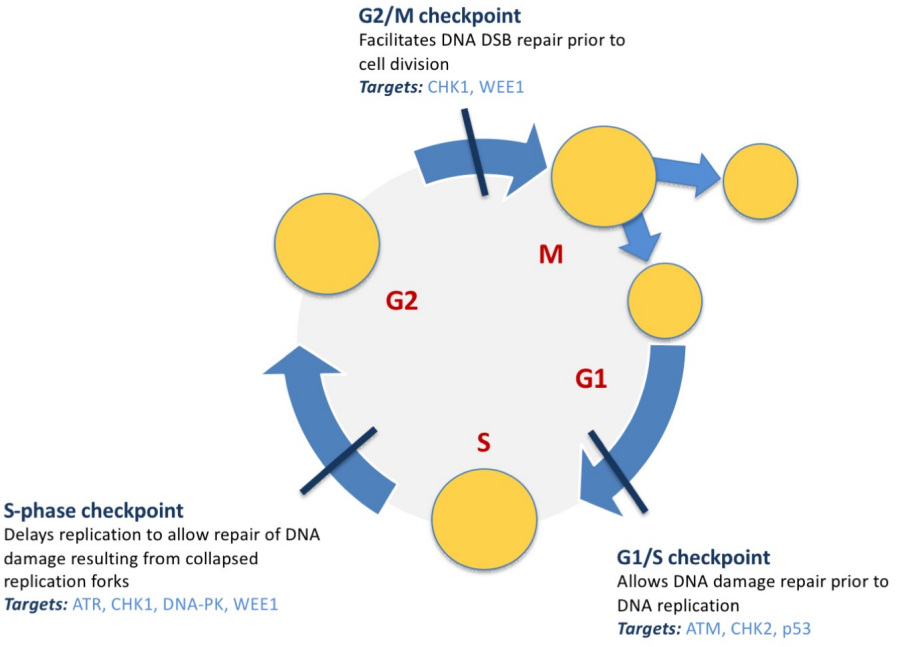

Figure 1.8: *DNA damage response (DDR) pathways.* A: Overview of the main DDR pathways, including potential therapeutic targets. B: Overview of key cell cycle checkpoints, their regulators and potential therapeutic targets. PARP, poly ADP-ribose polymerase; APE1, AP endonuclease 1; ATR, ataxia-telangiectasia and Rad3-related; ATM, ataxia-telangiectasia mutated; ERCC1, excision repair cross-complementation group 1; MLH, MutL homolog 1; MSH, MutS homolog 2, CHK1, checkpoint kinase 1; CHK2, checkpoint kinase 2; WEE1, WEE1 G2 checkpoint kinase; DNA-PK, DNA dependent protein kinase. Adapted from (O'Connor, 2015).

1.6.2 The DNA damage response and synthetic lethality

It is understood that whilst different forms of DNA damage trigger responses by specific DDR pathways, there is some redundancy within the DDR network that enables activation of other DDR pathways when the primary DDR pathway is absent, inactive or inhibited (Hoeijmakers, 2001, Garinis et al., 2008, Darzynkiewicz, 2011, Lans and Vermeulen, 2015). Therefore, if a cell has a full complement of repair pathways it is able to compensate for the loss of one pathway. However, subsequent loss of one or more additional pathways allows accumulation of mutations and further genomic instability, culminating in cell death; a process termed synthetic lethality. 'True' synthetic lethality occurs when a tumour harbours an existing germline or somatic DDR gene mutation and a second DDR pathway is targeted therapeutically. This concept is illustrated by the high sensitivity of *BRCA1/2* deficient tumours to poly(ADP-ribose) polymerase (PARP) inhibitors in patients with breast and ovarian cancer, as discussed in Section 1.6.3 (Lord et al., 2015, Lord and Ashworth, 2017). 'Contextual' synthetic lethality describes the situation in which two separate DDR pathways are therapeutically targeted to bring about the same effect in the absence of a pre-existing DDR mutation (O'Connor, 2015). Therefore, whilst being permissive of tumorigenesis, both DDR aberrations and functional DDR pathways also present therapeutic targets through either increasing sensitivity to DNA damaging agents such as radiotherapy or cytotoxic chemotherapy, or through induction of synthetic lethality by direct targeting of one or more arms of the DDR.

1.6.3 DNA damage response pathway aberrations in prostate cancer

Much of the characterisation of the genomic landscape of prostate cancer has focussed on DDR pathways. Whole-exome sequencing of a series of 333 localised prostate tumours by the Cancer Genome Atlas Research Network found that 62 (19%) had deleterious germline or somatic aberrations in genes involved in DDR pathways, including *BRCA2*, *BRCA1* and *ATM* (Abeshouse et al., 2015). These aberrations seem to be enriched in metastatic CRPC, with DDR gene alterations identified in 23% of 150 tumour biopsies in one series, the most common of which was *BRCA2* (13%) followed by *ATM* (7.3%) and *MSH2* (2%)(Robinson et al., 2015), and 33% of 49 patients in the TOPARP-A phase II clinical trial, again most commonly *BRCA2* (14.3%) (Mateo et al., 2015). However, the prevalence of DDR alterations in patients included in such studies varies depending on the number of genes assessed, the technique used and the characteristics of the patients (Lozano et al., 2021). The largest study to screen for DDR defects to date is the PROfound trial, a phase III study of the PARP inhibitor olaparib in men with mCRPC and DDR aberrations with evidence of disease progression whilst on second generation hormonal therapy (de Bono et al., 2020). Prior to randomisation, tumours of from 4425 patients were screened for defects in at least one of 15 prespecified DDR genes that are known to play

a role in HR. Of these, 2792 tumour samples were successfully sequenced and HR gene aberrations identified in 778 (28%), with similar frequencies in both primary tumours (27%) and metastases (32%). The most common aberrations were again those in *BRCA2* (8.7%), *CDK12* (6.3%) and *ATM* (5.9%), with alterations in two or more genes identified in 2.2% of cases (de Bono et al., 2020).

Interestingly, for germline mutations alone, Na et al. identified pathogenic *BRCA1/2* and *ATM* mutations in only 1.44% of 486 patients with low risk disease (Gleason score ≤6), compared with 6.07% of 313 those with lethal, metastatic disease (Na et al., 2017). Additionally, a study of 692 patients with metastatic prostate cancer identified 84 germline DDR mutations that were presumed to be deleterious in 82 men (11.8% of the cohort) (Pritchard et al., 2016). Mutations were found to involve 16 genes, most commonly *BRCA2* (37 men, 5.3%), *ATM* (11 men, 1.6%), *CHK2* (10 of 534 men for whom data were available, 1.9%), *BRCA1* (6 men, 0.9%) and *RAD51D* (3 men, 0.4%) (Pritchard et al., 2016). Collectively these studies indicate that either germline and/or somatic aberrations in DDR genes are relatively common in prostate cancer and are further enriched in advanced disease, thereby rendering the DDR and its associated constituents a promising therapeutic target in this patient group.

1.6.4 Targeting the DNA damage response: PARP inhibitors

One group of DDR proteins that demonstrate promise as therapeutic targets in a range of tumour types are the poly(ADP-ribose) polymerases (PARPs). This family of ADP-ribosyltransferase enzymes comprises at least 17 isoforms, as shown schematically in ***Figure 1.11***, with PARP1 possessing the most significant role in DDR, followed by PARP2 and 3 (Dulaney et al., 2017). PARP enzymes bring about the homopolymerisation of the ADP-ribose subunit of β-NAD^+ on amino acids of specific target proteins (a process known as PARylation), resulting in a diverse range of downstream processes including DNA damage repair, chromatin modulation, transcriptional regulation and cellular stress responses (Schreiber et al., 2006, Slade et al., 2011, Hottiger, 2015, Gupte et al., 2017). Whilst there is some overlap in function between PARP1 and PARP2 isoforms, recent evidence suggests that they have independent roles, with the latter implicated in a number of other diverse processes including haematopoiesis, spermatogenesis and T cell development (Dantzer et al., 2006, Nicolas et al., 2010, Bai and Cantó, 2012, Farrés et al., 2013, Schiewer and Knudsen, 2014, Ali et al., 2016, Mateo et al., 2017).

PARPs play an integral role in DDR through their action as both sensors and signal transducers. PARP1 binds to sites of single strand DNA breaks and other DNA lesions which in turn brings about a series of allosteric changes in structure that activate its catalytic function (Lord and Ashworth, 2017).

PARylation ensues, recruiting DNA repair effectors and facilitating the remodelling of chromatin around the damaged DNA to enable effective repair (Krishnakumar and Kraus, 2010). Eventually PARP enzymes are PARylated by themselves or other PARP isoforms (termed autoPARylation) which, through the negative charge imparted by the PAR chains, inhibits their DNA binding and catalytic activities and facilitates their dissociation from the repaired DNA and return to a catalytically inactive state (Krishnakumar and Kraus, 2010).

Whilst multiple DDR pathway inhibitors are being explored, PARP inhibitors (PARPi) have demonstrated particular efficacy in patients with ovarian cancer and existing DDR aberrations through the aforementioned process of true synthetic lethality and are therefore commercially available and licenced for use, with a proven safety profile (Bryant et al., 2005, Farmer et al., 2005, Ledermann et al., 2012, Ledermann et al., 2014). There are currently four PARP inhibitors under investigation in clinical trials involving patients with CRPC, as shown in ***Table 1.5***. These agents interact with the β-NAD^+ cofactor binding site in the catalytic domain of the PARP enzyme and as such it was originally thought that they exert their therapeutic action through the inhibition of SSB repair, resulting in persistent SSBs which, when encountered by a replication fork leads to fork collapse and formation of a DSB (Farmer et al., 2005). If the cell is then unable to repair the DSB, as is the case in those with pre-existing aberrations in HR repair genes such as *BRCA2*, they are then repaired through alternative error prone repair mechanisms such as NHEJ, resulting in yet more chromatid breaks and genomic instability, ultimately leading to permanent cell cycle arrest or death via apoptosis (Farmer et al., 2005, Lord and Ashworth, 2017). However, more recent studies have also identified that some PARPi also 'trap' PARP1 and PARP2 at the site of DNA damage, inhibiting their ability to undergo autoPARylation and subsequent release, effectively interfering with the catalytic cycle (Murai et al., 2012). These trapped PARP-DNA complexes are thought to be more cytotoxic than unrepaired SSBs that arise as a result of PARP inhibition, supporting the notion that this is the more significant mechanism of action (Murai et al., 2012). Finally, given that both PARP1 and PARP2 are involved in a number of other biological processes in addition to the DDR, it is also possible that some of the therapeutic effects of PARPi are exerted through inhibition of one or more of these functions (Krishnakumar and Kraus, 2010, Schiewer and Knudsen, 2014).

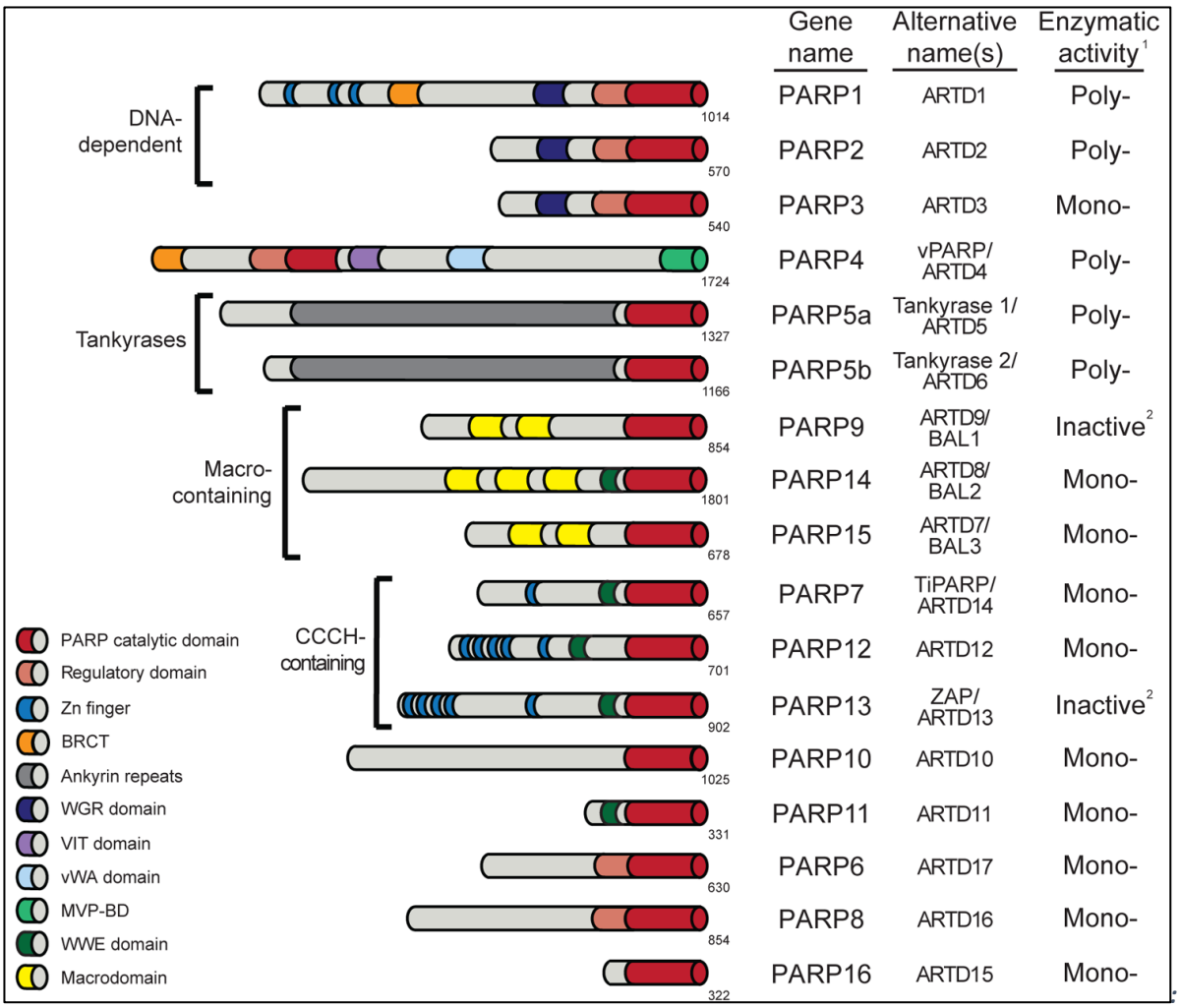

Figure 1.9: *Schematic representation of the poly ADP-ribose polymerase enzyme family.* Numbers in subscript indicate total amino acid length. BRCT, BRCA1 C-terminus domain; VIT: vault inter-trypsin domain; vWA, von Willebrand factor type A; MVP-BD, major vault protein binding domain. PARP enzymatic activity based on presence of conserved motifs and enzymatic assay data. Adapted from (Daugherty et al., 2014).

Table 1.5: *Clinical PARP inhibitors currently under investigation in phase I, II and III clinical trials involving patients with CRPC.* Regulatory approval status also dependent on other disease and genomic factors such as *BRCA1/2* status and previous treatments. FDA, Food and Drug Administration; EMA, European Medicines Agency. Adapted from (Adashek et al., 2019, Rose et al., 2020, Ziadeh and Kourie, 2021)

Agent	**PARP trapping potency**	**Regulatory approval**	**Ongoing trials involving patients with CRPC**
Olaparib *Lynparza* (AstraZeneca)	Medium	Ovarian, fallopian, primary peritoneal cancer (FDA, EMA) HER-2 negative breast cancer (FDA) Metastatic pancreatic cancer (FDA) Metastatic CRPC (FDA)	*Monotherapy:* NCT03263650 NCT03434158 NCT04951492 *In combination:* NCT03732820 NCT03874884 NCT04556617 NCT03787680 NCT01972217 NCT03834519 NCT03012321 NCT03317392 NCT03516812 NCT02893917 NCT05005728 NCT02861573 NCT02484404
Rucaparib *Rubraca* (Clovis Oncology)	Medium	Ovarian, fallopian, primary peritoneal cancer (FDA, EMA) Metastatic CRPC (FDA)	*Monotherapy:* NCT02975934 NCT03442556 NCT04171700 *In combination:* NCT04179396 NCT04253262 NCT03338790 NCT03840200 NCT04455750
Niraparib *Zejula* (GSK)	Medium	Ovarian, fallopian, primary peritoneal cancer (FDA, EMA)	*Monotherapy:* NCT02854436 NCT04288687 *In combination:* NCT03076203 NCT03431350 NCT03748641 NCT04592237
Talazoparib *Talzenna* (Pfizer)	High	HER-2 negative breast cancer (FDA, EMA)	*Monotherapy:* NCT03148795 *In combination:* NCT04824937 NCT04846478 NCT04019327 NCT04703920 NCT03395197 NCT03330405

1.6.5 PARP inhibition in prostate cancer

Given the efficacy seen in other solid tumour types, combined with the high prevalence of DDR aberrations in patients with advanced disease, PARPi have unsurprisingly progressed into clinical trials in men with prostate cancer. Whilst ***Table 1.5*** outlines ongoing clinical trials involving men with CRPC, a number have already reported their results. The TOPARP-A study, a phase II trial of the PARPi olaparib in heavily pre-treated patients with mCRPC, reported a response (defined as a radiological response according to RECIST criteria, a reduction in PSA of 50% or more, or a reduction in circulating tumour cell count) in 16 of 49 patients (Mateo et al., 2015). Of note, 16 patients had DDR gene homozygous deletions, deleterious mutations or both, of whom 14 (88%) demonstrated a response, indicating that this subset of patients to be particularly sensitive to PARPi. On the contrary, only 2 of the 33 patients (6%) lacking DDR aberrations responded.

On the basis of these findings a number of subsequent trials have sought to evaluate the clinical benefit of PARPi specifically in those patients with pre-existing DDR aberrations; a so-called biomarker selected population. A later phase II trial of olaparib undertaken by the same group (TOPARP-B) in patients with progressive CRPC that were selected on the basis of harbouring one of more DDR gene alteration reported the highest response rates in those patients with tumours possessing aberrations in *BRCA1/2* (83%), *PALB2* (57%) and *ATM* (37%) (Mateo et al., 2019). More recently the phase III PROfound study compared olaparib with the physicians choice of enzalutamide or abiraterone in men with CRPC and evidence of disease progression while receiving a second generation anti-androgen therapy (de Bono et al., 2020). Patients were selected on the basis of possessing an aberration in one of 15 prespecified DDR genes involved in HR and were stratified into two cohorts; one with *BRCA1*, *BRCA2* or *ATM* aberrations and the other with aberrations in any of the other 12 genes. Overall objective response rate in those treated with olaparib was 22% compared with only 4% in the control group, with an increase in median overall survival of 3.3 months (de Bono et al., 2020, Hussain et al., 2020). However, response rates were higher specifically in those with *BRCA1*, *BRCA2* or *ATM* aberrations (33%), together with an increase in median overall survival of 4.4 months compared with the control.

Interestingly, when progression free survival was explored according to individual gene in the PROfound patient population, olaparib treatment conveyed little advantage over control in those with *ATM* aberrations (5.36 versus 4.70 months) whilst it had a significant benefit in those with *BRCA2* aberrations (10.8 versus 3.48 months) (de Bono et al., 2020). Similar differences in response between tumours with specific DDR gene aberrations have been reported in other studies, with only 10.5% and

4.1% of patients with *ATM* defects demonstrating radiographic or PSA responses respectively compared with 43.9% and 52.0% of those with *BRCA* defects in the phase II TRITON2 study of rucaparib in men with CRPC that had progressed on AR directed therapy and chemotherapy (Abida et al., 2020).

Collectively these studies indicate that PARPi is effective in improving clinical outcomes in men with CRPC that harbour pre-existing aberrations in HR genes. However, these patients comprise only 22-33% of the total CRPC population (Mateo et al., 2015, Robinson et al., 2015, de Bono et al., 2020), thereby limiting their use in the majority. Furthermore, recent trials have also shown that responses differ according to specific HR gene, with those patients harbouring alterations in *ATM* proving significantly less responsive than those with alterations in *BRCA2*. This, together with the emerging issue of resistance that may form a barrier to long term treatment (Lord and Ashworth, 2017, D'Andrea, 2018), presents a need to identify means of increasing the efficacy of PARPi in those men with either less responsive or no pre-existing HR aberrations so as to harness the true potential of these agents in CRPC.

1.6.6 Combining PARP inhibitors with other anticancer therapies in prostate cancer

One approach to increasing the efficacy of PARPi is through their use in combination with other anticancer treatments. Given that PARPi reduces the ability of cells to repair DNA damage it was hypothesised that PARPi treatment would increase sensitivity to treatment modalities that induce cell death via direct and indirect DNA damage. Subsequent in vitro and in vivo studies have confirmed this to be the case, with PARPi shown to increase sensitivity to the alkylating agent temozolomide, along with other DNA damaging agents such as radiotherapy (Palma et al., 2009, Barreto-Andrade et al., 2011, Wu et al., 2014, Gani et al., 2015, Rae and Mairs, 2017). However, despite these observations, there is only one ongoing clinical trial investigating this approach specifically in patients with advanced prostate cancer, which seeks to determine the safety and optimal dosing of the PARP inhibitor niraparib in combination with Radium-223 (***Table 1.5***; NCT03076203).

Preclinical studies have also demonstrated that AR activity is induced by DNA damage and promotes the expression of genes involved in DNA repair (Goodwin et al., 2013). Furthermore, loss of the AR has been shown to downregulate HR gene expression, with reduced ATM signalling and meiotic recombination 11 (MRE11) foci formation, which are crucial for the resection of DSBs to allow binding of RAD51 and subsequent HR repair. This suggests that ADT acts to impair HR at the stage of DNA double strand end processing and provides a mechanistic rationale for combining ADT and PARPi. Indeed, PARP mediated repair pathways appear to be upregulated following ADT, with synthetic

lethality observed when PARPi and ADT are combined in vivo (Asim et al., 2017). These early preclinical studies hence paved the way for clinical trials of ADT and PARPi in advanced prostate cancer. A recently published double-blind, placebo controlled phase II trial of olaparib in combination with abiraterone versus olaparib alone in 142 patients with mCRPC demonstrated a significantly higher progression free survival in the combination group, regardless of the presence of HR defects (median progression free survival of 13.8 months versus 8.2 months respectively) (Clarke et al., 2018). Importantly, there were no differences in radiological or PSA response rates between the two treatment arms, and 54% of those in the combined olaparib and abiraterone group experienced severe adverse events compared with 21% in the control group. On the basis of these findings, other exploring the safety and efficacy of this combination in patients with both HR-proficient and deficient CRPC are currently ongoing (***Table 1.5***).

Based on the observation that PARPi induces synthetic lethality in cells that lack HR function through pre-existing genetic aberrations, the combination of PARPi with additional DDR inhibitors to induce contextual synthetic lethality may offer a means of increasing their efficacy in HR-proficient cancers. Two particular DDR proteins of interest are Ataxia-telangiectasia-mutated (ATM) and ataxia telangiectasia and Rad3-related (ATR). Both are serine/threonine-directed kinases that belong to the class IV phosphoinositide-3-kinase (PI3K)-related kinase family and are expressed in the majority of tissue types, with germline mutations in their encoding genes resulting in the autosomal recessive disorders of ataxia telangiectasia and Seckel syndrome respectively (O'Driscoll et al., 2003, Lavin, 2008). Although the full mechanism of ATM activation has not been completely elucidated, it is postulated that the MRE11-RAD50-NBS1 (MRN) complex forms at the site of DSBs and acts as a platform for ATM recruitment (Lee and Paull, 2005). ATM then undergoes autophosphorylation and dissociation into monomers, which in turn phosphorylate a number of downstream targets, most notably Checkpoint kinase 2 (CHK2), to bring about a spectrum of signal transduction events that are involved in DNA repair via HR, cell metabolism and transcriptional regulation (Maréchal and Zou, 2013, Paull, 2015).

Given that ATM is fundamental to DSB repair, it could be expected that ATM depletion would increase sensitivity of cancer cells to PARP inhibition via synthetic lethality and indeed this has been demonstrated in preclinical models of other solid tumour types (Schmitt et al., 2017). However, Rafiei and colleagues found that whilst prostate cancer cells in which *ATM* was depleted through either CRISPR/Cas9 gene editing or RNA interference with siRNA demonstrated altered DDR signalling, repair of DSBs via HR remained intact. Interestingly, whilst *ATM* loss increased the sensitivity of cell lines to

ionising radiation, no significant differences were observed in terms of cell viability or clonogenic survival between *ATM* deleted or *ATM* wild type cells following PARPi (Rafiei et al., 2020). Similar findings were observed by Neeb et al., with *ATM* deletion in 22Rv1 CRPC cells via CRISPR/Cas9 resulting in increased sensitivity to ionising radiation but not PARP inhibition when compared with *ATM* wild-type cells, with the latter proving variable depending on the clone (Neeb et al., 2021). Collectively these data therefore provide mechanistic support for the aforementioned clinical trials in which PARP inhibitor sensitivity in patients with pre-existing aberrations in *ATM* was found to be lower than that of other DDR genes such as *BRCA2* (Abida et al., 2020, de Bono et al., 2020), and suggest that combined pharmacological inhibition of both PARP and ATM may not prove an efficacious treatment approach in the setting of CRPC.

Similar to ATM, the bulk of ATR is composed of a large number of alpha-helical Huntington-elongation factor 3-proetin phosphatase 2A-TOR1 (HEAT) repeats, with its kinase domains located near their carboxyl termini, flanked by conserved FRAP-ATM-TRRAP (FAT) and FAT carboxy-terminal (GATC) domains (Maréchal and Zou, 2013). However, contrary to ATM, ATR is activated in response to a variety of DNA lesions including DSBs, SSBs, base adducts and crosslinks (Nam and Cortez, 2011). Although not completely understood, ATR activation itself is thought to be a multi-step process, beginning with the binding of Replication Protein A (RPA) to single strand DNA that is created as a result of direct SSBs, replication stress and nuclease mediated resection of DSBs (Huertas, 2010). ATR, along with its obligate partner ATR Interacting Protein (ATRIP), then binds to RPA-single strand DNA and subsequently interacts with the DNA-damage-specific RAD9-RAD1-HUS1 clamp that is bound to junctions between single strand and double strand DNA, bringing about its phosphorylation. This enables association of the DNA topoisomerase 2 binding protein (TopBP1) with the FATC domain of ATR, resulting in its activation (Choi et al., 2010). Similar to ATM, activated ATR then phosphorylates a wide range of proteins to bring about a number of downstream events in order to repair DNA damage and ameliorate replication stress. The most well characterised mediator of ATR activity is Checkpoint kinase 1 (CHK1), which in turn phosphorylates a multiple effectors to trigger a pleiotropic cellular response including transcriptional regulation, cell cycle arrest in the S and G2 phases of the cell cycle, and cell death if the damage is not deemed repairable (Zhang and Hunter, 2014).

Unlike *ATM*, *ATR* is an essential gene in replicating cells which, together with its multiple DDR functions including recognition and repair of SSBs and amelioration replication stress, renders it an ideal therapeutic target in cancer and also a strong candidate for induction of synthetic lethality in combination with PARPi (Nam and Cortez, 2011, Rundle et al., 2017). Indeed, early experiments in

mouse and human fibroblasts identified that PARP inhibition with 4-amino-1,8-napthalimide (4-AN) in conjunction with the monofunctional methylating agent methyl methanesulfonate (MMS) resulted in a significant increase in phosphorylation of CHK1 at serine 345 together with S-phase cell cycle arrest, both of which were overcome by inhibition of ATR mediated signalling (Horton et al., 2005, Horton et al., 2007). Whilst these observations were only seen when PARPi was combined with additional DNA methylation by MMS, work published at a similar time demonstrated that genetic knockdown of *ATR* using RNA interference was able to sensitise HeLa cells to the PARP inhibitor KU0058948, highlighting the potential role of ATR inhibition as a means of increasing the efficacy of PARP inhibitor monotherapy (McCabe et al., 2006).

More contemporary preclinical studies in *BRCA* mutant ovarian cancer models have similarly shown increased dependency on ATR-CHK1 signalling following PARPi treatment, again supporting the notion that its activation is required for maintaining genomic stability in conditions of reduced PARP function (Kim et al., 2016). Similarly, another study demonstrated that the ATR inhibitor VE-821 sensitised ovarian cancer cell lines to PARPi, irrespective of *BRCA* status (Huntoon et al., 2013). The specific combination of the PARPi olaparib with the orally active ATR inhibitor ceralasertib (AZD6738) has also been found to be synergistic across a range of preclinical models of gastric, lung and head and neck cancer, including primary explants (Lau et al., 2015). On the basis of these limited data, ceralasertib has recently been evaluated in combination with olaparib in a phase I dose escalation study in patients with advanced solid cancers, including prostate, with preliminary results showing it to be well tolerated with preliminary signals of antitumour activity (Krebs et al., 2018).

Despite the synergistic relationship between PARPi and ATRi in preclinical models of other solid cancers and a strong mechanistic rationale, there are a paucity of studies exploring this combination in prostate cancer specifically. Recently, Neeb et al. reported combined PARPi and ATRi to be synergistic in *ATM* depleted 22Rv1 CRPC cells, regardless of baseline sensitivity to PARP inhibition, with similar results seen in an *ATM* deficient mCRPC PDX model (Neeb et al., 2021). Whilst responses to combined PARPi and ATRi appeared limited in those cells without *ATM* depletion, additional experiments found that combined PARPi and ATRi resulted in moderate cytotoxicity in *ATM* wild type 22Rv1, LNCaP and DU-145 cells, with concurrent pharmacological *ATM* inhibition resulting in even more potent antitumour activity. However, given the relatively low prevalence of *ATM* aberrations in CRPC, combined with practical and toxicity issues surrounding the pharmacological targeting of three separate DDR proteins simultaneously, further research is needed to explore the therapeutic potential of combined PARPi and ATRi in *ATM* wild-type, HR proficient prostate cancer.

1.7 Conclusions

Prostate cancer is the most common cancer in men and whilst outcomes for those with localised disease are very good, the prognosis of those that progress to CRPC remains poor and there is hence and ongoing need to identify novel and efficacious therapies for this patient group. Although PARP inhibitors have progressed rapidly into clinical trials and demonstrated efficacy in patients with pre-existing defects in DDR genes encoding proteins involved in HR, responses remain poor in men with tumours that are HR-proficient. Furthermore, there is a relative paucity of preclinical data concerning the role of the PARP enzymes in either normal adult prostate homeostasis or prostate cancer development (Brenner et al., 2011, Schiewer et al., 2012, Han et al., 2013, Pu et al., 2014, Asim et al., 2017, Feiersinger et al., 2018). Whilst combined PARP and ATR inhibition may provide a means of improving PARPi efficacy and overcoming resistance in HR-proficient CRPC, few studies have sought to elucidate the underlying mechanisms or therapeutic relationship between these agents in this setting. Therefore, if we are to fully unlock the true therapeutic potential of PARPi in patients with HR-proficient CRPC, as well as those with DDR mutations that appear less responsive to PARPi monotherapy such as *ATM*, there is a clear need to establish a better understanding of PARP biology in prostate cancer and the mechanisms underlying combined PARPi and ATRi in this complex and heterogenous disease.

1.8 Hypothesis

I firstly hypothesise that combined inhibition of PARP and ATR will provide superior therapeutic efficacy to PARP inhibition alone in HR-proficient CRPC. Given that PARP enzymes are involved in a wide range of biological functions I secondly hypothesise that the most prevalent isoform, PARP1, plays an important role in normal prostate physiology and the pathobiology of prostate cancer and thus may present a novel treatment target for isoform selective PARP inhibition.

1.9 Aims

1. To characterise the response of HR-proficient castrate resistant prostate cancer cells to PARP and ATR inhibition in vitro.

2. To establish the therapeutic benefit of combined PARP and ATR inhibition using ex vivo and in vivo preclinical models of prostate cancer.

3. To delineate the mode of action of the PARP1 isoform in both normal prostate homeostasis and prostate cancer development and progression.

2 Materials and methods

2.1 In vitro experiments and laboratory techniques

2.1.1 Cell line selection

A number of established CRPC cell lines are available for use in pre-clinical research. The DDR mutational status of a range of these have already been evaluated and published by Feiersinger et al., through interrogation of Catalogue of Somatic Mutations in Cancer (COSMIC) database, the with the pathogenicity of *BRCA1/2* mutations determined via additional interrogation of the University of Utah Huntsman Cancer Institute (HCI) and WHO International Agency for Research on Cancer (IARC) *BRCA* Mutation Database (Feiersinger et al., 2018). A panel of three established CRPC cell lines, PC-3, DU-145 and 22Rv1, were subsequently selected on account of their properties in culture and DDR gene mutations profiles, as outlined in ***Table 2.1*** and ***Table 2.2***. The PC-3 line does not possess significant DDR gene mutations and can therefore be considered to represent tumours with wild type DDR functional activity. The DU-145 line is known to possess several DDR gene mutations, including *BRCA1* (p.E962K; heterozygous missense substitution) and *BRCA2* (p.S2284L; homozygous missense substitution), although these are considered to have a low likelihood of pathogenicity. The 22Rv1 line possesses both *ATM* (p.K1101E; heterozygous missense substitution) and *BRCA2* (p.V1810I; heterozygous missense substitution and p.T3033fs*11; heterozygous insertion frameshift) mutations, with the latter deemed to have a likelihood of pathogenicity (Feiersinger et al., 2018). However, despite these defects, both DU-145 and 22Rv1 cells have been shown to demonstrate intact DSB repair capacity via HR (Rafiei et al., 2020, Neeb et al., 2021), hence all three cell lines are considered to represent CRPC in which HR function is preserved.

Each cell line was sourced from the American Type Culture Collection (ATCC; Rockville, USA) either directly, or via collaborators in the University of York, UK, and underwent authentication by Short Tandem Repeat (STR) profiling and regular testing to exclude mycoplasma infection every 2-3 months.

Table 2.1: *Selected HR-proficient CRPC cell line characteristics*.

Name	Source	Approximate doubling time	PSA protein	AR RNA	AR protein	Original reference
PC-3	Vertebral metastasis of a 62-year-old Caucasian male (1979)	25 hours	No	No	No	(Kaighn et al., 1979)
DU-145	Cerebral metastasis of a 69-year-old Caucasian male (1975)	29 hours	No	No	No	(Stone et al., 1978)
22Rv1	Developed from castration induced regression and relapse of the androgen dependent CWR22 xenograft in mice (originally developed from a bone metastasis; 1999)	40 hours	Yes	Yes	Yes	(Sramkoski et al., 1999)

Table 2.2: *DDR mutational status of selected CRPC cell lines*, including pathogenicity of specific *BRCA* gene mutations. Adapted from (Feiersinger et al., 2018). AA mutation, a change that has occurred in the peptide sequence as a result of the mutation; CDS mutation, a change that has occurred in the nucleotide sequence as a result of the mutation.

Cell line	Gene	AA Mutation	CDS Mutation	Zygosity	Type	BRCA mutation pathogenicity
PC-3	GTF2H3	p.V110I	c.328G>A	Heterozygous	Substitution - Missense	
	SMARCAL1	p.S200S	c.600G>A	Heterozygous	Substitution - coding silent	
DU-145	BRCA1	p.E962K	c.2884G>A	Heterozygous	Substitution - Missense	Low
	BRCA2	p.S2284L	c.6851C>T	Homozygous	Substitution - Missense	Low
	BRIP1	p.T132N	c.395C>A	Heterozygous	Substitution - Missense	
	CDK7	p.?	c.1013-2A>T	Heterozygous	Unknown	
	DDB1	p.V510A	c.1529T>C	Heterozygous	Substitution - Missense	
	FANCB	p.R121C	c.361C>T	Heterozygous	Substitution - Missense	
	FANCB	p.G702W	c.2104G>T	Homozygous	Substitution - Missense	
	FANCI	p.H1218fs*2	c.3654delC	Heterozygous	Deletion - Frameshift	
	FLI1	p.Q264K	c.790C>A	Heterozygous	Substitution - Missense	
	IPMK	p.V409I	c.1225G>A	Heterozygous	Substitution - Missense	
	LIG4	p.R32C	c.94C>T	Heterozygous	Substitution - Missense	
	MAPK12	p.E195fs*4	c.584delA	Heterozygous	Deletion - Frameshift	
	MMS22L	p.F532fs*7	c.1596delT	Heterozygous	Deletion - Frameshift	
	PAPD7	p.?	c.1434+6G>A	Heterozygous	Unknown	
	POLQ	p.V257M	c.769G>A	Heterozygous	Substitution - Missense	
	RAD50	p.N370K	c.1110T>A	Heterozygous	Substitution - Missense	
	RBBP8	p.S679G	c.2035A>G	Heterozygous	Substitution - Missense	

	REV3L	p.R2445C	c.7333C>T	Heterozygous	Substitution - Missense	
	SLX4	p.L422L	c.1264C>T	Heterozygous	Substitution - coding silent	
	SLX4	p.R372R	c.1116G>T	Heterozygous	Substitution - coding silent	
	SMARCA2	p.P808L	c.2423C>T	Heterozygous	Substitution - Missense	
	SSRP1	p.M611T	c.1832T>C	Heterozygous	Substitution - Missense	
	STK36	p.G459V	c.1376G>T	Heterozygous	Substitution - Missense	
	TP53BP1	p.?	c.3661-1G>A	Heterozygous	Unknown	
	UBE2N	p.I75fs*6	c.223delA	Heterozygous	Deletion - Frameshift	
	USP1	p.N662fs*2	c.1978delA	Heterozygous	Deletion - Frameshift	
	XRCC2	p.K267fs*>14	c.801delA	Heterozygous	Deletion - Frameshift	
22Rv1	AR	p.H875Y	c.2623C>T	Homozygous	Substitution - Missense	
	AR	p.?	c.2319-9C>T	Homozygous	Unknown	
	ATAD5	p.N1019fs*7	c.3050_3051insA	Heterozygous	Insertion - Frameshift	
	ATM	p.K1101E	c.3301A>G	Heterozygous	Substitution - Missense	
	BARD1	p.K596fs*9	c.1788delA	Heterozygous	Deletion - Frameshift	
	BRCA2	p.V1810I	c.5428G>A	Heterozygous	Substitution - Missense	Low
	BRCA2	p.T3033fs*11	c.9097_9098insA	Heterozygous	Insertion - Frameshift	High
	CDK7	p.F276delF	c.826_828delTTC	Heterozygous	Deletion - In frame	
	CHD1	p.E1321fs*22	c.3960delA	Heterozygous	Deletion - Frameshift	
	DNMT3A	p.A398A	c.1194C>T	Heterozygous	Substitution - coding silent	
	EME1	p.D89Y	c.265G>T	Heterozygous	Substitution - Missense	
	FANCM	p.A421A	c.1263A>G	Heterozygous	Substitution - coding silent	
	FLI1	p.R324W	c.970C>T	Heterozygous	Substitution - Missense	
	HELLS	p.R319W	c.955C>T	Heterozygous	Substitution - Missense	
	INO80D	p.H145H	c.435C>T	Heterozygous	Substitution - coding silent	
	KAT5	p.R304H	c.911G>A	Heterozygous	Substitution - Missense	
	LIG4	p.V736V	c.2208A>G	Heterozygous	Substitution - coding silent	
	MCM3	p.N58fs*6	c.173_174insA	Heterozygous	Insertion - Frameshift	
	MUM1	p.G219*	c.655G>T	Heterozygous	Substitution - Nonsense	
	NBN	p.R43Q	c.128G>A	Heterozygous	Substitution - Missense	
	PALB2	p.V1123M	c.3367G>A	Heterozygous	Substitution - Missense	
	RAD54L	p.?	c.1169+7A>G	Heterozygous	Unknown	
	SHPRH	p.P595P	c.1785C>T	Heterozygous	Substitution - coding silent	
	SLX4	p.L470fs*8	c.1406_1407insC	Heterozygous	Insertion - Frameshift	
	SLX4	p.V1296V	c.3888A>G	Heterozygous	Substitution - coding silent	
	SMG1	p.A762T	c.2284G>A	Heterozygous	Substitution - Missense	
	STK36	p.A1253V	c.3758C>T	Heterozygous	Substitution - Missense	
	TP53BP1	p.T1055fs*36	c.3162delC	Heterozygous	Deletion - Frameshift	
	USP1	p.N662fs*2	c.1978delA	Heterozygous	Deletion - Frameshift	
	USP7	p.A197V	c.590C>T	Heterozygous	Substitution - Missense	
	WRN	p.S1128fs*37	c.3382_3383insA	Heterozygous	Insertion - Frameshift	
	XRCC2	p.F270fs*>11	c.810delT	Heterozygous	Deletion - Frameshift	

2.1.2 Cell line maintenance

PC-3, DU-145 and 22Rv1 cells were cultured in Roswell Park Memorial Institute (RPMI) 1640 medium with L-glutamine supplementation (Gibco, Thermo Fisher Scientific, Hampton, USA; 21875059) and 10% Foetal Bovine Serum (FBS; Gibco, Thermo Fisher Scientific, Hampton, USA; 10270106), supplemented with 100 U/ml penicillin and 100 μg/ml streptomycin (Gibco, Thermo Fisher Scientific, Hampton, USA; 15140122). All cultures were maintained at 37°C in 5% CO_2 and cells were passaged when they reached approximately 80% confluency, with medium renewal every 2-3 days. Adherent cells were detached from plastic tissue culture plates/flasks by incubation with 0.25% Trypsin-EDTA (Gibco, Thermo Fisher Scientific, Hampton, USA; 25200056). For cryopreservation, cells were resuspended in media containing 10% dimethyl sulfoxide (DMSO; Thermo Fisher Scientific, Hampton, USA; 15303671) and aiquots of 1ml were placed in a Corning LX CoolCell freezing system (Corning, New York, USA) at -80°C for 24 hours before being transferred for long term storage in liquid nitrogen in its vapor phase.

2.1.3 Selecting appropriate seeding density for functional in vitro assays

Optimal seeding density was dependent on the assay being performed. As such, cells of each line were plated at a range of densities and cultured under the required experimental conditions prior to undertaking each assay. For viability assays the optimal seeding density was defined as that which resulted in 20% confluency following 24 hours of culture at 37°C in 5% CO_2 in the absence of any treatment. For assays utilising the IncuCyte live cell imaging system (Essen Bioscience, Ann Arbor, USA), optimal seeding density was defined as that which allowed cells to reach between 90-100% confluency at the 96-hour timepoint in the absence of any treatment. An example graph demonstrating the change in confluence of PC-3 cells over 96 hours when plated at a range of densities in the IncuCyte system is given in ***Figure 2.1***.

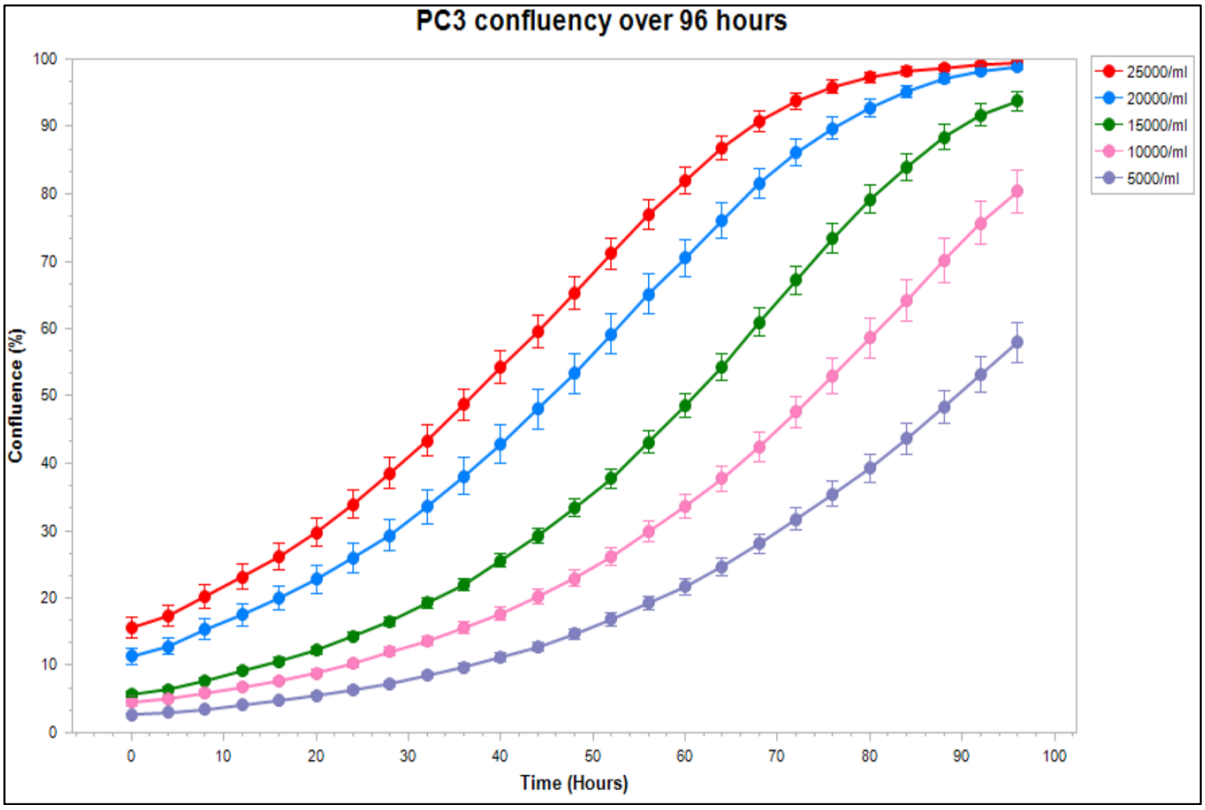

Figure 2.1: *Determining the optimal seeding density of PC-3 cells for functional in vitro assays.* Example growth curves demonstrating the change in confluency of PC-3 cells plated at differing densities and cultured over 96 hours in the IncuCyte live cell imaging system. Each point represents the confluency at a given time point, as assessed by application of a confluency mask to phase contrast images at 10x magnification. Three technical repeats per seeding condition. Error bars represent Standard Error of the mean.

2.1.4 Functional in vitro assays with prostate cancer cells

2.1.4.1 Determining half maximal inhibitory concentration (IC50) values in CRPC cells

Cells of each line were dissociated using Trypsin-EDTA as described in Section 2.1.2, centrifuged at 1000 RPM for 5 minutes and then resuspended in media at a concentration of 25000 cells/ml. 90 µl of cell suspension was then added to the appropriate wells of a 96-well plate (Greiner Bio-One, Kremsmunster, Austria; 655180), resulting in 2250 cells per well. The plate was then returned to the incubator for 24 hours at 37°C in 5% CO_2 for 24 hours to allow cells to fully adhere. After visual inspection and assessment to ensure confluency of between 15-25%, 10 µl of media containing either olaparib or ceralasertib at concentrations ranging from 0.01 µM - 1000 µM were added to the appropriate wells, giving a total volume of 100 µl per well. This 10-fold dilution resulted in final treatment concentrations of 0.0001 µM, 0.001 µM, 0.01 µM, 0.1 µM, 1 µM, 10 µM and 100 µM respectively. 10 µl of 1% DMSO containing media were added to control wells, giving a final concentration of 0.1%. Following treatment, the plate was returned to the incubator for a further 96

hours. Cell viability in each well at the 96-hour timepoint was then assessed using the CellTiter-Blue viability assay (Promega, Madison, USA; G8080) in accordance with the manufacturer's instructions, with fluorescence measured using a CLARIOstar plate reader (BMG Labtech, Ortenberg, Germany). Six technical repeats were performed for each drug concentration and the experiment repeated three independent times. Raw fluorescence readouts were combined and then normalised to the control for each agent to give a relative viability value ranging from 0 to 1. The means of each independent repeat were then combined to generate dose response curves and calculate relative IC50 values for each drug in each cell line using GraphPad Prism version 9.0 (GraphPad Software, La Jolla, USA).

2.1.4.2 Determining the efficacy of olaparib and ceralasertib in combination in CRPC cells

Cells of each line were dissociated, diluted and seeded into the appropriate wells of a 96-well plate and incubated for 24 hours at 37°C in 5% CO_2 as in 2.1.4.1. After visual inspection and assessment to ensure confluency of between 15-25%, cells were treated with media containing olaparib and/or ceralasertib at the respective IC50 doses for each cell line. Media containing the percentage of DMSO equivalent to that in the greatest treatment volume was added to cells in the control wells. The plate was then returned to the incubator for a further 96 hours, after which cell viability in each well was assessed using the CellTiter-Blue viability assay. Six technical repeats were performed for each treatment and the experiment repeated three independent times. Raw fluorescence readouts were combined and the mean for each treatment was normalised to the control to give a relative viability value ranging from 0 to 1.

2.1.4.3 Determining the therapeutic relationship of olaparib and ceralasertib in combination in CRPC cells

Cells of each line were dissociated, diluted and seeded into the appropriate wells of a 96-well plate as in 2.1.4.1. After 24 hours cells were treated with media containing olaparib and/or ceralasertib to give final concentrations of 100 μM, 25 μM, 6.25 μM, 1.56 μM and 0.391 μM and incubated for a further 96 hours. Media containing either 0.1% DMSO was added to cells in the control wells for comparison with each treatment alone or in combination, respectively. Cell viability in each well at the 96-hour timepoint was assessed using the CellTiter-Blue viability assay. Three technical repeats were performed for each drug concentration combination and the experiment repeated three independent times. Raw fluorescence readouts were combined and normalised to the control for each independent repeat to give a relative viability value ranging from 0 to 1. The relative viability values for each independent repeat were then combined to give an overall mean value for each concentration combination. These values were then entered into the SynergyFinder web application, an online tool implementing R package algorithms based on a number of reference models that calculate the

pharmacodynamics of drug combinations in biological model systems. These models include the HSA, which relates to the highest monotherapy effect, Lowe, which relates to the excess over the expected response if the two drugs are the same compound, Bliss, which relates to the effect if the two drugs were to act independently on the phenotype, and ZIP, which relates to the effect as if the two drugs do not potentiate each other (Ianevski et al., 2017). The software does not utilise specific threshold scores to determine synergy but instead generates a Summary Synergy Score for each given drug combination, which can in turn be interpreted as the average excess response beyond expectation (e.g. a Summary Synergy Score of 15 corresponds to a 15% response beyond expectation).

2.1.4.4 Colony forming assays

The capacity for replicative immortality and sustained proliferative signalling are two of the hallmarks of cancer described by Hanahan and Weinberg (Hanahan and Weinberg, 2000, Hanahan and Weinberg, 2011). The colony forming or 'clonogenic' assay is a well-established means of assessing the effects of external stress signals on a cells ability to undergo sufficient proliferation to form an established colony, thereby identifying those that retain the capacity for producing progeny during or after treatment with a particular agent that causes reproductive cell death (Franken et al., 2006, Menyhart et al., 2016).

2.1.4.4.1 Low density colony forming assay: during treatment

PC-3 and DU-145 cells were resuspended, counted and seeded into individual wells of a 12-well plate (Greiner Bio-One, Kremsmunster, Austria; 665180) containing 900 μl of media at a concentration of 250 cells/well. Given their reduced turnover, 22Rv1 cells were seeded at a higher concentration of 500 cells/well. The plate was returned to the incubator for 6-8 hours at 37°C in 5% CO_2 to allow cell adherence, after which 100 μl of media containing DMSO, olaparib, ceralasertib or both olaparib and ceralasertib at 10x IC50 concentrations was added to the respective wells. This 10-fold dilution resulted in the correct IC50 concentrations of each agent in each well, along with an appropriate DMSO control. The plate was then returned to the incubator for a total duration of 7 days for PC-3 and DU-145 cells and 10 days for 22Rv1 cells. These incubation times were chosen as they allowed the formation of adequate colonies in control wells without colony merger. At the end of the treatment period the media was aspirated and 500 μl of 0.5% crystal violet solution added to each well to fix and stain individual colonies. Each well was then rinsed with Phosphate-Buffered Saline (PBS; Gibco, Thermo Fisher Scientific, Hampton, USA; 10020023) and air dried, before the whole plate was scanned using the GelCount colony counter (Oxford Optronix, Oxford, UK). A colony was defined as any cluster of 10 cells or more. Each well was reviewed using a standard light microscope and colonies counted

manually. Colony number was transformed into colony forming efficiency (CFE) using the following formula:

Calculation 1: *CFE (%) = (number of colonies formed / number of cells seeded) x 100*

Early experiments utilising three technical repeats per treatment demonstrated minimal variation and therefore subsequent biological repeats were not performed in replicate. Three biological repeats were performed per cell line and CFE values combined to give a mean CFE for each treatment in each cell line.

2.1.4.4.2 Low density colony forming assay: following treatment

Cells of each line were dissociated, diluted and seeded into the appropriate wells of a 96-well plate and incubated for 24 hours at 37°C in 5% CO_2 as in 2.1.4.1. After visual inspection and assessment to ensure confluency of between 15-25%, cells were treated with media containing olaparib and/or ceralasertib at the respective IC50 doses together with a percentage matched DMSO control and the plate returned to the incubator for a further 96 hours. At the end of the treatment period media was aspirated from each well, 50 µl of 0.25% Trypsin-EDTA added and the plate incubated until all adherent cells had detached. The Trypsin-EDTA cell suspension for each technical repeat was then amalgamated and added to an Eppendorf tube containing 200 µl of media. Cells were counted manually using a FastRead disposable Haemocytometer slide (Immune Systems, Paignton, UK; BVS100) and the appropriate volume added to standard media to generate a concentration of 250 cells/ml (PC-3 and DU-145) or 500 cells/ml (22Rv1). 1ml of cell suspension was then added to the corresponding well of a 12-well plate and incubated for a total duration of 7 days for PC-3 and DU-145 cells and 10 days for 22Rv1 cells. At the end of the treatment period the colonies were stained and counted as in 2.1.4.4.1. Three biological repeats were performed per cell line and CFE values combined to give a mean CFE for each treatment in each cell line.

2.1.4.5 IncuCyte proliferation assay

Real-time automated monitoring using time-lapse imaging is a recognised means of measuring cellular proliferation. Following determination of optimal seeding density as outlined in 2.1.3, cells of each line were dissociated, diluted and seeded into the appropriate wells of a 96-well plate at concentrations of 1350 (PC-3), 2250 (DU-145) and 6750 (22Rv1) cells/well. The plate was then returned to the incubator for 24 hours at 37°C in 5% CO_2 to allow adhesion. After visual inspection, 10 µl of media containing DMSO, olaparib, ceralasertib or both olaparib and ceralasertib at 10x IC50 concentrations was added to the respective wells. The plate was then transferred to the IncuCyte live

cell imaging system and four images per well captured at 10x magnification at 4 hourly intervals over 96 hours. A confluency mask was optimised for each cell line and applied using the integrated IncuCyte S3 software (Essen Bioscience, Ann Arbor, USA) to generate confluence in percent, normalised to the starting timepoint. Three technical repeats were performed per cell line in at least three independent biological repeats.

2.1.4.6 IncuCyte apoptosis assay

Cells undergoing apoptotic cell death express phosphatidylserine (PS) on the outer surface of the plasma membrane, which can in turn be bound by Annexin V labelled with a fluorescent dye to enable detection and quantification during cell culture. Cells of each CRPC line were dissociated, diluted and seeded into the appropriate wells of a 96-well plate at concentrations as in 2.1.4.5. The plate was then returned to the incubator for 24 hours at 37°C in 5% CO_2 to allow adhesion. After visual inspection to ensure the appropriate confluence the existing media was aspirated from each well and discarded. 100 µl of media containing DMSO, olaparib, ceralasertib or both olaparib and ceralasertib at IC50 concentrations, together with IncuCyte Annexin V Green Reagent (Sartorious Biopharma, Goettingen, Germany; 4642) at a 1:2000 dilution was added to the appropriate wells. The plate was then transferred to the IncuCyte live cell imaging system and four images per well captured at 10x magnification at 4 hourly intervals over 96 hours. A fluorescence mask was optimised for each cell line and applied using the integrated IncuCyte S3 software to generate the apoptotic cell count and apoptotic cell confluence per image at each time point. Fluorescence demonstrated an artefactual peak within the first 24 hours of incubation; a phenomenon which has been previously described by other teams within our Institute (data not shown). As such, apoptotic cell confluence was firstly normalised to the 24 hour timepoint, after which it was normalised to overall confluence to control for differences in cell numbers between treatment groups. Three technical repeats were performed per cell line in at least three independent biological repeats.

2.1.4.7 Homologous recombination repair assay

As previously discussed, the repair of double strand DNA breaks via either HR or NHEJ is critical for the maintenance of genome stability. Assays that measure the efficiency of these repair pathways are therefore of great importance in the study of the mechanistic properties of therapeutic agents that target DDR pathways. A number of such assays that utilise the rare cutting endonuclease Intron-encoded endonuclease I-Sce I have been developed and have previously been described in detail (Gunn and Stark, 2012), one of which was used to evaluate the effect of the ATR inhibitor ceralasertib on HR repair in this thesis.

Due to the complexity of the protocol and time limitations arising due to the COVID-19 pandemic, experiments were kindly preformed in collaboration with Dr Greg Ngo and Professor Duncan Baird within the School of Medicine, Cardiff University. In brief, U2OS osteosarcoma cells harbouring a chromosomally integrated expression cassette for the green fluorescent protein (GFP) that has been interrupted by I-SceI recognition sites, termed DR-GFP, were cultured in DMEM medium supplemented with 10% FBS, 1% penicillin/streptomycin and 2mM L-glutamine until 80% confluent. Cells then underwent transfection with the pCBAScel plasmid (Addgene, Waterdown, USA; 26477) using DharmaFECT kb DNA transfection reagent in accordance with manufacturers instructions (Horizon Discovery, Cambridge, UK; T-2006). Once transfected, the expressed I-SceI induces DSBs within its 18 bp recognition sequence which are subsequently repaired via HR, leading to restoration of the GFP expression site and therefore green fluorescence (Seluanov et al., 2010). Detection of this fluorescence thereby enables calculation of the proportion of cells that are proficient for DDR repair via HR. After transfection, cells were cultured in the presence of DMSO or ceralasertib at either 1 μM or 5 μM concentrations for 48 hours. A separate parallel transfection with the mCherry2-C1 plasmid (Addgene, Waterdown, USA; 54563) was performed under each treatment condition such that evaluation of red fluorescence could be used to control for transfection efficiency.

Cells were harvested at the experiment endpoint as previously described and evaluated using flow cytometry, with 10 000 cells assessed per treatment condition. The percentage of cells positive for green fluorescence was taken to represent the percentage of cells proficient for HR repair whilst the percentage of cells positive for red fluorescence was taken to represent transfection efficiency. The percentage of cells proficient for HR repair following ceralasertib treatment was normalised to that of DMSO control cells and then divided by the transfection efficiency to give an overall value of HR repair efficiency, expressed as a percentage. Two technical replicates were performed per treatment condition.

2.1.4.8 Cell cycle analysis

During the G0 and G1 phases of the cell cycle each cell contains one copy of the genome. As cells progress into S phase DNA synthesis occurs producing two sister chromatids, thereby doubling the DNA content of cells entering into the G2 and M phases. As such, measurement of the DNA content of each cell using flow cytometry may be used as a surrogate marker of distribution among the various phases of the cell cycle at a given time point. With this approach three distinct phases can be identified within a proliferating cell population: G0-G1 (quiescence/gap phase), S (DNA synthesis phase) and G2-

M (mitosis). However, given that cells in G2 and M phases have identical DNA content, it is not possible to discriminate between the two using DNA content alone.

Cells of each line were dissociated using 0.25% Trypsin-EDTA, centrifuged at 1000 RPM for 5 minutes and then resuspended in media at a concentration of 25000 (PC-3), 50000 (DU-145) or 100000 cells/ml (22Rv1). 900 μl of each cell suspension was added to the corresponding well in a 12-well plate and incubated for 24 hours at 37°C in 5% CO_2 to allow adhesion. After visual inspection and assessment to ensure confluency of 10-40% depending on the cell line, 100 μl of media containing either DMSO, olaparib, ceralasertib or both olaparib and ceralasertib at 10 x IC50 concentrations were added to each corresponding well. Cells were then returned to the incubator for a period of 96 hours. Following incubation, plates were removed from the incubator and media aspirated from each well. 200 μl of 0.25% Trypsin-EDTA was then added to each well to detach the cells, after which they were added to 1.5ml Eppendorf tubes containing 500 μl of media and centrifuged at 1000 RPM for 5 minutes. The centrifugation process was repeated using ice cold media and the pellet then resuspended in 200 μl of ice-cold cell cycle reagent comprising of PBS containing 5 μg/ml DAPI, 50 μg/ml RNAaseA and 0.1% NP-40. The cell suspension was then passed through a 30 μm filter (Sysmex Partec, Milton Keynes, UK; 04-0042-2316) into 5ml tubes and incubated on ice for 30 minutes. Each sample then underwent flow cytometry using a BD FACSCanto flow cytometer (Becton Dickinson Biosciences, San Jose, USA) and the DAPI fluorescence signal collected for 10 000 cells. Histogram plots were generated using FlowJo version 8.0 (Tree Star Inc, Ashland, USA) and the percentage of cells in G0-1, S and G2-M phases determined using the 'Cell Cycle Analysis' tool. The gating strategy used and example histogram plots are shown in ***Figure 2.2***. Two technical repeats were performed per cell line in at least three independent biological repeats.

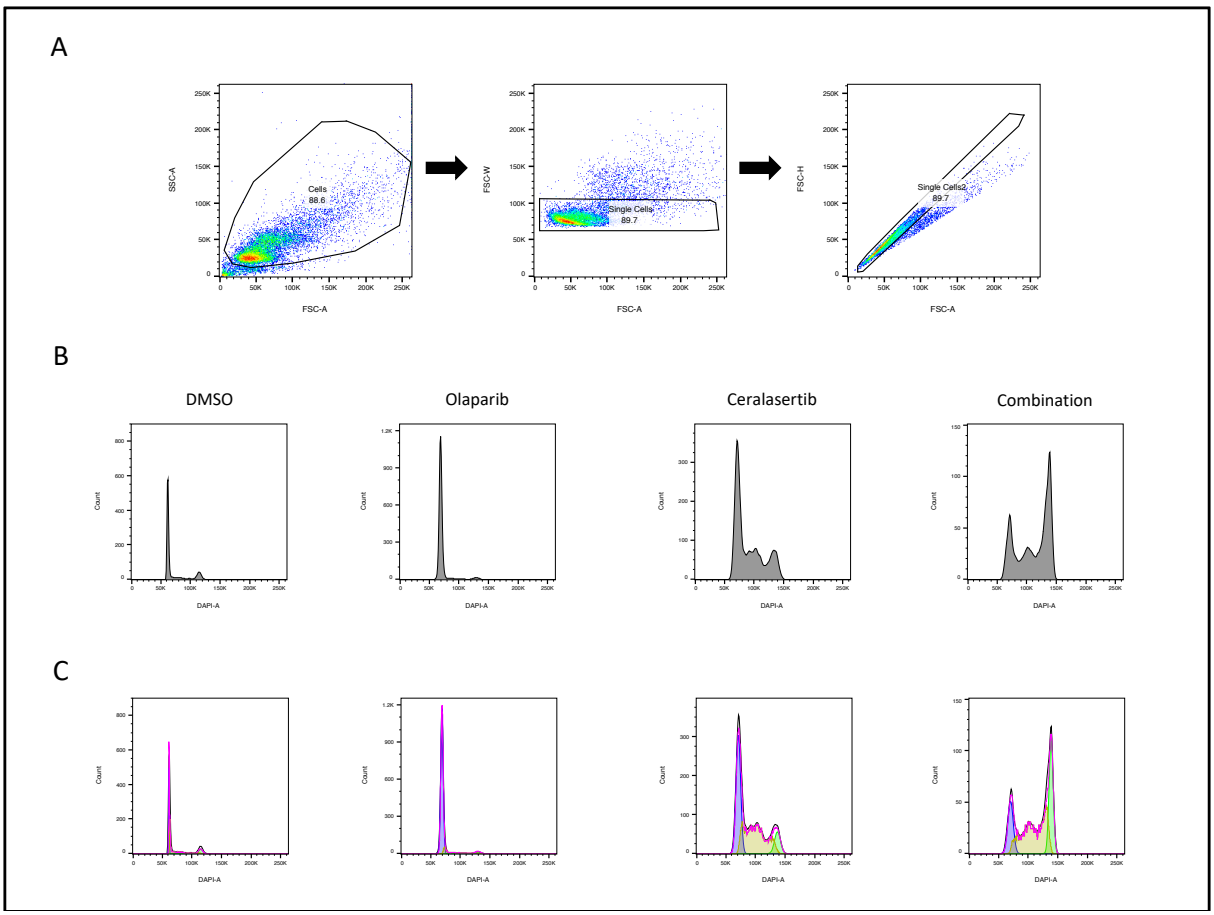

Figure 2.2: *Flow cytometry gating and cell cycle analysis.* A: Gating strategy involving selection of cells, followed by two phase doublet discrimination. B: Example histograms from PC-3 cell samples demonstrating cellular DNA content, as indicated by DAPI signal intensity. C: Application of the FlowJo cell cycle analysis tool to the DAPI histograms. Purple indicates cells in G0-1 phases, yellow indicates those in S phase and green indicates those in G2-M phases.

2.1.5 Quantification of proteins and phospho-proteins: Western Blotting

2.1.5.1 Whole cell lystate preparation and protein quantification

Cells of each line were dissociated using 0.25% Trypsin-EDTA, centrifuged at 1000 RPM for 5 minutes and then resuspended in media at a concentration of 25000 (PC-3), 50000 (DU-145) or 100000 cells/ml (22Rv1). 1800 µl of each cell suspension was added to the corresponding well in a 6-well plate and cells incubated for 24 hours at 37°C in 5% CO_2 to allow adhesion. After visual inspection and assessment to ensure confluency of 10-40% depending on the cell line, 200 µl of media containing either DMSO, olaparib, ceralasertib or both olaparib and ceralasertib at 10 x IC50 concentrations were added to each corresponding well. Cells were then returned to the incubator for a period of 96 hours.

Following incubation, each plate was visually inspected to ensure approximately 80% confluency in the control wells. The media was then aspirated from each well and cells washed with ice cold PBS. 200 µl of ice-cold RIPA buffer (50 mM TRIS pH 7.5, 150 mM NaCl, 1% Tritox X-100, 1% sodium deoxycholate, 0.1% SDS) freshly supplemented with mini cOmplete protease inhibitor cocktail (1 tablet per 10ml buffer; Roche, Basel, Switzerland; 4693124001) and PhosSTOP phosphatase inhibitor cocktail (1 tablet per 10ml buffer: Roche, Basel, Switzerland; 4906845001) was added to each well. Cells were then detached from the plate using manual disruption via a cell scraper, transferred to a 1.5 ml Eppendorf tube and incubated at 4°C for 30 minutes. Each tube was subsequently centrifuged at 14000 RPM for 20 minutes at 4°C and the pellet discarded. The concentration of protein in each sample was quantified using the Quick Start Bradford Protein Assay (Bio-Rad, Hercules, USA; 5000201) as per the manufacturer's instructions. Lysates were then stored at -80°C until further analysis.

2.1.5.2 Western Blotting

Lysates were diluted with 2 x Laemmli buffer (Bio-Rad) and distilled water to standardise protein concentration to that of the sample with the lowest concentration in the experimental set. After heating to 95°C for 5 minutes, 10-15 µl of each sample was loaded into the wells of a precast Mini-PROTEAN TGX 4-20% polyacrylamide gel (Bio-Rad, Hercules, USA; 4561096) and resolved at 150 mV until the ladder had separated sufficiently. Protein was then transferred to activated PVDF membranes using the Bio-Rad Transblot Turbo Transfer System. After transfer each membrane was blocked in either 5% milk or 5% BSA in 0.1% PBS with TWEEN (0.1% PBST) for 1 hour at 4°C.

Following blocking, membranes were transferred to 50 ml tubes containing 3ml of primary antibody diluted in either 5% milk or 5% BSA in 0.1% TBST and incubated overnight at 4°C. The primary and secondary antibodies and their respective dilutions are given in ***Table 2.3***. Membranes were then washed in 0.1% TBST for 5 minutes and the process repeated three times before being transferred to 50ml tubes containing 3ml of HRP-conjugated secondary antibodies in either 5% milk or 5% BSA in 0.1% TBST and incubated for a further 1 hour at 4°C. After a further three washes in 0.1% TBST the membranes were placed in a GelDoc Imaging System (Bio-Rad, Hercules, USA) and 1.5ml of 1:1 Clarity Western Peroxide Reagent and Clarity Western Luminol/Enhancer reagent (Bio-Rad, Hercules, USA; 1705061) to visualise the protein bands.

2.1.5.3 Densitometry analysis

Densitometry was performed using ImageJ software (National Institute for Health, Maryland, USA) to enable comparisons of protein concentration between samples. For comparison of total protein

concentrations between individual treatment groups in each cell line, densitometry values were first normalised to the β-actin loading control and then the untreated/DMSO control. For comparison of total- and phospho- protein concentrations, a concentration ratio was calculated by dividing the densitometry value of the phospho- protein by that of the total- protein. To enable comparisons between individual treatment groups in each cell line, concentration ratios were subsequently divided by that of the untreated/DMSO control to give a relative concentration ratio. At least three independent biological repeats were performed per cell line.

Table 2.3: *Primary antibodies and conditions used in Western Blotting.* CST; Cell Signalling Technology, BSA; bovine serum albumin, HRP; horseradish peroxidase.

Target	Manufacturer	Order number	Host	Dilution	Diluting solution
β-actin	Santa Cruz	Sc-47778	Mouse	1:10000	5% BSA in 0.1% TBST
GAPDH	Merk Millipore	MAB374	Mouse	1:5000	5% BSA in 0.1% TBST
ATR	CST	13934	Rabbit	1:1000	5% milk in 0.1% TBST
Phospho-ATR	CST	2853	Rabbit	1:1000	5% BSA in 0.1% TBST
CHK1	Santa Cruz	Sc-8408	Mouse	1:800	5% BSA in 0.1% TBST
Phospho-CHK1	CST	2348	Rabbit	1:500	5% BSA in 0.1% TBST
Gamma-H2AX	Novus	NB100-2280	Rabbit	1:1000	5% BSA in 0.1% TBST
PARP-1	Santa Cruz	Sc-8007	Mouse	1:400	5% BSA in 0.1% TBST
PARP-2	Novus	NBP2-47337	Rabbit	1:250	5% BSA in 0.1% TBST

2.1.6 Quantification of proteins and phospho-proteins: phosphoproteomics

2.1.6.1 Overview

Phosphorylation of proteins is one of the most predominant reversible post-translational modification events and is central to the activation of a range of complex signalling cascades and their downstream effects (Mayya and Han, 2009). As such, the identification of protein phosphorylation events can be used to characterise pathway activation or inactivation resulting from changes in cellular environment, such as following exposure to different drugs or chemicals. Mass spectrometry, an analytical approach that measures the mass-to-charge ratio of ions generated by targeting a sample with a beam of electrons, is used to identify the presence of specific phosphoproteins within the sample. This, together with bioinformatic analysis using specialist software, can provide insight into the concentrations of both total and phosphorylated forms of particular proteins of interest, as well as in-depth analysis of specific pathways or signalling cascades. In addition to standard Western Blot analysis, tumour samples from the PC-3 subcutaneous xenograft pre-clinical trial (described in Section 2.3.3) were subject to more extensive pathway characterisation using this technique, as outlined below.

2.1.6.2 Whole cell lystate preparation, protein quantification and transfer

Approximately 1 mm thick sections of PC-3 xenograft tumours were taken immediately after termination of the host animal and snap frozen in liquid nitrogen before being stored at -80 °C. At a later time, tissue sections were transferred to 2ml lysing matrix tubes containing sterile metal beads containing 600 μl of ice-cold RIPA buffer containing protease and phosphatase inhibitors as previously described in Section 2.1.5.1. Tubes were then loaded onto the FastPrep-24 5G homogeniser (MP Biomedicals, Santa Ana, USA) and two cycles of 30 seconds duration performed, after which they were centrifuged at 8000 rpm for 10 minutes at 4 °C. The supernatant was then carefully aspirated and transferred to new tubes and the concentration of protein quantified using the Quick Start Bradford Protein Assay as described in Section 2.1.5.1. Samples containing 100 μg of protein were transported on dry ice via next day courier service to the University of Bristol Proteomics Facility for analysis.

2.1.6.3 Phosphoproteomic analysis: performed by the University of Bristol Proteomics facility

2.1.6.3.1 TMT Labelling, high pH reversed-phase chromatography and phospho-peptide enrichment

Each sample was digested with trypsin at 37°C, labelled with Tandem Mass Tag (TMTpro) sixteen plex reagents according to the manufacturer's protocol (Thermo Fisher Scientific, Hampton, USA) and the samples pooled. For total proteome analysis, 50 μg of the pooled sample was desalted using a SepPak cartridge according to the manufacturer's instructions (Waters, Milford, Massachusetts, USA) and the

eluate evaporated to dryness and resuspended in buffer A (20 mM ammonium hydroxide, pH 10) prior to fractionation by high pH reversed-phase chromatography using an Ultimate 3000 liquid chromatography system (Thermo Fisher Scientific, Hampton, USA). For the phosphoproteome analysis, the remainder of the TMT-labelled pooled sample was also desalted using a SepPak cartridge and the eluate evaporated to dryness and subjected to TiO2-based enrichment using the Pierce Phosphoprotein Enrichment kit according to the manufacturer's instructions (Thermo Fisher Scientific, Hampton, USA). The flow-through and washes were then subjected to FeNTA-based phosphopeptide enrichment according to the manufacturer's instructions. The phospho-enriched samples were again evaporated to dryness and then resuspended in 1% formic acid prior to analysis by nano-LC MSMS using an Orbitrap Fusion Lumos mass spectrometer (Thermo Scientific).

2.1.6.3.2 Nano-LC Mass Spectrometry

High pH reversed-phase fractions (total proteome analysis) or the phospho-enriched fractions (phospho-proteome analysis) were further fractionated using an Ultimate 3000 nano-LC system and spectra were acquired using an Orbitrap Fusion Lumos mass spectrometer controlled by Xcalibur 3.0 software (Thermo Fisher Scientific, Hampton, USA) and operated in data-dependent acquisition mode using an SPS-MS3 workflow. FTMS1 spectra were collected at a resolution of 120 000, with an automatic gain control (AGC) target of 200 000 and a max injection time of 50 ms.

2.1.6.4 Bioinformatic analysis

Raw data files were processed and quantified using Proteome Discoverer software v2.4 (Thermo Fisher Scientific, Hampton, USA) and searched against the UniProt Human database (downloaded April 2021: 169297 entries) and the Uniprot Mouse database (downloaded February 2021: 55440 entries) using the SEQUEST HT algorithm. Search criteria included oxidation of methionine (+15.995 Da), acetylation of the protein N-terminus (+42.011 Da) and Methionine loss plus acetylation of the protein N-terminus (-89.03 Da) as variable modifications and carbamidomethylation of cysteine (+57.0214 Da) and the addition of the TMTpro mass tag (+304.207 Da) to peptide N-termini and lysine as fixed modifications. For the Phospho-proteome analysis, phosphorylation of serine, threonine and tyrosine (+79.966 Da) was also included as a variable modification. Searches were performed with full tryptic digestion and a maximum of 2 missed cleavages were allowed. The reverse database search option was enabled and all data was filtered to satisfy false discovery rate (FDR) of 5%. A master dataset was then generated containing the protein and encoding gene names, together with the comparison between total and normalised abundances for both total and phosphorylated protein forms for each of the treatment conditions (vehicle, olaparib, ceralasertib and combined olaparib and ceralasertib) with an associated P value generated using the students t-test. Full bioinformatic analysis

of the master dataset was undertaken by Dr Phil Lewis, University of Bristol, using Qiagen IPA software (Qiagen, Hilden, Germany) to enable identification of canonical, disease and biological function pathway activity in each of the treatment conditions.

2.1.7 Quantification of RNA expression: quantitative reverse transcription polymerase chain reaction (qRT-PCR)

2.1.7.1 RNA extraction and quantification

Cells were plated and treated as in 2.1.5.1 and returned to the incubator for 96 hours, after which each plate was visually inspected to ensure approximately 80% confluency in the control wells. Cells were then dissociated using Trypsin-EDTA, centrifuged at 1000 RPM for 5 minutes and resuspended in 350 µl of Buffer RLT solution (Qiagen, Hilden, Germany; 79216). RNA extraction was then immediately performed using the RNeasy Mini Kit in accordance with the manufacturers instructions (Qiagen, Hilden, Germany; 74104). The concentration and purity of extracted RNA was evaluated using spectrophotometry (Nanodrop ND-2000, Thermo Scientific, Waltham, USA) and used to determine volumes required for subsequent steps.

2.1.7.2 cDNA synthesis

For quantitative mRNA expression analysis, cDNA was synthesised using the Transcriptor 1st Strand cDNA kit (Roche, Basel, Switzerland; 4379012001). In brief, 1 µg of total RNA was combined with RNase free water to a volume of 11 µl. 2 µl of Random Hexamer Primers were then added and each sample was incubated at 65°C for 10 minutes before being placed on ice. 7 µl of a master mix comprising 4 µl of Transcriptor Reverse Transcriptase 5 x buffer, 2 µl of 2 mM deoxynucleotide mix, 0.5 µl Transcriptor Reverse Transcriptase and 0.5 µl of Protector RNase inhibitor was then added to each sample and the PCR commenced using the following thermocycling conditions: 25°C for 10 minutes, 55°C for 30 minutes and 85°C for 5 minutes. Samples were then diluted by adding 80 µl of RNase free water to give a final cDNA concentration of 10 ng/µl.

2.1.7.3 qPCR

1 µl of cDNA (total quantity of 10 ng) was added to a 9 µl master mix comprising 5 µl of KiCqStart SYBR green ReadyMix (Sigma-Aldrich, St Louis, USA; KCQS01-250RXN), 3 µl of RNAse free water and 0.5 µl of both forward and reverse primer stock solution (giving a final primer concentration of 300 nM ; ***Table 2.4***). The 10 µl reaction mix was pipetted into individual wells of a 384-well plate and thermocycling performed in a QuantStudio 7 Flex Real Time PCR System (Applied Biosystems, Foster City, USA) using the conditions outlined in ***Table 2.5***. The cycle threshold (CT; cycle number at which

the PCR product reaches an arbitrary abundance) of each sample was normalised by subtracting the CT value of the housekeeping gene (GAPDH) to give the ΔCT value. The previously described ΔΔCT method (Livak and Schmittgen, 2001) was then used to calculate the relative abundance of mRNA per treatment group, which was subsequently normalised to the untreated/DMSO control for each cell line to give relative fold change in expression. Three technical repeats were performed per cell line in at least three independent biological repeats.

Table 2.4: *Primer sequences for qRT-PCR reactions.*

Gene	Primer sequence
GAPDH (Human)	*Forward*: ACAGTTGCCATGTAGACC *Reverse*: TTGAGCACAGGGTACTTTA
CHEK1 (Human)	*Forward*: CAGCAAGAATTACCATTCCAG *Reverse*: TTTCTTCACTAGAAGCACTG
ATR (Human)	*Forward*: GTAACAGAGTTCCCAAGATTC *Reverse*: TCAAGTTCCTACAGAAGAGG
Beta-actin (Mouse)	*Forward:* GATGTATGAAGGCTTTGGTC *Reverse:* TGTGCACTTTTATTGGTCTC
PARP-1 (Mouse)	*Forward*: TCTAACATGAAGATCCTGACTC *Reverse*: TCTTCTCCACCTCCTTTTTAG

Table 2.5: *Thermocycling conditions sequences for qRT-PCR reactions.*

Temperature (°C)	Step	Time (Sec)	Number of cycles
95	Initial cDNA denaturation	180	1
95	cDNA denaturation	15	40
60	Annealing and extension	60	

2.1.8 Knockdown of PARP1 and PARP2 expression in CRPC cell lines: small interfering RNA (siRNA)

2.1.8.1 Rationale and siRNA constructs

RNA interference is the mechanism by which short sections of double stranded RNA, known as small interfering RNA (siRNA), induces the silencing of genes by targeting complementary mRNA for degradation, thus preventing its translation into functional protein (Dana et al., 2017). Such siRNA can be used to regulate the expression of specific genes, rendering it a valuable tool in the study of individual gene function in vitro. This method was chosen as the favoured means of studying the basic function of PARP1 and PARP2 isoforms in CRPC cell lines given that the effect of dual ablation was not known and the significant cost and time implications of other gene editing techniques such as CRISPR/Cas9. Commercially produced pools of 4 siRNAs specific for *PARP1* and *PARP2* mRNA, together with a pool of 4 non-targeting siRNAs were selected for use and are detailed in ***Table 2.6***. (ON-TARGET plus SMART pool, Dharmacon, Lafayette, USA).

2.1.8.2 Transfection

PC-3, DU-145 and 22Rv1 cells were dissociated using 0.25% Trypsin-EDTA, centrifuged at 1000 RPM for 5 minutes, resuspended in media at a concentration of 30000 cells/ml (PC-3), 50000 cells/ml (DU-145) and 150000 cells/ml (22Rv1) and returned to the incubator at 37°C in 5% CO_2. Using aseptic techniques in a tissue culture hood, 4.5 μL of Lipofectamine RNAiMAX transfection reagent (Invitrogen, Waltham, USA; 13778075) was added to 75 μL of opti-MEM serum free media (Gibco, Thermo Fisher Scientific, Hampton, USA; 31985062). 75 μL of the resulting solution was then transferred to a new 1.5ml Eppendorf tube and combined with 1.5 μL of 10 μM stocks of either the non-targeting siRNA pool, the *PARP1* siRNA pool, the *PARP2* siRNA pool and both the *PARP1* and *PARP2* siRNA pools and incubated for 5 minutes at room temperature to generate master mixes for each of the targets of interest. 10 μL of master mix was transferred to pre-labelled wells of a sterile 96 well plate, followed by 90 μL of the corresponding cell suspension to create a total volume of 100 μL. Plates were then incubated at 37°C in 5% CO_2 for 24 hours to enable cells to adhere and transfection to occur.

2.1.8.3 Validation of knockdown

Two plates underwent siRNA transfection as outlined above and were returned to the incubator for 48 and 96 hours respectively. At each timepoint whole cell lysis was performed using RIPA buffer supplemented with mini cOmplete protease inhibitor cocktail and PhosSTOP phosphatase inhibitor cocktail as described in 2.1.5.1. Protein concentration in the lysate was then quantified using the Quick Start Bradford Protein Assay and Western Blot performed for β-actin, PARP1 and PARP2. The

concentration of each protein at 48 and 96 hours following transfection was determined by densitometry analysis using ImageJ software. For comparison of total protein concentrations between individual siRNA pools in each cell line, densitometry values were first normalised to the β-actin loading control and then the non-targeting siRNA control. Three biological repeats were performed alongside the proliferation assay as outlined below.

2.1.8.4 Proliferation and viability assays

48 hours following transfection, plates were transferred to the IncuCyte live cell analysis system (Essen Bioscience, Ann Arbor, USA) and four images per well captured at 10x magnification at 4 hourly intervals over a further 48 hours incubation. A confluency mask was optimised for each cell line and applied using the integrated IncuCyte S3 software to generate confluence in percent, normalised to the starting timepoint. At the end of the 48 hours incubation (equivalent of 96 hours following transfection), 20 μL CellTiter-Blue viability reagent was added to each well and the plate incubated for a further 60 minutes. Fluorescence was then measured in accordance with the manufacturer's instructions and results were normalised to the non-targeting siRNA control to give a relative viability value ranging from 0 to 1. Three technical repeats were performed per cell line in at least three independent biological repeats.

Table 2.6: *Details of the Dhamacon ON-TARGET plus siRNA smart pools used in siRNA knockdown experiments.*

Pool target	ID code	Target sequence
PARP-1 (Human)	J-006656-06	GAAAACAGGUAUUGGAUAU
	J-006656-07	GUUCUUAGCGCACAUCUUG
	J-006656-08	CCAAUAGGCUUAAUCCUGU
	J-006656-22	CCGAGUACAGUGCGAGUCA
PARP-2 (Human)	J-010127-05	CAUCACAGGUUACAUGUUU
	J-010127-06	AAGGAUUGCUUCAAGGUAA
	J-010127-07	GCAAGUGACACAGGAAUUC
	J-010127-08	CAGGUUACCAGUCUCUUAA
Non-targeting pool	D-001810-10-05	UGGUUUACAUGUCGACUAA
	D-001810-10-05	UGGUUUACAUGUUGUGUGA
	D-001810-10-05	UGGUUUACAUGUUUUCUGA
	D-001810-10-05	UGGUUUACAUGUUUUCCUA

2.1.9 Immunohistochemistry

2.1.9.1 Overview

Immunohistochemistry is a frequently utilised form of immunostaining that enables the quantification of antigens (most commonly proteins) within cells of a tissue. The technique has been used extensively throughout this thesis for the quantification of proteins in tissue from patient derived explants, xenograft tumours and transgenic mice. The reagents and conditions vary depending on the antigen of interest. As such, a generic IHC protocol is outlined below, with the modifications and specific primary and secondary antibodies required for each antigen given in ***Table 2.7***.

2.1.9.2 Tissue preparation

Animals were culled via a Schedule 1 approved method and the tissue harvested as outlined in Section 2.2 and Section 2.3. Immediately after dissection the tissue was placed in 10% neutral buffered formalin (Sigma-Aldrich, St Louis, USA; HT501128) and fixed overnight at 4°C. The following day the tissue was transferred to 70% ethanol and stored at 4°C until later being embedded in paraffin. 4 μm sections were then mounted on microscopy slides and stained for H&E using standard protocols performed by the members of staff in the Cardiff University Bioimaging Hub. Additional 4 μm sections were then mounted on microscopy slides for use in IHC.

2.1.9.3 Generic IHC protocol

Slides were dewaxed and rehydrated by serial submersion in xylene (2 x 5 minutes), 100% ethanol (2 x 3 minutes), 95% ethanol (1 x 3 minutes), 70% ethanol (1 x 3 minutes), followed by submersion in distilled H_2O (dH_2O). Antigen retrieval was then performed by submerging in 1 x DAKO antigen retrieval solution (Dako, Glostrup, Denmark), heating in a pressure cooker containing 500ml of dH_2O for 10-15 minutes and then allowing to cool to room temperature over 30 minutes. After washing for 5 minutes in dH_2O, endogenous peroxidase activity was blocked using 3% H_2O_2 in dH_2O for 10 minutes, followed by 3 x 5 minute washes in 0.1% TBS/T. Sections were then blocked with 2% BSA in TBS/T for 30 minutes before being incubated with primary antibody diluted in 2% BSA in 0.1% TBS/T overnight at 4°C. The following day, after 3 x 5 minute washes in 0.1% TBS/T, sections were then incubated with biotinylated secondary antibody diluted to 1:300 in 2% BSA in 0.1% TBS/T for 30 minutes. After performing 3 x 5 minute washes in 0.1% TBS/T, sections were HRP labelled by incubating with the Vectastain Elite Averdin-Biotin-Complex HRP kit (Vector Laboratories, Peterborough, UK; PK-6200) for 30 minutes. Further 3 x 5 minute washes in 0.1% TBS/T were then performed, followed by visualisation of positivity using the DAB chromogen reagents (Dako, Glostrup, Denmark; K346811-2) in accordance with manufacturers instructions. After positive staining was visualised the reaction was ceased by submerging in 0.1% TBS/T, followed by 5 minute washes in dH_2O and tap water respectively. Sections

were then counterstained by the addition of haematoxylin for 30 seconds and washed in running tap water for 5 minutes, after which the tissue was dehydrated by serial submersion in 70% ethanol (1 x 3 minutes), 95% ethanol (1 x 3 minutes), 100% ethanol (2 x 3 minutes) and xylene (2 x 5 minutes). Finally, sections were mounted using DPX mounting media (Sigma-Aldrich, St Louis, USA; 44581) and glass coverslips applied.

2.1.9.4 Imaging and quantification

The type of imaging and method of quantification of IHC stained tissue sections was dependent on the tissue being analysed. Due to their small size, tissues from patient derived explants were imaged using an Olympus microscope with Leica Application Suite software (Version 4.6.1, Leica Microsystems, Wetzlar, Germany) at x20 objective. At least 3 representative digital photographs were taken of each tissue and cells counted manually using ImageJ software. Other IHC stained slides of tissues such as those from transgenic mice and tumours generated during preclinical trials were scanned and digitised using an Olympus Slide Scanner (Olympus Corporation, Shinjuku, Japan). Cells were then counted automatically using QuPath open source software (Bankhead et al., 2017), with manual counts performed to ensure accuracy of the automated scripts. The exact method of quantitation depended on the protein or marker, as outlined below.

2.1.9.4.1 Cleaved caspase-3 and proliferating cell nuclear antigen

In the case of proteins for which cells are either positive or negative, such as cleaved caspase-3 (CC-3) and proliferating cell nuclear antigen (PCNA), the number of positive cells expressing the protein of interest were counted and then divided by the total number of cells and multiplied by 100 to give an expression index in percent (termed CC-3 and PCNA indices). At least 1000 cells were counted per sample.

2.1.9.4.2 γ-H2AX

For proteins with variable levels of expression, such as γ-H2AX, staining intensity was scored as either high, low or negative, as demonstrated in ***Figure 2.3***. The percentage of cells with high levels of expression was then calculated by dividing the number of cells with high staining intensity by the total cell number in the tissue region of interest and multiplying by 100. At least 1000 cells were counted per sample.

2.1.9.4.3 CD34 and microvessel density

CD34 is a transmembrane glycoprotein that is expressed on the surface of haematopoietic progenitor cells and endothelial cells. As such, IHC staining for CD34 is a means of identifying the endothelial cells that line small blood vessels, therefore enabling identification and quantification of microvessels within tumour tissue. The method of tumour microvessel quantification is well established and has been described elsewhere (Weidner et al., 1991, Fontanini et al., 1997, Loggini et al., 2003). In brief, IHC stained section images were overlaid with a standard grid comprising of squares of $1mm^2$. The whole specimen was examined at low power to identify the three squares containing the greatest number of microvessels, termed 'hot spots'. The number of microvessels in each square was then counted to give a number per mm^2. A single microvessel was defined as a CD34 positive endothelial cell separated from adjacent microvessels or other cell types as shown in ***Figure 2.4***. A visible lumen was not required and those vessels with a muscular wall (i.e. arterioles) were excluded. Counts were taken from 3 'hot spots' per tumour and tissue from at least three independent specimens were evaluated. The mean number of microvessels per 'hot spot' was then calculated and represented graphically alongside example microscopy images.

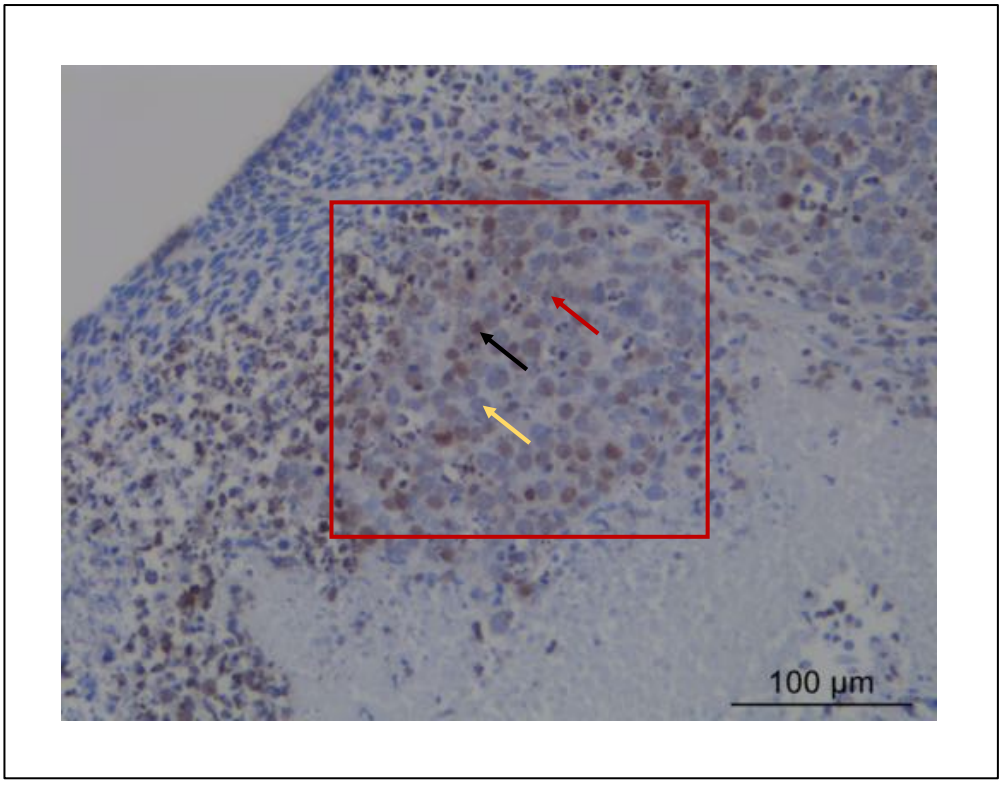

Figure 2.3: *Quantitation of γ-H2AX staining intensity.* A: Representative explant tumour section stained for *γ-H2AX* at x20 magnification. Black arrow demonstrates an example of high staining intensity, red arrow demonstrates an area of low staining intensity and yellow arrow demonstrates an example of negative staining.

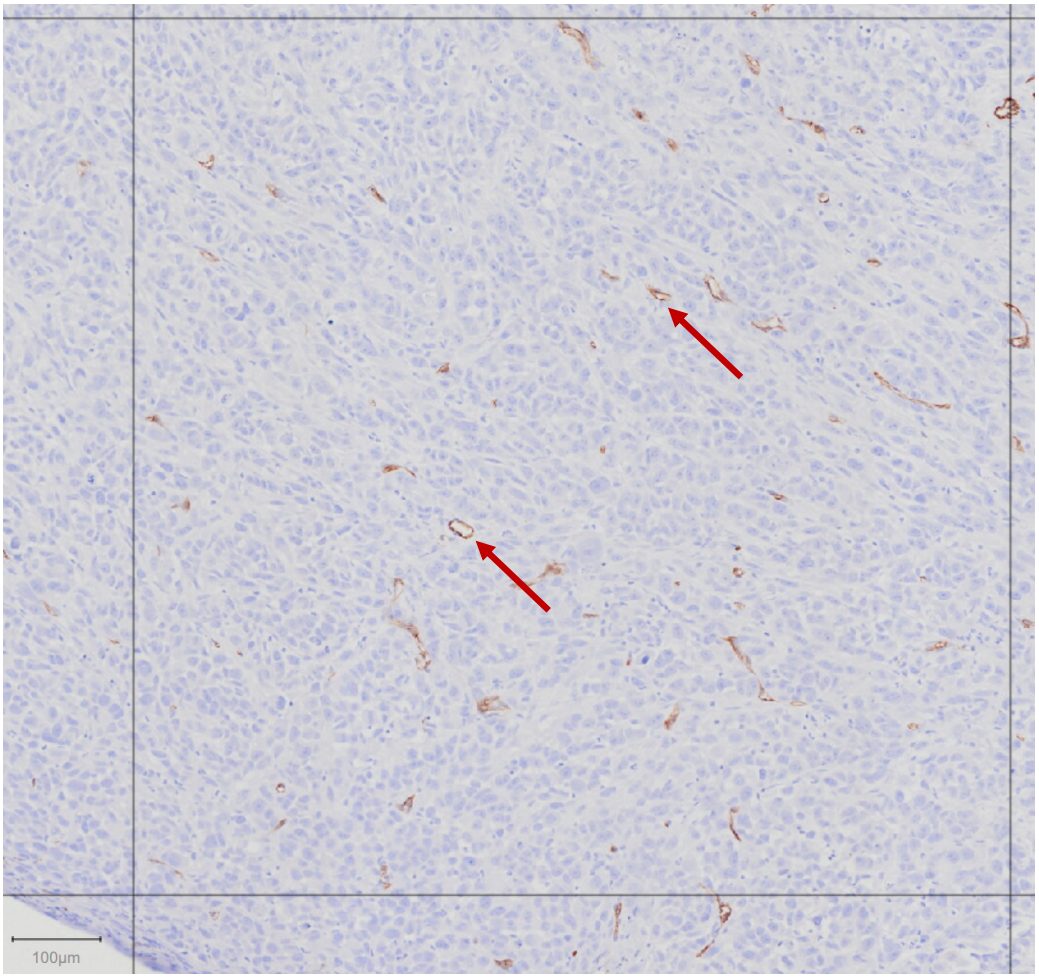

Figure 2.4: *Quantitation of CD34 staining for use in determining microvessel density.* Representative section of vehicle treated PC-3 xenograft tumour tissue stained for CD34 and overlayed with a 1mm^2 grid using QuPath software. Individual collections of endothelial cells representing microvessels are seen (red arrows), rendering this area a 'hot spot' for quantification.

Table 2.7: *Primary antibodies and conditions used in immunohistochemistry staining.*

Primary antibody	**Manufacturer and ID**	**Host**	**Dilution**	**Modification to the generic IHC protocol**
Cleaved caspase-3	CST 9664	Rabbit	1:300	*Antigen retrieval:* DAKO Target Retrieval Solution, pH 9 (DAKO 237584) *2°ab:* biotinylated goat-anti-rabbit (Dako, E0432)
PCNA	Becton Dickinson 610665	Mouse	1:400	*Antigen retrieval:* 1mM EDTA pH 8 *2°ab:* incubation with ImmPRESS anti-mouse Ig polymer detection kit (Vector Laboratories, MP7402) No additional labelling using ABC-HRP kit required
Surface of intact human mitochondria	Merck Millipore MAB1273	Mouse	1:100	*Antigen retrieval:* 1 x citrate solution, pH 6 *2°ab:* biotinylated rabbit-anti-mouse, 1:500 dilution Blocking and antibody dilution in 1% BSA in TBS/T
γ-H2AX	Novus Bio NB100-2280	Rabbit	1:300	*Antigen retrieval:* 1 x citrate solution, pH 6 *2°ab:* biotinylated goat-anti-rabbit, 1:500 dilution Blocking and antibody dilution in 2% BSA in TBS/T
CD34	Abcam Ab81289	Rabbit	1:5000	*Antigen retrieval:* 1 x citrate solution, pH 6 *2°ab:* biotinylated goat-anti-rabbit, 1:300 dilution Blocking and antibody dilution in 1% BSA in TBS/T
Cytokeratin 5	Abcam Ab52635	Rabbit	1:500	*Antigen retrieval:* DAKO Target Retrieval Solution, pH 9 (DAKO 237584) *2°ab:* biotinylated goat-anti-rabbit, 1:500 dilution Blocking and antibody dilution in 2% BSA in TBS/T
Cytokeratin 8	Abcam Ab52635	Rabbit	1:500	*Antigen retrieval:* DAKO Target Retrieval Solution, pH 9 (DAKO 237584) *2°ab:* biotinylated goat-anti-rabbit, 1:500 dilution Blocking and antibody dilution in 2% BSA in TBS/T

2.2 Ex vivo experiments

2.2.1 Background

A wide range of prostate cancer model systems have been developed for use in basic science and translational research, as discussed in Section 1.5. Whilst established cell lines such as PC-3, DU-145 and 22Rv1 have proved invaluable in prostate cancer research, it is now appreciated that these alone do not recapitulate a number of important components of this complex disease, including tumour heterogeneity, microenvironment and immune system interactions. As such, novel model systems that take these aspects into consideration and hence better represent the full spectrum of disease have been developed. Many of these models utilise tumour tissue taken directly from patients, as summarised in ***Figure 2.5***. Fresh tumour tissue obtained during surgery, through biopsy or at autopsy can either be deconstructed and the cells cultured in 2D or 3D (termed organoids), or transferred directly into immunocompromised mice to generate patient derived xenografts (PDX). An alternative to using tumour tissue for PDX development is the direct culture of tumour fragments ex vivo; termed patient derived explant culture (PDE). Such techniques have evolved considerably years and whilst several have been described, one of the most widely adopted involves culturing small pieces of tissue on gelatin sponge that is partially submerged in media (Risbridger et al., 2018, Powley et al., 2020). Through using this approach, primary tissue has been shown to remain viable for up to 7 days, with preservation of its tissue architecture and cell-cell signalling within the microenvironment (Centenera et al., 2012). In addition, a hybrid approach in which explant cultures are established from tumour tissue that has first been expanded in immunocompromised mice as a PDX has emerged as a valuable tool for short-term, high-throughput preclinical drug testing in disease subsets for which primary tissue is not readily available, including CRPC (Risbridger et al., 2018). As such, this is the approach utilised for the ex vivo PDE experiments described in this thesis.

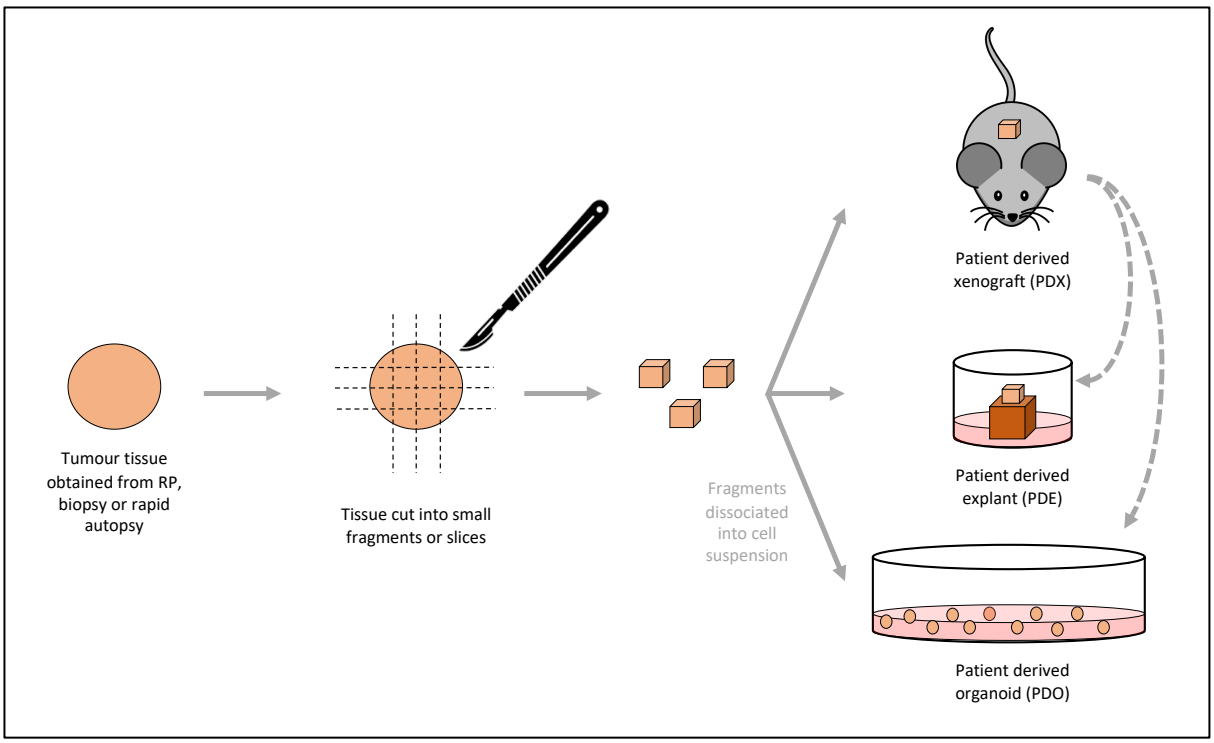

Figure 2.5: *Schematic overview of patient derived prostate cancer models established from human prostate cancer tissue.* Both PDE and PDO can be obtained from primary tissue fragments directly, or indirectly from tissue fragments harvested from pre-established PDX tumours. RP; radical prostatectomy. Adapted from (Risbridger et al., 2018).

2.2.2 Cardiff neuroendocrine CRPC patient derived explant model

Whilst collaboration between Cardiff University, Cardiff and Vale University Health Board and the Wales Cancer Bank has enabled development of a pipeline for transfer of fresh prostate tumour tissue to the laboratory, the majority of available samples are from men with localised disease undergoing radical prostatectomy and are therefore not relevant to the study of CRPC. However, acquisition of tissue from a lymph node metastasis of a heavily pre-treated patient with neuroendocrine variant CRPC has enabled development of a new PDX model that can be successfully serially propagated with preservation of histological features of the original tumour (termed LN-NEPC-1; generated by Dr H Pearson, Dr G Seaton and Dr D Turnham, unpublished; Wales Cancer Bank application approval 17-014, Research Ethics Approval SREC1810-01). Whilst the exact genomic landscape of the model is still under investigation and the DDR mutational status unknown, basic characterisation has demonstrated it to be insensitive to androgen deprivation and both AR and PTEN negative, with only low levels of PSA expression (data not shown). LN-NEPC-1 PDX tumours were subsequently expanded through serial propagation and used to optimise a local PDE culture protocol for use in preclinical trials, as outlined below.

2.2.3 LN-NEPC-1 PDE drug combination pre-clinical trial

2.2.3.1 Experimental overview

Preclinical trials were conducted using PDEs generated from LN-NEPC-1 PDX tumours, as outlined schematically in ***Figure 2.6***. Whole tumours were harvested prior to reaching the ethical limit for size and were placed immediately in transport media at 4°C (***Table 2.8***). In the laboratory the tumours were transferred to a mould containing 4% low melt agarose in its liquid phase at 35°C (Promega, Madison, USA; V2111). The mould was then transferred to ice to facilitate solidification, after which it was removed. The agarose embedded tumour was then sliced to produce sections of 250 μm depth using a Leica VT1200 vibratome (Leica Microsystems, Wetzlar, Germany). Individual sections were placed on 1cm^3 gelatin sponges (SURGISPON, Aegis Lifesciences, Gujarat, India; SGSP001) within a 24-well plate that had been soaked in 500 μl of explant media (***Table 2.9***) containing either olaparib at a concentration of 10 μM, ceralasertib at a concentration of 5 μM, or both, for 30 minutes. Further sections were either placed on sponges soaked in 500 μl of explant media containing 0.015% DMSO to serve as an untreated control or submerged in 10% formalin to serve as a zero hour timepoint control. Each plate was then incubated for either 48 hours at 37°C in 5% CO_2, after which individual sections were removed from their sponges and submerged in 10% formalin for fixation. 24 hours later each slice was transferred to 70% ethanol solution for storage at 4°C until paraffin embedding and sectioning could be performed. Three technical repeats were performed per treatment and three independent biological repeats performed, each using tissue from a different passage of LN-NEPC-1 tumour.

2.2.3.2 Analysis

Explant tissue derived from LN-NEPC-1 PDX tumours comprise of a number of cell types, including human tumour cells together with immune and stromal cells originating from the murine host. In order to correctly identify the human tumour cells so that protein expression could be evaluated, IHC was performed using an antibody specific for the surface of intact human mitochondria (MAB1273; Merck-Millipore, Massachusetts, USA) using the conditions outlined in Section 2.1.9. The tumour cell population exhibited mild-moderate surface of intact human mitochondria staining as demonstrated in ***Figure 2.7****;* with these cells verified to be tumour cells in concordance with standard H&E staining by Dr Murali Varma, Consultant Urological Pathologist, University Hospital of Wales, Cardiff. Digitised images then evaluated, tumour cell populations encircled, and individual cells manually counted. Subsequent IHC staining of the same population was then undertaken and the number of positive cells within each predefined tumour cell population manually counted to enable calculation of the percentage of total tumour cells expressing the target antigen.

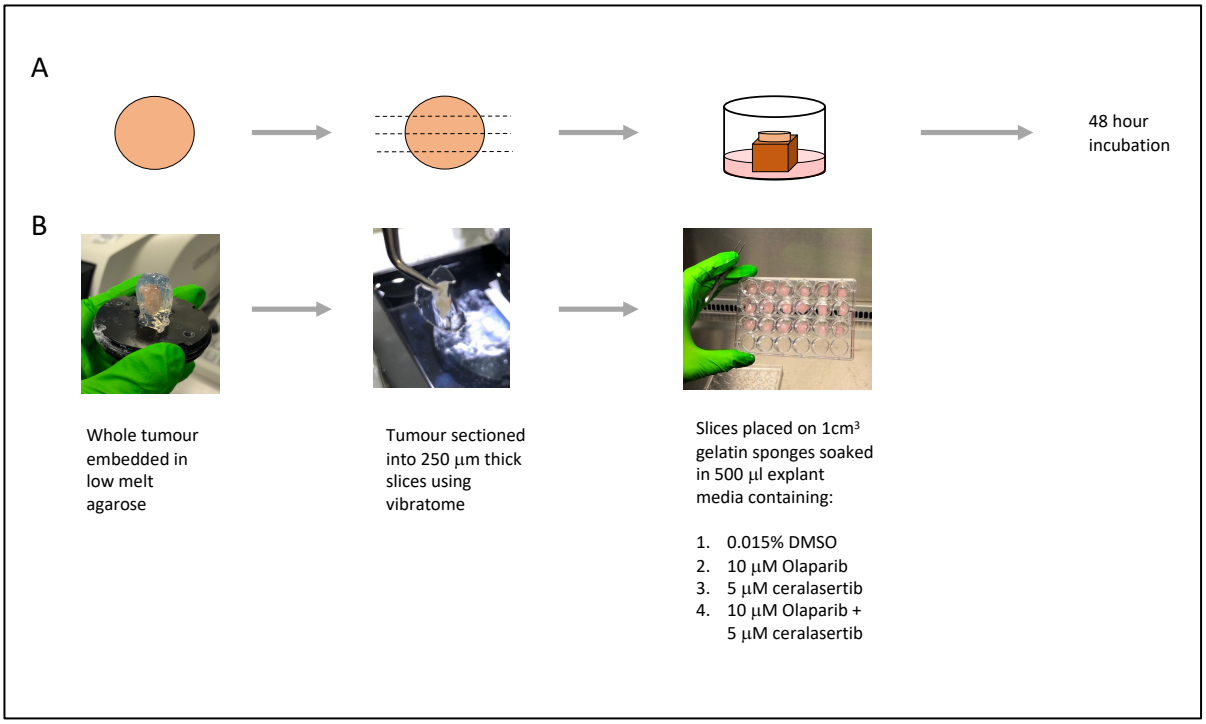

Figure 2.6: *Overview of the LN-NEPC-1 PDE drug combination experiment protocol.* A: Schematic representation of key steps. B: Example photographs and description. Following the 48 hour incubation period, slices were removed from the sponge and fixed in 10% formalin prior to undergoing analysis via IHC.

Table 2.8: *Composition of LN-NEPC-1 transport media.*

Component	Stock concentration	Final concentration	Manufacturer	Order number
RPMI 1640	1 x	90% (v/v)	Gibco	21875-059
Foetal bovine serum (FBS)	1 x	10% (v/v)	Gibco	10270106
Penicillin / Streptomycin	10 000 U/ml	1% (v/v)	Gibco	15140-122
Amphotericin B	250 µg/ml	0.5 µg/ml	Gibco	15290-026
Gentamicin	50 mg/ml	100 µg/ml	Lonza	17-518Z
Rock inhibitor Y-27632	100 mM	5 µM	HelloBio	HB2297

Table 2.9: *Composition of LN-NEPC-1 explant culture media.*

Component	Stock concentration	Final concentration	Manufacturer	Order number
RPMI 1640	1 x	90% (v/v)	Gibco	21875-059
Foetal bovine serum (FBS)	1 x	10% (v/v)	Gibco	10270106
Penicillin / Streptomycin	10 000 U/ml	1% (v/v)	Gibco	15140-122
Amphotericin B	250 µg/ml	0.5 µg/ml	Gibco	15290-026
Gentamicin	50 mg/ml	100 µg/ml	Lonza	17-518Z
Rock inhibitor Y-27632	100 mM	5 µM	HelloBio	HB2297
Dihydrotestosterone	1 mg/ml	1 nM	Unknown	Unknown
Hydrocortisone	2 mg/ml	1 µg/ml	Sigma	H6909
Insulin	10 mg/ml	1 µg/ml	Sigma	I0516

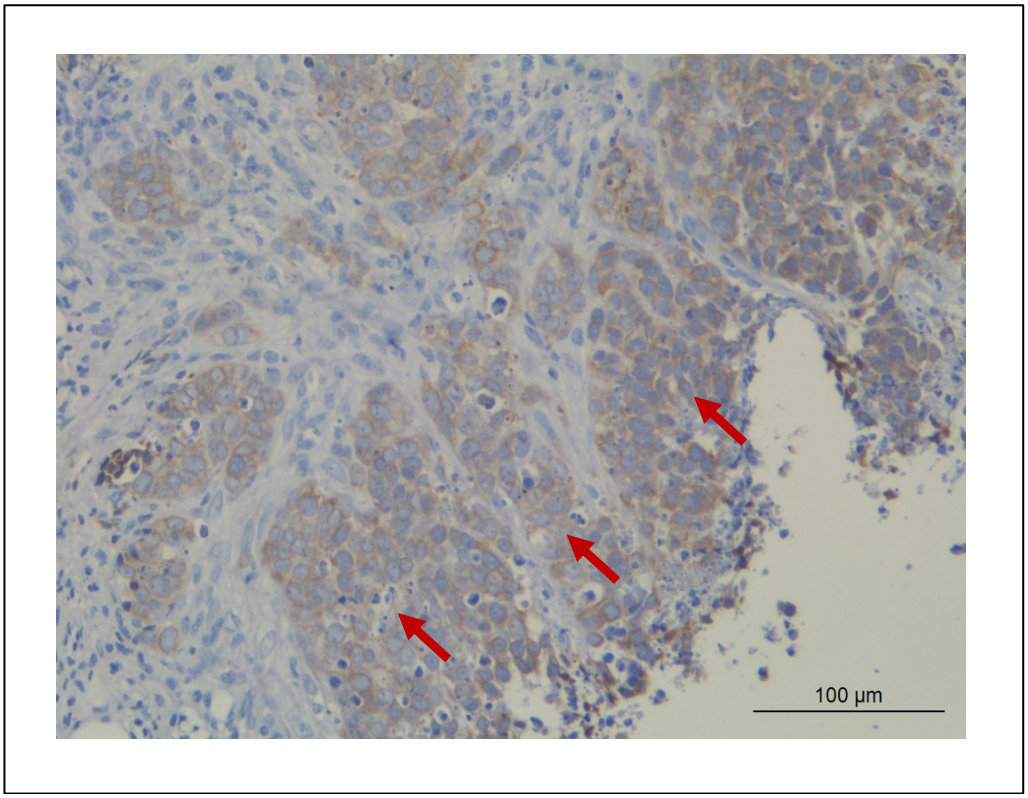

Figure 2.7: *Use of IHC staining of surface of intact human mitochondria to identify human tumour cell populations within LN-NEPC-1 PDE sections.* Example IHC image at x20 magnification demonstrating distinct clusters of positive tumour cells (red arrows) surrounded by murine stroma.

2.3 In vivo experiments

2.3.1 Animal husbandry

All animal experiments were undertaken in accordance with the UK Home Office regulations under valid Personal and Project licences and with Cardiff University Animal Welfare and Ethical Review Board (AWERB) approval. Mice were kept in Specific and Opportunistic Pathogen Free conditions and given free access to standard irradiated diet and water, with a maximum of six mice of the same sex per cage. All cages were provided with environmental enrichment to maximise the wellbeing of both breeding stock and experimental animals, with each inspected regularly in accordance with Home Office requirements. Colony management was performed using Tick@Lab software (A-Tune Software Inc, Jonestown, USA).

2.3.2 Genetically engineered mouse model (GEMM) experiments

2.3.2.1 Cre-LoxP recombination technology

Cre-LoxP mediated recombination is a highly specific means of editing specific genes in vivo that exploits the activity of the Cre recombinase enzyme of the P1 bacteriophage. This enzyme, which belongs to the integrase family of site-specific recombinases, recognises specific *loxP* sequences (locus of X-over P1; which includes an asymmetric 8 bp spacer sequence between two symmetric and palindromic 13 bp recognition sequences) that have previously been inserted either side of a specific target gene, which is said to be 'floxed' (Tronche et al., 2002). Two Cre recombinase enzymes bind to the *loxP* site, forming a dimer, which in turn come together to form a tetramer, bridging two *loxP* sites together with opposing directionality and thereby facilitating excision of the region in-between (Tronche et al., 2002), as outlined schematically in ***Figure 2.8***.

Whilst initially originating in the P1 bacteriophage, the Cre recombinase enzyme has been demonstrated to work successfully in mice when expressed from a transgene under the control of a promoter. If this promoter is ubiquitous then Cre expression is systemic and leads to indiscriminate gene editing that may be lethal to the mouse if an essential gene is targeted. Alternatively, use of a lineage or cell type-specific promoter enables spatial control of *Cre* expression, thereby limiting gene editing to a specific cell or tissue of interest (Kim et al., 2018). In addition, *Cre* expression can also be regulated through induction by pharmacological agents, enabling temporal control of gene editing (Kim et al., 2018). A commonly used inducible system is that which utilises the selective oestrogen receptor modulating agent tamoxifen and a modified form of Cre that is fused with an oestrogen receptor containing a mutated ligand binding domain. This protein is known collectively as Cre-ER^{T} and is normally present in the cytoplasm bound to heat shock protein 90 (HSP90), which prevents its

translocation to the nucleus. The binding of tamoxifen induces a conformational change that disrupts the interaction with HSP90, thereby enabling translocation to the nucleus where interaction with *loxP* sites and subsequent gene editing can occur, as illustrated in ***Figure 2.9.*** More recently, a modified version of Cre-ER^{T} termed Cre-ER^{T2} has been developed which is approximately 10 times more sensitive to the active metabolite of tamoxifen, 4-hydroxytamoxifen (4-OHT), than Cre-ER^{T} in terms of both recombinase activity and nuclear translocation (Indra et al., 1999). This enables lower doses of tamoxifen to be used for induction, hence reducing possible toxicity and side effects in animal models.

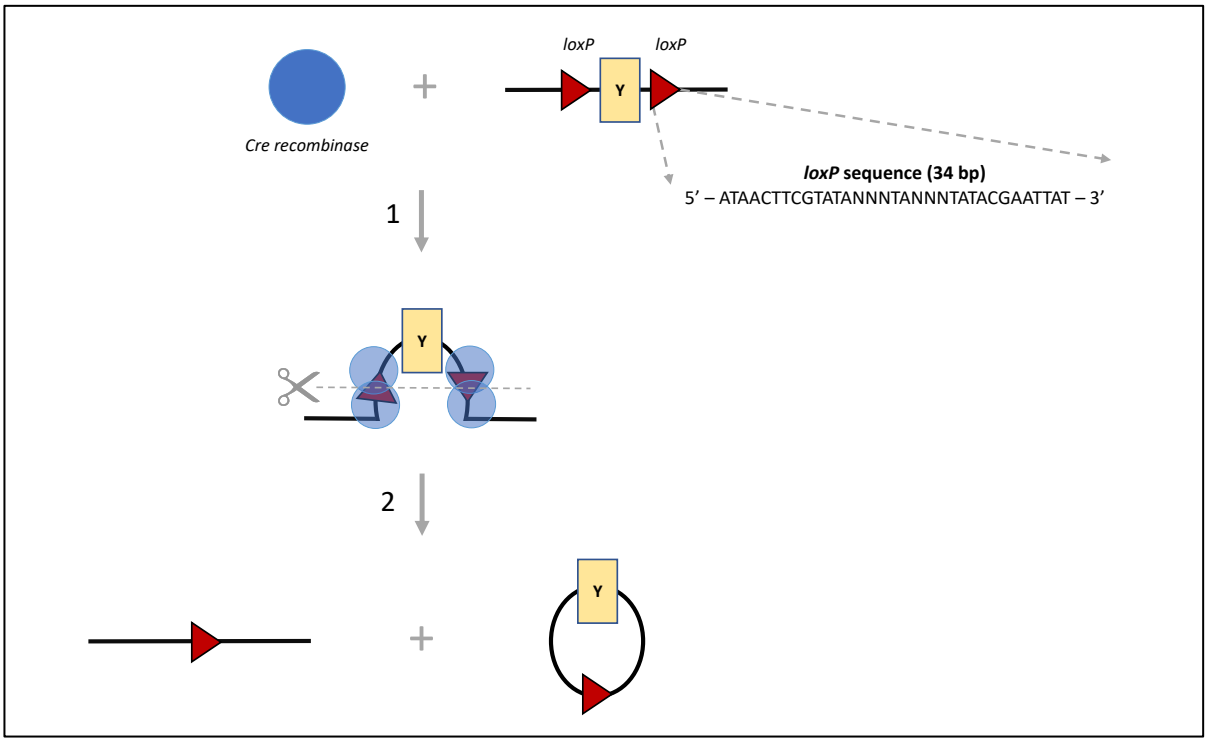

Figure 2.8: *Schematic overview of Cre-LoxP recombination resulting in deletion of a gene of interest (Y).* 1. Two Cre recombinase enzymes recognise and bind to each *loxP* site, forming dimers. The two dimers come together to form a tetramer, bridging the *loxP* sites with opposing directionality. 2. Double strand DNA cleavage occurs in the centre of the *loxP* sites, gene Y is excised as a circular piece of DNA and continuity of the DNA is restored. Alternative outcomes of gene inversion and translocation are also possible if the *loxP* sites are in opposite orientations or on separate pieces of DNA respectively (mechanisms not shown).

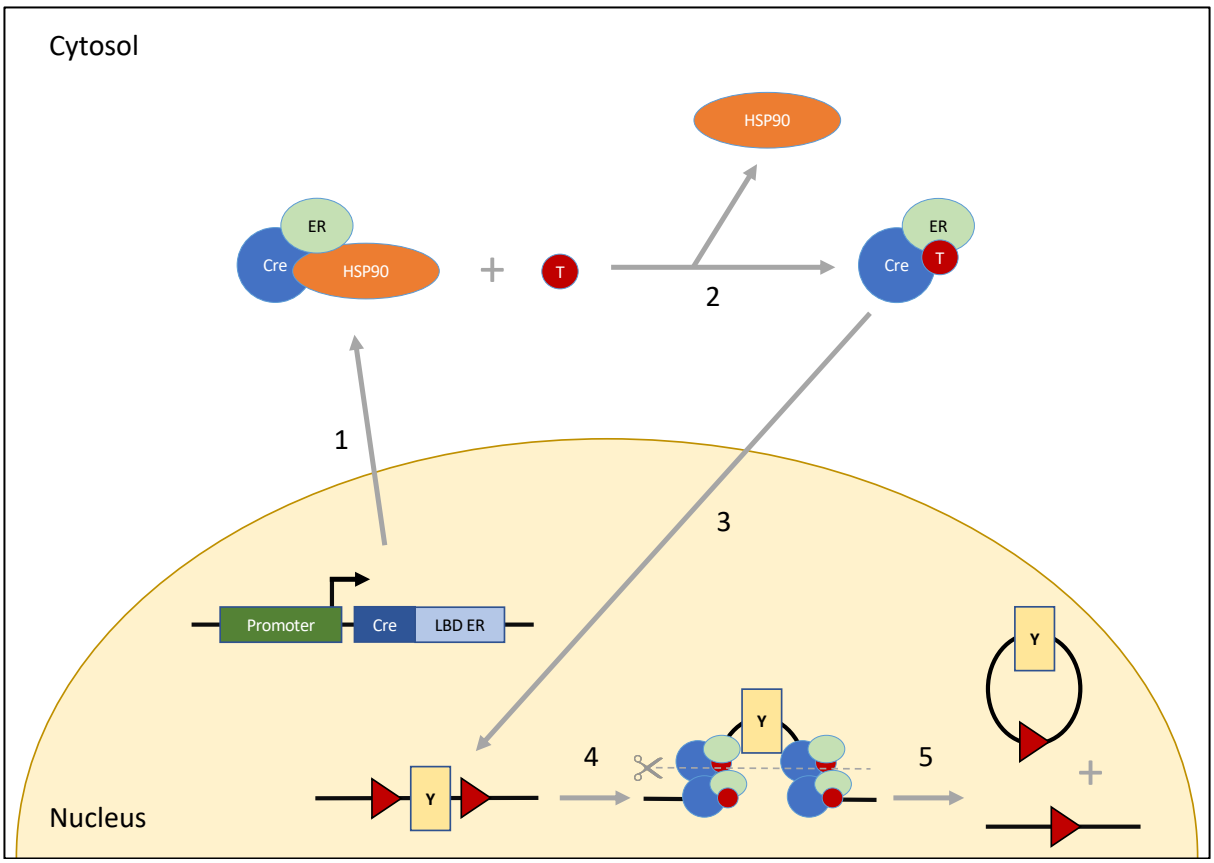

Figure 2.9: *Schematic overview of the tamoxifen inducible Cre-LoxP recombination system.* 1. Expression of Cre-ER^T occurs in the tissue of interest under the influence of a site specific promoter. The Cre-ER^T translocates to the cytosol where it is associated with HSP90, preventing nuclear translocation. 2. The introduction of tamoxifen (e.g. via intraperitoneal injection of the mouse) results in a conformational change that enables dissociation of HSP90. 3. Cre-ER^T translocates back to the nucleus and interacts with *loxP* sites flanking the specific gene of interest (Y). 4. Two Cre-ER^T molecules recognise and bind to each *loxP* site, forming dimers. The two dimers come together to form a tetramer, bridging the *loxP* sites with opposing directionality. 5. Double strand DNA cleavage occurs in the centre of the *loxP* sites, gene Y is excised as a circular piece of DNA and continuity of the DNA is restored. Adapted from (Kim et al., 2018).

2.3.2.2 PSA-Cre-ER^{T2}

Transgenic mouse experiments in this thesis utilise Cre-ER^{T2} recombinase under the control of the human PSA promoter and androgen-dependent enhancer sequences, termed PSA-Cre-ER^{T2}, as described by Ratnacaram et al. in 2008 and illustrated schematically in ***Figure 2.10*** (Ratnacaram et al., 2008). Given that PSA is expressed exclusively by cells of the prostatic epithelium, use of this construct enables the highly selective excision of floxed alleles within the prostatic epithelium of mice following intraperitoneal administration of tamoxifen. When evaluated using quantitative PCR on DNA isolated 12 days following induction, recombination efficiency was found to vary according to prostate lobe and floxed target gene. Recombination efficiency for floxed retinoid X receptor alpha (*RXRα)* was found to be approximately 75-85% in the DLP, 75-85% in the VP, and 65% in the AP, whereas for floxed *Pten* it was only 35%, 31% and 8% respectively (Ratnacaram et al., 2008).

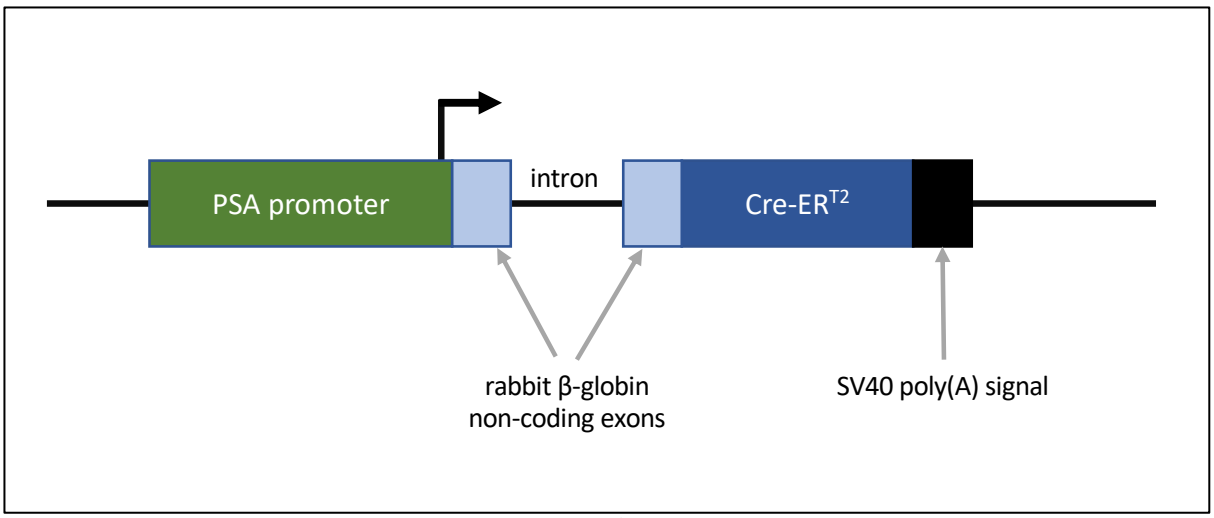

Figure 2.10: *Schematic representation of the PSA-Cre-ER^{T2} gene construct. The* human PSA promoter is followed by two rabbit β-globin non-coding exons interrupted by an intron. These are in turn followed by the Cre-ER^{T2} coding region and a simian virus 40 (SV40) poly(A) signal. The black arrow represents the transcription initiation site. Adapted from (Ratnacaram et al., 2008).

2.3.2.3 Floxed gene constructs

To achieve the in vivo components of Chapters 4 and 5 of this thesis, Cre-LoxP recombination with PSA-Cre-ER^{T2} was used to enable spatial and temporal control of expression of a range of genes specifically within the prostate epithelium of transgenic mice. Mice on a C57BL/6 background harbouring the *PSA-Cre-ER^{T2}* gene construct were crossed with those harbouring *Parp1* floxed, *Trp53* floxed and *Pten* floxed alleles sourced from collaborators in Cardiff University and elsewhere to generate the colonies outlined in Section 2.3.2.6. The *Trp53* gene encodes the p53 tumour suppressor protein in mice and hence the *Trp53* floxed allele is referred to as '*p53* floxed' throughout the remainder of this thesis for clarity. The individual floxed gene constructs are demonstrated schematically in ***Figure 2.11*** and have previously been validated to provide successful knockout of their respective genes using a range of Cre recombinase enzyme systems (Jonkers et al., 2001, Suzuki et al., 2001, Luo et al., 2017, Navarro et al., 2017).

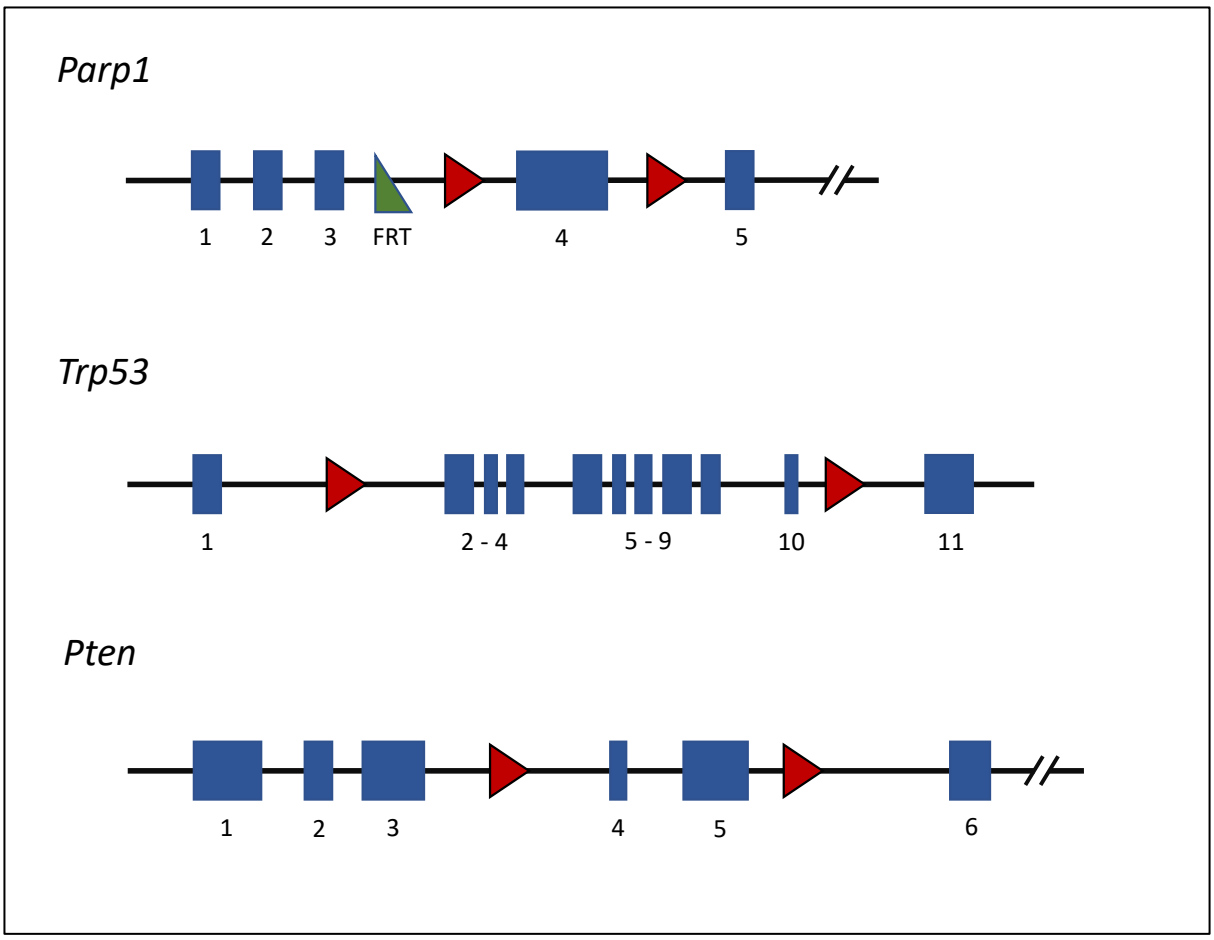

Figure 2.11: *Schematic representation of the floxed gene constructs used in conditional knockout experiments in Chapters 4 and 5. LoxP* sites illustrated as red triangles, exons as blue rectangles. FRT; flippase recognition target, Adapted from (Jonkers et al., 2001, Suzuki et al., 2001, Luo et al., 2017).

2.3.2.4 Import and rederivation of required floxed gene constructs

The *PSA-Cre-ER*^{T2} gene construct*, p53* floxed and *Pten* floxed alleles were sourced in house from colleagues within Cardiff University with permission following previous collaborations with external research groups. The *Parp1* floxed allele was developed by Dr Kraus and colleagues at the Cecil H. and Ida Green Centre for Reproductive Biology Sciences, University of Texas Southwestern Medical Centre, USA, and provided on a collaborative basis following acceptance of a Materials Transfer Agreement (MTA) (Luo et al., 2017). This construct comprises *LoxP* sequences flanking exon 4 of the *Parp1* gene, as shown in ***Figure 2.11***, with exposure to Cre recombinase resulting in excision of exon 4 and hence loss of functional protein (Luo et al., 2017). Imported *Parp1*$^{fl/fl}$ males on a C57BL/6 background were mated with *Parp1* wild-type C57BL/6 females and embryo transfer using standard techniques performed to rederive the allele into the Transgenic T2 Facility at Cardiff University.

2.3.2.5 GEM breeding strategy and generation of experimental cohorts

The experimental cohorts required for Chapters 4 and 5 of this thesis and outlined in ***Figure 2.12***. These were generated by a series of breeding, initially involving the crossing of mice harbouring one copy of the *PSA-Cre-ER^{T2}* construct (heterozygous) with those harbouring two copies of the necessary floxed alleles (homozygous) and then crossing the heterozygous offspring together**.** All experimental cohort mice were heterozygous for *PSA-Cre-ER^{T2}* (denoted as *PSA-Cre-ER$^{T2+/-}$*). After reaching sexual maturity, adult mice of known genotypes were placed in breeding cages consisting of one male and two females. Pups were weaned at 21 days and when independently feeding. Ear biopsies were taken shortly after weaning to allow prompt genotyping and allocation to required experimental cohorts.

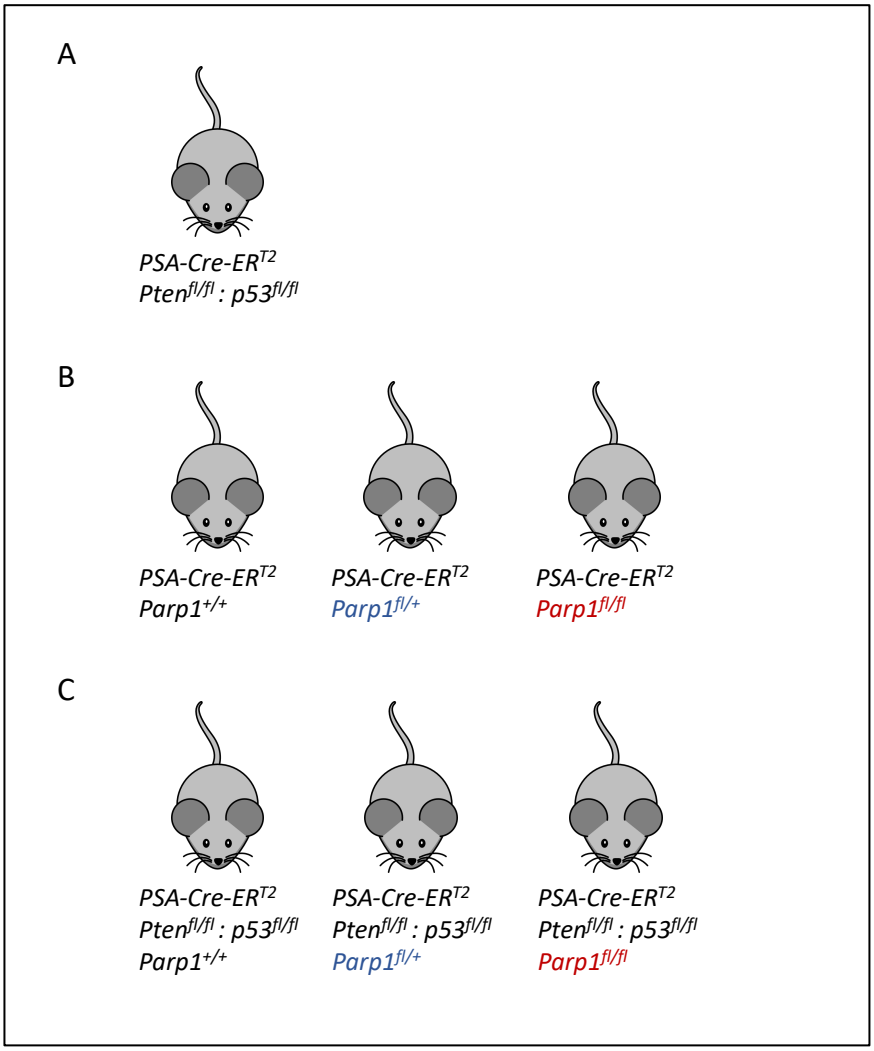

Figure 2.12: *Genotypes of genetically modified mice required in transgenic experiments.* A: Genotype of those mice used as the GEMM of localised prostate cancer in Chapter 4. B: Genotype of transgenic mice used in the study of PARP1 physiology in the normal prostate in Chapter 5. C: Genotype of transgenic mice used in the study of PARP1 physiology in prostate cancer in Chapter 5. Fl/fl, wild type for floxed allele construct; fl/+; heterozygous for floxed allele construct; fl/fl, homozygous for floxed allele construct.

2.3.2.6 Tamoxifen induction of PSA-Cre-ER^{T2}

Tamoxifen preparation and induction of PSA-Cre-ER^{T2} was undertaken as previously described (Metzger et al., 2005, Ratnacaram et al., 2008). In brief, a stock solution of tamoxifen at a concentration of 1 mg/ml was prepared on the day of first induction by aseptically weighing 1 mg of tamoxifen powder (Sigma-Aldrich, St Louis, USA; TG5648) and dissolving in 2 µl of 100% ethanol and 998 µl of corn oil (Sigma-Aldrich, St Louis, USA; C8267), followed by four hours in a shaking incubator at 50°C. 100 µl of stock solution (giving a total dose of 0.1 mg) was administered to 56 day old (+/- 7 days) experimental mice via intraperitoneal injection using a 26-guage needle at the same time each day for 5 consecutive days.

2.3.2.7 Genotyping of experimental mice

2.3.2.7.1 DNA extraction and isolation

An extraction master mix comprising 250 µl of cell lysis solution (Qiagen, Hilden, Germany; 158906) and 5 µl of recombinant Proteinase K (20 mg/ml; Roche, Basel, Switzerland; RPROTKSOL-RO) per mouse was produced. A volume of 255 µl of master mix was added to 1.5 ml Eppendorf tubes containing the individual ear biopsy each mouse requiring genotyping and left to incubate overnight at 37°C with gentle agitation. The following day, 100 µl of protein precipitation solution (Qiagen, Hilden, Germany; 158910) was added to each tube, after which they were centrifuged at 13000 RPM for 10 minutes at room temperature. The supernatant was then transferred to a new 1.5 ml Eppendorf tube containing 250 µl of isopropanol and centrifuged at 13000 RPM for 15 minutes at room temperature. The supernatant was then discarded and, after being airdried for 5 minutes, the DNA pellet was resuspended in 200 µl of DNAse free / MilliQ water and stored at 4°C until PCR could be performed.

2.3.2.7.2 Polymerase Chain Reaction (PCR)

A master mix containing the reagents and primer sequences outlined in ***Table 2.10*** and ***Table 2.11*** respectively was prepared on ice. 9.5 µl of master mix was added to a prelabelled PCR tube and combined with 0.5 µl of extracted DNA. A negative control containing 0.5 µl of DNAse free / MilliQ water and a positive control using DNA from a mouse known to possess the desired genotype was included for each reaction performed. Thermocycling was then performed using the conditions outlined in ***Table 2.12*** using a T100 Thermal Cycler (Bio-Rad, Hercules, USA).

2.3.2.7.3 Visualisation of PCR products

Each 10 µl gDNA PCR product and their respective controls were electrophoresed at 90 V in a 100ml 2% Agarose/TBE (TRIS, borate and EDTA) gel containing 4 µl of SafeView nucleic acid stain (NBS

Biologicals, Huntingdon, UK; NBS-SV1) for 45 to 60 minutes, depending on the gene. This stain binds to DNA and fluoresces under UV light, thus enabling visualisation of DNA bands of a given size following their expansion via PCR using the GelDoc Imaging System. 5 µl of 100 – 1000 bp DNA ladder was also run on the gel to identify product sizes. Genotype information was added contemporaneously onto mouse database and repeated for all experimental animals using a second ear biopsy taken following their termination at the experimental endpoint.

Table 2.10: *Components of the PCR master mix used for the genotyping of experimental animals.* Values given per individual sample, making a total volume of 9.5 µl for each reaction. All reagents purchased from Promega, Madison, USA. MgCl2; magnesium chloride, dNTP; deoxyribonucleotide triphosphate.

Reagent	**Volume per sample (µl)**
5 x Green Buffer	2
25 mM $MgCl_2$	1
100 mM dNTPs	0.08
100 µM Forward Primer	0.02
100 µM Reverse Primer	0.02
GoTaq Enzyme	0.04
MilliQ Water	6.34

Table 2.11: *Primer sequences used in genotyping PCR reactions.*

Gene	**Primer sequence**	**Reference**
Cre recombinase (generic)	*Forward*: GGGATTGCTTATAACACCCTGTTACG *Reverse*: TATTCGGATCATCAGCTACACCAGAG	(Gangoda et al., 2012)
Parp1 floxed	*Forward*: CTGTGGTCCTCTTGCCTCTG *Reverse*: ACTTCCCCAGGGATGGGTTA	(Luo et al., 2017)
p53 floxed	*Forward*: CACAAAAACAGGTTAAACCCAG *Reverse*: AGCACATAGGAGGCAGAGAC	(Jonkers et al., 2001)
Pten floxed	*Forward*: CTCCTCTACTCCATTCTTCCC *Reverse*: ACTCCCACCAATGAACAAAC	(Ratnacaram et al., 2008)

Table 2.12: *Thermocycling conditions used in genotyping PCR reactions.*

Temperature (°C)	Time (min)	Number of cycles
95	2.5	1
94	1	35
58	1	
72	1	
72	10	1
12	∞	NA

2.3.2.8 Tissue harvest and processing

2.3.2.8.1 Dissection and formalin fixation for histological and IHC analysis

At the time of experimental endpoint, or sooner if predefined ethical limits were being approached, mice were culled via a Schedule 1 approved method. For those designated to provide tissue for RNA and protein analysis the prostate was dissected in situ immediately after confirmation of death. One of each of the VP, DLP and AP lobes were individually weighed before being placed into Eppendorf tubes and snap frozen in liquid nitrogen. The remaining prostate was then excised en bloc and weighed collectively before being submerged in 10% neutral buffered formalin. The remainder of the GU tract and internal organs were then dissected and submerged in 10% neutral buffered formalin. After fixation at 4°C overnight, the remaining prostate was divided into individual lobes and, together with all other tissue, transferred to 70% ethanol and stored at 4°C. For those mice designated to provide tissue for IHC analysis only, the prostate was excised en bloc and weighed collectively before being submerged in 10% neutral buffered formalin and fixed at 4°C overnight. The following day the individual lobes were dissected from the main specimen and, together with all other tissues, transferred to 70% ethanol and stored at 4°C. Samples were later arranged into appropriately sized histocasettes, embedded in paraffin and cut into 4 μm sections that were either stained with H&E using standard protocols or stored for use in IHC.

2.3.2.8.2 Nucleic acid extraction and quantification

DNA and RNA was extracted from individual snap frozen prostate lobes using the AllPrep DNA/RNA/Protein Mini Kit (Qiagen, Hilden, Germany; 80004) in accordance with manufacturers instructions. The concentration and purity of extracted RNA was evaluated using spectrophotometry as described in Section 2.1.7.1.

2.3.2.8.3 Protein extraction and quantification

Individual prostate lobes were placed in 2 ml lysing matrix tubes containing 0.5 mm sterile ceramic beads and 600 µl of ice-cold RIPA buffer containing protease and phosphatase inhibitors as described in Section 2.1.5.1. Tubes were loaded onto the FastPrep-24 5G homogeniser and two cycles of 30 seconds duration performed. Tubes were then transferred to ice and centrifuged at full speed for 3 minutes at 4 °C. The supernatant was the aspirated and the concentration of protein quantified using the Quick Start Bradford Protein Assay as described in Section 2.1.5.1.

2.3.3 In vivo preclinical trials

2.3.3.1 Welfare, ethics and funding

All preclinical trials were performed in accordance with UK Home Office regulations under valid Personal and Project licences and designed following the principles of the National Centre for the Replacement, Refinement and Reduction of Animals in Research. The health and welfare of mice was evaluated daily using a standardised assessment tool and overseen by the Named Animal Care and Welfare Officer at the facility in which the experiments were performed. All drugs used in the experiment were provided by AstraZeneca (Cambridge, UK) following a Preclinical Partnership and Materials Transfer Agreement.

2.3.3.2 PC-3 subcutaneous xenograft preclinical trial

2.3.3.2.1 Model overview

Immunocompromised mice can be engrafted with human cancer cells to create xenografts that enable the in vivo study of human tissue in murine organisms. The subcutaneous approach in which tumour cells are injected into the flank is the most common xenograft model used in anticancer drug research as the tumour location results in minimal distress to the animal and enables regular and simple evaluation of tumour size during longitudinal monitoring. Given that PC-3 cells do not harbour clinically significant DDR aberrations, we opted to use the PC-3 subcutaneous xenograft model for the first preclinical trial to explore the efficacy of combined PARP and ATR inhibition in HR-proficient CRPC.

2.3.3.2.2 Model optimisation

A range of conditions for the propagation of PC-3 subcutaneous xenograft tumours have been described in the literature. As our group did not have prior experience with this model, an initial optimisation experiment was performed to establish tumour growth rates and ensure adequate conditions for the preclinical trial. As such, a six-week-old male athymic nude mouse (Charles River, Massachusetts, USA) was injected subcutaneously with 1.5 x 10^6 PC-3 cells into the left flank and 3 x 10^6 PC-3 cells into the right flank in accordance with the protocol described below. Serial length and

width measurements were taken using digital callipers and the maximum diameter recorded every 1-5 days. The mouse was terminated when the tumours approached ethical limits in order to determine the optimal treatment timeframe. The growth curves of the two tumours are demonstrated in ***Figure 2.13***. The tumour propagated from 3 x 10^6 cells demonstrated preferable growth properties, reaching a minimum diameter of 5 mm within three days of injection and remaining below the ethical size limit for the proposed 21 day dosing schedule. On the basis of these findings 3 x 10^6 cells was selected as the optimal number for tumour propagation in the preclinical trial.

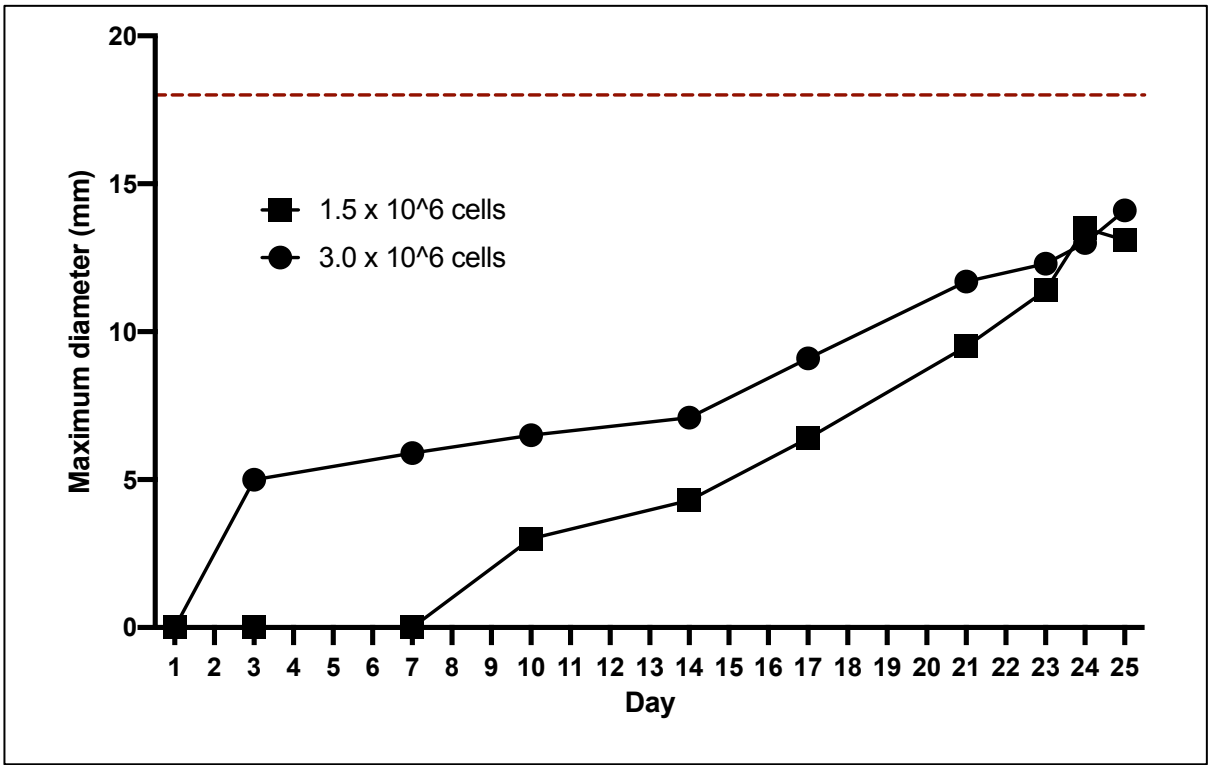

Figure 2.13: *Determining the optimal number of PC-3 cells required for propagation of subcutaneous xenograft tumours.* Growth curves of PC-3 subcutaneous xenograft tumours propagated from injection of 1.5 x 10^6 and 3.0 x 10^6 cells in a 6 week old male athymic nude mouse. Maximum diameter measured using digital callipers by the same operator every 1-5 days. Red line indicates 17mm maximum diameter ethical limit as determined by the Project Licence under which the experiment was undertaken.

2.3.3.2.3 Tumour propagation

Low passage PC-3 cells were expanded in vitro to 80% confluence using the standard conditions outlined in Section 2.1.2, after which they were dissociated using with 0.25% Trypsin-EDTA and counted. After centrifugation at 1000 RPM for 5 minutes cells were then resuspended in ice cold PBS to a concentration of 3 x 10^7 per ml. 500 µl of cell suspension was then combined with 500 µl of Matrigel (Corning Life Sciences, New York, USA; 11553620) at 4°C. 200 µl of the resulting suspension

was injected into the left and right flank of 6–8-week-old male athymic nude mice using a standard aseptic technique. Mice were monitored for a period of 3 days and tumour length and width measured on day 4 using digital callipers. Those tumours with a minimum diameter of 5 mm were considered eligible for inclusion in the preclinical trial.

2.3.3.2.4 Trial protocol

Mice bearing tumours meeting the inclusion criteria were allocated to the treatment groups outlined in ***Table 2.13***. Olaparib (100 mg/kg once daily PO; continuous), ceralasertib (25 mg/kg daily split into two 12.5 mg/kg doses PO; 7 days on, 14 days off) and their respective vehicles were reconstituted in accordance with instructions provided by AstraZeneca, as outlined in ***Tables 2.14*** and ***2.15***. All drug preparation was performed aseptically in the laboratory at the start of each dosing week, with drugs stored at room temperature and protected from light for up to 7 days. The dosing schedule is outlined in ***Figure 2.14*** and was designed in collaboration with AstraZeneca based on previous preclinical studies in other solid tumour models (data not provided). The second of the morning (AM) doses was given at least 1 hour after the first dose, with afternoon (PM) doses given at least 6 hours later. For logistical reasons, on weekends in which ceralasertib or the corresponding vehicle were administered, this was given as a single 25 mg/kg dose at least 1 hour after the first AM dose. Mice were monitored and weighed daily, with drug doses adjusted accordingly. Each agent was administered by an appropriately trained operator by oral gavage and recorded in accordance with Home Office guidelines. Tumour length and width were measured on Monday, Wednesday and Friday of each treatment week and tumour volume calculated. Mice were terminated at their designated timepoint, or when ethical limits concerning wight loss, health or tumour size/ulceration were approached.

Table 2.13: *Treatment groups, drug doses and timepoints for the PC-3 subcutaneous xenograft preclinical trial.*

Treatment group	Treatment	Timepoint
Vehicle	Olaparib vehicle Ceralasertib vehicle	21 days
Olaparib Short term	Olaparib 100 mg/kg Ceralasertib vehicle	21 days
Olaparib Long term	Olaparib 100 mg/kg Ceralasertib vehicle	Long term
Ceralasertib Short term	Olaparib vehicle Ceralasertib 25 mg/kg	21 days
Ceralasertib Long term	Olaparib vehicle Ceralasertib 25 mg/kg	Long term
Combination Short term	Olaparib 100 mg/kg Ceralasertib 25 mg/kg	21 days
Combination Long term	Olaparib 100 mg/kg Ceralasertib 25 mg/kg	Long term

Table 2.14: Reconstitution of olaparib to a 10mg/ml solution. After aseptic measurement of the required mass of olaparib, this was combined with the required volume of DMSO and agitated gently. The DMSO was then added drop wise to the 2-hydroxypropyl-β-cyclodextrin whilst being continually stirred for 20 minutes. The water for injection was then slowly added to the stirring mixture. Olaparib vehicle was made in the same manner, without the addition of olaparib powder.

Component	Stock concentration	Final concentration	Manufacturer	Order number
Olaparib powder	-	10mg/ml	AstraZeneca	-
DMSO	1 x	10% (v/v)	Sigma	D2650
2-hydroxypropyl-β-cyclodextrin	60%	50% (v/v)	Sigma	332593
Water for injection	1 x	40% (v/v)	Thermofisher	A1287301

Table 2.15: *Reconstitution of ceralasertib to a 2.5mg/ml solution*. After aseptic measurement of the required mass of ceralasertib, this was combined with the required volume of DMSO and agitated gently. The DMSO was then added drop wise to the Propylene glycol whilst slowly agitating. The water for injection was then slowly added to the mixture. Ceralasertib vehicle was made in the same manner, without the addition of ceralasertib powder.

Component	Stock concentration	Final concentration	Manufacturer	Order number
AZD6738	-	2.5mg/ml	AstraZeneca	-
DMSO	1 x	10% (v/v)	Sigma	D2650
Propylene glycol	1 x	40% (v/v)	Sigma	P4347
Water for injection	1 x	40% (v/v)	Thermofisher	A1287301

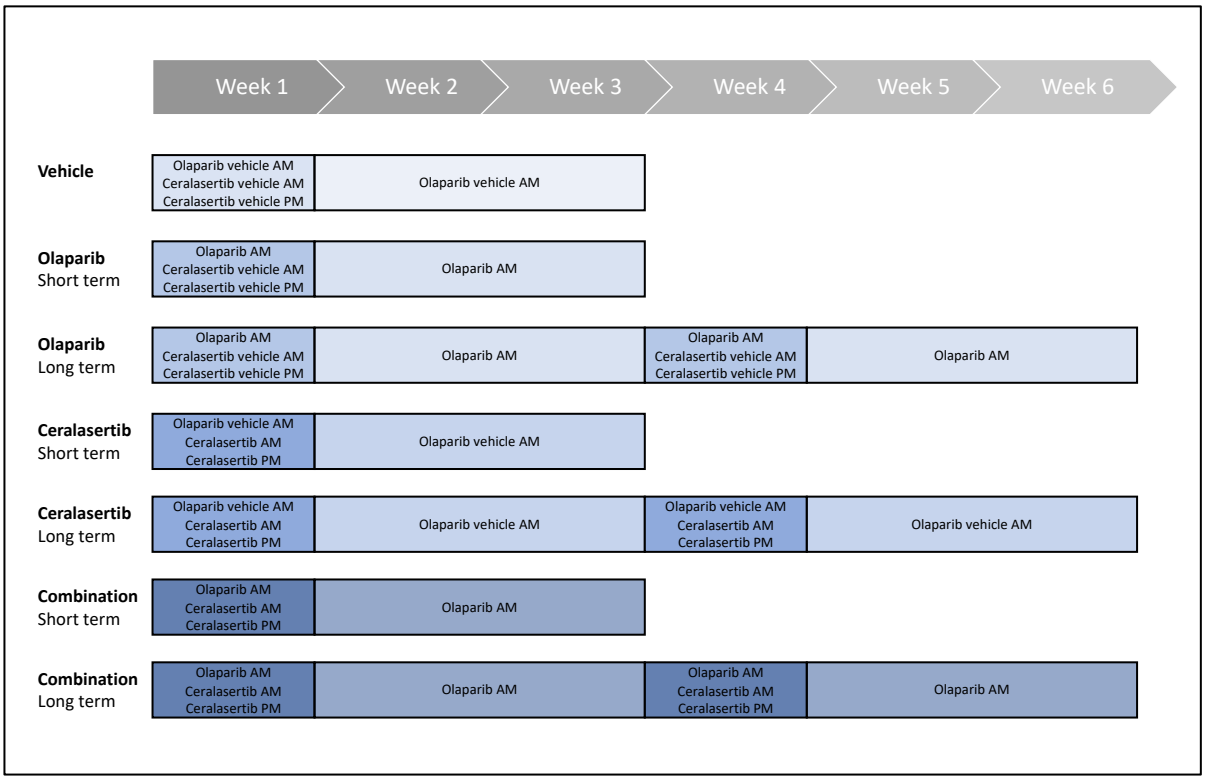

Figure 2.14: *Schematic overview of the PC-3 xenograft preclinical trial dosing schedule.* Olaparib and ceralasertib were given at doses of 100 mg/kg and 12.5 mg/kg respectively. The second AM dose was given 1 hour after the first dose, with PM doses given at least 6 hours later. For logistical reasons, on weekends in which ceralasertib or its vehicle were given, a 25 mg/kg dose of equivalent volume to the 12.5 mg/kg dose was given at least 1 hour after the first AM dose.

2.3.3.2.5 Primary and secondary outcomes

Safety and efficacy outcomes were predetermined prior to commencing the study. Safety outcomes were overall mortality and percentage weight loss compared with starting weight, as measured on the Monday, Wednesday and Friday of each treatment week and study timepoints. Primary efficacy outcome was tumour volume, as calculated on the Monday, Wednesday and Friday of each treatment week using the modified ellipsoid formula as given below (Euhus et al., 1986, Tomayko and Reynolds, 1989).

Calculation 2: *Tumour volume = ½(length x width^2)*

Secondary efficacy outcomes included tumour weight at the study endpoint and the presence of macroscopic neovascularisation, defined as subcutaneous vessels feeding and draining the tumour at the time of dissection, the presence of pathological lymphadenopathy, defined as enlarged lymph nodes within the regions draining the tumour, and invasion of local structures at the time of dissection.

2.3.3.2.6 Tissue harvest and analysis

At either the allocated timepoint or earlier if an ethical limit was approached, mice were treated with either olaparib 100 mg/kg or olaparib vehicle, followed by ceralasertib 25 mg/kg or ceralasertib vehicle one hour later. After two hours the mice were culled via a Schedule 1 approved method and the left and right tumours dissected separately. After photographing, each tumour was divided longitudinally and a central 1 mm thick section taken and snap frozen by placing in liquid nitrogen and stored at -80°C. The remaining tumour and any associated lymph nodes were then placed in 10% neutral buffered formalin and fixed overnight at 4°C. The following day the tissue was transferred to 70% ethanol and stored at 4°C until later being embedded in paraffin. Samples were later arranged into appropriately sized histocasettes, embedded in paraffin and cut into 4 μm sections that were either stained with H&E using standard protocols or stored for use in IHC. DNA, RNA and protein were extracted from snap frozen tumour tissue at a later date as previously described.

2.3.3.3 PSA-Cre-ER$^{T2(+/-)}$; p53$^{fl/fl}$; Pten$^{fl/fl}$ GEMM preclinical trial

2.3.3.3.1 Model overview

A wide range of prostate cancer model systems have been established for use in basic science and translational research, as discussed in Section 1.5. GEMMs are of particular value due to the level of genetic manipulation that can be achieved, short gestation times, intact tumour microenvironment, competent immune function and ability to recapitulate human prostate cancer (Cunningham and You,

2015, Huang et al., 2016). The GEMM selected for use in this thesis is the *PSA-Cre-ER$^{T2(+/-)}$; p53$^{fl/fl}$; Pten$^{fl/fl}$* model which enables deletion of *Trp53* and *Pten* tumour suppressor genes specifically within the cells of the prostatic epithelium upon induction of Cre recombinase activity with intraperitoneal administration of tamoxifen, thereby mirroring clinical prostate cancer with *TP53* and *PTEN* loss of function genetic variants that occur in 42% and 37% of cases of metastatic CRPC respectively, with co-occurrence in up to 56% (Grasso et al., 2012, Robinson et al., 2015, Kumar et al., 2016, Abida et al., 2019, Hamid et al., 2019). A full description of this model, together with the rationale for its use in this thesis is given in Section 4.1.

2.3.3.3.2 Trial protocol

Male C57BL/6 mice with the confirmed *PSA-Cre-ER$^{T2(+/-)}$; p53$^{fl/fl}$; Pten$^{fl/fl}$* genotype were induced after reaching sexual maturity at 8 weeks of age by intraperitoneal injection of tamoxifen as described in Section 2.3.2.6. Six months following induction, mice were randomly allocated to one of four treatment groups as outlined in ***Table 2.16***. Olaparib (100 mg/kg once daily PO; continuous), ceralasertib (25 mg/kg daily split into two 12.5 mg/kg doses PO; 7 days on, 14 days off) and their respective vehicles were reconstituted as in ***Table 2.14*** and ***Table 2.15*** at the start of each dosing week and stored at room temperature and protected from light for up to 7 days. The dosing schedule was again predetermined by AstraZeneca and is outlined in ***Figure 2.15***. Each agent was administered by an appropriately trained operator by oral gavage and recorded in accordance with Home Office guidelines. Mice were weighed and underwent health assessment on each day of study and were terminated at the study endpoint, or when predetermined ethical limits concerning wight loss, health or tumour size were approached.

Table 2.16: *Treatment groups, drug doses and timepoints for the PSA-Cre-ER$^{T2(+/-)}$; p53$^{fl/fl}$; Pten$^{fl/fl}$ GEMM preclinical trial.*

Group name	Treatment	Timepoint
Vehicle	Olaparib vehicle Ceralasertib vehicle	21 days
Olaparib	Olaparib 100 mg/kg Ceralasertib vehicle	21 days
Ceralasertib	Olaparib vehicle Ceralasertib 25 mg/kg	21 days
Combination	Olaparib 100 mg/kg Ceralasertib 25 mg/kg	21 days

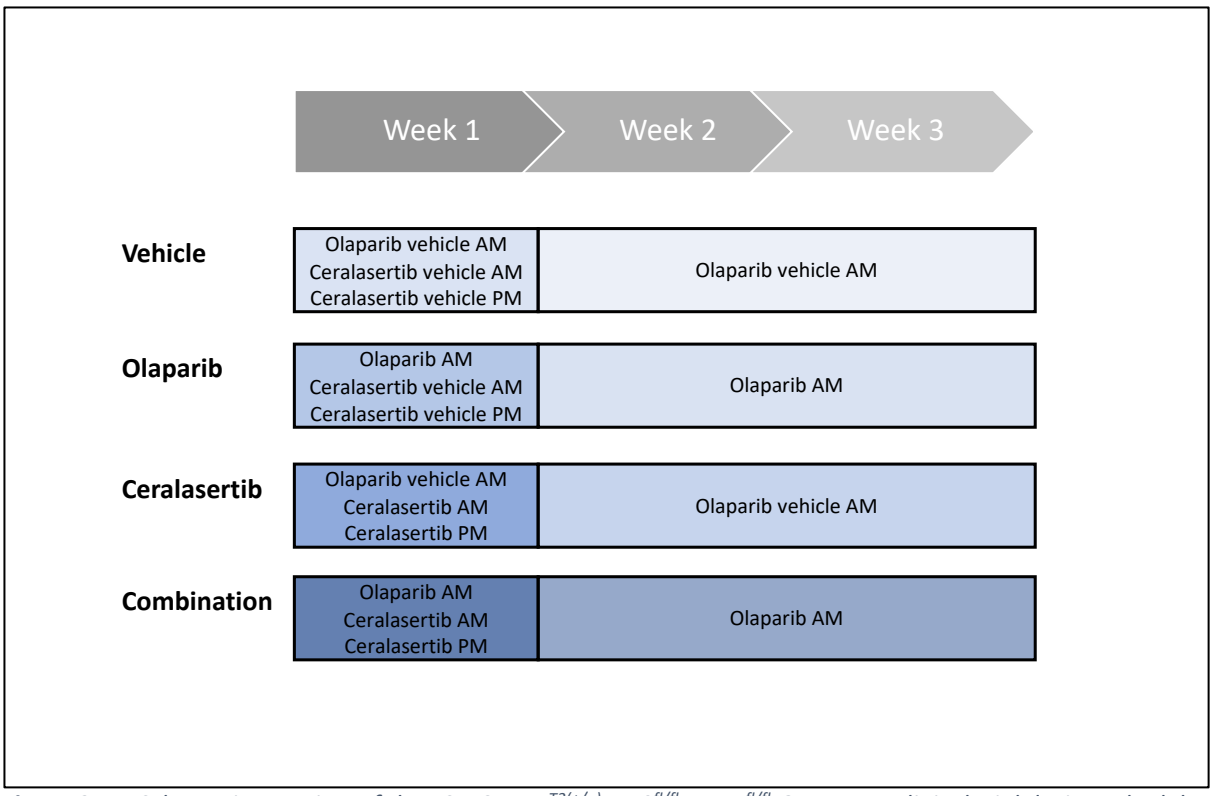

Figure 2.15: *Schematic overview of the PSA-Cre-ER$^{T2(+/-)}$; p53$^{fl/fl}$; Pten$^{fl/fl}$ GEMM preclinical trial dosing schedule.* Olaparib and ceralasertib were given at doses of 100 mg/kg and 12.5 mg/kg respectively. The second AM dose was given at least 1 hour after the first dose, with PM doses given at least 6 hours later. For logistical reasons, on weekends in which ceralasertib or its vehicle were given, a 25 mg/kg dose of equivalent volume to the 12.5 mg/kg dose was given at least 1 hour after the first AM dose.

2.3.3.3.3 Primary and secondary outcomes

Safety and efficacy outcomes were again pre-determined prior to commencing the study. Safety outcomes were overall mortality and percentage weight loss compared with starting weight, as measured on the Monday, Wednesday and Friday of each week of treatment and at the study endpoint. Primary efficacy outcome was the weight of the total prostate and individual lobes at the time of dissection, represented as both an overall weight in mg and a relative weight in percent, as calculated using the formula below.

Calculation 3: *Relative weight = (overall weight / total body weight) x 100*

2.3.3.3.4 Tissue harvest and analysis

At the study endpoint or earlier if an ethical limit was approached, mice were treated with either olaparib 100 mg/kg or olaparib vehicle, followed by ceralasertib 25 mg/kg or ceralasertib vehicle one hour later. After two hours the mice were then culled via a Schedule 1 approved method and the left

and right tumours dissected separately. The prostate was dissected in situ immediately after confirmation of death and one of each of the VP, DLP and AP lobes were individually weighed before being rapidly placed into Eppendorf tubes and snap frozen in liquid nitrogen. The remaining prostate was then excised en bloc and weighed collectively before being submerged in 10% neutral buffered formalin. The remainder of the GU tract and internal organs were then dissected and submerged in 10% neutral buffered formalin. After fixation at 4°C overnight, the remaining prostate was divided into individual lobes and, together with all other tissue, transferred to 70% ethanol and stored at 4°C. Samples were later arranged into appropriately sized histocasettes, embedded in paraffin and cut into 4 μm sections that were either stained with H&E using standard protocols or stored for use in IHC. DNA, RNA and protein was extracted from the snap frozen tissue at a later date as previously described.

2.4 Statistical analysis

All statistical analyses were undertaken using GraphPad Prism version 9.0 (GraphPad Software, La Jolla, USA) and/or IBM SPSS Statistics for Macintosh, version 25.0 (IBM Corm, Armonk, USA). Continuous parametric data were presented as mean (+/- Standard Error of the mean; SEM), with a two-tailed unpaired student's t-test or one-way analysis of variance (ANOVA) with Tukey correction used to compare the means of two groups or more than two groups respectively. For IncuCyte data with multiple timepoints and multiple treatment groups a repeated measures one-way ANOVA was performed. Continuous non-parametric variables were presented as median (range), with a Mann-Whitney test or Kruskal-Wallis test used to compare the medians of two or more groups respectively. Categorical data were presented as percentages and Chi-squared tests used to assess differences between groups. The type of statistical test used for each comparison are denoted in the relevant figure legends. A value of $p \leq 0.05$ was used to determine statistical significance.

3 Characterising the response of HR-proficient castrate resistant prostate cancer cells to PARP and ATR inhibition in vitro

3.1 Introduction

PARP enzymes are ubiquitous nuclear proteins that play a key role in a number of biological processes ranging from DNA damage repair and chromatin modulation to transcriptional regulation and the cellular stress response (Schreiber et al., 2006, Slade et al., 2011, Hottiger, 2015, Gupte et al., 2017). Whilst 17 isoforms have been identified, PARP1 is the most abundant and is known to play the greatest role in the DDR, followed by PARP2 and PARP3 (Dulaney et al., 2017). The best characterised DDR function of PARPs is their involvement in the recognition and repair of single strand DNA breaks via BER, as discussed in Section 1.6. However, there is also evidence to suggest that through binding to sites of DNA DSBs and subsequent recruitment of PAR-binding proteins such as Nijmegen breakage syndrome 1 (NBS1) and MRE11, PARP1 is also involved in the repair of DSBs via HR (Haince et al., 2008).

Given these key DDR functions, small molecule inhibitors which interact with the β-NAD^+ cofactor binding site in the catalytic domain of PARP enzymes have been developed (PARPi). Early studies focussed on the role of PARPi as a means of increasing sensitivity to other DNA damaging therapies, with 3-aminobenzamide being the first to be extensively characterised (Purnell and Whish, 1980). However, whilst this first-generation PARPi did demonstrate efficacy as a radiosensitiser, it was not selective or potent enough by current standards, thereby prompting the search for more competitive inhibitors (Rouleau et al., 2010). Newer, third generation PARPi have much greater specificity and potency, with several agents in varying stages of development.

Although firstly intended for use as sensitisers to other treatments, seminal work by Bryant et al. identified that cells deficient in *XRCC2*, *XRCC3* or *BRCA2*, all of which are crucial to DSB repair via HR, were highly sensitive to PARPi in vitro. Similar results have also been observed in *BRCA2* deficient V-C8 xenograft tumours treated with the PARPi AG14361 in vivo (Bryant et al., 2005). These findings were corroborated by Farmer et al., who observed that *BRCA1* and *BRCA2* deficient embryonic stem cells were extremely sensitive to the PARPi with KU0058684 and KU0058948 compared with either heterozygous *BRCA1* or *BRCA2* mutant or wild-type cells, with treatment resulting in chromosomal instability, cell cycle arrest and subsequent apoptosis (Farmer et al., 2005).

These preclinical findings paved the way for the entry of PARPi into early phase clinical trials in patients with cancer, with the PARP1 and PARP2 inhibitor olaparib being well tolerated and demonstrating

antitumour activity in patients with *BRCA1* and *BRCA2* deficient ovarian, breast and prostate cancer (Fong et al., 2009). Later phase trials have since confirmed olaparib to demonstrate synthetic lethality in patients with *BRCA* mutant solid tumours such that it is now recommended for use in *BRCA* mutant platinum chemotherapy responsive ovarian, fallopian tube or primary peritoneal cancer in the UK (Ledermann et al., 2012, Ledermann et al., 2014, Kaufman et al., 2015).

The observed efficacy in *BRCA* deficient solid tumours, together with the high prevalence of DDR mutations in advanced prostate cancer, prompted the clinical evaluation of PARPi in the setting of CRPC. As discussed in Section 1.6.4, the first of these was the TOPARP-A study, which demonstrated a response to olaparib monotherapy in 14 of the 16 patients with pre-existing DDR gene aberrations (Mateo et al., 2015). Subsequent larger trials have gone on to confirm PARPi efficacy in this patient cohort, demonstrating a role for PARPi as a single agent in men with CRPC and pre-existing aberrations in DDR genes, particularly those involved in HR (Mateo et al., 2019, de Bono et al., 2020, Hussain et al., 2020). However, given that this only represents 22-33% of the total CRPC population (Mateo et al., 2015, Robinson et al., 2015, de Bono et al., 2020), other approaches are needed to expand the use of PARPi to patients with HR proficient CRPC.

One approach to increasing the efficacy of PARP inhibition and therefore expanding the use of PARPi beyond patients with pre-existing DDR aberrations would be their combination with another DDR inhibitor such to induce contextual synthetic lethality. Through targeting a protein that is pivotal to DSB repair via HR it may be possible to increase the sensitivity of cancer cells to PARPi much like is seen in homozygous *BRCA2* loss (so called 'BRCAness'). ATR is one such potential target, as discussed in Section 1.6.6. ATR activation occurs in response to a broad range of DNA damage including SSBs, DSBs and a variety of DNA lesions that interfere with replication, after which it phosphorylates a number of downstream targets including its main effector, Checkpoint kinase 1 (CHK1), to bring about cell cycle arrest, DNA repair and amelioration of replication stress through replication fork stabilisation (Maréchal and Zou, 2013, Rundle et al., 2017).

A small number of studies have explored the effects of PARPi on the ATR-CHK1 axis in cancer. Huntoon at al. identified that the ATR inhibitor VE-821 sensitised ovarian cancer cells to a range of chemotherapy agents, including the PARPi veliparib in vitro (Huntoon et al., 2013). Whilst this effect was most pronounced in cells in which HR function had been reduced by means of siRNA mediated *BRCA1* depletion, it was also seen in HR-proficient cells, suggesting that ATRi enhances the efficacy of PARPi, regardless of HR status. More recently, Kim et al. found that the PARPi olaparib increased

phosphorylation of both ATR and CHK1 in ovarian cancer cells in vitro irrespective of *BRCA* status, suggesting increased dependency on ATR-CHK1 signalling in both HR-deficient and proficient settings (Kim et al., 2016). Furthermore a synergistic relationship was observed between PARPi and ATRi irrespective of HR status, with cells treated with both olaparib and the ATRi ceralasertib (AZD6738) demonstrating a significant decrease in viability compared with either treatment alone (Kim et al., 2016). Based on these observations, the experiments in this chapter therefore firstly sought to explore the biological effects of PARPi in CRPC cells, including the effect on ATR-CHK1 signalling, followed by an evaluation of the therapeutic relationship between pharmacological PARPi and ATRi in the setting of CRPC in vitro.

3.2 Chapter aims

1. To characterise the response of HR-proficient CRPC cells to the PARP1/2 inhibitor olaparib (AZD2281) in vitro.
2. To characterise the response of HR-proficient CRPC cells to the ATR inhibitor ceralasertib (AZD6738) in vitro.
3. To determine whether combined olaparib and ceralasertib is more efficacious than monotherapy for the treatment of HR-proficient CRPC cells in vitro.

3.3 Results

3.3.1 Characterising the response of HR-proficient CRPC cells to the PARP1/2 inhibitor olaparib (AZD2281)

3.3.1.1 CRPC cells demonstrate differential sensitivity to the PARPi Olaparib

A panel of three HR-proficient CRPC cell lines, PC-3, DU-145 and 22Rv1, were used for the reasons outlined in Section 2.1.1. To determine the sensitivity of these cells to the PARPi olaparib, cell viability dose response curves were generated for olaparib treatment (dose range 0 – 100 μM) and the relative IC50 values calculated at the 96 hour timepoint (***Figure 3.1)***. Even at the maximum dose of 100 μM, cell viability was only partially reduced in all cell lines at the timepoint assessed. These data therefore indicate that HR-proficient cells are only partially sensitive to olaparib treatment in this setting at this timepoint. Moreover, PC-3 cell viability plateaued at 53.5% in the presence of olaparib doses ≥10 μM, indicating the reduction in cell viability is not dose dependent. Similarly, DU145 and 22RV1 cell viability also plateaued without a complete reduction in cell viability, albeit at a higher dose than the PC-3 cells. As such, the IC IC50 values calculated for olaparib represent the 'relative' rather than 'absolute' IC50, which is defined as the concentration required to achieve a response half way between the top

and bottom plateaus of the curve (Sebaugh, 2011). PC-3 cells were the least sensitive to olaparib treatment at the 96 hour timepoint (relative IC50 1.251 μM, minimum viability = 53.5%) compared to the DU-145 (relative IC50 = 23.77 μM, minimum viability = 36.1%) and 22Rv1 cells (relative IC50 = 3.882 μM, minimum viability = 27.5%). Whilst these findings are similar to those described by Feiersinger et al. in which only a partial response to olaparib and other PARP inhibitors was identified in the same cell lines at the 96 hour timepoint (Feiersinger et al., 2018), further dose response curves in cells that are known to be HR-deficient and thereby sensitive to PARPi are required in order confirm the extent of insensitivity. Nevertheless, collectively these data support the notion that HR-proficient CRPC cells are poorly responsive to PARP inhibition, thereby corroborating the limited responses to olaparib observed in patients with CRPC lacking significant DDR aberrations in the TOPARP-A trial (Mateo et al., 2015).

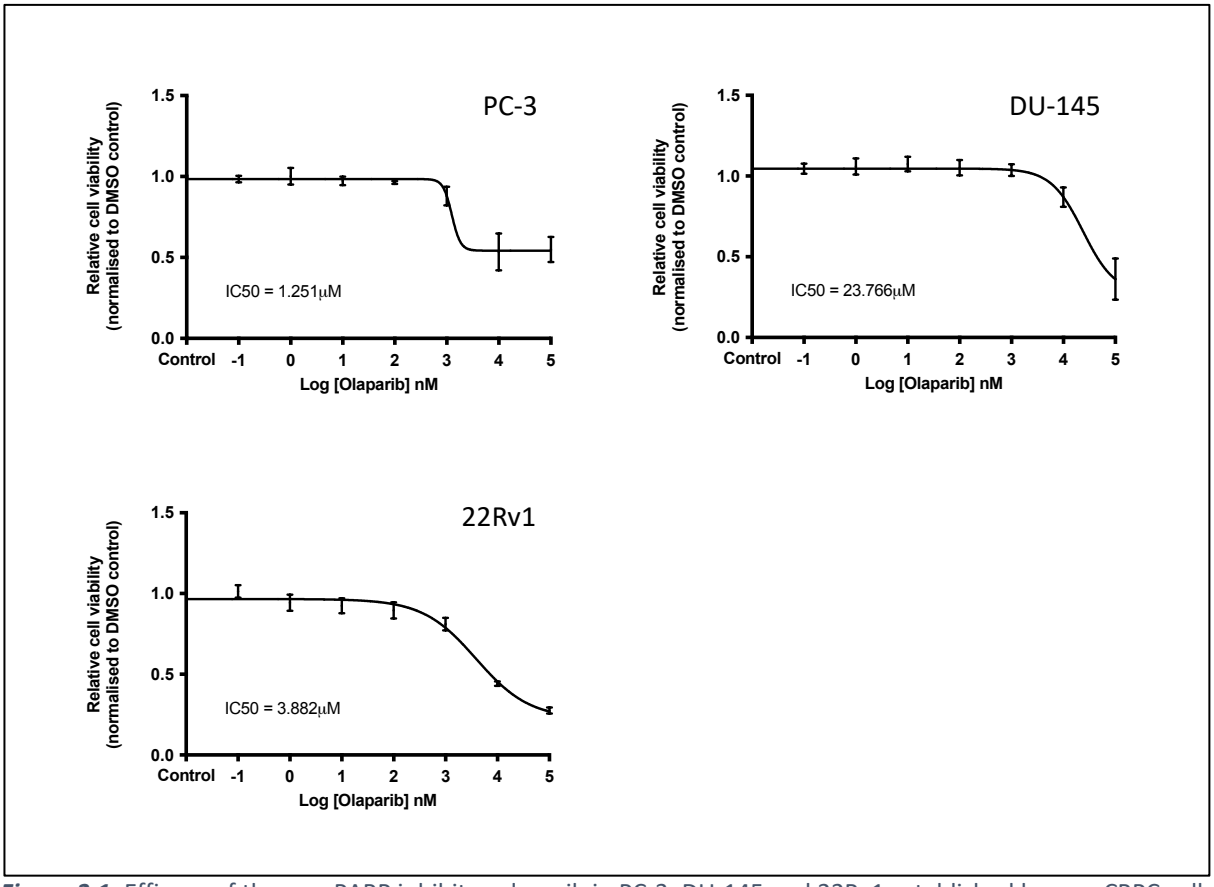

Figure 3.1: Efficacy of the pan-PARP inhibitor olaparib in PC-3, DU-145 and 22Rv1 established human CRPC cell lines. Cells were grown in 2D culture and exposed to increasing doses of Olaparib (0-100 μM) for 96 hours, after which cell viability was assessed using the Cell Titre Blue assay. Dose response curves and relative IC50 values in μM were generated using GraphPad Prism software and are represented for each cell line. Three independent repeats performed per cell line; error bars represent Standard Error of the mean.

3.3.1.2 PARP inhibition partially reduces CRPC cell proliferation and inhibits colony forming ability in vitro.

To determine the effects of PARP inhibition on the proliferative capacity of CRPC, PC-3, DU-145 and 22Rv1 cells were treated with olaparib at relative IC50 concentrations over a 96 hour period and cell confluency measured in real time relative to the DMSO treated controls using IncuCyte live cell imaging analysis software (***Figure 3.2A***). PARPi resulted in a statistically significant reduction in relative confluency compared with DMSO treated controls in all three cell lines after 48 hours exposure. However, despite ongoing treatment a continual increase in confluency was observed throughout the treatment period in all cell lines, indicating an incomplete suppression of proliferation and again corroborating the findings that CRPC cells are only partially sensitive to PARPi.

To establish the effect of PARPi on the stem cell properties of CRPC we utilised the colony formation or 'clonogenic' assay, a well-established means of identifying cells that retain the capacity for producing progeny during or after treatment with a particular agent that causes reproductive cell death. PC-3, DU-145 and 22Rv1 cells were seeded at low density during treatment with olaparib at relative IC50 concentrations, together with DMSO treated controls. Colony forming efficiency (CFE) was quantitated at either 7 days (PC-3 and DU-145) or 10 days (22Rv1) and is demonstrated in ***Figure 3.2B*** and ***Figure 3.2C***. Both PC-3 and DU-145 cells demonstrated high innate levels of colony forming ability, with CFE values of 59.8% (+/- 4.71% SEM) and 43.7% (+/- 2.87% SEM) respectively in DMSO treated controls. On the contrary, 22Rv1 cells possessed a lower innate level of colony forming ability, with a control CFE value of 20.2% (+/- 0.91% SEM). This could be explained by lower proliferative capacity of 22Rv1 cells, which are known to possess a doubling time of approximately 40 hours compared with 25 and 29 hours for PC-3 and DU-145 cells respectively. Treatment with olaparib resulted in a highly significant decrease in the CFE compared with DMSO treated controls in each of the three cell lines (25-fold, 35-fold and 6-fold reductions respectively; $P \leq 0.001$). These findings indicate that PARPi treatment at relative IC50 concentrations can inhibit CRPC cell clonogenicity.

To determine if the effect on clonogenicity was maintained following cessation of treatment, a second colony formation experiment was performed using cells that were pre-treated for 96 hours with either vehicle or olaparib at relative IC50 concentrations before seeding at low density. CFE was again assessed at 7 days (PC-3 and DU-145) or 10 days (22Rv1). As shown in ***Figure 3.2C***, whilst olaparib withdrawal partially restored clonogenicity in PC-3 and DU-145 cells, CFE was completely restored in 22Rv1 cells, with no difference between olaparib and DMSO treated controls (19.1 % +/- 3.65% SEM versus 24.3% +/- 2.71% SEM respectively, P=0.431). Taken together, these data suggest that PARPi with olaparib is not sufficient to completely block the proliferative capacity of CRPC cells in 2D culture

assays. However, treatment with olaparib is able to significantly reduce CPRC cell clonogenicity during treatment, although this effect is not maintained following withdrawal, suggesting this phenomenon can only be maintained through continuous drug administration.

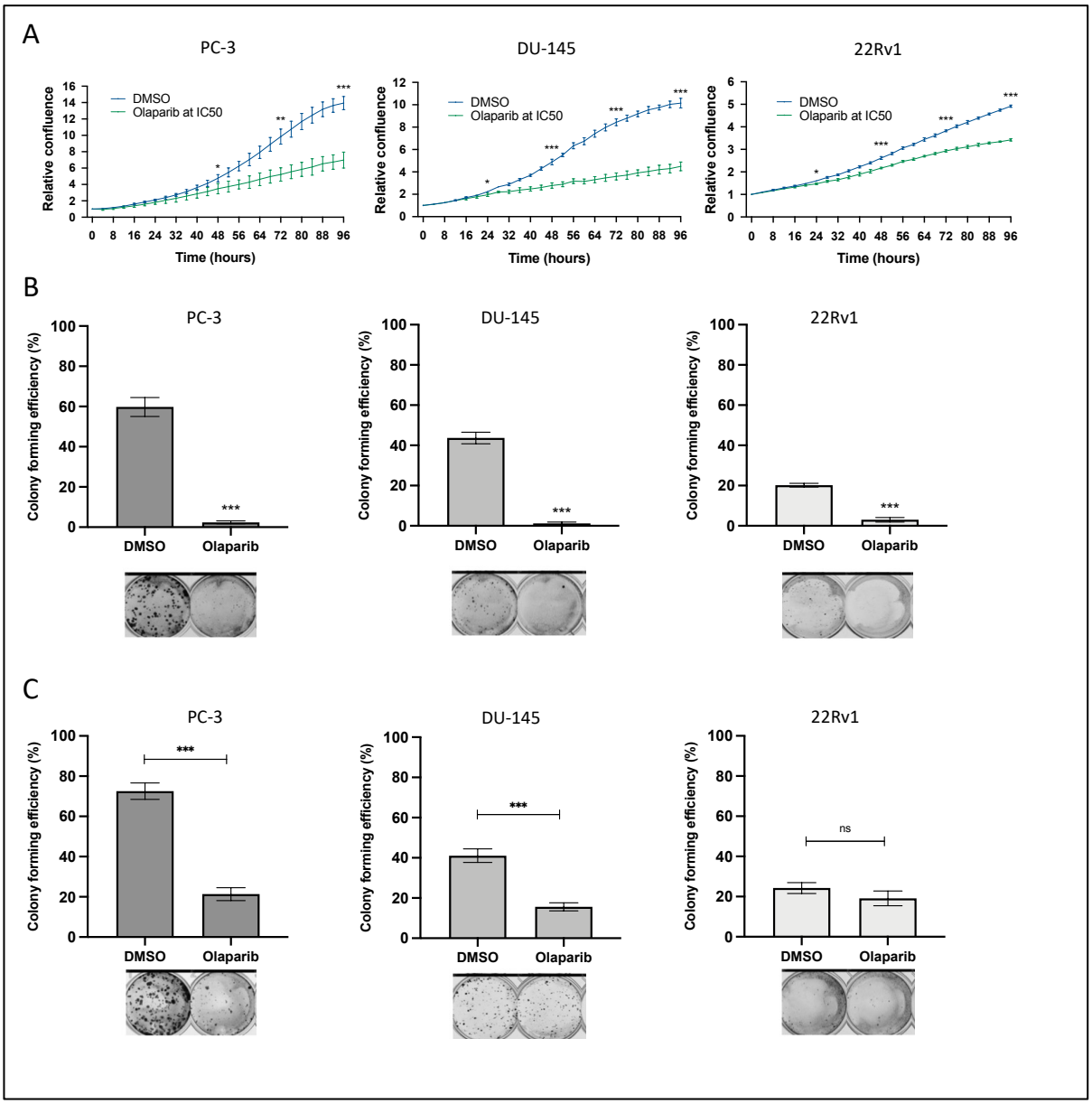

Figure 3.2: *Functional response of HR-proficient CRPC cells to olaparib treatment*. A: Cell confluency plots demonstrating relative confluency of cells treated with olaparib at relative IC50 concentrations compared with DMSO vehicle treated controls over 96 hours. 3 independent repeats performed with identical trends; one repeat shown. B: Low-density 2D colony forming efficiency (CFE) plots and representative whole well images of crystal violet stained colonies after treatment with olaparib (at relative IC50 concentration) or DMSO for 7 days (PC-3, DU-145) or 10 days (22Rv1). C: Colony forming efficiency (CFE) and representative whole well images of cells pre-treated for 96 hours with olaparib (relative IC50 concentration) or DMSO prior to being seeded at low density and cultured for 7 days (PC-3, DU-145) or 10 days (22Rv1). Three independent repeats per cell line. Error bars represent Standard Error of the mean. Statistical significance calculated using the unpaired Student's t-test. ***: $P \leq 0.001$, **: $P \leq 0.01$, *: $P \leq 0.05$, ns: $P > 0.05$.

3.3.1.3 Treatment with olaparib increases the quantity of double strand DNA breaks in CRPC cells and results in cell death via apoptosis in vitro

DNA DSBs are widely considered to be the most genotoxic form of DNA damage, as discussed in Section 1.6. An early response to the formation of DSBs is phosphorylation of the minor histone H2A variant H2AX at mammalian Ser-139 to form γ-H2AX, which in turn results in increased accessibility of the damaged DNA for recruitment and accumulation of DDR proteins (Mah et al., 2010). As such, assays that detect γ-H2AX are a recognised means of measuring and quantifying DSBs. To determine if PARP inhibition results in DSB formation, WB was performed to detect γ-H2AX concentration in PC-3, DU-145 and 22Rv1 cells treated with olaparib for 96 hours. Olaparib treatment resulted in a significant increase in γ-H2AX compared to DMSO treated controls in PC-3 and 22RV1 cells (***Figure 3.3A***). Whilst olaparib treatment also resulted in an increase in γ-H2AX concentration in DU-145 cells, this response was not statistically significant when compared with DMSO treated controls (P=0.540). These data collectively indicate that PARPi monotherapy increases DSBs in HR-proficient CRPC cells, although further experiments are required to elucidate the exact mechanisms responsible.

To determine whether an increase in cell death was the mechanism responsible for the reduction in proliferation and colony formation (***Figure 3.2***), cells undergoing apoptosis were stained using a fluorescent marker of Annexin V and fluorescence measured in real-time throughout 96 hours of treatment at IC50 concentrations using the IncuCyte live cell imaging system. The confluence of apoptotic cells was then normalised to the overall cell confluence at each time point, giving a relative measure of apoptotic cell count as demonstrated in ***Figure 3.3B***. Data for the first 24 hours of treatment was excluded from analysis on account of an artefactual peak in fluorescence during this period. Whilst the proportion of apoptotic cells at any given time point was low, the number of cells undergoing apoptosis in DMSO treated controls gradually reduced in all cell lines throughout the 96 hour period. On the contrary, the proportion of olaparib treated cells undergoing apoptosis remained at a higher level, with differences proving significant at 48, 72 and 96 hours in DU-145 and 22Rv1 cells and 72 and 96 hours in PC-3 cells. However, the trend in proportion of apoptotic cells over time differed between cell lines, with a gradual increase seen in PC-3 cells, a constant level in DU-145 cells and a gradual decrease in 22Rv1 cells. Collectively these data indicate that whilst olaparib treatment does induce apoptosis in a small proportion of CRPC cells, this is at a low level that does not mirror the more pronounced reduction in proliferation and colony formation, hence indicating that PARP inhibition alone is predominantly cytostatic rather than cytotoxic in CRPC.

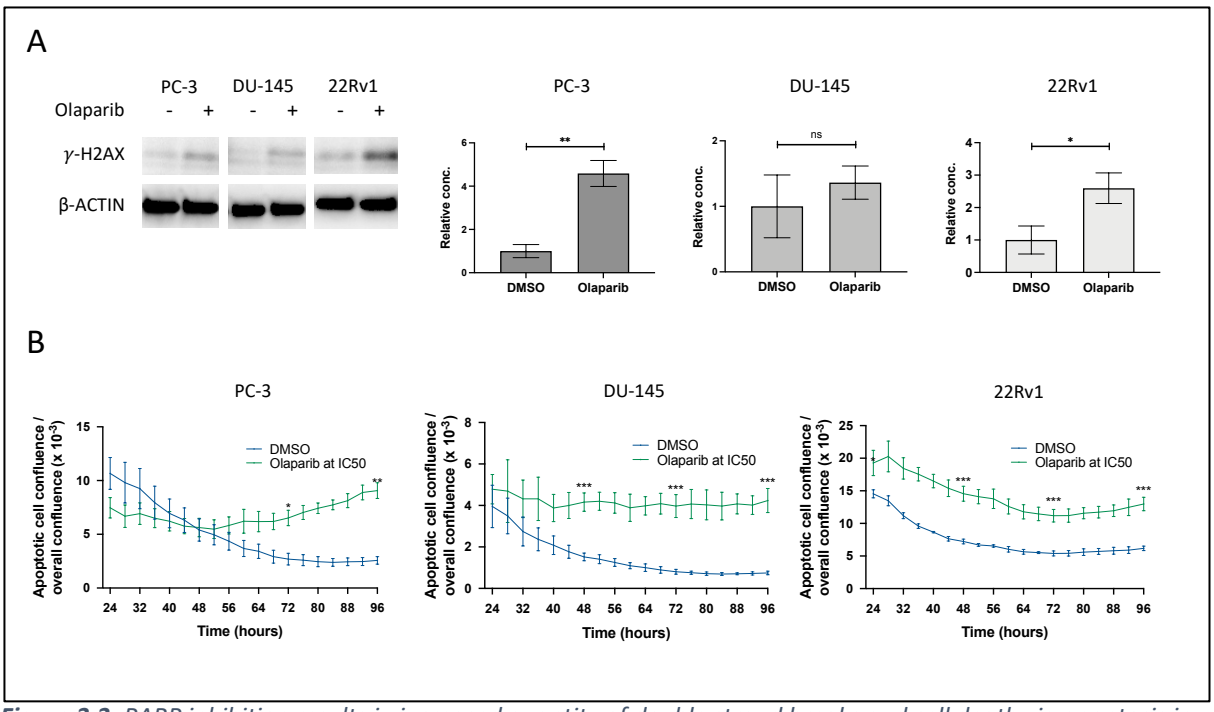

Figure 3.3: *PARP inhibition results in increased quantity of double strand breaks and cell death via apoptosis in HR-proficient CRPC cells treated in vitro.* A: Representative Western Blot images and densitometry bar charts demonstrating relative changes in quantity of γ-H2AX following 96 hours of treatment with olaparib at IC50 concentrations compared with DMSO treated controls. Densitometry data normalised to B-actin loading controls. Three independent repeats per cell line; error bars represent Standard Error of the mean. Statistical significance calculated using unpaired Student's t-test. B: Representative plots demonstrating the proportion of CRPC cells undergoing apoptosis during 96 hours of olaparib treatment at IC50 doses compared with DMSO treated controls. 3 independent repeats performed with identical trends; one repeat shown; error bars represent Standard Error of the mean. Statistical significance calculated using the unpaired Student's t-test. ***: $P \leq 0.001$, **: $P \leq 0.01$, *: $P \leq 0.05$, ns: $P > 0.05$.

3.3.1.4 ATR-CHK1 signalling is altered in CRPC cells treated with olaparib at IC50 doses

As discussed in Section 3.1, preclinical studies in ovarian cancer have demonstrated that ATR-CHK1 signalling is increased following PARP inhibition, with a synergistic relationship between PARPi and ATRi in both HR-proficient and deficient cells in vitro (Huntoon et al., 2013, Kim et al., 2016). The next set of experiments therefore sought to determine the effect of PARP inhibition on ATR-CHK1 signalling in HR-proficient CRPC cells, beginning with qRT-PCR to evaluate changes in expression of *ATR* and *CHEK1* (the gene encoding the CHK1 protein) following olaparib treatment.

ATR is activated by means of phosphorylation in response to a variety of DNA lesions through the interaction between itself, its obligate partner ATR Interacting Protein (ATRIP), DNA damage bound Replication Protein A (RPA) and the DNA-damage-specific RAD9-RAD1-HUS1 clamp. Activated ATR then phosphorylates a wide range of proteins, most notably Checkpoint kinase 1 (CHK1), which in turn phosphorylates a number of effectors to trigger a range of cellular responses including transcriptional

regulation, cell cycle arrest in the S and G2 phases of the cell cycle, and cell death if the damage is not deemed repairable (Zhang and Hunter, 2014). Accordingly, an increase in the ratio of phospho-ATR (p-ATR) and phospho-CHK1 (p-CHK1) to total ATR and total CHK1 respectively serve as surrogate markers of ATR-CHK1 pathway activation. WB was therefore used to detect total and p-ATR and p-CHK1 to enable calculation of these ratios and hence determine the effect of olaparib treatment on activation of each protein.

Firstly, ATR expression and activation in PC-3, DU-145 and 22Rv1 cells following 96 hours of olaparib treatment at the relative IC50 concentrations was assessed. At the mRNA level, olaparib treatment resulted in variable but low-level changes in *ATR* mRNA transcription, with a 51.7% (+/- 6.0% SEM; P=0.046) and 7.1% (+/- 17.7% SEM; P=0.355) reduction seen in PC-3 and DU-145 cells respectively and a 34.2% (+/- 14.9% SEM; P=0.046) increase detected in 22Rv1 cells relative to the vehicle control (***Figure 3.4A)***. Similarly at the protein level, olaparib treatment resulted in a reduction in total ATR in both DU-145 and 22Rv1 but not PC-3 cells, with no apparent change in p-ATR levels compared with DMSO treated controls in any cell line (***Figure 3.4B)***. However, when changes in total ATR concentration were accounted for by calculation of the p-ATR to total ATR ratio, a 1.40-fold and 1.35-fold increase ATR activation was seen in DU-145 and 22Rv1 cells respectively following olaparib treatment, although this did not reach statistical significance (P=0.108 and P=0.248 respectively; ***Figure 3.4C***). Together these data indicate that PARP inhibition does bring about a cell line specific alteration in ATR gene transcription, most notably in PC-3 cells, which may be the result of the differing genetic and epigenetic profiles of each. However, these changes were not reflected at the protein level, with olaparib treatment bringing about small but non-significant increases in p-ATR to total ATR ratio in both DU-145 and 22Rv1 cells. Nevertheless, it is possible that this may be an underestimation of ATR activation as only one p-ATR antibody was used in the WB analysis. The chosen antibody, which has been used in previously published studies, is selective for ATR that is phosphorylated at Serine-428, a well characterised response to UV induced DNA damage. However, more contemporary research suggests that autophosphorylation of threonine-1989 in response to DNA damage is also important in the activation of ATR (Nam et al., 2011).

Analysis of *CHEK1* mRNA by qRT-PCR demonstrated that 96 hours of olaparib treatment led to a significant reduction in expression compared with DMSO treated controls in PC-3 cells (29.1% +/- 9.4% SEM; P=0.047) and 22R1 cells (42.4% +/- 14.4% SEM; P=0.021), while a similar but statistically insignificant trend was observed in DU-145 cells (12.8% +/- 19.3% SEM; P=0.271; ***Figure 3.5A***). However, WB analysis revealed that 96 hours of olaparib treatment does not appear to dramatically

alter total CHK1 levels compared to DSMO controls (***Figures 3.5B)***. On the contrary, olaparib treatment resulted in a significant increase in p-CHK1 levels in each cell line compared with DMSO treated controls. Calculation of the p-CHK1 to total CHK1 ratio revealed that olaparib treatment resulted in 4.31-fold (P=0.01) and 2.16-fold (P=0.037) increases in CHK1 activation in PC-3 and DU-145 cells respectively and a smaller, non-significant increase in 22Rv1 cells (1.51-fold increase; P=0.107; ***Figure 3.5C***).

Collectively, these findings indicate that PARPi results in a marked increase in CHK1 activation in HR-proficient CRPC cells in vitro. Whilst there appears to be a corresponding increase in ATR activation, this is disproportionately lower; although this may have been an underestimation due to the issues mentioned above and must therefore be interpreted with caution. Nevertheless, taken together these data indicate that PARPi induced DNA damage results in activation and therefore increased dependency on ATR-CHK1 signalling in HR-proficient CRPC cells, supporting the rationale for co-inhibiting PARP and ATR-CHK1 activation in this setting.

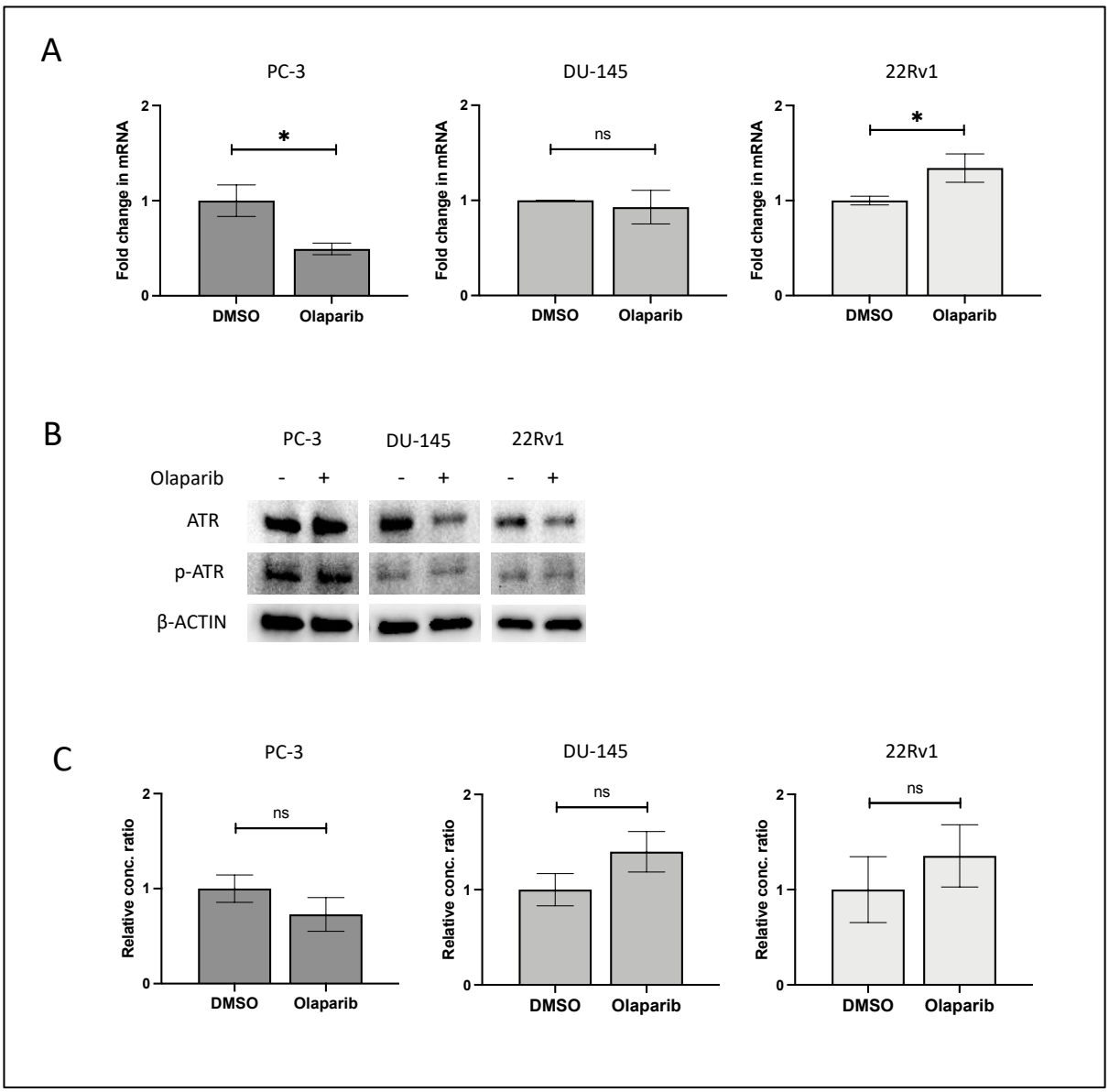

Figure 3.4: *ATR transcription is deregulated in response to olaparib whereas ATR activity remains unchanged in HR-proficient CRPC cells in vitro.* A: Relative fold change in *ATR* mRNA expression following 96 hours olaparib treatment at IC50 doses compared with DMSO treated controls, as measured using qRT-PCR. Three independent repeats per cell line; error bars represent Standard Error of the mean. B: Representative Western Blots demonstrating total ATR and p-ATR protein levels following 96 hours olaparib treatment at IC50 doses compared with DMSO treated controls. C: Western Blot densitometry bar charts demonstrating relative concentration ratio of p-ATR to total ATR compared with DMSO treated controls. Densitometry data normalised to B-ACTIN loading controls. Three independent repeats per cell line; error bars represent Standard Error of the mean. Statistical significance calculated using unpaired Student's t-test. *: $P \leq 0.05$, ns: $P > 0.05$.

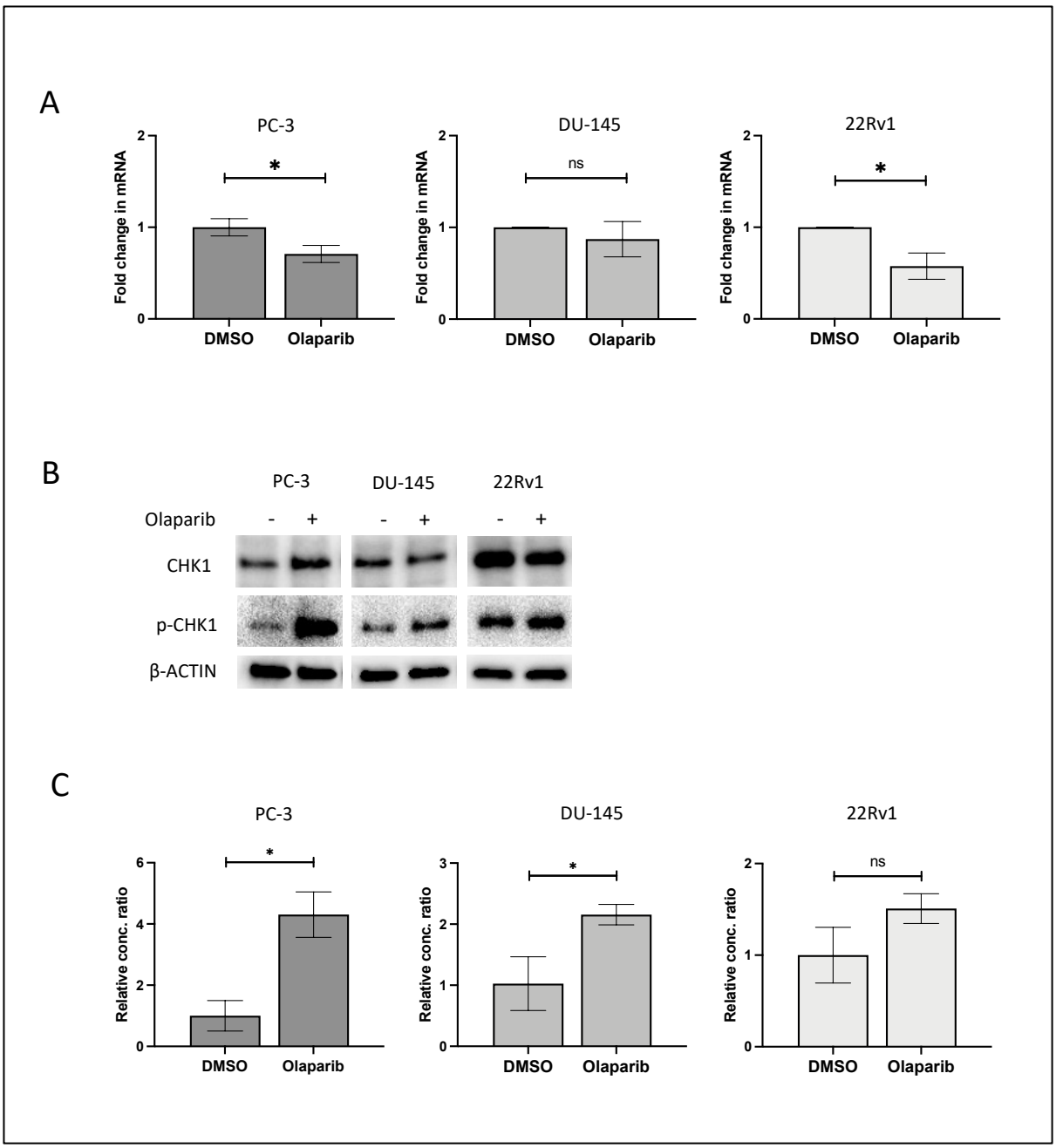

Figure 3.5: *CHEK1 mRNA transcription is reduced whilst CHK1 protein activation is increased in HR-proficient CRPC cells treated with olaparib in vitro.* A: Relative fold change in *CHEK1* mRNA expression following 96 hours of olaparib treatment at IC50 doses compared with DMSO treated controls, as measured using qRT-PCR. Three independent repeats per cell line; error bars represent Standard Error of the mean. B: Representative Western Blots demonstrating total CHK1 and p-CHK1 protein levels following 96 hours of olaparib treatment at IC50 doses compared with DMSO treated controls. C: Western Blot densitometry bar charts demonstrating relative concentration ratio of p-CHK1 to total CHK1 compared with DMSO treated controls. Densitometry data normalised to B-ACTIN loading controls. Three independent repeats per cell line; error bars represent Standard Error of the mean. Statistical significance calculated using unpaired Student's t-test. *: $P \leq 0.05$, ns: $P > 0.05$.

3.3.2 Characterising the response of HR-proficient CRPC cells to the ATR inhibitor ceralasertib alone and in combination with olaparib

3.3.2.1 The ATR inhibitor ceralasertib reduces HR repair of DNA DSBs in vitro

Whilst several ATR inhibitors have been developed, ceralasertib (AZD6738; AstraZeneca, Cambridge, UK), was selected for further characterisation in this thesis on the basis that it is orally bioavailable and has already entered early phase clinical trials both alone and in combination with other treatments including olaparib in patients with advanced solid tumours (Foote et al., 2018). Prior to evaluating the effects of ceralasertib in the setting of CRPC, its ability to reduce the efficiency of DSB repair via HR was assessed using an established HR assay performed in collaboration with Dr Greg Ngo and Professor Duncan Baird within the School of Medicine, Cardiff University. A full description of the assay is given in Section 2.1.4.7. In brief, U2OS osteosarcoma cells harbouring a chromosomally integrated expression cassette for the green fluorescent protein (GFP) that has been interrupted by I-SceI recognition sites, termed DR-GFP, were transfected with either pCBAScel or mCherry2-C1 plasmids and then cultured in media containing DMSO or ceralasertib at either 1 μM or 5 μM concentrations for 48 hours. Flow cytometry was then used to determine transfection efficiency and the proportion of cells that were proficient in HR repair, with the gating strategies outlined in ***Figures 3.6A*** and ***3.6B*** respectively. HR repair efficiency was calculated as described in Section 2.1.4.7 and is demonstrated in ***Figure 3.6C***.

Treatment with ceralasertib at 1 μM resulted in a highly significant reduction in HR repair efficiency compared with DMSO treated controls (63.4% reduction, P=0.005). Similarly, treatment with ceralasertib at 5 μM also resulted in a highly significant reduction (78.8% reduction, P=0.003) compared with DMSO treated controls, although this did not reach statistical significance when compared to the 1 μM concentration (P=0.196). These data therefore confirm that ATRi with ceralasertib results in the inhibition of DNA DSB repair via HR in a dose dependent manner, thereby supporting the notion that this agent may be used to induce a *BRCA* deficient phenotype in cancer cells that are otherwise proficient in DNA damage response pathways.

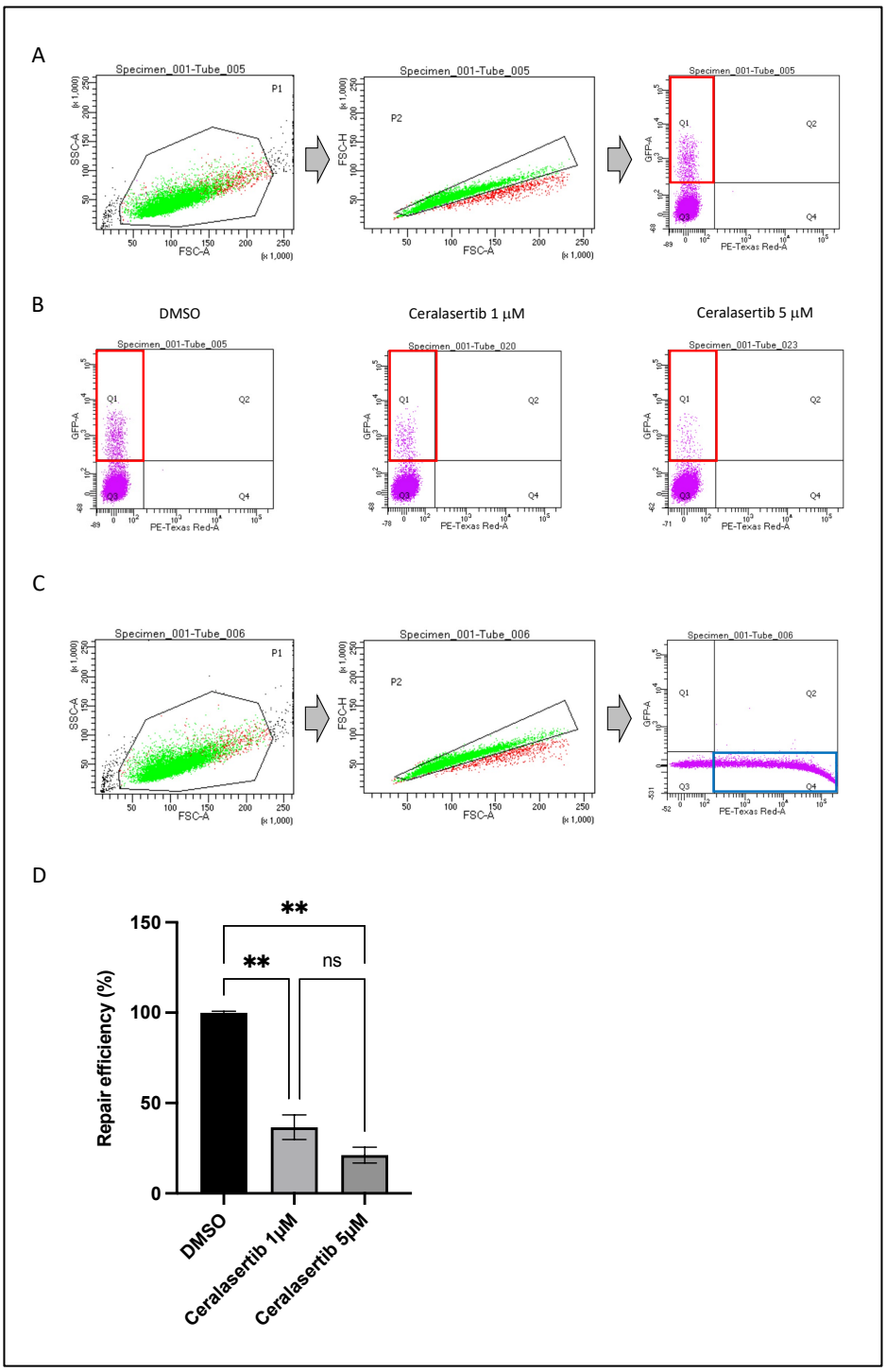

Figure 3.6: *The ATR inhibitor ceralasertib significantly inhibits HR repair of DSBs in osteosarcoma cells.* A: Flow cytometry gating strategy for the identification of cells proficient in HR repair. Firstly, cells were identified based on size, followed by doublet discrimination and then the identification of GFP positive cells (Q1 – red box) in which HR repair had occurred. B: Example plots demonstrating a reduction in the proportion of GFP positive cells (Q1 – red boxes) with increasing concentrations of ceralasertib, thereby indicating a reduction in the proportion capable of HR repair. C: Flow cytometry gating strategy for the identification of cells in which transfection had occurred. Firstly, cells were identified based on size, followed by doublet discrimination and then the identification of mCherry positive cells (Q4 – blue box) in which transfection had occurred. C: Bar graph demonstrating the HR repair efficiency of cells treated with ceralasertib at 1 µM and 5 µM concentrations relative to DMSO treated controls. Two technical repeats per treatment; error bars represent Standard Error of the mean. Statistical significance calculated using one-way ANOVA with Tukey correction for multiple comparisons. **: $P \leq 0.01$, ns: $P > 0.05$.

3.3.2.2 CRPC cell lines are sensitive to the ATR inhibitor ceralasertib

Following confirmation that ceralasertib results in a significant reduction in DNA DSB repair via HR, subsequent experiments sought to determine its effects when used as monotherapy in the setting of HR-proficient CRPC. The dose response curves for ceralasertib treatment in PC-3, DU-145 and 22Rv1 cell lines at the 96 hour timepoint, along with their respective relative IC50 values in μM are shown in ***Figure 3.7***. All cell lines displayed sensitivity to ceralasertib treatment, with the bottom plateau of the curves reaching a relative viability of close to 0. This therefore means that in contrast to olaparib, the calculated ceralasertib IC50 values of 6.195 μM, 3.116 μM and 1.706 μM for PC-3, DU-145 and 22Rv1 cells respectively are representative of the absolute rather than relative IC50 values. 22Rv1 cells appeared most sensitive, as demonstrated by the lowest IC50 value and highest overall maximum response. The reasons for this are not certain but may be due to differences in mutational status when compared with the other two cell lines. Together these data indicate that HR-proficient CRPC cells are more sensitive to ATRi than PARPi alone, perhaps due to the more widespread role of ATR in the DDR.

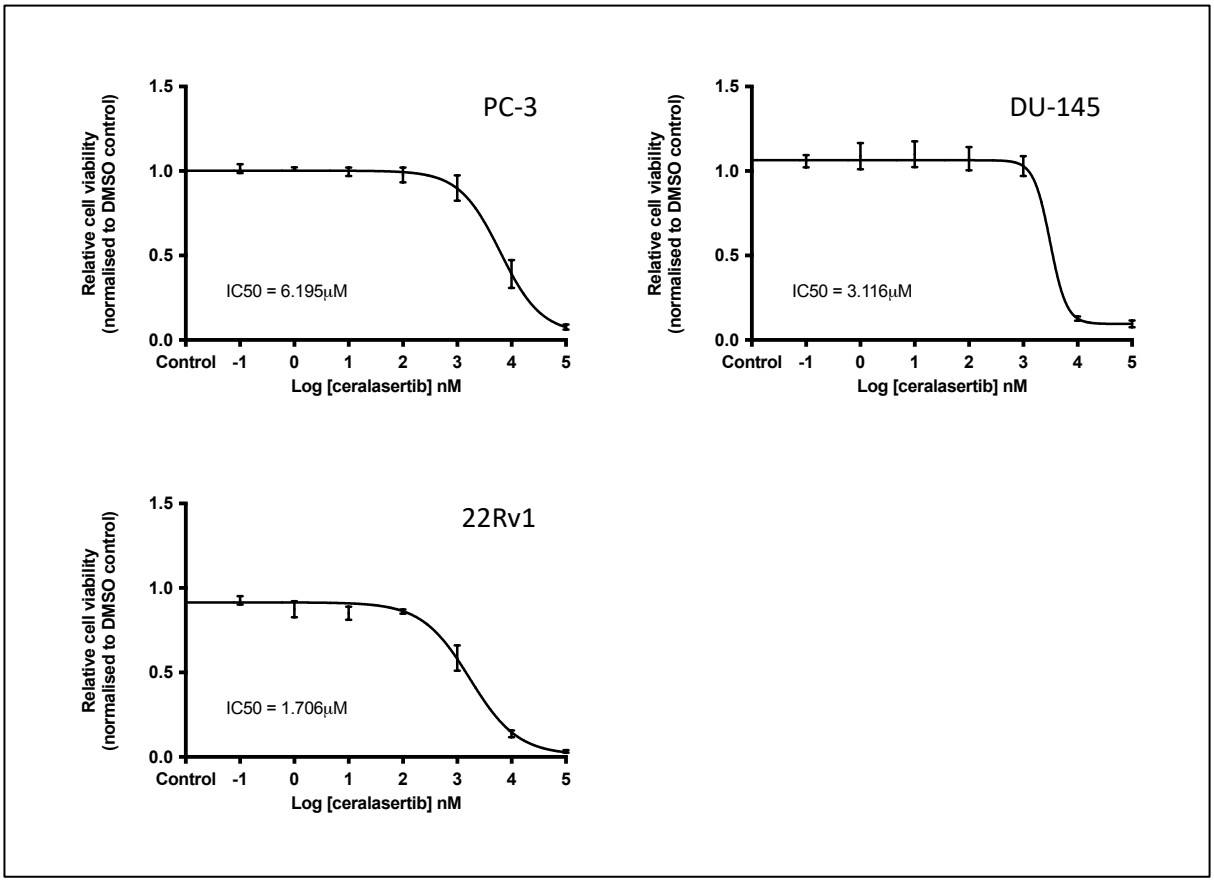

Figure 3.7: *Efficacy of the ATR inhibitor ceralasertib in PC-3, DU-145 and 22Rv1 established human CRPC cell lines.* Cells were grown in 2D culture and exposed to increasing doses of ceralasertib (0-100 μM) for 96 hours, after which cell viability was assessed using the Cell Titre Blue assay. Dose response curves and IC50 values in μM were generated using GraphPad Prism software and are represented for each cell line. Three independent repeats were performed per cell line; error bars represent Standard Error of the mean.

3.3.2.3 Combined PARP and ATR inhibition is synergistic in CRPC cells

To determine the efficacy of combined PARPi and ATRi, PC-3, DU-145 and 22Rv1 cells were treated with either olaparib or ceralasertib alone and in combination at IC50 concentrations for 96 hours and cell viability assessed using the Cell Titre Blue assay. The relative viability of each cell line at the 96 hour timepoint is shown in ***Figure 3.8A***. In both PC-3 and DU-145 cells the response to ceralasertib monotherapy was greater than that to olaparib monotherapy, reflecting the lower overall sensitivity to PARP inhibition, as previously discussed. The combination of olaparib and ceralasertib at IC50 doses was more efficacious relative to monotherapy in all three cell lines, with differences being highly statistically significant for all comparisons ($P<0.001$). The observed effect was most pronounced in the DU-145 cell line, where combination therapy resulted in a relative viability of 0.128 (+/- 0.006 SEM; $P<0.001$) compared with DMSO treated controls. These findings indicate that combined PARP and ATR inhibition is highly effective at suppressing the viability of HR-proficient CRPC cells.

To determine the therapeutic relationship between olaparib and ceralasertib treatment in CRPC cells, further dose response experiments were performed in which PC-3, DU-145 and 22Rv1 cells were treated with each agent alone and in combination at concentrations of 100 μM, 25 μM, 6.25 μM, 1.56 μM and 0.391 μM for 96 hours, after which viability was again assessed using the Cell Titre Blue assay. Viability was normalised to that of DMSO treated controls and then entered into the SynergyFinder web application to generate dose response matrices (***Figure 3.8B***) and synergy maps containing Summary Synergy Scores calculated using the Highest Single Agent (HSA) method (***Figure 3.8C***). As illustrated by the dose response matrices, combination treatment at lower concentrations resulted in greater efficacy at each specific concentration than monotherapy with either agent, with percentage inhibition being higher than the sum of percentage inhibition for each of the single agents alone at the same concentration. For example, in PC-3 cells, combining olaparib and ceralasertib at 0.4 μM resulted in 17.7% inhibition whereas each agent alone at the same concentration resulted in 10.4% and 3.3% inhibition respectively. This phenomenon was lost as doses increased, most likely due to the greater number of off-target effects seen at higher concentrations of either drug. This is of clinical relevance as the most favourable combination effects are observed at the lower doses, therefore potentially enabling lower doses of each agent to be utilised with greater efficacy, limiting toxicity.

Summary Synergy Score is defined as the average excess response for a drug combination beyond the expectation based on each drug being utilised as monotherapy. For example a Summary Synergy Score of 15 corresponds to a 15% response beyond expectation (Ianevski et al., 2017). The calculated scores for combined olaparib and ceralasertib in PC-3, DU-145 and 22Rv1 cells were 12.4, 13.2 and 7.9

respectively, thereby confirming a synergistic interaction between the two agents in each cell line. The synergy maps shown in ***Figure 3.8C*** demonstrate the degree of synergy for each drug concentration combination in each, with the dark box indicating the most synergistic range. Importantly, the previously calculated IC50 values for both olaparib and ceralasertib fall within the most synergistic area for each cell line, supporting their use at these concentrations in vitro.

Taken together these data indicate that olaparib and ceralasertib are synergistic in vitro when used in combination at IC50 concentrations. Importantly, early phase human clinical studies of olaparib 300 mg twice daily and ceralasertib 160 mg twice daily have demonstrated peak plasma concentrations of 16.1 μM and 14.5 μM respectively (Dillon et al., 2019, Pilla Reddy et al., 2019). This therefore indicates that the observed synergy occurs at doses that are clinically achievable with oral administration of both agents, increasing the clinical relevance of these findings.

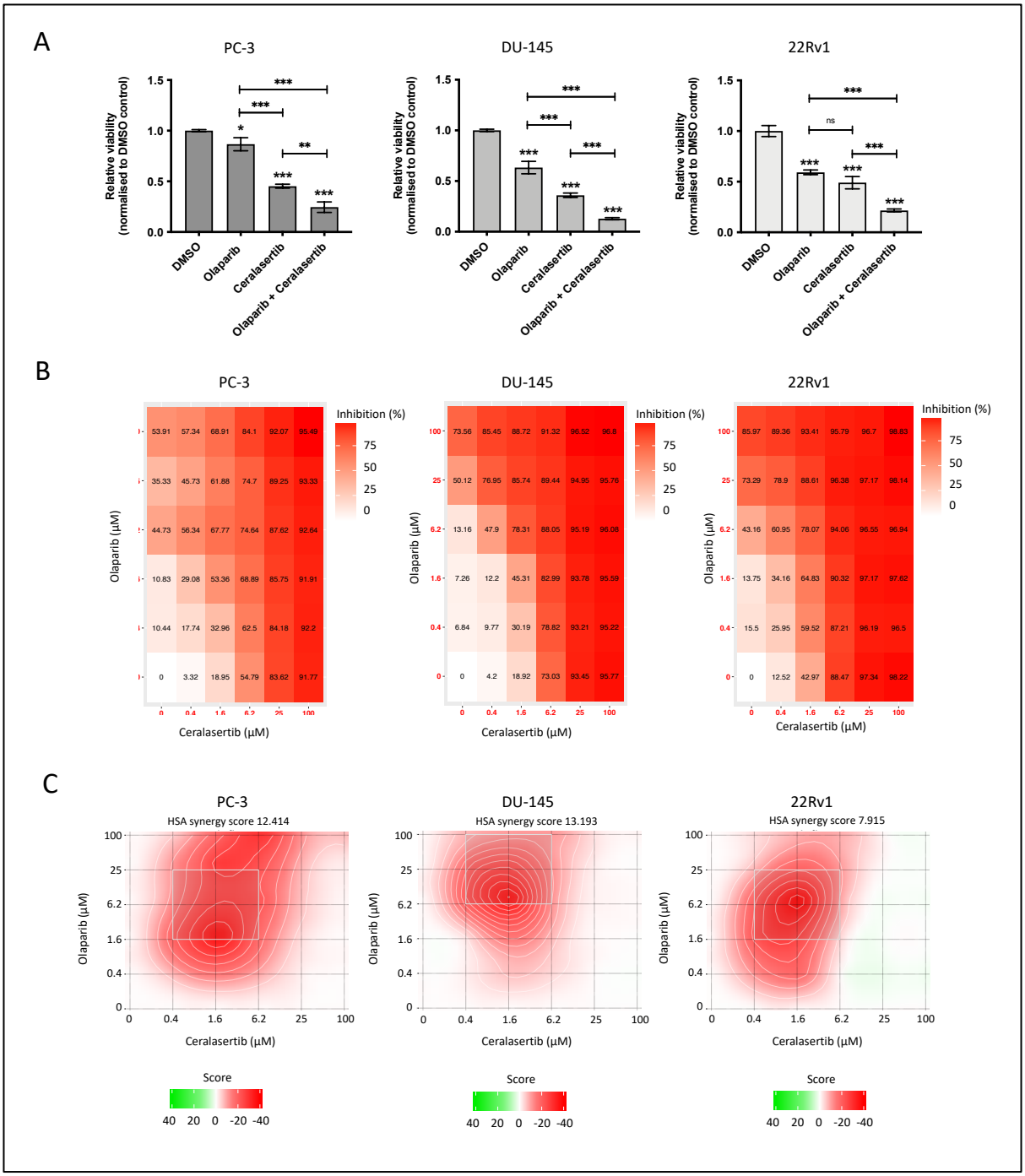

Figure 3.8: *Combined PARP and ATR inhibition is synergistic at IC50 concentrations in HR-proficient CRPC cells in vitro. A:* Relative viability of PC-3, DU-145 and 22Rv1 cells when treated with olaparib and ceralasertib alone and in combination for 96 hours at relative IC50 concentrations. Three independent repeats performed per cell line; error bars represent Standard Error of the mean. Statistical significance calculated using one-way ANOVA with Tukey correction for multiple comparisons. ***: $P \leq 0.001$, **: $P \leq 0.01$, ns: $P > 0.05$. B: Dose-response matrices demonstrating responses of PC-3, DU-145 and 22Rv1 cells to olaparib and ceralasertib treatment for 96 hours at doses of 100 μM, 25 μM, 6.25 μM, 1.56 μM and 0.391 μM, with heat map colour intensity representing percentage inhibition. C: Synergy Maps produced by the Synergy Finder web application using the HSA method with summary synergy scores for each cell line. Heat map colours represent Synergy Score at each specific drug concentration combination as shown, with highly synergistic dose regions depicted in red and the most synergistic area identified by the dark box.

3.3.2.4 *Ceralasertib alone and in combination with olaparib significantly inhibits the proliferative capacity of CRPC cells*

Having identified synergy between PARPi and ATRi with respect to viability, the next set of experiments sought to characterise whether combined treatment had a greater effect on other key properties of CRPC cells, starting with proliferative capacity. As such, PC-3, DU-145 and 22Rv1 cells were treated with olaparib and ceralasertib alone and in combination at IC50 concentrations and confluence measured at 4 hourly intervals over a 96-hour period using the IncuCyte live cell imaging system. When confluence over time was used as a surrogate marker of proliferation, ceralasertib monotherapy led to significantly greater inhibition in proliferation compared with olaparib monotherapy in all cell lines, with confluence reaching a plateau by the 96 hour timepoint (***Figure 3.9A)***. However, combination therapy resulted in almost complete inhibition of proliferation in each cell line, with differences proving statistically significant when compared with both DMSO and each agent alone ($P=0.0264$ to $P<0.0001$). These data therefore indicate that combined PARPi and ATRi results in a highly significant reduction in proliferation in HR-proficient CRPC cells, warranting further investigation into the underlying mechanisms responsible.

As previously described, olaparib monotherapy resulted in a highly significant reduction in colony forming ability during treatment in each of the CRPC cell lines. To determine whether a similar effect was seen with ceralasertib, low-density colony forming assays were again performed during treatment with ceralasertib alone and in combination with olaparib. As with olaparib, ceralasertib resulted in highly significant inhibition of colony formation during treatment when compared with DMSO controls ($P \leq 0.001$ for all comparisons; ***Figure 3.9B)***. Although CFE appeared to be lower in those treated with ceralasertib compared with olaparib, differences failed to reach statistical significance. Similarly, combination therapy led to almost complete inhibition of colony formation during treatment. However, given the magnitude of effect seen with either agent alone there was no significant benefit observed when both agents were used in combination.

Whilst olaparib monotherapy was able to significantly suppress colony formation during treatment, previous experiments demonstrated this effect to be partially reversible following treatment withdrawal. To address whether the addition of ceralasertib was able to overcome this phenomenon, CFE was assessed for each of the CRPC cell lines pre-treated for 96 hours with either DMSO, olaparib, ceralasertib or combined olaparib and ceralasertib at IC50 concentrations. In contrast to olaparib, almost no restoration of colony forming ability was seen following pre-treatment with ceralasertib, with CFEs of 0.27% (+/- 0.26% SEM) versus 21.3% (+/- 3.20% SEM; P=0.002), 0.40% (+/- 0.00% SEM) versus 15.6% (+/- 2.0% SEM; P=0.003) and 0.27% (+/- 0.18% SEM) versus 19.1% (+/- 3.65% SEM;

P=0.002) in PC-3, DU-145 and 22Rv1 cells respectively (***Figure 3.9C)***. Once again, the magnitude of effect observed with ceralasertib alone meant that no apparent benefit was seen with the addition of olaparib. Thus, in contrast to olaparib monotherapy, ceralasertib monotherapy is sufficient to suppress colony formation both during and after treatment.

Taken together these results indicate that treatment with ceralasertib is more effective than olaparib at inhibiting the proliferative capacity of CRPC cells, whilst combination therapy is even more effective than either agent alone. The failure of ceralasertib pre-treated cells to regain colony forming ability after withdrawal of treatment suggests that ATR inhibition, unlike PARP inhibition, may irreversibly target the stem-cell like population. This sustained effect on clonogenicity therefore indicates that continuous administration of ceralasertib may not be necessary, hence a cyclical treatment approach may offer means of reducing toxicity whilst retaining efficacy. The lack of additional benefit seen with combination therapy indicates that this particular mechanism is unlikely to be responsible for the synergy observed between PARP and ATR inhibition in HR-proficient CRPC cells. However, further experiments utilising reduced doses of both olaparib and ceralasertib are required to fully determine whether combination therapy offers benefit over monotherapy with respect to colony formation.

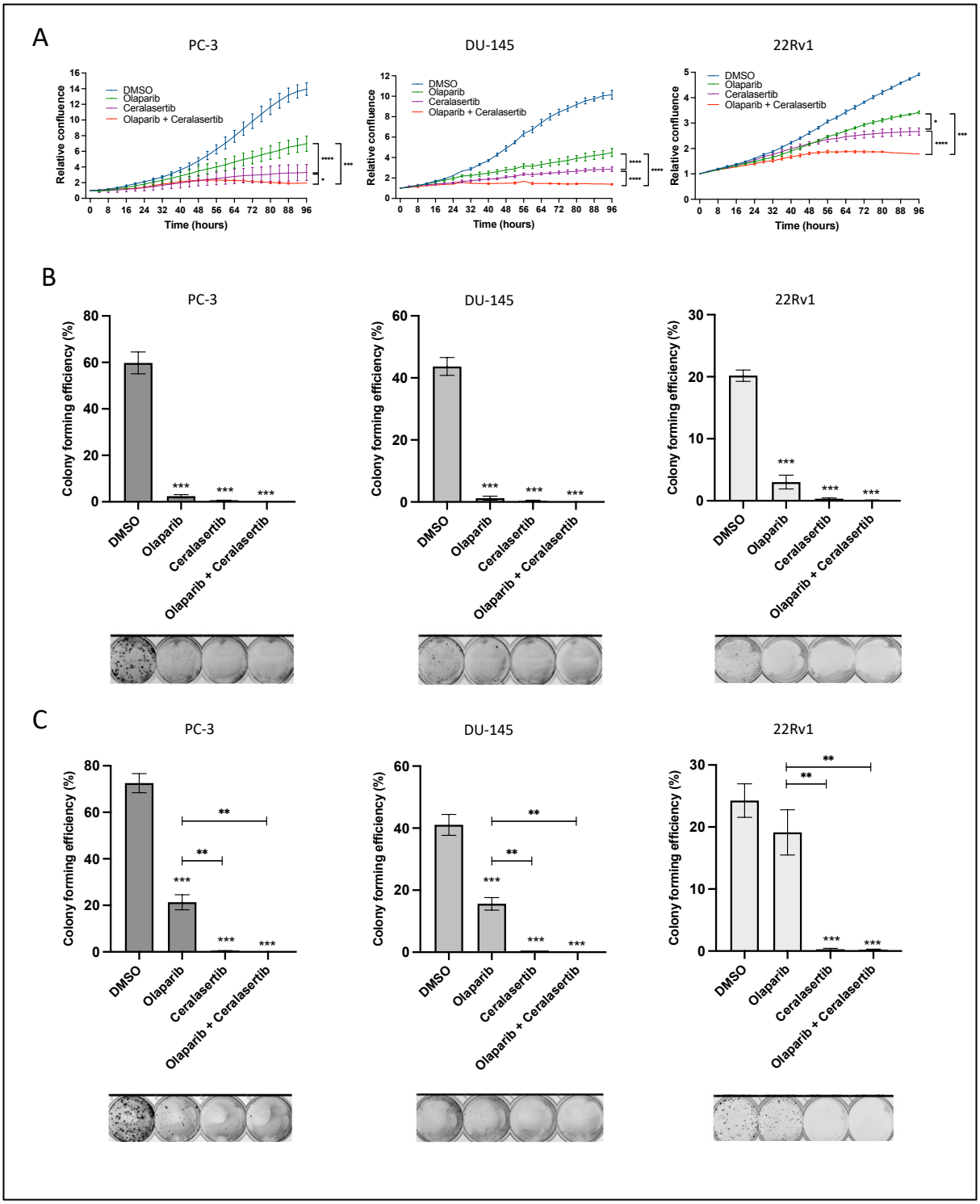

Figure 3.9: *Olaparib and ceralasertib monotherapy significantly reduce the colony forming ability of HR-proficient CRPC cells*. A: Cell confluency plots demonstrating relative confluency of cells treated with olaparib and ceralasertib alone and in combination at relative IC50 doses compared with DMSO vehicle controls over 96 hours. Three independent repeats performed with identical trends; one repeat shown. B: Low-density 2D colony forming efficiency (CFE) plots and representative whole well images of crystal violet stained colonies after treatment with olaparib and ceralasertib alone and in combination at relative IC50 doses or DMSO for 7 days (PC-3, DU-145) or 10 days (22Rv1). C: Colony forming efficiency (CFE) and representative whole well images of cells pre-treated for 96 hours with olaparib and ceralasertib alone and in combination at relative IC50 doses or DMSO prior to being seeded at low density and cultured for 7 days (PC-3, DU-145) or 10 days (22Rv1). Three independent repeats per cell line. Error bars represent Standard Error of the mean. Statistical significance calculated using the unpaired Student's t-test. ***: $P \leq 0.001$, **: $P \leq 0.01$, *: $P \leq 0.05$, ns: $P > 0.05$.

3.3.2.5 Treatment with ceralasertib alone and in combination with olaparib increases the quantity of double strand DNA breaks and results in increased apoptosis in CRPC cells

As demonstrated in 3.3.1.3, 96 hours of olaparib treatment results in a significant increase in DSBs in both PC-3 and 22Rv1 cells (***Figure 3.3***). Given that ceralasertib is able to inhibit the repair of DSBs via HR (***Figure 3.6***), we next sought to investigate whether combined PARP and ATR inhibition results in a greater increase in DSBs than either agent alone. As such, γ-H2AX protein levels were analysed by WB following 96 hours of treatment with either DMSO, olaparib, ceralasertib and combined olaparib and ceralasertib at IC50 concentrations in PC-3, DU-145 and 22Rv1 cells (***Figure 3.10A***). Densitometry analysis of WB bands revealed that ceralasertib monotherapy resulted in an increase in γ-H2AX compared to both olaparib monotherapy and DMSO. However, combined treatment with both agents resulted in significantly greater concentrations of γ-H2AX, representing 19-fold, 5-fold and 7-fold increases in DSBs in PC-3, DU-145 and 22Rv1 cells respectively (***Figure 3B***).

These findings suggest that both agents enable the development and accumulation of DSBs which, in the case of olaparib is likely through both the accumulation of SSBs and replication fork collapse (Pommier et al., 2016). In the case of ceralasertib it is probable that the observed increase in DSBs is the result of inhibition of ATRs wide-ranging role in the recognition and repair of a variety of DNA lesions including SSBs and DSBs (Nam and Cortez, 2011). However, as γ-H2AX is only taken as a surrogate maker of DSBs, further experiments are required in order to fully elucidate the spectrum of DNA damage occurring in response to treatment, such as use of the comet assay to measure SSBs (Collins, 2004) .

To determine the effects of increased DNA damage on cell death, the proportion of cells undergoing apoptosis following treatment with olaparib and ceralasertib both alone and in combination was measured using a fluorescent marker of Annexin V throughout 96 hours of treatment at IC50 concentrations with the IncuCyte live cell imaging system. As shown in ***Figure 3.10B***, treatment with ceralasertib led to a gradual increase in the proportion of cells undergoing apoptosis in all three cell lines, with differences proving statistically significant in PC-3 and DU-145 cells when compared with those treated with olaparib alone ($P<0.0001$ for all comparisons). However, combination therapy resulted in a dramatic and sustained increase in apoptosis over time. These differences proved highly statistically significant when compared with DMSO control and both olaparib and ceralasertib monotherapy ($P=0.003$ to $P<0.0001$ for all comparisons).

Collectively these data indicate that combined PARPi and ATRi results in the accumulation of highly genotoxic DSBs and an increase in apoptosis in a time dependent manner in HR-proficient CRPC cells.

The latter differs significantly from either PARPi or ATRi alone, in which apoptosis was seen at much lower levels, suggesting that combination therapy exerts some of its inhibitory effects through cytotoxicity, whilst monotherapy with either agent is predominantly cytostatic.

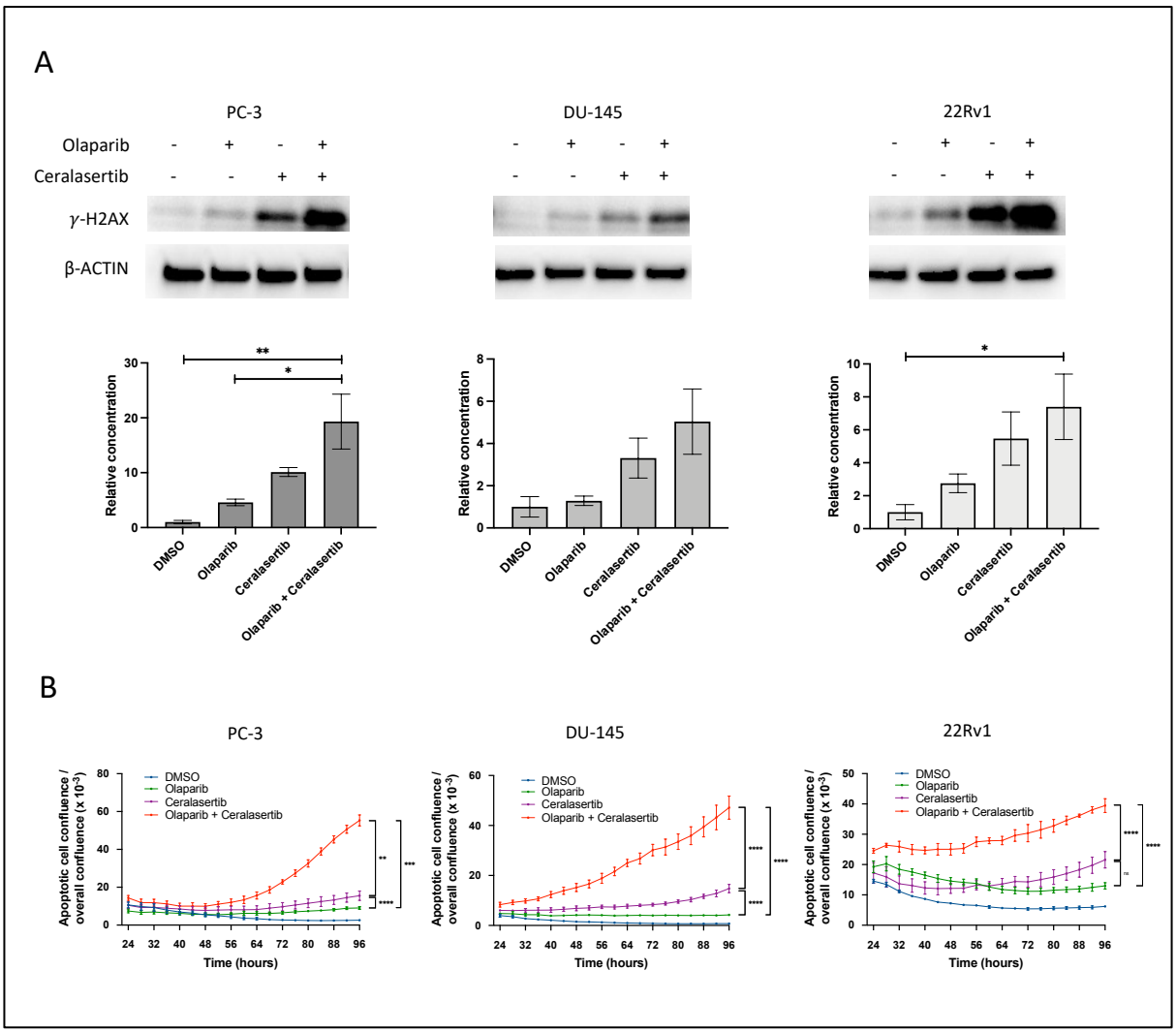

Figure 3.10: *Combined PARP and ATR inhibition results in a significant increase in quantity of double strand DNA breaks and cell death via apoptosis in HR-proficient CRPC cells.* A: Representative Western Blot images and densitometry bar charts demonstrating relative changes in quantity of γ-H2AX following 96 hours of treatment with olaparib and ceralasertib alone and in combination at IC50 doses compared with DMSO treated controls. Densitometry data normalised to B-ACTIN loading controls. Three independent repeats per cell line; error bars represent Standard Error of the mean. Statistical significance calculated using unpaired Student's t-test. **: $P \leq 0.01$, *: $P \leq 0.05$, ns: $P > 0.05$. B: Representative plots demonstrating the proportion of CRPC cells undergoing apoptosis during 96 hours of treatment with olaparib and ceralasertib alone and in combination at IC50 doses compared with DMSO treated controls. Three independent repeats performed with identical trends; one repeat shown; error bars represent Standard Error of the mean. Statistical significance calculated using repeated measure one-way ANOVA with Tukey correction for multiple comparisons. ****: $P \leq 0.0001$, ***: $P \leq 0.001$, **: $P \leq 0.01$, *: $P \leq 0.05$, ns: $P > 0.05$.

3.3.2.6 Ceralasertib overcomes PARP inhibition induced CHK1 phosphorylation and permits cell cycle progression despite increased DNA damage

As shown in ***Figure 3.4***, 96 hours treatment with olaparib results in a significant increase in the phosphorylation and hence activation of CHK1 in CRPC cells. To explore whether this activation could be overcome with concurrent ATR inhibition, CRPC cells were treated with olaparib and ceralasertib alone and in combination at IC50 concentrations for 96 hours and ATR/CHK1 phosphorylation assessed using WB as previously described. Treatment with ceralasertib resulted in a reduction in phospho-ATR in PC-3, DU-145 and 22Rv1 cells relative to those treated with olaparib or DMSO (Figure ***3.11A)***, with further reductions seen when given in combination with olaparib. However, reductions were also seen in total ATR concentration which, when accounted for through analysis of the p-ATR to total ATR ratio, meant there was no discernible difference in ATR phosphorylation and hence activation following treatment with ceralasertib either alone or in combination with olaparib when compared with olaparib or DMSO controls. Whilst these results may suggest that ceralasertib does not effectively inhibit the activation of ATR, it is again possible that the assay may have not captured the full extent of ATR phosphorylation, as only phosphorylation at Serine-428 was explored.

On the contrary, whilst treatment with ceralasertib had little impact on total CHK1 levels it did result in a highly significant reduction in CHK1 phosphorylation when compared with olaparib, as demonstrated by the reduction in p-CHK1 to total CHK1 ratio in each cell line ($P \leq 0.01$ for all comparisons; ***Figure 3.11B)***. Importantly, whilst no additional reduction was seen in those cells treated with both olaparib and ceralasertib compared with ceralasertib alone, the effect was sustained. As discussed previously, CHK1 phosphorylation results in a pleiotropic cellular response including transcriptional regulation, cell cycle arrest in the S and G2 phases of the cell cycle and cell death if the damage is not deemed repairable (Zhang and Hunter, 2014). These data indicate that ceralasertib is able to overcome olaparib-induced CHK1 phosphorylation and in doing so presents a further mechanism by which combined PARPi and ATRi enables highly genotoxic DNA damage to accumulate within CRPC cells.

Given the importance of ATR-CHK1 signalling in cell cycle regulation, the effects of olaparib and ceralasertib treatment on the distribution of CRPC cells throughout the cell cycle was also investigated. The proportion of PC-3, DU-145 and 22Rv1 cells in each phase of the cell cycle following 96 hours of treatment at IC50 concentrations was characterised using flow cytometry as described in Section 2.1.4.8. Treatment with both olaparib and ceralasertib led to an increase in the proportion of PC-3 cells in both the S and G2-M phases when compared with control, with a corresponding decrease in the proportion of cells in G0-1 (***Figure 3.11C***). This effect was more pronounced in cells treated with

both agents in combination, with the proportion of cells in S and G2-M phases increasing by 20.7% (+/- 2.64% SEM) and 11.30% (+/- 1.94% SEM) respectively when compared with the DMSO control (P=0.001 and P=0.006). A similar trend was seen in the DU-145 cell line, although the effect of combination treatment was even more pronounced, with the proportion of cells in S and G2-M phases increasing by 30.24% (+/- 5.32% SEM) and 36.4% (+/- 5.21% SEM) respectively compared with control (P=0.008 and P=0.005). However, this trend was not seen in the 22Rv1 cell line, in which combination treatment reduced the proportion of cells in the S phase by 20.1% (+/- 0.67% SEM; P=0.004) compared to DMSO treated controls, with no significant change in G2-M.

These data suggest that in PC-3 and DU-145 cells, treatment with olaparib or ceralasertib monotherapy results in a modest increase in progression of cells into the S and G2-M phases of the cell cycle despite increased levels of DNA damage. Combined treatment greatly enhances this effect, particularly the proportion of cells in G2-M, despite even higher levels of DNA damage. However, this trend was not observed in 22Rv1 cells, with combination therapy actually resulting in a reduction in the proportion of cells progressing into the S phase and a corresponding increase in the proportion in G0-1. The exact reasons for this remain to be elucidated but may again result from genomic and in vitro culture profile differences between the individual cell lines, as discussed in Section 3.4.

Collectively these data indicate that ATR inhibition, through its ability to overcome PARPi induced CHK1 phosphorylation, enables certain HR-proficient CRPC cells to progress through the cell cycle despite possessing significant DNA damage that would ordinarily trigger cell cycle arrest.

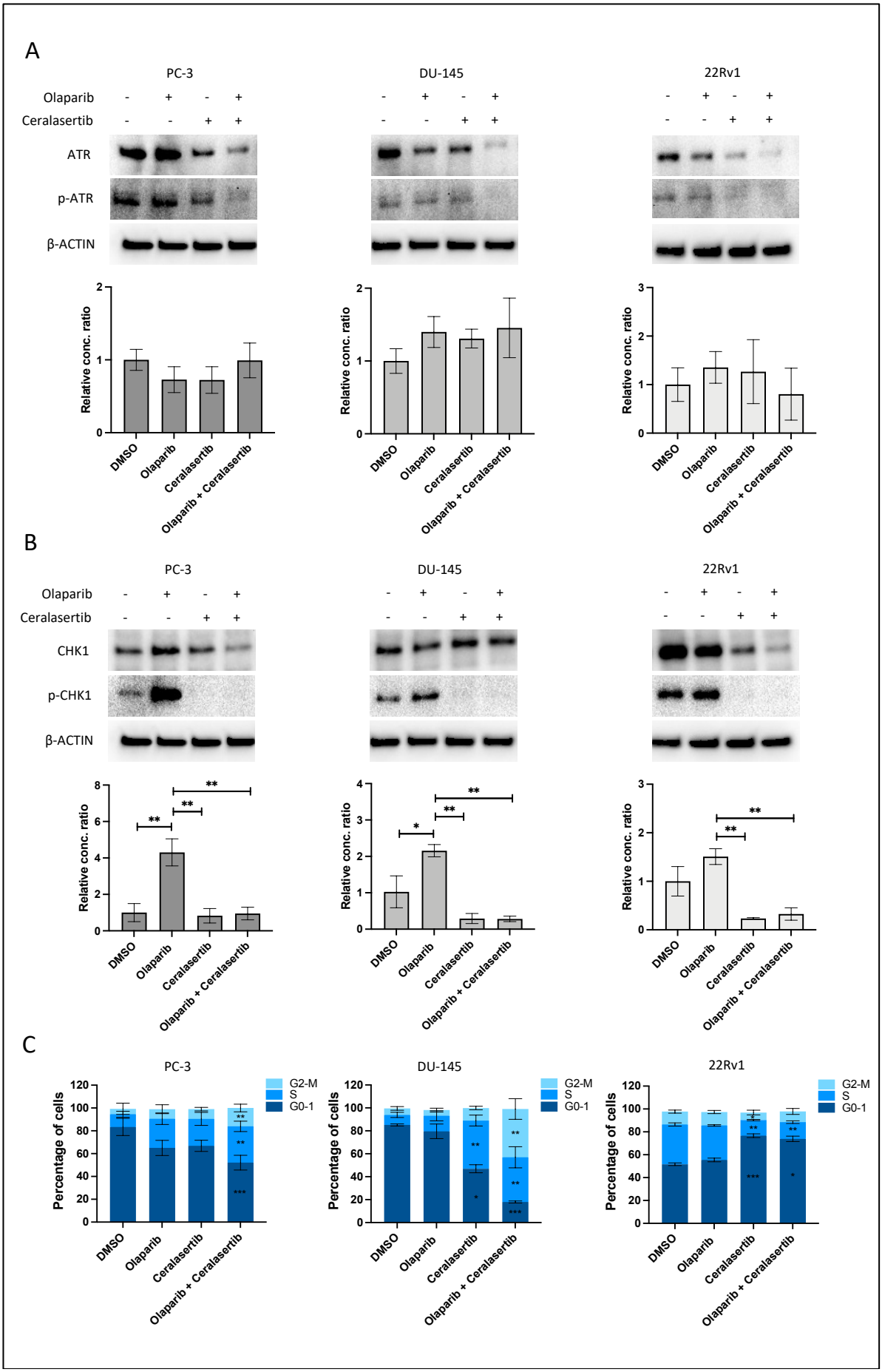
A
PC-3
DU-145
22Rv1
Olaparib
Ceralasertib
ATR
p-ATR
β-ACTIN
Relative conc. ratio
DMSO
Olaparib
Ceralasertib
Olaparib + Ceralasertib
B
CHK1
p-CHK1
C
G2-M
S
G0-1
Percentage of cells

Figure 3.11: *Effects of combined PARP and ATR inhibition on ATR-CHK1 signalling and the cell cycle in HR-proficient CRPC cells.* A: Representative Western Blots and bar charts showing relative concentration ratio of p-ATR to total ATR in CRPC cells treated with olaparib and ceralasertib alone and in combination at IC50 doses, as assessed using Western Blot. Densitometry data normalised to B-ACTIN loading controls. Three independent repeats per cell line; error bars represent Standard Error of the mean. Statistical significance calculated using one-way ANOVA with Tukey correction. B: Representative Western Blots and bar charts showing relative concentration ratio of p-CHK1 to total CHK1 in CRPC cells treated with olaparib and ceralasertib alone and in combination at IC50 doses, as assessed using Western Blot. Densitometry data normalised to B-ACTIN loading controls. Three independent repeats per cell line; error bars represent Standard Error of the mean. Statistical significance calculated using one-way ANOVA with Tukey correction. **: $P \leq 0.01$, *: $P \leq 0.05$, ns: $P > 0.05$. C: Percentage of PC-3, DU-145 and 22Rv1 cells in each phase of the cell cycle following 96 hours of treatment with olaparib and ceralasertib alone and in combination at IC50 doses. Statistical significance calculated using the Kruskal-Wallis H test with multiple comparisons, with * symbols showing significance of comparisons with DMSO treated controls. ***: $P \leq 0.001$, **: $P \leq 0.01$, *: $P \leq 0.05$, ns: $P > 0.05$.

3.4 Discussion

The experiments reported in this chapter firstly sought to characterise the response of HR-proficient PC-3, DU-145 and 22Rv1 CRPC cells to the PARP inhibitor olaparib in vitro. Each cell line was only partially sensitive to 96 hours treatment, with each possessing different IC50 concentrations ranging from 1.25 µM – 23.8 µM. Furthermore, whilst olaparib treatment at relative IC50 concentrations did appear to have a dramatic inhibitory effect on colony formation when cells were seeded at low density, proliferation was only partially inhibited under standard growth conditions and the level of apoptosis, whilst higher than that of DMSO treated controls, was relatively low and did not increase significantly over time. These findings are consistent with literature published within the first year of this project in which Feiersinger et al. also identified the same CRPC cell lines to have partial sensitivity to 96 hours of PARPi with olaparib, veliparib and rucaparib at doses of 2.5 – 20 µM in terms of both viability and induction of apoptosis in vitro (Feiersinger et al., 2018). Recently, a similar study published by Rafiei et al. in which DU-145 and 22Rv1 cells were treated with olaparib at doses of 0 – 10 µM for 72-96 hours also demonstrated partial sensitivity in terms of viability (Rafiei et al., 2020). These findings may therefore in part explain the limited response to olaparib monotherapy in CRPC patients without pre-existing DDR aberrations in the TOPARP-A clinical trial (Mateo et al., 2015).

However, despite only demonstrating limited sensitivity in terms of viability and proliferation, 96 hours PARPi with olaparib resulted in a significant increase in the quantity of DNA DSBs, as measured using γ-H2AX, in both PC-3 and 22Rv1 cells, with a similar yet non-significant trend observed in DU-145 cells. This corroborates the findings of other studies in which increased levels of γ-H2AX were identified in HR-proficient 22Rv1 CRPC cells treated with PARPi monotherapy (Neeb et al., 2021), as well as in HR-proficient PEO4 ovarian cancer cells (Kim et al., 2016). In the former study, increased γ-H2AX and 53BP1 foci were found to colocalise with RAD51 foci when evaluated using

immunofluorescence, thereby indicating activation of HR repair in response to the DSBs. Whilst the exact mechanism underlying the formation of DSBs was not fully elucidated in our experiments, it is probable that these are the result of both persistent SSBs and PARP trapping resulting in replication fork collapse, as has been previously described by others (Farmer et al., 2005, Murai et al., 2012).

As well as increased DSB formation, 96 hours of PARPi with olaparib also significantly increased phosphorylation of CHK1 at serine-345 (S345), a site targeted by ATR, in PC-3 and DU-145 cells, with a similar non-significant response observed in 22Rv1 cells. This phenomenon has also been described in other studies utilising established cell lines of solid cancers. For example, Lloyd et al. reported an increase in phosphorylation of CHK1 at S345 in FaDu hypopharyngeal carcinoma cells following 24 hours treatment with olaparib at concentrations of up to 1 μM (Lloyd et al., 2020). This resulted in a corresponding increase in the proportion of cells in the G2-M phase of the cell cycle, regardless of HR status, suggesting that PARPi induced DNA damage and subsequent phosphorylation of CHK1 results in cell cycle arrest at the G2/M checkpoint. In a similar study, 24 hours of olaparib treatment at 1 μm also increased concentrations of p-CHK1 in HR-proficient PEO4 ovarian cancer cells compared with vehicle, with even higher levels identified in HR-deficient *BRCA* mutant PEO1 and JHOS4 cells (Kim et al., 2016). Again, PARPi increased the proportion of HR-deficient cells in G2-M phase of the cell cycle compared with vehicle treated controls, with a similar but less pronounced trend seen in HR-proficient cells. However, these findings are in conflict to those of Huntoon et al., who reported that 24 hours of PARPi with veliparib had no effect on the cell cycle distribution of OVCAR-8 ovarian cancer cells (Huntoon et al., 2013). Similarly, our results also failed to demonstrate any alteration in the proportion of cells in G2-M phase of the cell cycle after 96 hours of olaparib treatment compared with vehicle in any of the evaluated HR-proficient CRPC cell lines. However, regardless of the effect on cell cycle distribution, our data, with support of the wider literature, suggest that short term PARPi increases the formation of DNA DSBs in HR-proficient CRPC cells, which in turn increases dependency on CHK1 signalling and activates HR repair.

Given that ATR plays an important role in both CHK1 signalling and HR repair, subsequent experiments in this chapter sought to characterise the response of HR-proficient CRPC cells to the ATR inhibitor ceralasertib, both alone and in combination with olaparib. Firstly, experiments undertaken using a well-established HR activity assay confirmed that ceralasertib has a dose dependent inhibitory effect on HR efficiency in vitro, with 1 μM and 5 μM doses resulting in 63.4% and 78.8% reductions respectively. Whilst these experiments were conducted using U2OS osteocarcinoma cells, other authors have explored the effect of ATR inhibition using the same technique in other solid cancer cells,

including CRPC. Using similar methods, Neeb et al. identified that 22Rv1 cells treated for 48 hours with the ATRi VE-822 at a dose of 200 nM demonstrated a significant reduction in HR efficiency compared with controls (Neeb et al., 2021). This effect was even more pronounced when ATM function was also lost, either through genetic knockout with CRISPR/Cas9 or pharmacologically with the ATM inhibitor KU-60019. Similar reductions in HR efficiency were also seen with ATR depletion using siRNA in OVCAR-8 ovarian cancer cells (Huntoon et al., 2013). Taken together, these results confirm that inhibition of ATR function results in a reduction in the efficiency of DSB repair by HR, hence indicating this to be a means of inducing a 'BRCAness' phenotype in CRPC cells.

Having established that ATR inhibition successfully reduces HR in cancer cells, we next explored the effect of ceralasertib in our panel of HR-proficient CRPC cell lines. Cells were more sensitive to 96 hours of treatment with ceralasertib monotherapy compared with olaparib monotherapy, with higher doses resulting in almost complete loss of cell viability, enabling calculation of absolute IC50 concentration values for each line. Treatment at IC50 concentrations led to a greater reduction in cell viability and proliferation, together with a higher level of DSB formation and apoptosis, compared with vehicle and olaparib monotherapy. However, when cells were treated with both olaparib and ceralasertib in combination, even more pronounced effects were observed. Importantly, co-treatment with ceralasertib was able to overcome olaparib induced CHK1 phosphorylation in each cell line. This phenomenon has also been reported in other HR-proficient cancer cells, with ATRi treatment overcoming PARPi induced increases in p-CHK1 in HR-proficient ovarian and hypopharyngeal carcinoma cells in the previously discussed studies (Kim et al., 2016, Lloyd et al., 2020).

These results demonstrate that 96 hours of combined olaparib and ceralasertib at IC50 concentrations results in a significantly greater reduction in viability and proliferation in vitro than vehicle or monotherapy with either agent alone. Furthermore, this combination appeared to be synergistic in PC-3, DU-145 and 22Rv1 cells, with HAS Summary Synergy Scores of 12.4, 13.2 and 7.9 respectively, as discussed in Section 3.3.2.3. A similar synergistic relationship between PARPi and ATRi treatment in vitro has been reported in ovarian cancer cells, HeLa cells and high-risk neuroblastoma cells, irrespective of HR status (Kim et al., 2016, Schoonen et al., 2019, Southgate et al., 2020). However, in other solid cancer cells, synergy only appears to exist in those with pre-existing DDR aberrations, most notably *ATM*. For example, when the cytotoxicity of olaparib in combination with ceralasertib was assessed in a panel of different head and neck and lung cancer cell lines, synergy was only observed in *ATM* knockout FaDu hypopharyngeal carcinoma and *ATM* mutant NCL-H23 non-small cell lung cancer cells (Lloyd et al., 2020).

In a similar study utilising the 22Rv1 CRPC cell line, combined rucaparib and VE-822 was only synergistic when *ATM* had been depleted by means of CRISPR/Cas9 technology, with little effect seen in *ATM* wild-type cells (Neeb et al., 2021). A similar result was observed in LNCaP and DU-145 cells, with combined PARPi, ATRi and ATMi resulting in much lower levels of viability compared with PARPi and ATRi alone. This suggests that additional loss of ATM function is required to maximise efficacy, leading the authors to assert that combined ATR and ATM blockade is necessary to abrogate HR function and enable synthetic lethality with PARPi. However, the results presented in this thesis indicate the existence of synergy between PARPi and ATRi irrespective of *ATM* status, with only one out of the three cell lines (22Rv1) possessing a pre-existing *ATM* mutation in the form of a heterozygous missense substitution. The reasons for these differences may arise due to differing methodology. For example, Neeb et al. utilised different agents for PARPi and ATRi (rucaparib and VE-22), which have differing pharmacological properties to olaparib and ceralasertib used in this thesis. Although olaparib and rucaparib are relatively comparable in terms of their ability to inhibit PARP catalytic function and PARP trapping (Murai et al., 2014), VE-822 has a much greater potency in terms of reducing cell free ATR activity (IC50 0.2 nM) than ceralasertib (IC50 4 nM) (Barnieh et al., 2021). Likewise, the concentrations of each agent differed significantly. After firstly determining the IC50 values for both olaparib and ceralasertib in each cell line, subsequent experiments in this thesis were then conducted using these concentrations. In contrast, Neeb et al. utilised set concentrations of rucaparib (0.3 - 9.0 μM) and VE-822 (0 - 200 nM), with the latter being significantly lower than the ceralasertib doses used in our experiments (1.71 - 6.20 μM). Whilst VE-822 is a more potent ATR inhibitor than ceralasertib and lower doses are favourable in terms of reducing off target effects and toxicity, early phase human clinical studies of olaparib 300mg twice daily and ceralasertib 160mg twice daily have demonstrated peak plasma concentrations of 16.1 μM and 14.5 μM respectively, meaning the concentrations utilised in this thesis are clinically relevant and achievable (Dillon et al., 2019, Pilla Reddy et al., 2019). It is therefore possible that synergy may have been observed in *ATM* wild-type cells if VE-822 was used at higher concentrations.

Having identified synergy between olaparib and ceralasertib in our panel of HR-proficient CRPC cell lines we next sought to determine the mechanisms responsible, starting with the formation of DNA DSBs. In both PC-3 and 22Rv1 cells, 96 hours treatment with combined olaparib and ceralasertib at IC50 concentrations resulted in a significant increase in DSBs, as measured by γ-H2AX, compared with vehicle treated controls, with a similar but non-significant trend seen in DU-145 cells. This was accompanied by a highly significant increase in apoptosis, collectively indicating that combined PARPi and ATRi results in higher levels of DNA damage and cell death when compared with vehicle or either

agent alone. Other authors have also reported increased levels of DNA damage with combined PARPi and ATRi, with corresponding changes in the distribution of cells within each phase of the cell cycle. For example, Lloyd et al. reported that 24 hours of combined olaparib and ceralasertib prevented the accumulation of HR-proficient and deficient FaDu cells in G2-M phase seen with olaparib monotherapy, enabling progression into a second S phase and permitting cells to undergo mitosis despite the presence of DNA damage (Lloyd et al., 2020). Whilst Kim et al. reported a similar trend in HR-deficient ovarian cancer cells, the opposite effect was seen in HR-proficient cells, with combined PARPi and ATRi resulting in a significant increase in the proportion of cells in G2-M phase (Kim et al., 2016). Likewise, the same trend was observed in both PC-3 and DU-145 cells in this thesis, with 96 hours treatment with combined olaparib and ceralasertib at IC50 concentrations resulting in an increase in the proportion of cells in S and G2-M phases compared with vehicle or either agent alone.

It is possible that the increase in proportion of cells in G2-M is the result of activation of different checkpoint proteins that bring about cell cycle arrest in response to the increased levels of DNA damage. Alternatively, this may be due to the aberrant progression of cells into M phase with subsequent stalling therein, as proposed by Kim et al. (Kim et al., 2016). In their study, ATRi significantly increased chromosomal gaps and breaks in M phase HR-deficient PPEO1 ovarian cancer cells compared with untreated controls, with a combined PARPi and ATRi resulting in a further three-fold increase, suggesting large quantities of unrepaired DSBs inappropriately enter M phase. This in turn results in mitotic catastrophe (MC), which is the process by which premature or inappropriate entry of cells into mitosis results in an inability to correctly partition broken chromatid fragments symmetrically (Vakifahmetoglu et al., 2008). There are several means by which MC then results in death, including apoptosis through caspase-dependent or independent pathways, or cellular escape from mitosis resulting in tetraploid cells which in turn become arrested at the G1 checkpoint and die through p53-dependent apoptosis or do not arrest and enter S phase, during which they die through necrosis (Vakifahmetoglu et al., 2008). This concept is further supported by a recent study by Schoonen et al. in which combined PARPi and ATRi was shown to promote premature entry of *BRCA* depleted (and therefore HR-deficient) HeLa cells into mitosis, with associated increases in genomic instability as measured using single-cell whole-genome sequencing (Schoonen et al., 2019). Furthermore, regardless of HR status, the number of chromatin bridges and lagging chromosomes during anaphase and telophase was also increased with combined PARPi and ATRi, thus supporting the theory that combination treatment enables aberrant cell cycle progression despite increased levels of DNA damage.

Contrary to the findings in PC-3 and DU-145 cells, ceralasertib treatment alone and in combination with olaparib resulted in an increase in proportion of 22Rv1 cells in G0-1 phases, with a corresponding decrease in the proportion of cells in S phase. The exact reasons for this remain to be elucidated but may be due to differences in p53 status between the cell lines. This well characterised transcription factor and tumour suppressor, which is the protein product of the *TP53* gene, is critical for the arrest of cells at the G1-S checkpoint, as well as several other responses to DNA damage (Senturk and Manfredi, 2013). Whilst PC-3 and DU-145 cells harbour pairs of deleted or inactivated *TP53* alleles that result in a loss of p53 function, 22Rv1 cells contain both a wild-type and mutant *TP53* allele and hence retain some p53 function (van Bokhoven et al., 2003, Lehmann et al., 2007). It is therefore possible that the increased DNA damage occurring with ceralasertib alone and in combination with olaparib resulted in p53 mediated G1-S checkpoint activation in 22Rv1 cells, which is a well characterised response to DSBs arising as a result of unrepaired SSBs and collapse of replication forks during S phase (Haynes et al., 2018). Given the lack of p53 function in both PC-3 and DU-145 cells, this G1-S checkpoint activation may not have been able to occur, enabling them to progress through the cell cycle despite harbouring significant DNA damage, which may in part explain the higher level of synergy between the two agents observed in these cell lines, as indicated by higher Summary Synergy Scores. This is supported by the findings of a previously reported study in which *TP53* null chronic lymphocytic leukaemia cells treated with ceralasertib were able to progress through to mitosis despite accumulation of unrepaired DNA damage, resulting in death via mitotic catastrophe (Kwok et al., 2015). Additionally, greater levels of synergy were seen with combined ATRi and the chemotherapeutic agent cisplatin in *TP53* null lung cancer cells and those in which p53 was depleted using siRNA or expression of the human papilloma virus E6 protein, suggesting that loss of p53 function may further enhance sensitivity to ATRi (Reaper et al., 2011).

Collectively these results, together with those of the few similar studies exploring the biological effects of combined PARPi and ATRi in solid cancer cells, may be explained by the proposed mechanism outlined in ***Figure 3.12***. Firstly, PARPi prevents SSBs repair and results in PARP trapping at replication forks, leading to collapse and formation of DSBs. Under normal circumstances, ATR is activated in response to the resulting replication stress and DNA damage, in turn activating several downstream processes including phosphorylation of CHK1 and cell cycle arrest at the G2-M checkpoint together with DSB repair via HR. However, if ATR function is inhibited, DNA damage continues to accumulate and, in the absence of CHK1 activation, cells are able to aberrantly progress through the cell cycle and finally undergo apoptosis as a consequence of mitotic catastrophe.

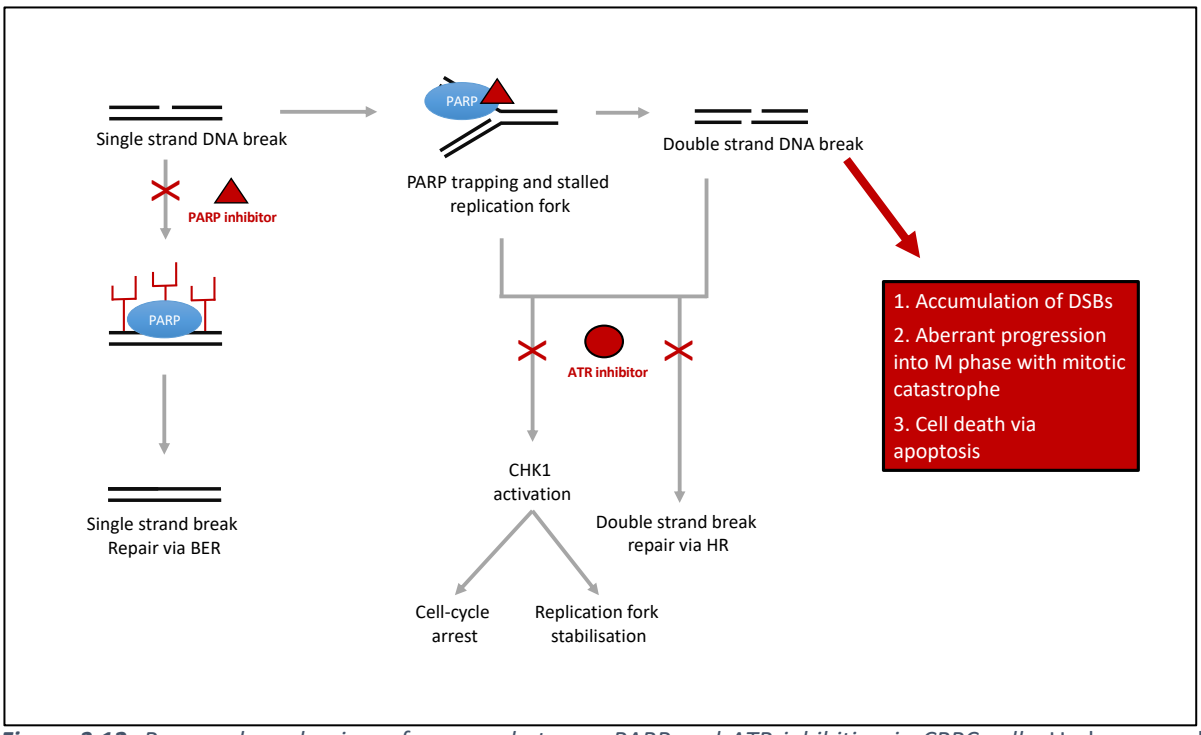

Figure 3.12: *Proposed mechanism of synergy between PARP and ATR inhibition in CRPC cells.* Under normal circumstances, DNA single strand breaks (SSBs) result in homopolymerisation of the ADP-ribose subunit of β-NAD^+ on amino acids of specific target proteins (a process known as PARylation), resulting in DNA repair via the base excision repair pathway (BER). PARP inhibition prevents this process and results in the trapping of PARP at the site of DNA damage, leading to replication fork collapse and the formation of double strand DNA breaks (DSBs). In turn this leads to CHK1 activation and its associated downstream processes such as cell cycle arrest to enable double strand break repair via homologous recombination (HR). The inhibition of ATR simultaneously inhibits both CHK1 activation and HR repair, leading to accumulation of highly genotoxic DSBs. Loss of the G2-M cell cycle checkpoint enables aberrant progression into the M phase of the cell cycle, resulting in

3.5 Limitations

It is possible that some of the results reported in this chapter may be subject to limitations based on the experimental methods used. Firstly, it is difficult to draw definitive conclusions regarding the effect of PARPi and ATRi on the phosphorylation and therefore activation of ATR in the panel of HR-proficient CRPC cells in vitro due to the choice of antibody used for WB. The chosen antibody was selective for ATR that has been phosphorylated at serine-428, a well characterised response to UV induced DNA damage, with the data failing to demonstrate any significant change in relative concentration ratio of p-ATR between treatment groups. However, previous research indicates that autophosphorylation of threonine-1989 (Thr-1989) in response to DNA damage is also important in the activation of ATR (Nam et al., 2011). Other studies investigating the effect of PARPi on ATR-CHK1 signalling utilised antibodies specific for the Thr-1989 phosphorylation site and did identify an increase in p-ATR concentration similar to that of p-CHK1 in response to PARPi with olaparib in both HR-proficient and deficient ovarian cancer cells (Kim et al., 2016, Schoonen et al., 2019). Future experiments using a p-ATR (Thr-1989)

antibody are therefore necessary to fully assess the effect of PARP inhibition on ATR activation and hence draw comparisons with other similar studies in the literature.

Similarly, the use of WB as a means of quantifying the expression or activation of particular proteins of interest may by a limitation in itself. Although a widely utilised technique, the original purpose of WB was to provide a yes or no answer about the presence or absence of a target protein in a given sample using simple visual assessment. While quantitative analysis is now possible using methods such as the densitometry approach described in this thesis, variations in experimental design and technique may be sources of error. To mitigate against this, densitometry was performed on blots obtained from three independent repeats and amalgamated to enable statistical analysis. However, in order to fully characterise the effects of treatment on protein concentration and post-translational modification, including interactions between different signalling pathways, more complex methods such as mass spectrometry-based phosphoproteomics are necessary, as discussed in Section 2.1.6. Furthermore, additional issues may relate to the specific protein being quantified. For example, while γ-H2AX is an established means of identifying the presence of DNA DSBs, the use of whole cell lysate γ-H2AX concentration measured by WB as a surrogate marker of DSB quantity has its own limitations given that γ-H2AX is cell cycle dependent and its overall concentration may not directly correlate with the number of DSBs (Löbrich et al., 2010). Given that each γ-H2AX focus is considered to represent a single DSB, quantification of individual foci within the nucleus using immunofluorescence microscopy, with or without co-localisation with other DSB responsive proteins such as p53 binding protein 1 (53BP1), would provide a more accurate means of evaluating the effects of PARPi and ATRi on DSB formation in future experiments (Popp et al., 2017).

Secondly, whilst a well-established assay was used to determine the effect of ceralasertib on HR, this was conducted in U2OS osteosarcoma cells harbouring the DR-GFP reporter. Furthermore, cells were only treated for a duration of 48 hours, rather than 96 hours as was standard for most other functional assays reported in this chapter. Additional studies in which the DR-GFP reporter has been integrated into the specific HR-proficient CRPC cell lines utilised in this thesis, together with treatment at the respective IC50 concentrations for a duration of 96 hours, are therefore required to fully determine the effect of ceralasertib on HR efficiency in this setting.

Thirdly, whilst cell cycle analysis was undertaken using a standard protocol performed by several groups in the Institute, the measure of DNA content of each cell was used as a surrogate marker of cell cycle distribution at a given time point. With this approach three distinct phases can be identified

within a proliferating cell population: G0-G1 (quiescence/gap phase), S (DNA synthesis phase) and G2-M (mitosis). However, given that cells in G2 and M phases have identical DNA content, it is not possible to discriminate between the two using DNA content alone. Additionally, this approach is also limited by the inability to differentiate between tetraploid cells in G2/M and those which have aberrantly progressed through mitosis into G1 as a consequence of mitotic catastrophe, which is of particular importance to this study. Additional experiments using a more sensitive and specific means of measuring the cell cycle, such as the fluorescence ubiquitinisation-based cell cycle indicator (FUCCI) method, are therefore necessary to fully characterise the effect of the various treatments on cell cycle distribution.

Finally, the choice of timepoint and concentration of each agent used potentially limits the ability to compare findings with those in the published literature. The majority of assays evaluated outcomes during and at the end of a 96 hour treatment period. This timepoint was based on that used in other in vitro studies of PARPi activity in CRPC cells (Feiersinger et al., 2018). However, it is possible that by restricting analyses to this period, early or delayed effects may have been missed. Furthermore, whilst concentrations used for in vitro treatment with olaparib and ceralasertib were based on relative and absolute IC50 values respectively, these were calculated using cell viability at 96 hours as the outcome and would potentially differ if alternative timepoints, treatment conditions or outcome were used. Although these concentrations were within a range that is clinically achievable (Dillon et al., 2019, Pilla Reddy et al., 2019), their specificity must be taken into account when attempting to make direct comparisons with other similar studies using these or similar agents.

3.6 Conclusions and future work

In summary, this chapter has confirmed that HR-proficient CRPC cells are inherently insensitive to the PARPi olaparib, corroborating the findings of clinical trials exploring its use in patients with heavily pre-treated CRPC. However, combined treatment with both olaparib and the ATR inhibitor ceralasertib greatly reduces the viability of HR-proficient CRPC cells in a synergistic manner in vitro, providing a potentially efficacious therapeutic option for men with CRPC that lack pre-existing DDR aberrations. In addition, the potential mechanism by which this observed synergy may occur has been hypothesised, providing an avenue for further exploration. Future experiments should therefore be designed to overcome some of the limitations discussed in Section 3.5 and to test this mechanistic hypothesis in more detail, with particular focus on chromosomal aberrations, cell cycle progression and the degree of genomic instability arising as a result of each treatment alone and in combination

in the panel of CRPC cells. Collectively, these data provide sufficient evidence to support the further investigation of combined PARP and ATR inhibition using more complex ex vivo and in vivo models of HR-proficient prostate cancer, as outlined in Chapter 4 of this thesis.

4 Establishing the therapeutic benefit of combined PARP and ATR inhibition using ex vivo and in vivo preclinical models of prostate cancer

4.1 Introduction

The experiments outlined in the previous chapter identified that combined PARP and ATR inhibition is synergistic in reducing the viability of HR-proficient CRPC cells in vitro. However, such studies using established cell lines have a number of limitations that often restrict the translatability to findings to the clinical setting, with high failure rates of new candidate therapies in clinical trials (Risbridger et al., 2018). Since their development, immortalised cell lines have been the cornerstone of prostate cancer research, providing a well characterised, low cost and easily manipulatable platform for preclinical studies exploring biology and testing novel therapeutics. However, despite their extensive use, many established CRPC cell lines, including those in the previous chapter, contain a highly specific set of genetic and phenotypic characteristics that only represent a very particular subset of this diverse disease. Furthermore, cells are also subject to secondary genomic changes with prolonged use in culture, resulting in copy number variations and transcriptomic drifts that render them different to the originally characterised line (Gillet et al., 2013). Whilst we endeavoured to overcome several of these issues by using a panel of three previously validated HR-proficient CRPC cell lines with varying genetic characteristics at low passage number, such in vitro experiments still fail to recapitulate many important elements of clinical prostate cancer, including tumour heterogeneity, microenvironment and immune system interactions.

More complex preclinical models seek to overcome some of these limitations and hence facilitate more successful translation into the clinical setting. Advances in cell culture techniques and gene editing in recent decades now mean that there are many options available, each with its own advantages and limitations, as outlined in Section 1.5. To this end, preclinical testing of olaparib and ceralasertib was undertaken using three different models to provide mechanistic insight into responses within a range of disease settings.

A major source of progress in the preclinical modelling of prostate cancer has been the development of models that utilise tumour tissue taken directly from patients (described in detail in Section 2.2). Fresh tumour tissue obtained during surgery, through biopsy or at autopsy can either be deconstructed and the cells cultured in 2D or 3D (termed organoids), transferred directly into immunocompromised mice to generate patient derived xenografts (PDX) or tissue slices directly cultured ex vivo; termed patient derived explant culture (PDE). First described in the 1950s, prostate

PDE culture techniques have evolved considerably in recent years, with one of the most widely adopted involving the culture of small pieces of tissue on gelatin sponge that is partially submerged in media (Risbridger et al., 2018, Powley et al., 2020). Through using this approach, primary tissue has been shown to remain viable for up to 7 days, with preservation of its tissue architecture and cell-cell signalling within the microenvironment (Centenera et al., 2012). This method enables quantitative evaluation of clinically relevant endpoints and has hence been utilised in preclinical drug response experiments, including those evaluating the efficacy of the PARP inhibitor ABT888 in samples of localised prostate cancer obtained at radical prostatectomy (Schiewer et al., 2012). Given these advantages, we therefore firstly opted to evaluate the effects of combined olaparib and ceralasertib using the LN-NEPC-1 PDE model that has recently developed by the Pearson group using tissue obtained from a metastatic pelvic lymph node of a patient with heavily pre-treated neuroendocrine CRPC (manuscript in preparation).

Despite the many advantages of PDE culture, the model still possesses several limitations, including lack of blood supply, limited immune interaction and most importantly the short timeframe of tissue viability, thereby preventing its use in longer term studies. One alternative is to grow tumour tissue within immunocompromised mice as a PDX, which have been shown to retain the architecture and morphology of the original tumour, even after serial propagation (DeRose et al., 2011). Furthermore, propagated tumours can be re-transplanted to multiple recipient mice or frozen for expansion at a later date, thereby enabling tissue from one tumour to be used for a range of purposes. However, despite these advantages, prostate tumours are difficult to culture, engraft and/or serially propagate on account of factors such as low tumour proliferation and lack of stroma (Risbridger and Taylor, 2016). As such, there are fewer prostate cancer PDX models available than for other tumour types, with further limitations in terms of access, cost and throughput often providing a barrier to widespread use in preclinical drug studies (Risbridger et al., 2018).

Xenograft models generated from established human cell lines provide a more rapidly growing and readily available alternative to PDXs and, although they lack the tissue architecture of original prostate tumours, they provide a well characterised and valuable tool for the in vivo study of human tissue in murine organisms. The subcutaneous approach in which tumour cells are injected into the flank is the most common xenograft model used in anticancer drug research as it is relatively less invasive than the alternative orthotopic approach in which tumour cells are injected into the organ from which they originate. Furthermore, the location of the tumours results in minimal distress to the animal during longitudinal monitoring, hence rendering them an excellent starting point for in vivo testing of

experimental agents. A recent study that included genomic analysis of 285 samples from patients with localised, metastatic hormone sensitive and hormone refractory disease identified the frequency of co-alterations in *TP53* and *PTEN* to be 7%, 16% and 56% respectively, with cumulative tumour suppressor gene alterations (including *TP53*, *PTEN* and retinoblastoma protein 1; *RB1*) associated with increased risk of relapse and shorter time to development of CRPC (Hamid et al., 2019). Therefore, given that PC-3 cells do not harbour clinically significant DDR aberrations but are AR negative and hence hormone insensitive with both *PTEN* and *p53* loss, this model mirrors clinical HR-proficient CRPC and hence was considered an appropriate model for the in vivo preclinical study of olaparib and ceralasertib in this setting.

Although an ideal starting point for in vivo drug testing, xenograft models are limited by their lack of tumour heterogeneity and immune system interactions. Genetically engineered mouse models (GEMM) provide a valuable alternative due to the level of genetic manipulation that can be achieved, short gestation times, intact tumour microenvironment and competent immune function. Thanks to the advent of Cre-Lox technology, such models can be used to recapitulate genetic events occurring within human prostate cancer with both spatial and temporal control, as discussed in Section 2.3.2. Previous studies have utilised a GEMM in which Cre recombinase downstream of the rat probasin promoter/enhancer segment, termed Probasin-Cre4 (PB-Cre4), induces genetic deletion of *Trp53* and *Pten* within the mouse prostate, thereby recapitulating genetic aberrations commonly seen in prostate cancer and enriched in advanced disease. This model results in locally advanced but not metastatic adenocarcinoma in 50% of mice by 10 weeks, with death from complications such as obstructive renal failure invariably occurring by 7 months of age (Chen et al., 2005). However, rare expression of *PB-Cre4* has also been identified in stromal and cutaneous epithelial cells and is diffuse in the seminal vesicles, testis and epididymis (Wu et al., 2001), with off target recombination found to result in the development of penile lesions when combined with simultaneous p53 and PTEN inactivation that are a source of distress to the mouse. Furthermore, the probasin promoter is active throughout life and therefore *PB-Cre4* expression cannot be temporally regulated. As described in Section 2.3.2, as PSA-Cre-ER^{T2} is more tissue specific and under the temporal control of tamoxifen, it offers an alternative to PB-Cre4 without these undesirable effects. As such, the final preclinical study in this chapter utilised the *PSA-Cre-ER*$^{T2(+/-)}$*; p53*$^{fl/fl}$*; Pten*$^{fl/fl}$ GEMM to explore responses to combined PARPi and ATRi in p53 and PTEN deficient localised prostate cancer with an intact tumour microenvironment and immune system response.

4.2 Chapter aims

1. Explore the therapeutic benefit of combined PARP and ATR inhibition ex vivo using a PDE of metastatic neuroendocrine CRPC.
2. Determine the efficacy of combined PARP and ATR inhibition in vivo using the PC-3 subcutaneous xenograft model of CRPC.
3. Establish the efficacy of combined PARP and ATR inhibition in vivo using the immune proficient *PSA-Cre-ER^{T2} ; p53$^{fl/fl}$; Pten$^{fl/fl}$* GEMM of localised prostate cancer.

4.3 Results

4.3.1 Combined PARP and ATR inhibition results in decreased proliferation and increased apoptosis in castrate resistant neuroendocrine prostate cancer cells ex vivo

Prior to undertaking in vivo preclinical trials, the therapeutic benefit of combined PARP and ATR inhibition was first explored using the LN-NEPC-1 PDX explant model of treatment-induced neuroendocrine mCRPC. A full description of the model, together with the method of explant culture is outlined in Section 2.2. In brief, explants were established by placing 250 μm LN-NEPC-1 PDX tumour sections on 1cm^3 gelatin sponges soaked in media supplemented with either vehicle, olaparib (10 μM), ceralasertib (5 μM), or both for a period of 48 hours (n=3, 3 independent repeats). Sections were then harvested, formalin-fixed and paraffin embedded for histopathological assessment and analysis using immunohistochemistry (IHC). Given that the tumour sections contained human prostate cancer cells within murine stroma, an antibody targeting the intact surface of human mitochondria was initially used to identify human prostate tumour cells for analysis. Further IHC staining was then performed to evaluate proliferation (proliferating cell nuclear antigen; PCNA), apoptosis (cleaved caspase-3; CC-3) and the quantity of double strand DNA breaks (surrogate marker: γ-H2AX) specifically within the human tumour cell population in response to each treatment.

As shown in ***Figure 4.1A***, tumour cells that stained positive for human mitochondria were largely identified in distinct clusters surrounded by stromal and immune cells from the murine host (black arrows). Histopathological analysis confirmed the phenotype of neuroendocrine prostate cancer, which was comparable to that of the original patient and PDX tumour specimens. Distinct areas of necrosis were also observed in all sections, irrespective of the treatment arm. Although it is possible that necrosis may have been due to drug effect, it may also have occurred due to inherent issues with the culture conditions themselves, such as loss of contact with media, tissue drying or poor oxygenation. Furthermore, the proportion of necrotic tissue increased substantially in explant tissue

treated for 96 hours regardless of treatment (data not shown), thus this study was limited to the 48 hour timepoint.

The proportion of PCNA-positive proliferative tumour cells, termed the PCNA index, was 63.4% in DMSO treated controls, indicating a high level of ongoing proliferation at 48 hours and hence confirming viability within the tumour cell population at the study timepoint (***Figure 4.1B***). Treatment with olaparib or ceralasertib monotherapy resulted in a reduction in the PCNA index to 48.7% (+/- 1.26% SEM) and 48.5% (+/- 3.72% SEM) respectively, although differences did not prove statistically significant compared with DMSO treated controls (P=0.60 and P=0.057). On the contrary, combined olaparib and ceralasertib had a greater effect than either agent alone and was the only treatment to prove statistically more effective in reducing proliferation when compared with DMSO treated controls, reducing the PCNA index to 36.5% (+/- 5.28% SEM; P=0.002). These findings therefore indicate that 48 hours of combined PARPi and ATRi results in a greater reduction in tumour cell proliferation than either agent alone relative to vehicle, thereby corroborating the results of the in vitro CRPC cell line experiments.

To determine if combined PARPi and ATRi results in apoptosis in LN-NEPC-1 explant cultures, the number of CC-3-positive apoptotic cells were quantitated and normalised to the total number of cells to give the CC-3 index. The CC-3 index in DMSO treated control LN-NEPC-1 PDX explants was 8.9% (+/- 1.98% SEM), again supporting the notion that the majority of cells within individual tumour clusters were viable at the 48 hour timepoint. Relative to vehicle, treatment with olaparib monotherapy led to a modest but non-significant increase in CC-3 index to 22.3% (+/- 3.09% SEM; P=0.089), whilst treatment with ceralasertib monotherapy resulted in a significantly higher CC-3 index of 32.2% (+/- 4.95% SEM; P=0.005). However, combined treatment with olaparib and ceralasertib resulted in the greatest increase in apoptosis relative to vehicle, with a CC-3 index of 36.5% (+/- 2.76% SEM; P=0.002). These findings demonstrate that 48 hours treatment with ceralasertib, either alone or in combination with olaparib increases apoptosis by over 3 and 4 fold respectively in the tumour cells of LN-NEPC-1 PDX explants. However, the difference between ceralasertib alone and ceralasertib in combination with olaparib did not prove statistically significant, thereby indicating that based on these data, combination therapy is no more effective than ceralasertib in terms of inducing cell death by apoptosis in this particular model of CRPC.

To establish if combined PARPi and ATRi enhances the number of DNA double stranded breaks relative to monotherapies and vehicle, the surrogate DSB marker γ-H2AX was stained using IHC and the

positive cells quantitated. As shown in ***Figure 4.1B***, treatment with DMSO resulted in 8.03% (+/- 1.25% SEM) of cells exhibiting high levels of γ-H2AX, while treatment with either olaparib or ceralasertib alone increased this to 14.48% (+/- 5.15% SEM) and 18.11% (+/- 4.22% SEM) respectively, although these differences failed to reach statistical significance. Combined olaparib and ceralasertib further increased the proportion of cells demonstrating high levels of γ-H2AX to 34.13% (+/- 6.44% SEM) and was the only treatment to induce significantly greater numbers of DSBs compared with DMSO treated controls (P=0.49). These data therefore indicate that 48 hours of combined PARPi and ATRi results in a greater number of DSBs compared to vehicle treated controls than either agent alone, again corroborating the results of the in vitro CRPC cell line experiments.

Collectively these data indicate that 48 hours of treatment with olaparib alone results in both a modest but non-significant decrease in proliferation along with an increase in apoptosis and DNA DSB formation when compared with DMSO treated controls in neuroendocrine mCRPC PDX tumour explants. Similarly, treatment with ceralasertib also results in a modest but non-significant decrease in proliferation and increase in DNA DSB formation, together with a more substantial and statistically significant increase in apoptosis. However, combined PARPi and ATRi treatment led to the greatest reduction in proliferation and increase in apoptosis and DNA DSB formation, thereby supporting the in vitro evidence that combined PARP and ATR inhibition results in potent antitumour activity in CRPC cells reported in Chapter 3 of this thesis.

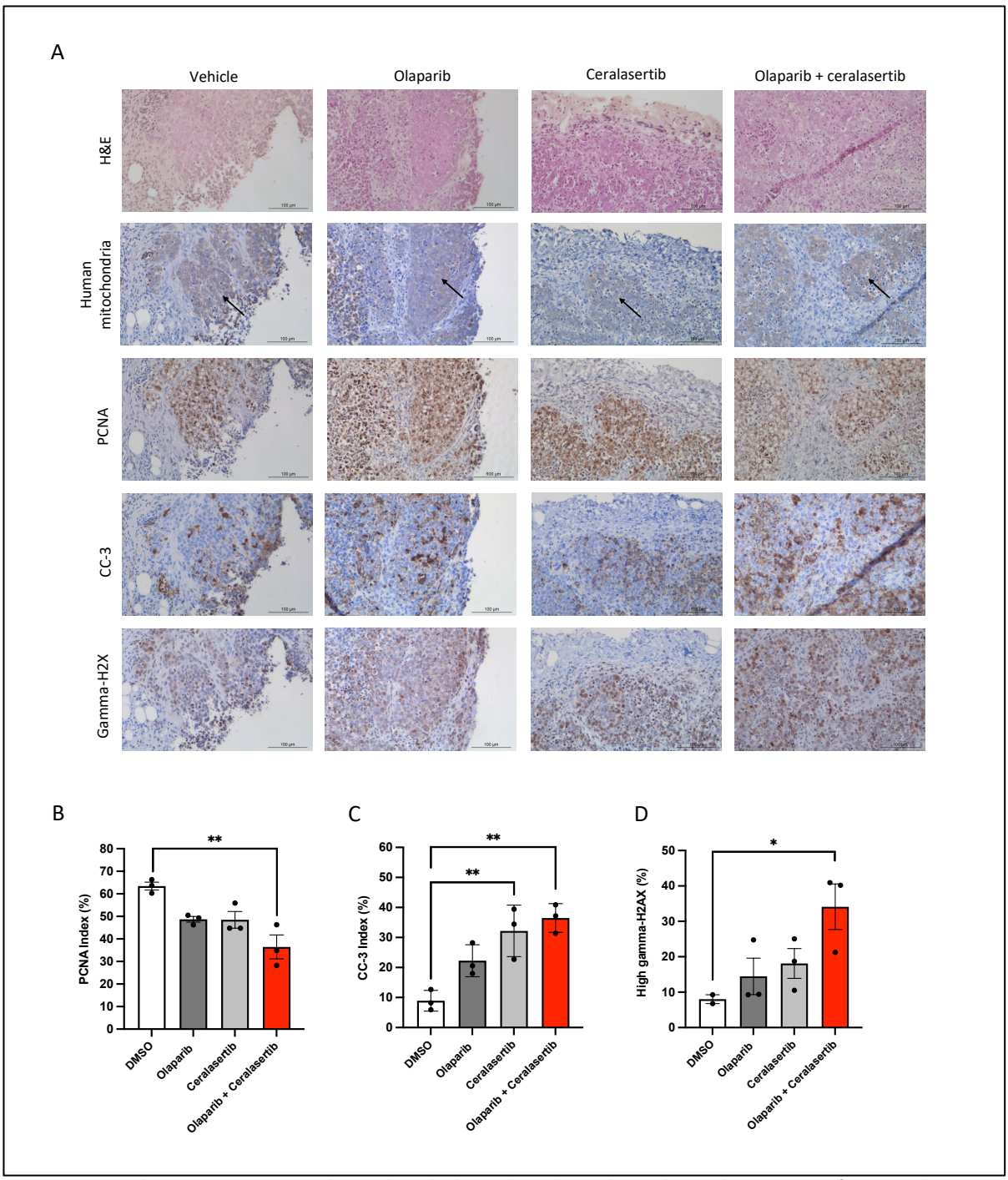

Figure 4.1: *48 hours treatment with combined olaparib and ceralasertib results in a significant reduction in proliferation along with increased apoptosis and DNA double strand breaks in LN-NEPC-1 PDX ex vivo explant cultures compared with DMSO treated controls*. A: Representative H&E and anti-human mitochondrial stained images at x20 magnification to demonstrate tumour cell clusters (black arrows), followed by corresponding IHC images demonstrating expression of PCNA, CC-3 and γH2AX in the tumour cell population of explants treated with DMSO, olaparib (10 µM), ceralasertib (5 µM) and olaparib (10 µM) + ceralasertib (5 µM). Scale bars represent 100 µm. B: Bar chart demonstrating quantitation for PCNA within the tumour cell population (expressed as the proportion of cells positive for PCNA; PCNA index). C: Bar chart demonstrating quantitation for CC-3 within the tumour cell population (expressed as the proportion of cells positive for CC-3; CC-3 index). D: Bar chart demonstrating the percentage of cells demonstrating high levels of γ-H2AX expression within the tumour cell population. Three technical repeats per treatment group and three independent biological repeats. Error bars represent Standard Error of the mean. Statistical significance between means of treatment groups calculated using one-way ANOVA with Tukey correction for multiple comparisons. **: $P \leq 0.01$, *: $P \leq 0.05$.

4.3.2 Combined PARP and ATR inhibition is well tolerated in mice and reduces tumour burden in the PC-3 subcutaneous xenograft model of CRPC

4.3.2.1 Model characteristics and experimental cohort demographics

To determine the therapeutic benefit of co-targeting PARP and ATR in vivo, a preclinical trial was undertaken using the well described and previously published PC-3 subcutaneous xenograft model of CRPC (Jung et al., 2012, Wu et al., 2013). A full description of the model, together with its optimisation is outlined in Section 2.3.3.2. In brief, male athymic nude mice were aged to 6-8 weeks and 3 x 10^6 PC-3 cells implanted bilaterally by subcutaneous injection. Tumour volume was measured on day three post implantation and those mice with tumours with a minimum diameter of 5 mm were allocated into treatment groups as outlined in ***Table 4.1.*** A total of two tumours did not meet size inclusion criteria and hence were excluded from further analysis. Overall mean starting weight of mice was 29.26 g (range 25.6 – 35.2 g), with no significant difference between individual treatment groups, as shown in ***Figure 4.2***. Mice were assigned to either 21 or 42 day cohorts to assess short-term and long-term treatment responses respectively. The mean tumour volume of those eligible for inclusion was 172.5 mm^3 (range 53 – 390 mm^3) at the time of study commencement. Mice were treated according to the dosing schedule outlined in Section 2.3.3.2. Safety outcomes were overall mortality and percentage weight loss compared with starting weight, as measured on the Monday, Wednesday and Friday of each treatment week and at the study endpoints. Primary efficacy outcome was tumour volume, as calculated using the modified ellipsoid formula on the Monday, Wednesday and Friday of each treatment week. Secondary efficacy outcomes included tumour weight at the study endpoint and the presence of macroscopic neovascularisation, pathological lymphadenopathy and invasion of local structures at the time of dissection.

Table 4.1: Allocation of mice and tumours to each treatment group in the PC-3 subcutaneous xenograft preclinical trial.

Treatment group	Treatment	Number of mice	Number of tumours
Vehicle	Olaparib vehicle Ceralasertib vehicle	4	7
Olaparib *Short term*	Olaparib 100 mg/kg Ceralasertib vehicle	3	5
Olaparib *Long term*	Olaparib 100 mg/kg Ceralasertib vehicle	4	8
Ceralasertib *Short term*	Olaparib vehicle Ceralasertib 25 mg/kg	4	8
Ceralasertib *Long term*	Olaparib vehicle Ceralasertib 25 mg/kg	4	8
Combination *Short term*	Olaparib 100 mg/kg Ceralasertib 25 mg/kg	3	6
Combination *Long term*	Olaparib 100 mg/kg Ceralasertib 25 mg/kg	3	6

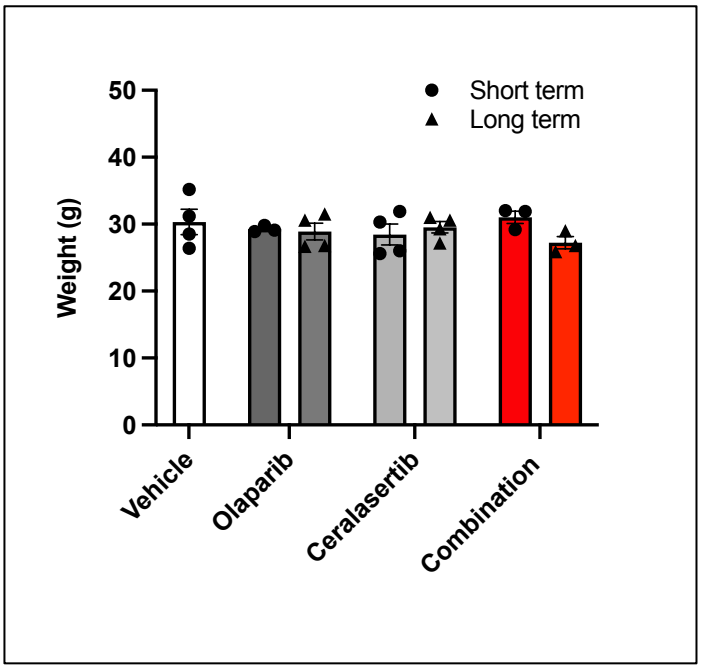

Figure 4.2: *PC-3 subcutaneous xenograft preclinical trial experimental mouse demographics.* Bar chart illustrating mean weight of mice on Day 0 as stratified according to treatment group. Individual mice represented to indicate number per treatment group. Error bars represent Standard Error of the mean. Statistical significance calculated using one-way ANOVA with Tukey correction for multiple comparisons, with no differences reaching the significance threshold.

4.3.2.2 Safety and tolerability

As outlined above, the intended duration of the short term treatment study was 21 days. However, tumours progressed more rapidly in the vehicle group than anticipated, requiring two mice to be terminated on treatment day 11 and 15 respectively on account of approaching tumour size and ulceration ethical limits. The short term endpoint was therefore revised to 18 days in order to ensure ethical limits were not breached and that there were sufficient numbers in each group for statistical analysis. One mouse in the olaparib short term treatment group was also terminated early owing to weight loss, as outlined in ***Table 4.2.***

Table 4.2: Details of experimental mice that required termination prior to the 18 day short term endpoint.

Mouse ID	Treatment group	Treatment day	Cause of death / reason for termination
067097	Vehicle	11	Tumour size ethical limit reached
067117	Vehicle	15	Tumour ulceration severity limit reached
067112	Olaparib Long term	15	Weight loss ethical limit reached

In general, short term treatment with olaparib and ceralasertib, alone and in combination, was well tolerated. ***Figure 4.3A*** shows the mean percentage change in weight of experimental mice according to treatment received during the first 18 days, regardless of whether in a short or long term cohort (n = 4-8 mice per treatment). There was no significant difference between groups, although the greatest weight loss was seen in those treated with vehicle, most likely on account of these mice harbouring the greatest tumour burden. ***Figure 4.3B-E*** illustrates the percentage change in weight of individual experimental mice according to the treatment received throughout the entire study period. In the majority of mice, a small transient loss in weight was seen between treatment days 1 and 7 during which each mouse received three oral gavages per day. This was followed by a partial restoration in weight in nearly all mice during the subsequent period of once daily gavage, followed by either a stabilisation or gradual weight loss, most likely due to increasing tumour burden over time. A small number of mice treated with either ceralasertib or combined olaparib and ceralasertib demonstrated a period of sustained weight gain above their original starting weight (***Figure 4.3D and 4.3E***). Overall, no clear trend was identified to suggest one treatment resulted in greater weight loss than the others.

Additionally, no mice exhibited symptoms or signs suggestive of gastrointestinal or other organ system side effects during the study period. Collectively these data indicate that male athymic nude mice bearing bilateral subcutaneous PC-3 xenograft tumours are able to tolerate olaparib and ceralasertib treatment, both alone and in combination, with no evidence of severe side effects or significant weight loss over time.

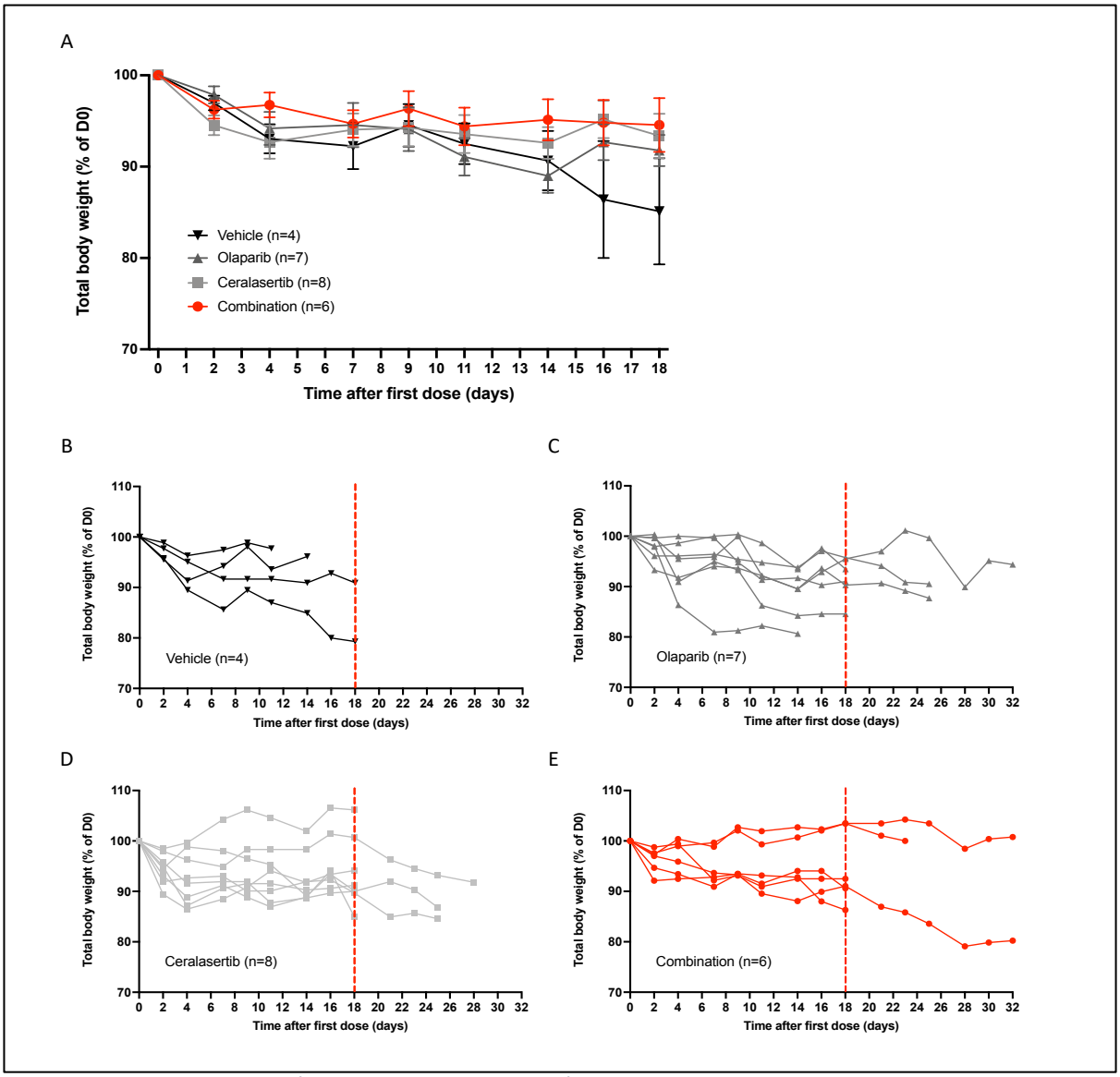

Figure 4.3: *Olaparib (100 mg/kg) or ceralasertib (25 mg/kg) alone or in combination does not significantly alter total body wight of experimental mice during short or long term treatment compared with vehicle treated controls.* A: Mean change in total body weight of experimental mice as measured at Day 0, stratified according to treatment received. Error bars represent Standard Error of the mean. Statistical significance calculated using one-way ANOVA with Tukey correction for multiple comparisons at each time point, with no differences reaching the significance threshold. B-D: Percentage change in total body weight as measured at Day 0 of individual mice treated with vehicle (B), olaparib (C), ceralasertib (D) or combined olaparib and ceralasertib (E) throughout the entire study period. Each line represents one experimental mouse. Red line; day 18 short-term timepoint.

4.3.2.3 Short term efficacy

4.3.2.3.1 Short term combination treatment with olaparib and ceralasertib significantly reduces PC-3 xenograft tumour burden, local invasion and macroscopic neovascularisation

The therapeutic benefit of short term combined ATR and PARP inhibition was firstly assessed with respect to the predefined primary outcome of tumour volume on the Monday, Wednesday and Friday of each treatment week. To overcome statistical differences in starting tumour volume between individual treatments, analysis was restricted to those tumours with starting volumes of between 125-350 mm^3 (n = 5-9 tumours per treatment group).

Changes in tumour volume over time and at the D18 timepoint are demonstrated in ***Figure 4.4A***. Irrespective of treatment, all tumours reduced in size in the first three days of the study such that by D2 there was no difference between the four groups. This phenomenon is known to occur in subcutaneous xenograft tumour models and is likely to have been multifactorial in origin, resulting from a combination of absorption of the Matrigel component of the inoculated suspension, resolution of the inflammatory response at the injection site and death of engrafted cells, which has been shown to be in the order of up to 90% following initial injection (Hoffmann et al., 2020).

From D2 onwards, tumours in mice treated with vehicle exhibited a progressive increase in volume up to a final mean of 869.3 mm^3 (+/- 93.4 mm^3 SEM). Tumours in those mice treated with olaparib and ceralasertib alone demonstrated a slower rate of growth up to day 14, after which growth accelerated substantially to reach final mean volumes of 661.8 mm^3 (+/- 87.8 mm^3 SEM) and 666.1 mm^3 (+/- 65.1 mm^3 SEM) respectively, with no significant difference compared with vehicle treated controls (P=0.305 and P=0.304). In contrast, tumours in those mice treated with combined olaparib and ceralasertib remained static during the first 11 days, after which they began to gradually increase in size up to a mean volume of 275.4 mm^3 (+/- 46.7 mm^3 SEM) at the D18 timepoint, with significant differences seen when compared with vehicle treated controls and those treated with olaparib and ceralasertib monotherapy (P=0.015, P=0.011 and P<0.001 respectively). Furthermore, significant differences in volume were also seen in comparison to vehicle treated controls at every timepoint beyond D4, which is in contrast to both olaparib and ceralasertib monotherapy, in which differences were only seen at D9 and D11. Collectively these data indicate that combined olaparib and ceralasertib is superior to both vehicle and either agent alone in suppressing CRPC tumour growth in vivo, thereby corroborating the previously described in vitro and ex vivo findings.

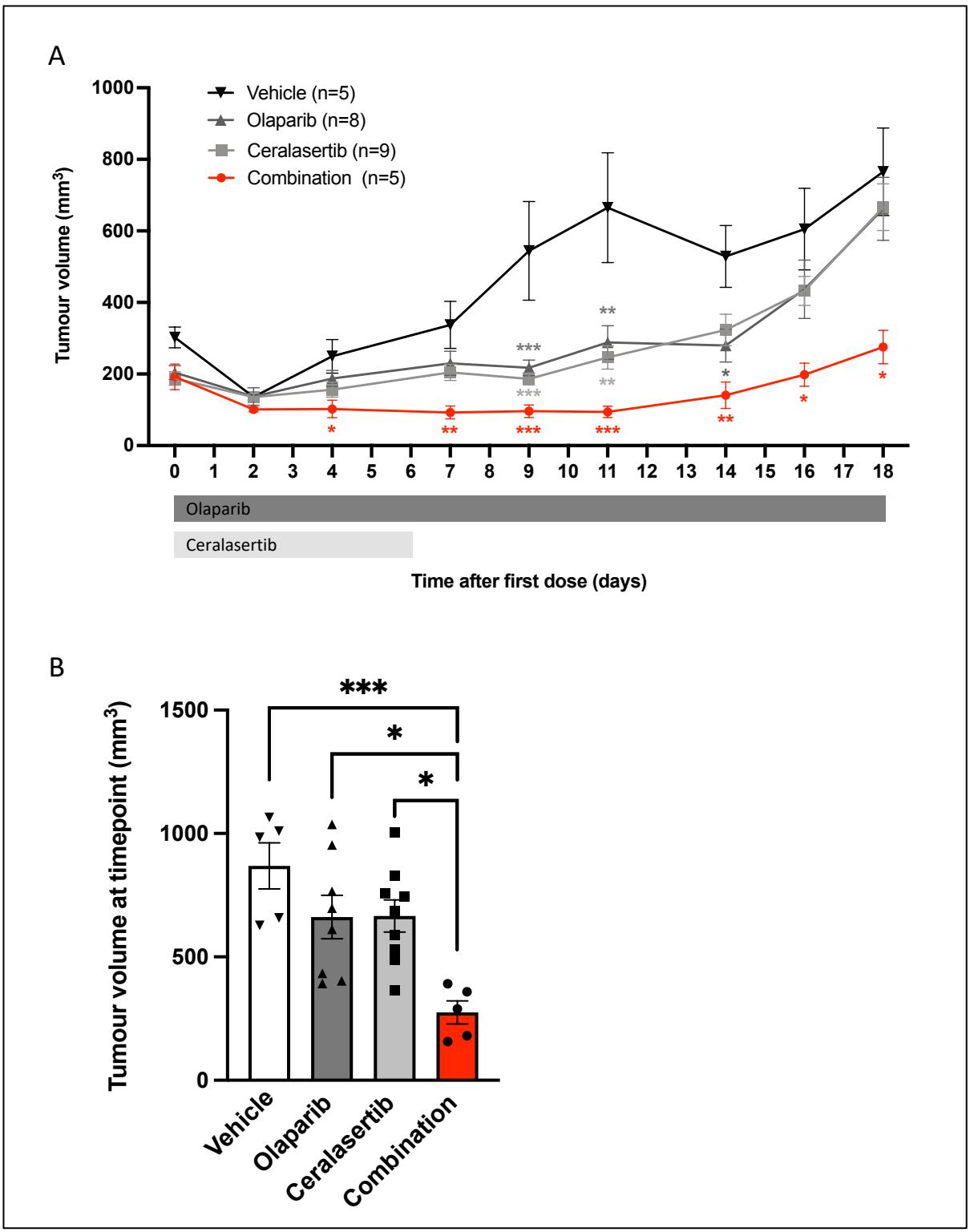

Figure 4.4: *Short term treatment with combined olaparib (100 mg/kg) and ceralasertib (25 mg/kg) results in a significant reduction in the volume of PC-3 xenograft tumours compared with those treated with vehicle or olaparib (100 mg/kg) or ceralasertib (25 mg/kg) monotherapy.* A: Mean tumour volume over time, stratified by treatment group. Tumour numbers displayed as n values. Error bars represent Standard Error of the mean. Statistical comparisons at each time point conducted using one-way ANOVA with Tukey correction for multiple comparisons, with * symbols denoting significance when compared with vehicle treated controls. B: Mean tumour volume as measured at the D18 timepoint. Tumour numbers displayed as symbols. Error bars represent Standard Error of the mean. Statistical comparisons at each time point conducted using one-way ANOVA with Tukey correction for multiple comparisons, with * symbols denoting significance when compared with vehicle treated controls. ***: $P \leq 0.001$, **: $P \leq 0.01$, *: $P \leq 0.05$

Next, differences in therapeutic effect between treatment groups were assessed with respect to secondary outcomes of tumour weight, the presence of macroscopic neovascularisation, local tumour invasion and lymphadenopathy at the short term D18 timepoint. ***Figure 4.5*** depicts the macroscopic appearance of the tumours in each treatment group at the time of dissection. Those treated with combined olaparib and ceralasertib appeared noticeably smaller and globally paler, with fewer visible surface blood vessels than those treated with vehicle or either agent alone.

The secondary endpoints were quantitated as described in Section 2.3.3.2, with results illustrated in ***Figure 4.6***. Both olaparib and ceralasertib monotherapy resulted in a reduction in tumour weight compared with vehicle treated controls (427.8 mg (+/- 69.9 mg SEM) and 570.4 mg (+/- 72.9 mg SEM) versus 634.0 mg (+/- 24.2 mg SEM) respectively), although differences were highly variable and failed to reach statistical significance. However, tumours in those mice treated with combined olaparib and ceralasertib had a mean weight of 269.0 mg (+/- 47.0 mg SEM), demonstrating a highly significant reduction compared with both ceralasertib monotherapy and vehicle treated controls (P=0.020 and P=0.005 respectively). Despite also resulting in a reduction in mean weight at the D18 timepoint compared with those treated with olaparib monotherapy, differences failed to reach statistical significance (P=0.348), most likely due to the level of variation between individual tumours. Collectively these findings correlate with effects on tumour volume and indicate that combined treatment with olaparib and ceralasertib results in both slower growing, lower mass tumours than treatment with vehicle or either agent alone, thereby warranting further mechanistic evaluation.

Macroscopic neovascularisation was defined as either positive or negative depending on the identification of subcutaneous vessels feeding and draining the tumour at the time of dissection. Whilst all tumours in mice treated with vehicle, olaparib or ceralasertib displayed macroscopic neovascularisation, this was not seen in any of those treated with combination therapy (***Figure 4.6B***), potentially explaining the paler appearance of tumours noted in ***Figure 4.5***. Local invasion was defined as the presence of invasion of structures adjacent to the subcutaneous tumours at the time of dissection. The most common sites of invasion were the musculature of the abdominal wall and the overlying skin, with the latter resulting in the formation of ulcers which were a predefined ethical limit mandating termination of the animal. Treatment with ceralasertib alone or in combination with olaparib resulted in a reduction in tumour invasion of surrounding structures when compared with vehicle treated controls, with the greatest and only statistically significant effect observed with ceralasertib monotherapy (P=0.049; ***Figure 4.6C***). Pathological lymphadenopathy was defined as the presence of one or more enlarged lymph nodes in the regions draining the tumour and adjacent

structures at the time of dissection. The most commonly observed sites were in the midline posteriorly and in each flank, lateral to the tumours. Ceralasertib monotherapy was the only treatment associated with a reduction in the presence of lymphadenopathy compared with vehicle treated controls, although the difference failed to reach statistical significance.

Taken together, these data suggest that combined olaparib and ceralasertib may provide a further advantage over monotherapy in terms of inhibiting the formation of new feeding vessels. However, combination therapy did not appear to result in significant reductions in local invasion or pathological lymphadenopathy, with only ceralasertib monotherapy associated with a significant reduction in the former compared with vehicle treated controls.

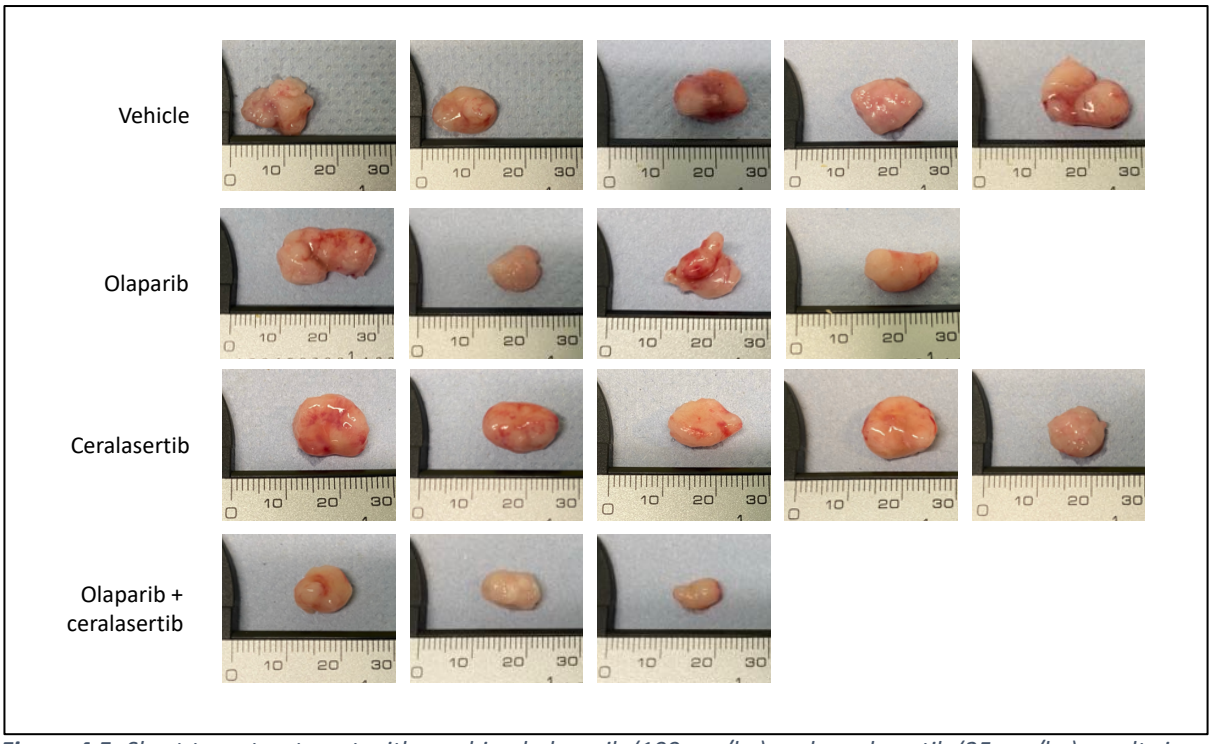

Figure 4.5: *Short term treatment with combined olaparib (100 mg/kg) and ceralasertib (25 mg/kg) results in a globally smaller and paler appearance of PC-3 xenograft tumours compared with those treated with vehicle or olaparib (100 mg/kg) or ceralasertib (25 mg/kg) monotherapy.* Photographs displaying the macroscopic appearance of tumours in each treatment group immediately after dissection at the D18 timepoint (n=3-5 tumours per treatment).

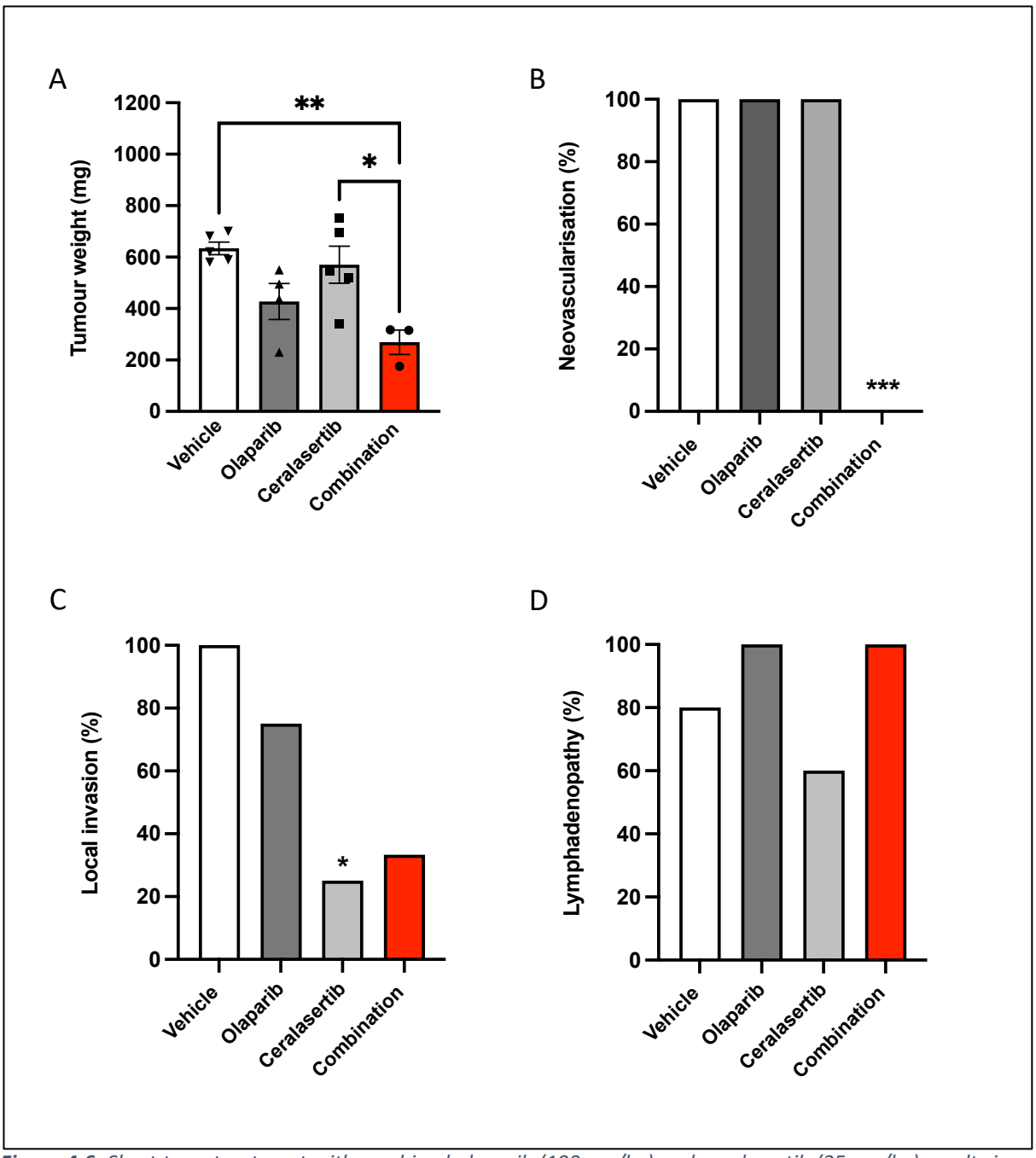

Figure 4.6: *Short term treatment with combined olaparib (100 mg/kg) and ceralasertib (25 mg/kg) results in a reduction in the weight and neovascularisation of PC-3 xenograft tumours at the Day 18 timepoint compared with those treated with vehicle or olaparib (100 mg/kg) or ceralasertib (25 mg/kg) monotherapy.* A: Mean tumour weight at the time of termination, stratified by treatment group. Tumour numbers displayed as symbols. Error bars represent Standard Error of the mean. Statistical comparisons at each time point conducted using one-way ANOVA with Tukey correction for multiple comparisons. **: $P \leq 0.01$, *: $P \leq 0.05$. B: Percentage of tumours demonstrating macroscopic neovascularisation at the time of dissection. C: Percentage of tumours demonstrating local invasion at the time of dissection. D: Percentage of tumours with evidence of pathological lymphadenopathy at the time of dissection. Vehicle (n=5), olaparib monotherapy (n=4), ceralasertib monotherapy (n=5), combined olaparib and ceralasertib (n=3). Statistical comparisons conducted using the Chi-squared test. ***: $P \leq 0.001$, **: $P \leq 0.01$, *: $P \leq 0.05$.

4.3.2.3.2 Short term combination treatment with olaparib and ceralasertib significantly reduces microvessel density and diameter in PC-3 xenograft tumours compared with either agent alone

Given that tumours treated with combined olaparib and ceralasertib appeared paler, with fewer surface vessels and macroscopic neovascularisation at the time of dissection, IHC was performed to detect the endothelial cell marker CD34 to evaluate microvessel density and hence quantify tumour vascularity at the microscopic level. Images of IHC stained sections were digitally overlaid with a standard grid comprising of squares of $1mm^2$ and the whole specimen examined at low power to identify the three squares containing the greatest number of microvessels, termed 'hot spots'. The number of microvessels in each square was then counted to give a number per mm^2. Counts were taken from 3 'hot spots' per tumour and tissue from at least three independent specimens and the mean value taken to represent microvessel density. To evaluate the effect of treatment on vessel size, the diameter of microvessels within each tumour 'hot spot' was also measured and the mean calculated for each treatment group.

Representative images of CD34 IHC stained sections of PC-3 xenograft tumours from each treatment group at the D18 timepoint together with mean microvessel density and diameter are shown in ***Figure 4.7***. Although treatment with olaparib or ceralasertib alone led to a reduction in microvessel density when compared with vehicle treated controls (42.8 vessels/mm^2 +/- 4.46 SEM and 39.8 vessels/mm^2 +/- 5.85 SEM respectively versus 66.9 vessels/mm^2 +/- 8.12 SEM), these differences did not prove statistically significant. Additionally, monotherapy with either agent did not result in a reduction in microvessel diameter compared with vehicle treated controls. Conversely, combined treatment with both olaparib and ceralasertib resulted in a highly significant reduction in microvessel density when compared with vehicle (27.9 vessels/mm^2 +/- 5.13 SEM versus 66.9 vessels/mm^2 +/- 8.12 SEM, P=0.008), together with a relative reduction compared with both olaparib and ceralasertib monotherapy, although these differences did not reach statistical significance. Furthermore, microvessel diameter was considerably smaller in those tumours treated with combination therapy (35.8 +/- 0.81 SEM) compared with vehicle (54.5 +/- 0.71 SEM; P<0.001) or either olaparib (52.7 µm +/- 1.08 SEM; P<0.001) or ceralasertib monotherapy (58.0 µm +/- 1.38 SEM, P=<0.001; ***Figure 4.7C***). These data therefore indicate that short term combined PARP and ATR inhibition not only reduces the vascularity of PC-3 xenograft tumours, but also reduces the size of the vessels themselves, thereby supporting the macroscopic observations that tumours were paler and less vascular within this treatment group. Whilst further experiments are needed to elucidate the mechanisms underlying these observations it is possible that combined PARPi and ATRi may impair angiogenesis, thereby providing a mechanism whereby dual inhibition beneficially cooperates to reduce tumour burden.

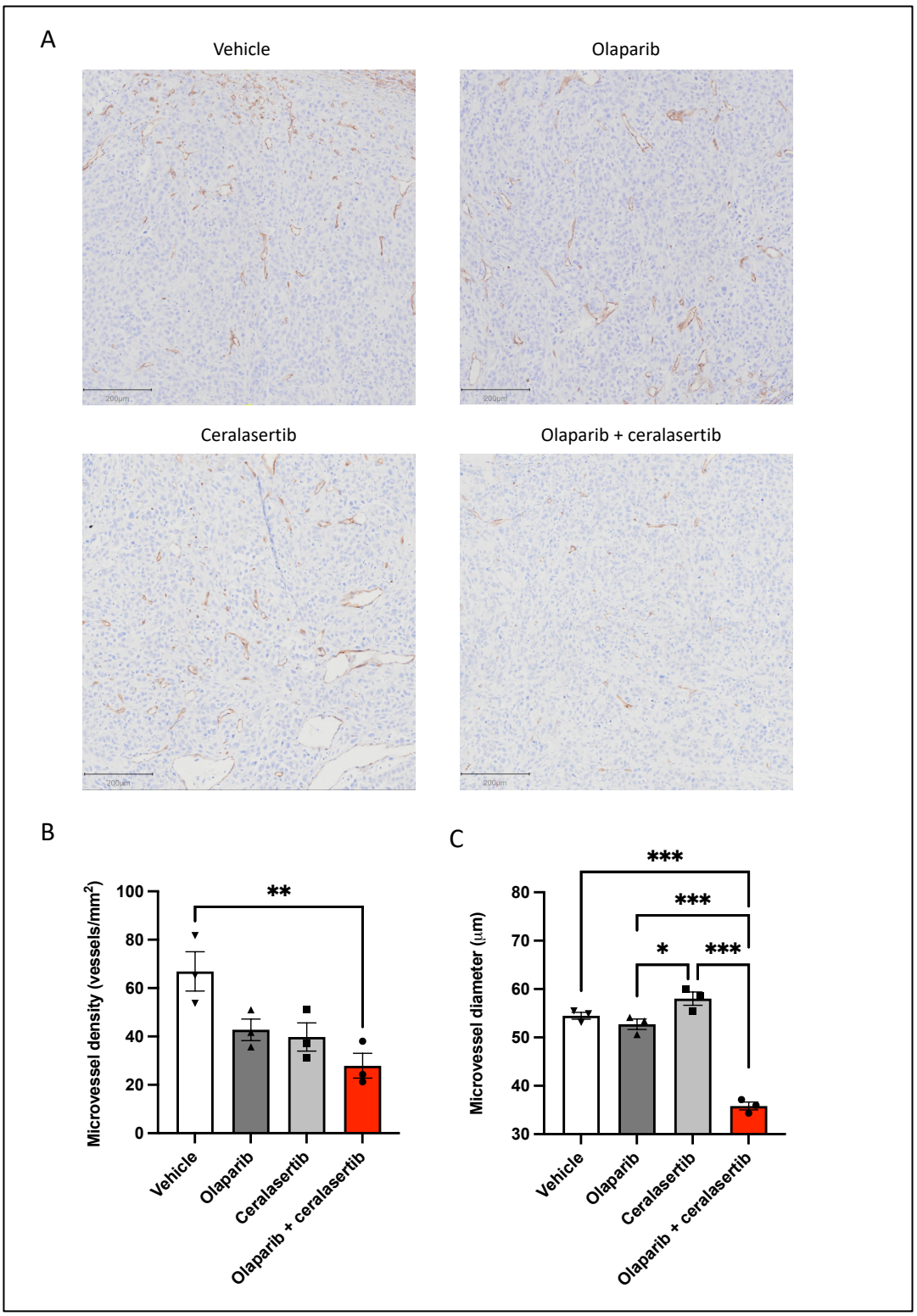

Figure 4.7: *Short term treatment with combined olaparib (100 mg/kg) and ceralasertib (25 mg/kg) results in a reduction in microvessel density and diameter within of PC-3 xenograft tumours at the Day 18 timepoint compared with those treated with vehicle or olaparib (100 mg/kg) or ceralasertib (25 mg/kg) monotherapy.* A: Representative sections at low power demonstrating vessel rich 'hot spots' containing CD34 stained microvessels. Scale bars 200 µm. B: Bar chart depicting the mean microvessel density of 'hot spots' within tumours of each treatment group, expressed as vessels per mm^2. C: Bar chart depicting the mean diameter of microvessels within the evaluated 'hot spot' regions of each treatment group. Tumour numbers displayed as symbols. Error bars represent Standard Error of the mean. Statistical comparisons at each time point conducted using one-way ANOVA with Tukey correction for multiple comparisons. ***: $P \leq 0.001$**: $P \leq 0.01$, *: $P \leq 0.05$.

4.3.2.3.3 Short term combination treatment with olaparib and ceralasertib results in a significant reduction in tumour cell proliferation and an increase in apoptosis

The microscopic appearance of a representative PC-3 xenograft tumour is shown in ***Figure 4.8A***. Tumours comprised predominantly of PC-3 cells in clusters or sheets, interspersed with stromal cells, vessels, immune cell infiltrate, as demonstrated at higher power in ***Figure 4.8B***. Independent of treatment, the centre of the tumours was often necrotic, particularly in those of larger size, as shown in ***Figure 4.8C***. This is a well described phenomenon in rapidly growing solid tumours and occurs as a result of insufficient vasculature in the centre with ensuing metabolic stress in the form of nutrient deprivation and hypoxia, ultimately leading to necrosis (Liu and Jiao, 2020). As a result, only non-necrotic areas towards the periphery of tumours that contained viable cell populations underwent full assessment via microscopy and IHC to ensure equivalence between treatment groups. Evaluation of H&E stained sections at both low and high power did not demonstrate a discernible change in cellular phenotype or tissue architecture between treatment groups, as determined by Dr Murali Varma, Consultant Urological Pathologist, University Hospital of Wales, Cardiff (***Figure 4.9A***).

Prior to full characterisation, tumour sections were firstly stained for surface of intact human mitochondria to enable identification of the human cell populations as previously described. Following this, IHC staining was then performed to evaluate proliferation (PCNA) and apoptosis (CC-3) specifically within the human tumour cell population, as illustrated in ***Figure 4.9A-D***. In the vehicle group, 72.0% (+/- 2.60 SEM) of tumour cells demonstrated positivity for PCNA, indicating a large proportion of cells were actively proliferating at the D18 short term timepoint. This was consistent with the rapid tumour growth curves observed during the treatment period as shown in ***Figure 4.4A***, supporting the use of the PC-3 subcutaneous xenograft as a model of highly aggressive CRPC. Treatment with olaparib or ceralasertib alone did not result in a significant reduction in actively proliferating cells when compared with vehicle, with PCNA indices of 72.9% (+/- 5.61% SEM) and 64.2% (+/- 3.17% SEM) respectively. In contrast, treatment with both agents in combination resulted in a PCNA index of 42.3% (+/- 2.06% SEM), thereby representing a highly significant reduction in actively proliferating cells when compared with either vehicle or each agent alone (P=0.002, P=0.002 and P=0.012), corroborating the in vitro findings reported in Section 3.3.2.

In contrast to the high levels of PCNA positivity, only 0.77% (+/- 0.02% SEM) of cells in vehicle treated tumours exhibited positive CC-3 staining, thereby indicating a very low background level of apoptosis at the D18 timepoint. Treatment with olaparib alone led to a reduction in CC-3 index to 0.45% (+/- 0.12% SEM), although this failed to reach statistical significance when compared to vehicle. On the contrary, treatment with ceralasertib alone or in combination with olaparib resulted in an increase in

CC-3 indices to 0.94% (+/- 0.14% SEM) and 1.27% (+/- 0.09% SEM) respectively, with the latter reaching statistical significance when compared with both vehicle and olaparib alone (***Figure 4.9C***; P=0.039 and P=0.003).

To investigate the effects of each treatment on the formation of DNA DSBs, sections were also stained for γ-H2AX. Unlike the LN-NEPC-1 explant tumour cells, PC-3 xenograft tumour cells showed a marked reduction in the level of background γ-H2AX staining at the D18 timepoint, likely reflecting differences in tumour biology, growth conditions and tissue processing between ex vivo and in vivo models (e.g. the level of genomic instability between the models and the formalin fixation rate of whole tissues versus tissue slices). As such, cells expressing any level of γ-H2AX staining were deemed positive for the purposes of comparative analysis. In total, 21.2% (+/- 8.49% SEM) of vehicle treated tumour cells displayed γ-H2AX staining, compared with 20.2% (+/- 5.34% SEM) and 13.4% (+/- 5.06% SEM) in those treated with olaparib and ceralasertib respectively, with neither comparison reaching statistical significance. Whilst treatment with combined olaparib and ceralasertib was associated with an increase in γ-H2AX staining to 28.1% (+/- 2.64% SEM), this was variable between tumours and not statistically significant when compared with vehicle or either agent alone. However, given the apparent trend towards increased DNA damage with combination therapy, further analysis of additional tissue regions together with experiments utilising alternative means of quantifying DNA damage at a range of timepoints is needed to determine whether combined PARPi and ATRi results in higher levels of DSBs relative to monotherapy in this model.

Collectively these results suggest that the significant reduction in tumour growth observed during short term combined treatment with olaparib and ceralasertib is predominantly the result of reduced tumour cell proliferation. Whilst combination therapy does also appear to result in increased levels of apoptosis, the absolute numbers are low and unlikely to have had a significant impact on overall tumour growth. Furthermore, although not statistically significant, combination therapy also appeared to result in a trend towards increased levels of DNA damage as measured using the surrogate DSB maker γ-H2AX, corroborating the findings seen both in vitro (***Figure 3.10***) and ex vivo (***Figure 4.1***). However, given that ceralasertib was only given in combination with olaparib for the first 7 days of the treatment cycle and the analysed tissue harvested after a further 11 days of olaparib monotherapy, it is possible that the cytotoxic effects of combination therapy may have occurred earlier in the cycle and may have been missed by IHC characterisation at the D18 timepoint. Alternatively, other factors unique to this in vivo model may have provided protection, such as a

relative reduction in hypoxia and nutrient depletion as a consequence of continual blood flow to tumour tissue.

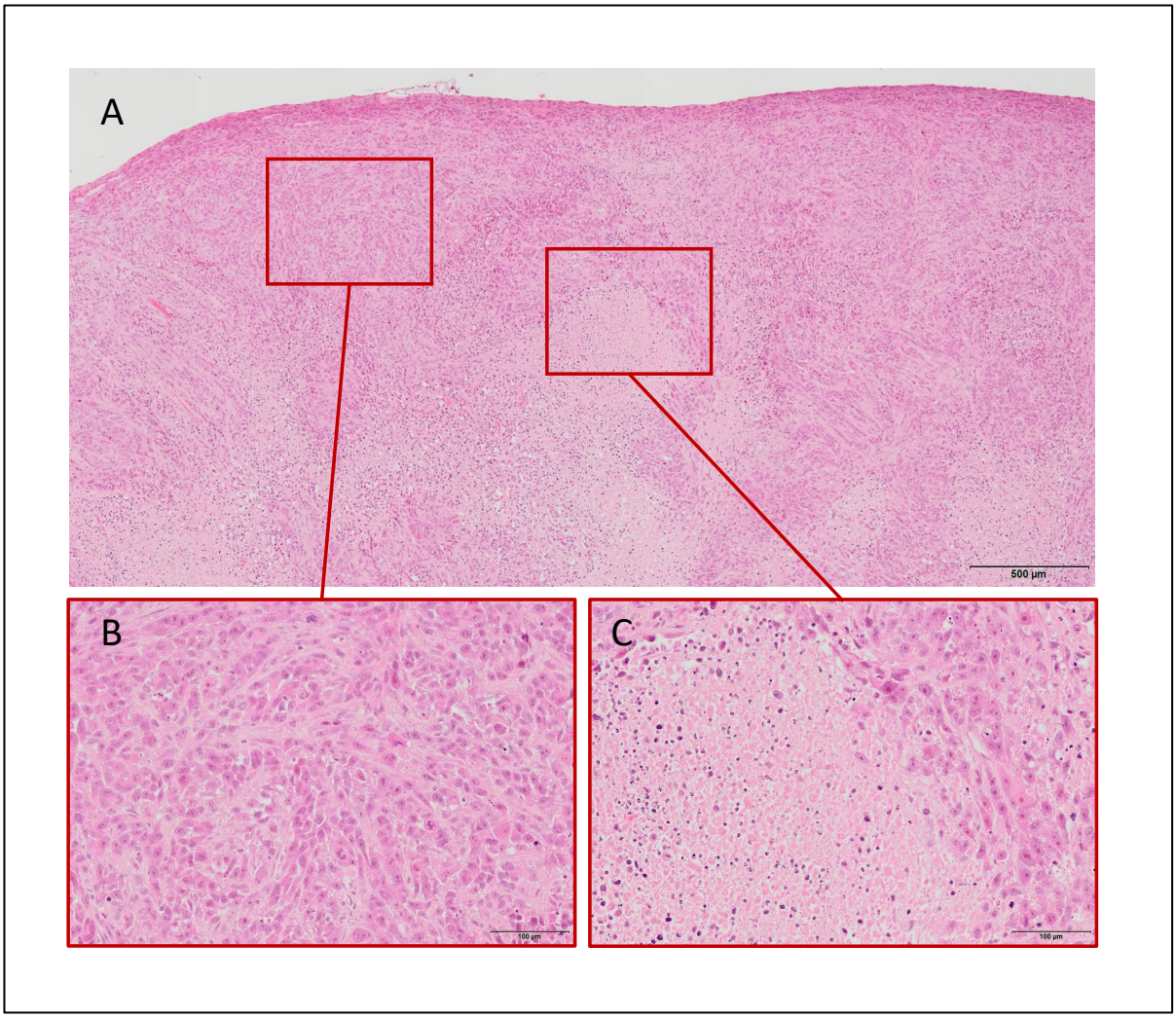

Figure 4.8: *PC-3 xenograft tumours comprise of PC-3 prostate cancer cells in clusters or sheets, interspersed with stromal cells, vessels and immune cell infiltrate, with central areas of necrosis.* Representative H&E stained section of a vehicle treated PC-3 xenograft tumour to demonstrate its microscopic architecture. A: Section at low power. B: Example of sheets of PC-3 tumour cells at higher power. C: Example central area of necrosis with immune cells and cellular debris at higher power. Scale bars represent 500 and 100 µm respectively.

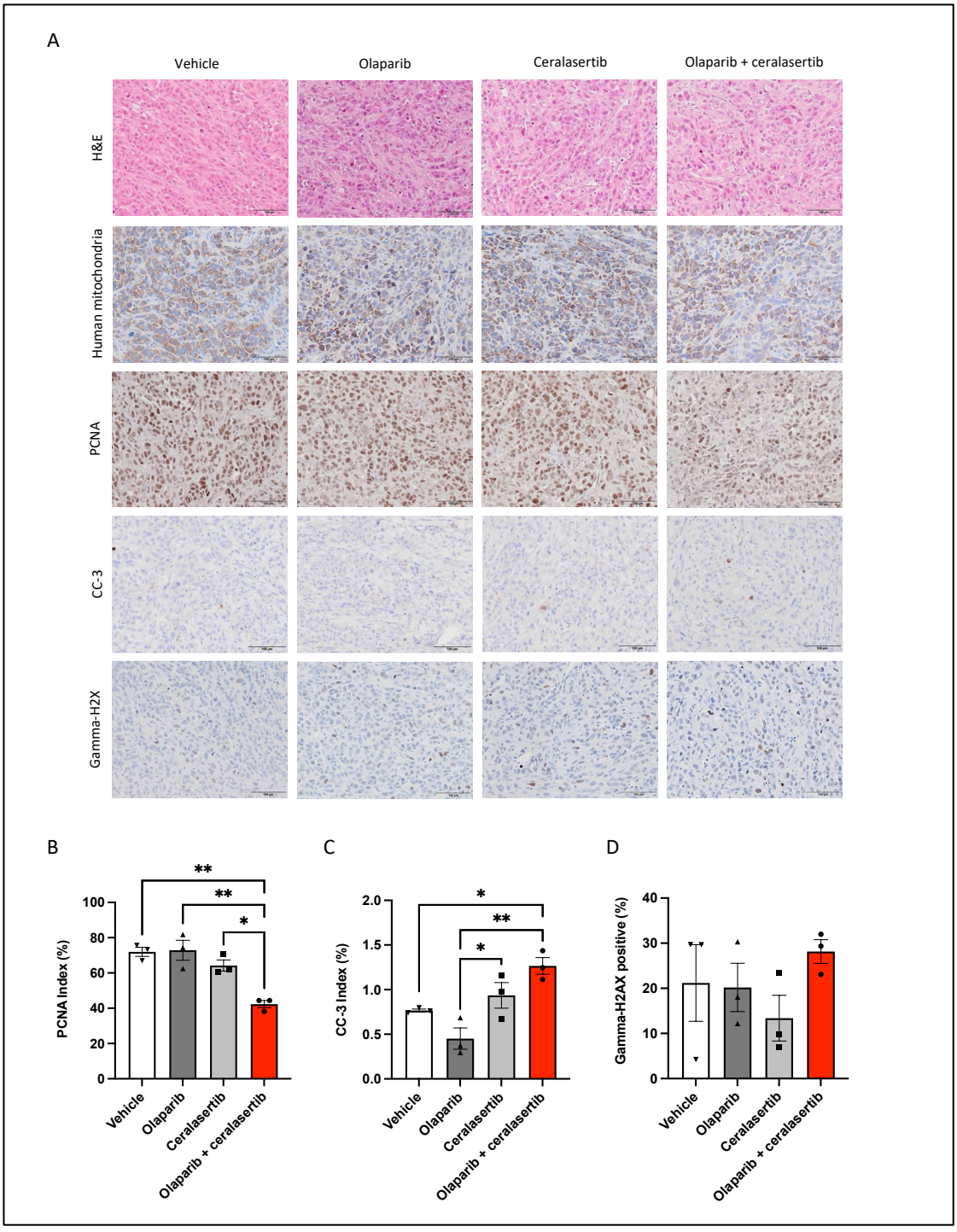

Figure 4.9: *Short term treatment with combined olaparib (100 mg/kg) and ceralasertib (25 mg/kg) results in a significant reduction in actively proliferating PCNA positive cells and an increase in apoptotic CC-3 positive cells at the D18 timepoint compared with those treated with vehicle or olaparib (100 mg/kg) or ceralasertib (25 mg/kg) monotherapy.* A: Representative H&E and IHC images of tumour cells stained for human mitochondria, PCNA, CC-3 and γH2AX at x20 magnification. Scale bars represent 100 µm. B: Bar chart demonstrating quantitation for PCNA within the tumour cell population (expressed as the proportion of cells positive for PCNA; PCNA index). C: Bar chart demonstrating quantitation for CC-3 within the tumour cell population (expressed as the proportion of cells positive for CC-3; CC-3 index). D: Bar chart demonstrating the percentage of cells demonstrating γ-H2AX expression within the tumour cell population. Tumour numbers displayed as symbols. Error bars represent Standard Error of the mean. Statistical comparisons conducted using one-way ANOVA with Tukey correction for multiple comparisons. **: $P \leq 0.01$, *: $P \leq 0.05$.

4.3.2.3.4 Olaparib monotherapy results in a significant increase in CHK1 phosphorylation that is overcome by co-administration of ceralasertib

Given the previous observation that ATR-CHK1 signalling is upregulated in CRPC cell lines following treatment with olaparib (Section 3.3.1.4, ***Figure 3.5***), protein from PC-3 xenograft tumour tissue harvested at the D18 timepoint was also evaluated via WB to assess whether this effect was conserved in vivo. ***Figure 4.10*** demonstrates representative blots for total ATR, p-ATR, total CHK1 and p-CHK1. Whilst total ATR concentration increased in those tumours treated with either olaparib or ceralasertib alone and in combination compared with vehicle treated controls, these differences did not reach statistical significance when assessed via densitometry. Similarly, although treatment with ceralasertib did result in a decrease in p-ATR concentration, a similar reduction was also observed with olaparib monotherapy and again the differences did not prove statistically significant. However, as discussed previously, it is again possible that this may be an underestimation of ATR activation as only an antibody specific for p-ATR at serine-428 was used in the WB analysis. Further IHC using antibodies specific for ATR that has been phosphorylated at alternative sites are therefore necessary to fully assess the effect of combined PAPR and ATR inhibition on ATR phosphorylation and hence activation in PC-3 xenograft tumours.

On the contrary, treatment with olaparib either alone or in combination with ceralasertib resulted in a highly significant increase in total CHK1 concentration when compared with vehicle or ceralasertib monotherapy (12.2 and 14.1 fold increases versus 1.0 and 2.1 fold respectively, $P<0.001$ for all comparisons). Furthermore, treatment with olaparib alone resulted in an increase in p-CHK1 concentration when compared with vehicle or ceralasertib monotherapy (3.6 fold versus 1.0 and 0.40 fold respectively), corroborating the findings observed in CRPC cell lines and demonstrating that PARPi results in increased CHK1 concertation and activation in vivo. The addition of ceralasertib was again found to overcome PARPi induced CHK1 activation, with relative p-CHK1 concentration falling to 0.49 of vehicle treated controls in tumours treated with combination therapy, a difference which proved statistically significant when compared with olaparib alone ($P=0.028$).

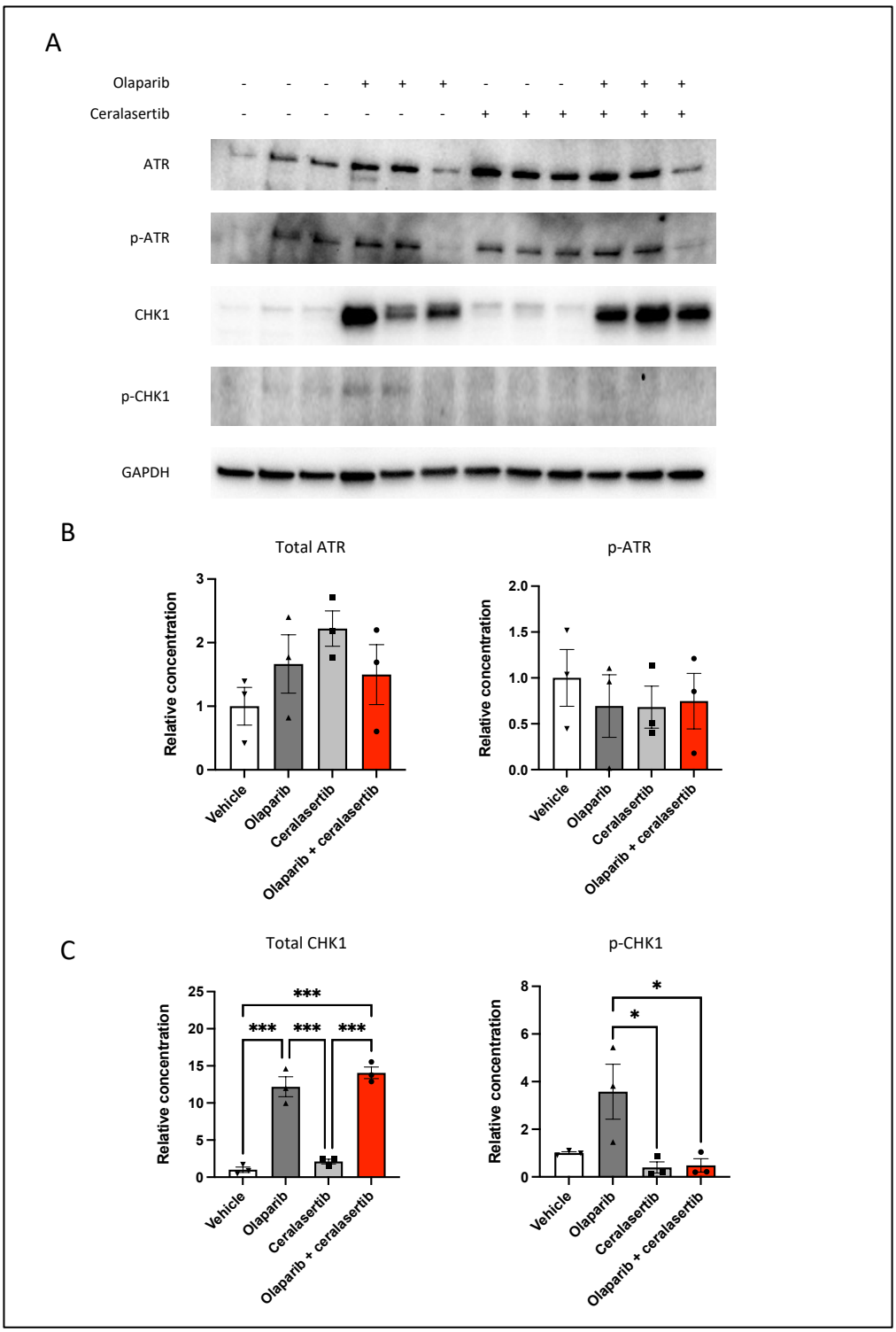

Figure 4.10: *Short term treatment with olaparib (100 mg/kg) results in a significant increase in total and phosphorylated CHK1 concentration in PC-3 subcutaneous xenograft tumours, the latter of which can be overcome through combination with ceralasertib (25 mg/kg).* A: Representative Western Blots demonstrating ATR, p-ATR, CHK1 and p-CHK1 expression in tumour tissue harvested at the 18 day timepoint (n=3 per treatment). B: Bar charts showing the concentration of total ATR and p-ATR relative to vehicle treated controls as assessed using densitometry (n=3 per treatment). C: Bar charts showing the concentration of total CHK1 and p-CHK1 relative to vehicle treated controls as assessed using densitometry (n=3 per treatment). Tumour numbers displayed as symbols. Error bars represent Standard Error of the mean. Statistical comparisons conducted using one-way ANOVA with Tukey correction for multiple comparisons. ***: $P \leq 0.001$, **: $P \leq 0.01$, *: $P \leq 0.05$.

4.3.2.4 Long term efficacy

4.3.2.4.1 Combination therapy with olaparib and ceralasertib results in increased long term survival when compared to monotherapy with either agent

To establish if combined PARPi and ATRi could extend survival, long term experimental cohorts were treated with either olaparib, ceralasertib or combined olaparib and ceralasertib for an intended additional treatment cycle of 21 days. However, tumours continued to progress rapidly such that the by D32, all mice except those in the combination therapy treatment group required termination on account of approaching predefined ethical limits. Consequently, the long term timepoint was revised to 32 days. Noticeably, 66.7% of the combination treatment cohort survived to the D32 endpoint, whereas none of the monotherapy cohort mice reached D32, as mice that approached ethical limits were terminated early (***Figure 4.11A***). For those mice treated with olaparib or ceralasertib alone the median survival was 27 and 26 days respectively. Of those that received olaparib alone, half were terminated on account of tumour ulceration and weight loss respectively, whilst all of those treated with ceralasertib alone were terminated on account of tumour ulceration (***Figure 4.11B***). In contrast, only one mouse in the combination therapy group was terminated prior to the D32 endpoint, which was on the basis of tumour ulceration. Interestingly there was no apparent correlation between tumour size and the development of ulceration, with smaller tumours ulcerating as frequently as larger tumours, suggesting factors other than size alone to be responsible.

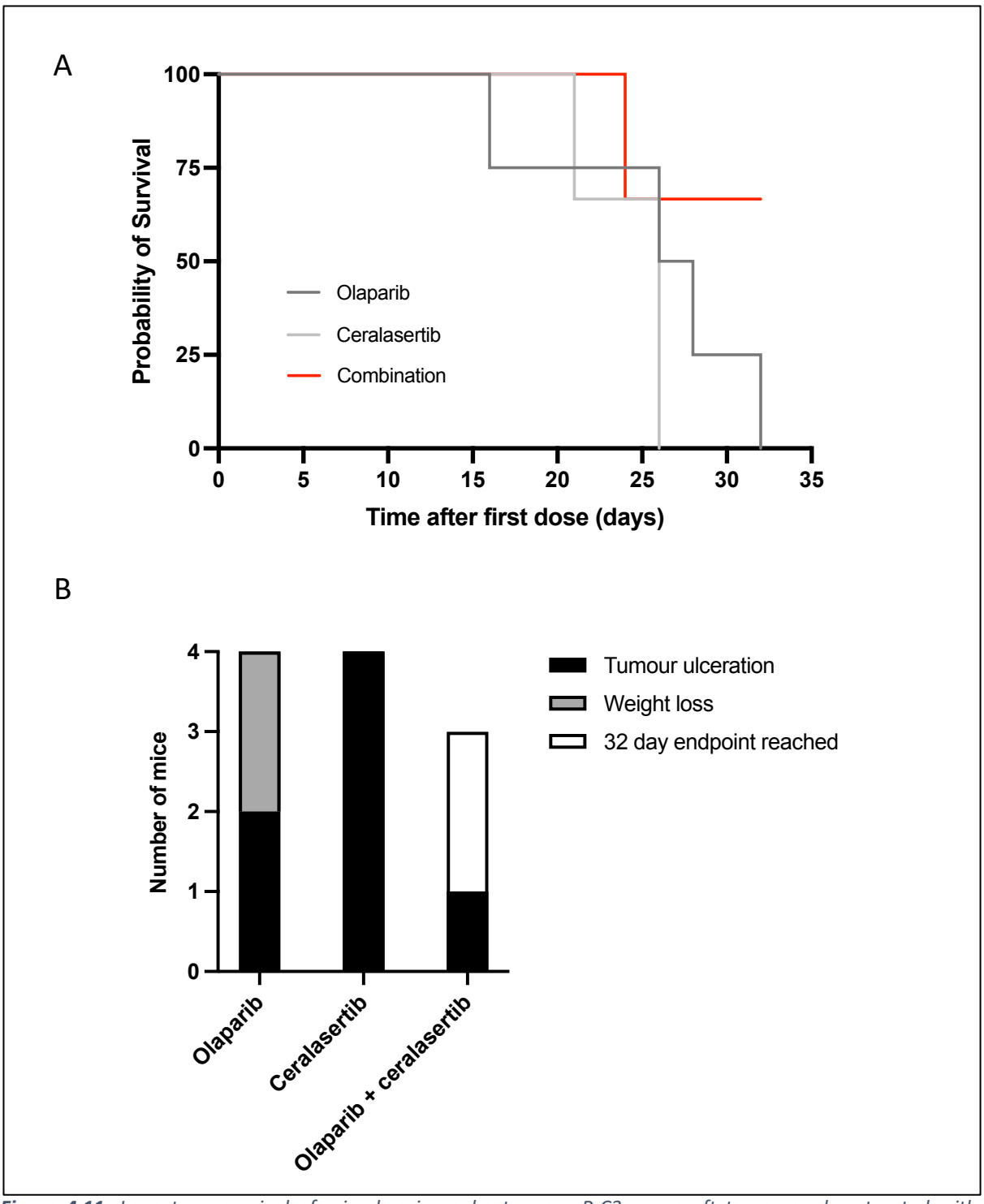

Figure 4.11: *Long term survival of mice bearing subcutaneous P-C3 xenograft tumours when treated with olaparib (100 mg/kg) and ceralasertib (25 mg/kg), alone and in combination.* A: Kaplan-Meier survival curve demonstrating overall survival as stratified by treatment received up to the 32 day long term timepoint. Olaparib (n=4 mice), ceralasertib (n=3 mice) and combined olaparib and ceralasertib (n=3 mice). B: Bar chart demonstrating the indications for termination of the mice in the long term treatment cohorts, including those surviving to the 32 day timepoint.

4.3.2.4.2 Extended treatment with olaparib and ceralasertib in combination reduces tumour growth compared with monotherapy

To establish if extended treatment with olaparib and ceralasertib provides additional tumour growth control compared with monotherapy, tumour volumes of those in the long term treatment cohorts were measured on the Monday, Wednesday and Friday of each treatment week between the D18 short term timepoint and D32 day long term timepoint. ***Figure 4.12*** shows the individual tumour growth curves for all tumours treated with olaparib (B; n=13), ceralasertib (C; n=16) and combined olaparib and ceralasertib (D; n=12), irrespective of initial starting volume, including those in the D18 short term cohorts. Due to the growth dynamics of vehicle treated tumours, this group could not be aged beyond the D18 short term timepoint on account of tumour size surpassing ethical limits, hence a long term vehicle cohort could not be included for comparison.

Those tumours treated with a second cycle of either olaparib or ceralasertib alone beyond the D18 short term timepoint continued to increase in volume until the host mouse required termination (***Figure 4.12A*** and ***Figure 4.12B***). In contrast, all tumours that received a second cycle of combined olaparib and ceralasertib demonstrated either regression or slowing of growth shortly after the reintroduction of ceralasertib at 21 days. This partial restoration of tumour growth control lasted for approximately the duration of olaparib and ceralasertib co-administration, after which some of the tumours once again began to increase in volume (***Figure 4.12C***). Whilst the exact reason for this phenomenon remains to be elucidated, the acceleration of growth again appears to occur once ceralasertib has been withdrawn, potentially reflecting the known insensitivity of PC-3 cells to olaparib monotherapy.

When the tumour growth curves are appreciated throughout the 32 day study period it appears that the maximal benefit of combined olaparib and ceralasertib is observed in the first two weeks of a treatment cycle, corresponding to one week of olaparib and ceralasertib co-administration followed by one week of olaparib monotherapy. Together with the observation that a second cycle of combination therapy is able to partially restore tumour growth control it can be postulated that a two weekly treatment cycle may provide more optimal long term efficacy than the three week cycle examined in this preclinical trial. Further studies are therefore necessary to evaluate this approach, paying close attention to the risk of increased toxicity with increased frequency of dosing with ceralasertib.

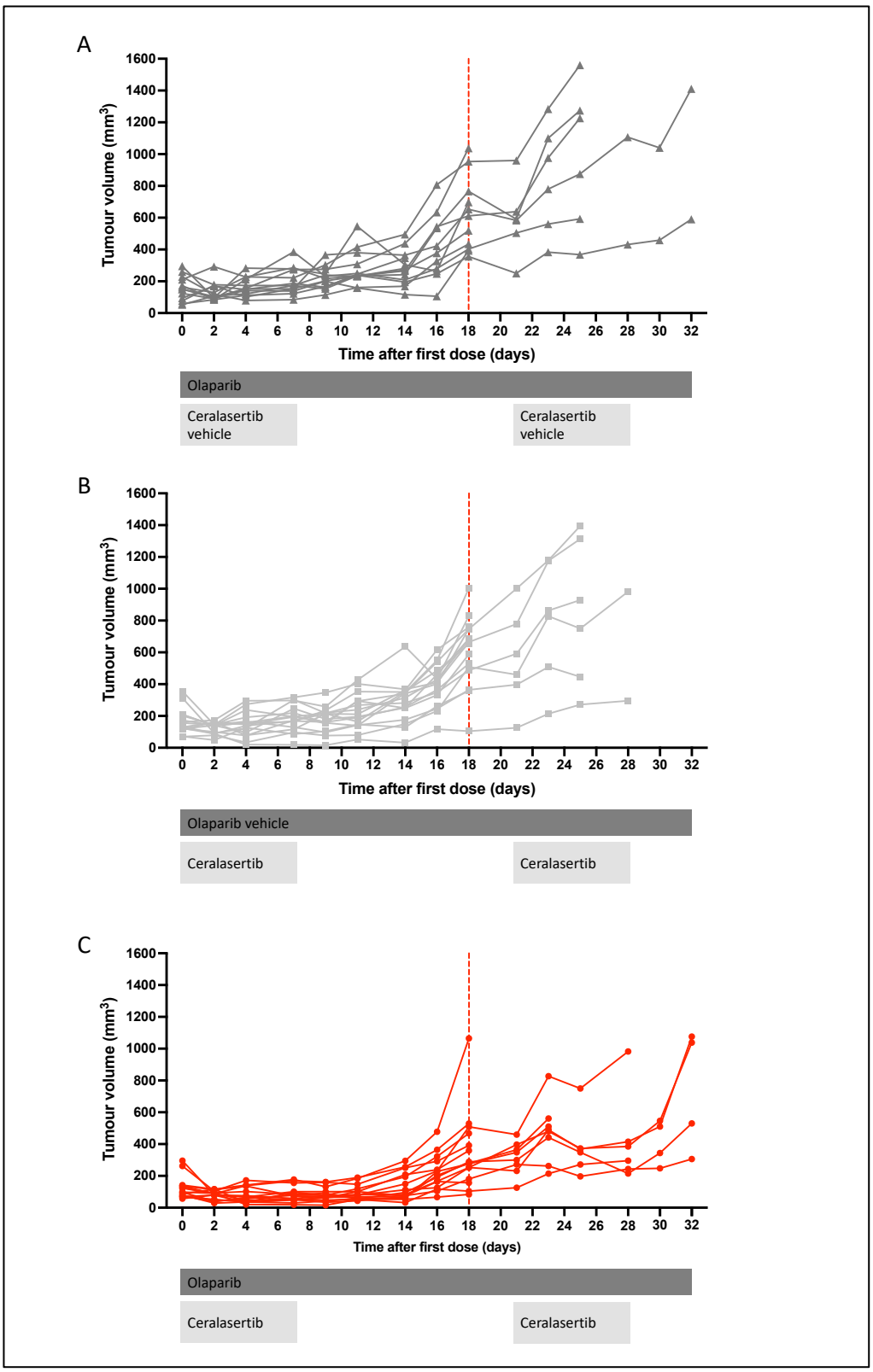

Figure 4.12: *Long term treatment with combined olaparib (100 mg/kg) and ceralasertib (25 mg/kg) reduces growth of PC-3 subcutaneous xenograft tumours beyond the D18 short term time point compared with olaparib (100 mg/kg) and ceralasertib (25 mg/kg) monotherapy.* A: Growth curves of individual tumours treated with olaparib (n=13). B: Growth curves of individual tumours treated with ceralasertib (n=16). C: Growth curves of individual tumours treated with combined olaparib and ceralasertib (n=12). Duration of each treatment indicated below X axis. Dotted red line indicates the D18 short term timepoint at which point the short term cohort mice were terminated.

4.3.2.4.3 Long term treatment with olaparib and ceralasertib in combination results in a significant reduction in macroscopic neovascularisation and pathological lymphadenopathy compared with either agent alone

Finally, differences in therapeutic effect between treatment arms were assessed with respect to the secondary outcomes of tumour weight, macroscopic neovascularisation, local tumour invasion and lymphadenopathy in those mice treated beyond the D18 short term timepoint, as illustrated in ***Figure 4.13A-D***. Tumours treated with olaparib alone had a mean endpoint weight of 1584 mg (+/- 265.6 mg SEM, n =6) whilst treatment with ceralasertib alone resulted in a significant reduction, with a mean endpoint weight of 842.4 mg (+/- 180.1 mg SEM, n =8 ; P=0.034). Those tumours treated with combined olaparib and ceralasertib had the lowest mean endpoint weight of 486.0 mg (+/- 95.19 mg SEM, n=6), with differences proving statistically significant when compared with olaparib monotherapy (P=0.004) but not ceralasertib monotherapy (P=0.400). However, given that several mice in the ceralasertib monotherapy group were terminated prior to the D32 timepoint, tumour weight differences between treatments may have been more apparent if all mice were terminated at the same timepoint.

Further analysis revealed that combination therapy led to a significant reduction in pathological lymphadenopathy, local invasion and macroscopic neovascularisation at end point, with no tumours demonstrating evidence of large feeding vessels at the time of dissection. This finding is consistent with the observation at the D18 short term timepoint, with tumours again appearing macroscopically paler and more translucent as shown in ***Figure 4.14***. Collectively these data indicate that as well as resulting in reduced tumour growth and increased survival, combined olaparib and ceralasertib leads to other favourable tumour outcomes that may prove to be efficacious in the clinical setting.

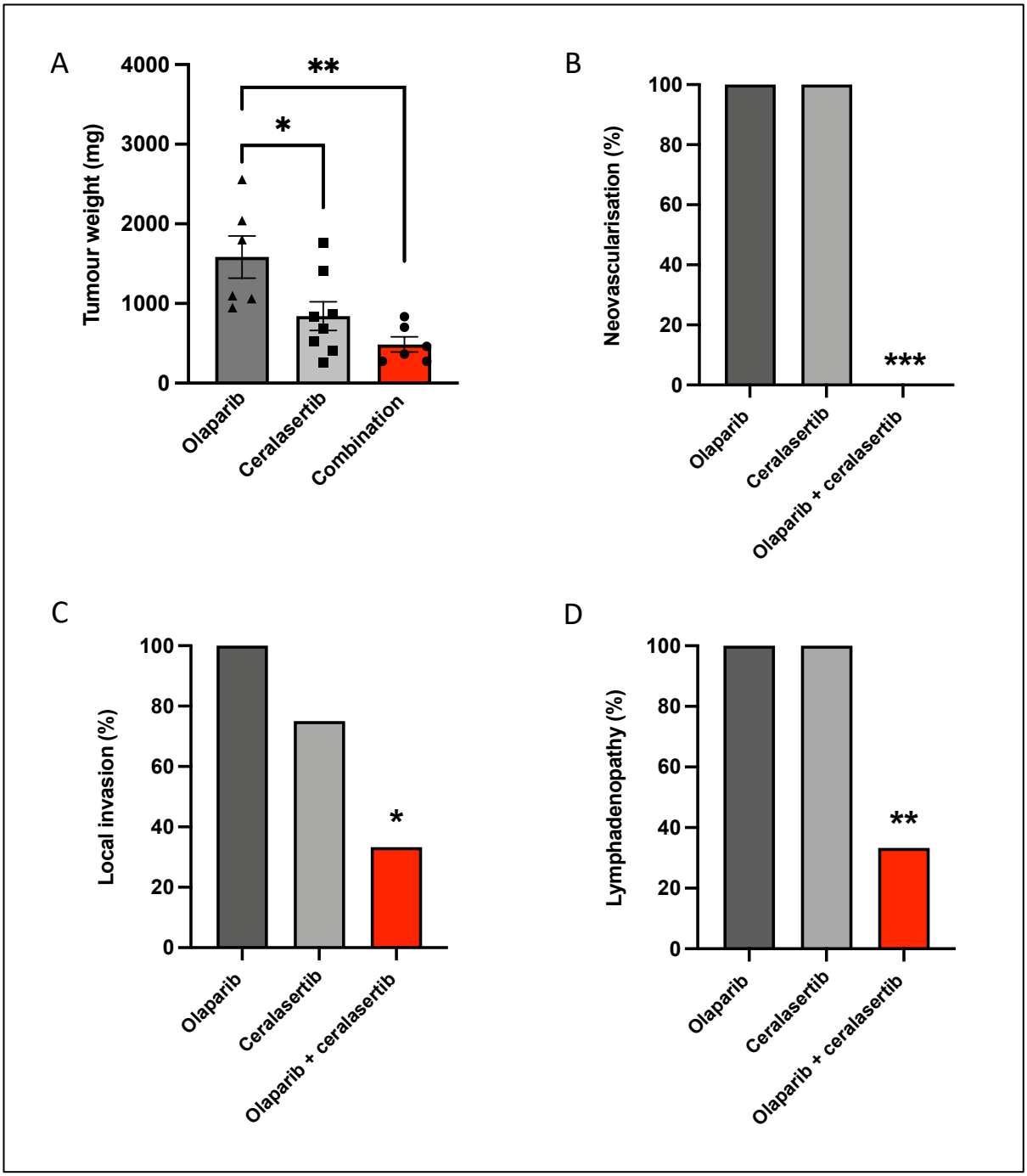

Figure 4.13: *Long term treatment with combined olaparib (100 mg/kg) and ceralasertib (25 mg/kg) reduces weight, macroscopic neovascularisation and the presence of pathological lymphadenopathy of PC-3 subcutaneous xenograft tumours compared with olaparib (100 mg/kg) and ceralasertib (25 mg/kg) monotherapy.* A: Tumour weight at the time of dissection according to treatment group. Tumour numbers displayed as symbols. Error bars represent Standard Error of the mean. Statistical comparisons conducted using one-way ANOVA with Tukey correction for multiple comparisons. **: $P \leq 0.01$, *: $P \leq 0.05$. B: percentage of tumours demonstrating macroscopic neovascularisation at the time of dissection. C: percentage of tumours demonstrating local invasion at the time of dissection. D: percentage of mice with evidence of pathological lymphadenopathy at the time of dissection. Two tumours in the olaparib group excluded due to termination of the mouse at D15. Olaparib monotherapy (n=6 tumours), ceralasertib monotherapy (n=8 tumours), combined olaparib and ceralasertib (n=6 tumours). Statistical comparisons conducted using the Chi-squared test. ***: $P \leq 0.001$, **: $P \leq 0.01$, *: $P \leq 0.05$.

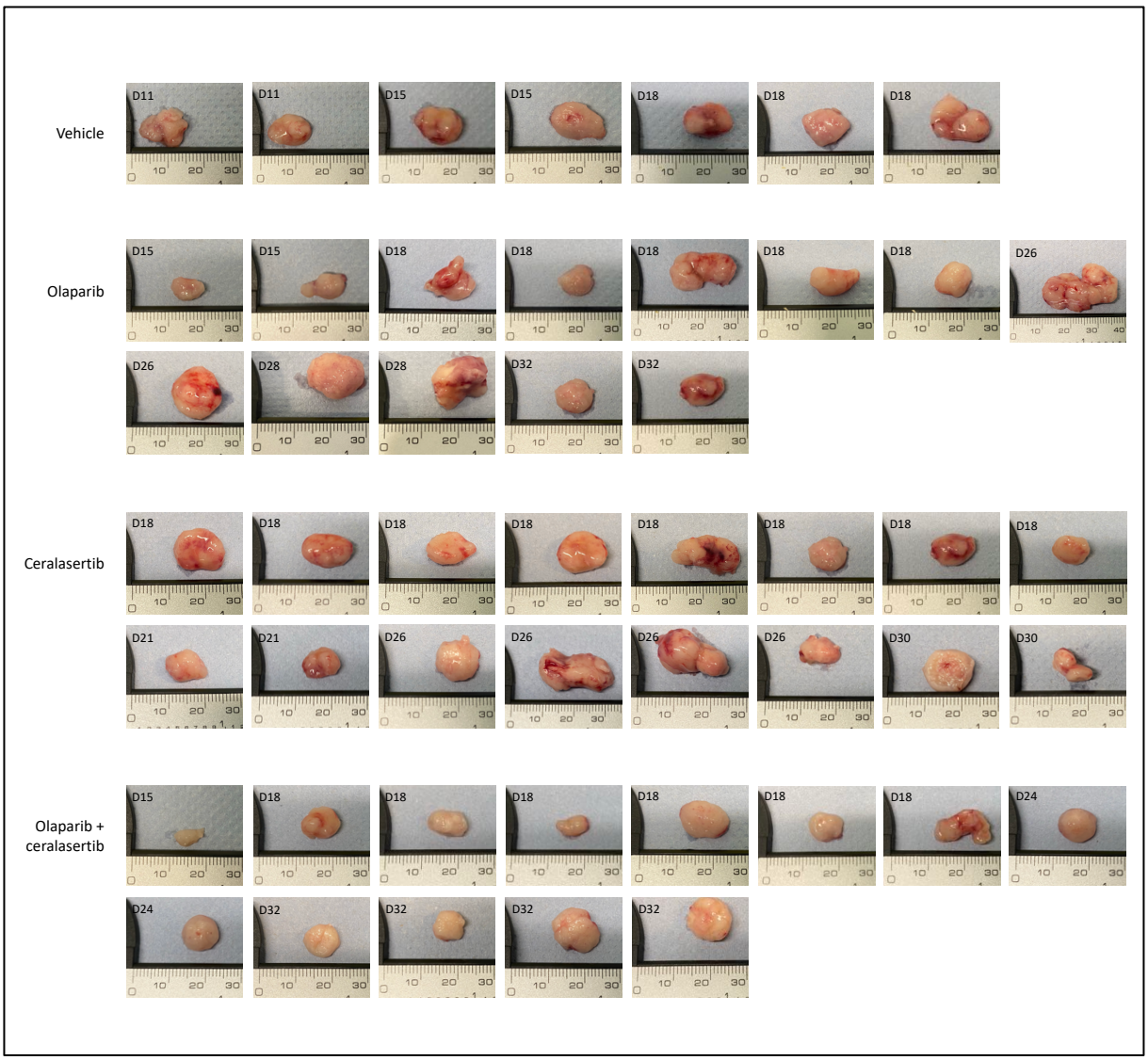

Figure 4.14: *Treatment with combined olaparib (100 mg/kg) and ceralasertib (25 mg/kg) results in a globally paler appearance of PC-3 xenograft tumours compared with those treated with vehicle or olaparib (100 mg/kg) or ceralasertib (25 mg/kg) monotherapy.* Macroscopic appearance of all tumours in each treatment group immediately after dissection. Those treated with combined olaparib and ceralasertib were paler, with fewer visible surface blood vessels. Number of days following first treatment denoted in the upper left corner of each image.

4.3.2.4.4 Phosphoproteomic approach to establish the mechanisms underpinning the enhanced efficacy of combined PARP and ATR inhibition in the PC-3 subcutaneous xenograft model of CRPC

As demonstrated, combined PARPi and ATRi resulted in improved short and long term outcomes compared with either agent alone in the PC-3 subcutaneous xenograft model. Whilst conventional methods have enabled insight into the biological mechanisms underpinning these results, the exact reason for the significant reduction in tumour cell proliferation remains unclear. As such a phosphoproteomic approach was utilised to evaluate key pathway alterations in response to each treatment alone and in combination compared with vehicle treated controls at the D18 timepoint. An overview of this approach is given in Section 2.1.6.3. In brief, sections of PC-3 xenograft tumours were taken immediately after termination of the host animal at the D18 timepoint and snap frozen in liquid nitrogen before being stored at -80 °C. Tissue from three mice in each treatment group were subsequently lysed and samples containing 100 μg of protein were transported on dry ice to the University of Bristol Proteomics Facility where the total and phosphoprotein concentrations in each sample were quantified using standard methods. Raw data files were processed and quantified using Proteome Discoverer software v2.4 (Thermo Fisher Scientific, Hampton, USA) and searched against the UniProt Human and Mouse databases, with further analysis restricted to those proteins with human signatures to reflect events specifically within the human PC-3 tumour cells. In collaboration with Dr Kate Heesom and Dr Phil Lewis (University of Bristol Phosphoproteomics Facility), bioinformatic analysis was then performed using Qiagen Ingenuity Pathway Analysis software (IPA; Qiagen, Hilden, Germany).

Prior to proceeding to full analysis, the total protein distribution of each sample was plotted as a heat map to evaluate overall concentration, along with hierarchical clustering to assess for similarity between samples of the same treatment group. This identified that one of the samples in the olaparib group contained significantly greater protein concentrations than all others, despite having undergone formal quantification following the extraction process. The exact reasons for this are unknown but may include contamination of the sample with non-homogenised tissue, or degradation during transport. To avoid skewing of the combined data this sample was therefore considered an outlier and excluded from further analysis. The full heatmap and associated dendrogram of the remaining samples is demonstrated in ***Figure 4.15***. Whilst there is some clustering of samples from the same treatment groups, there appeared to be heterogeneity between individual samples. The reasons for this variation are unclear but again it may have been due to contamination of the sample with non-homogenised tissue, or degradation during transport. Alternatively, some variation may

have arisen due to individual tumour sections being taken from different regions of the parent tumour, perhaps leading to contamination with proteins from central necrotic tissue.

To further evaluate similarities between treatment groups at a proteome level, principal component analysis (PCA) was performed. This is a method of reducing multidimensional protein and phosphoprotein expression data to a smaller number of groups that can be more readily visualised and patterns assessed. The PCA plots for total and phosphoprotein concentration are shown in ***Figure 4.16*** and reveal that 39.4% and 58.6% of the variance in concentration can be explained by the first principal component respectively. Total protein PCA analysis demonstrated some clustering of both ceralasertib (termed AZD6738 on the plots) and combination groups, although the proteomic profiles of those tumours treated with vehicle and olaparib appeared to differ significantly between samples. A similar pattern was seen for phosphoprotein PCA, with clustering of ceralasertib and combination treated samples. Collectively these indicate that treatment with either ceralasertib and combined olaparib and ceralasertib led to fairly consistent changes in the proteome and phosphoproteome, whilst there was much greater inconsistency resulting from treatment with vehicle or olaparib.

Having identified significant variation between samples, together with the apparent lack of clustering in some treatment groups and exclusion of one sample from the olaparib group, full phosphoproteomic analysis was not undertaken as originally planned. A subsequent repeat experiment involving a larger number of protein samples taken from the same tumour regions in each treatment group is therefore necessary in order to fully and accurately interrogate the effects of each agent on total and phosphoprotein concentrations so as to elucidate the key cell signalling pathways underpinning the observed treatment responses in the preclinical trial.

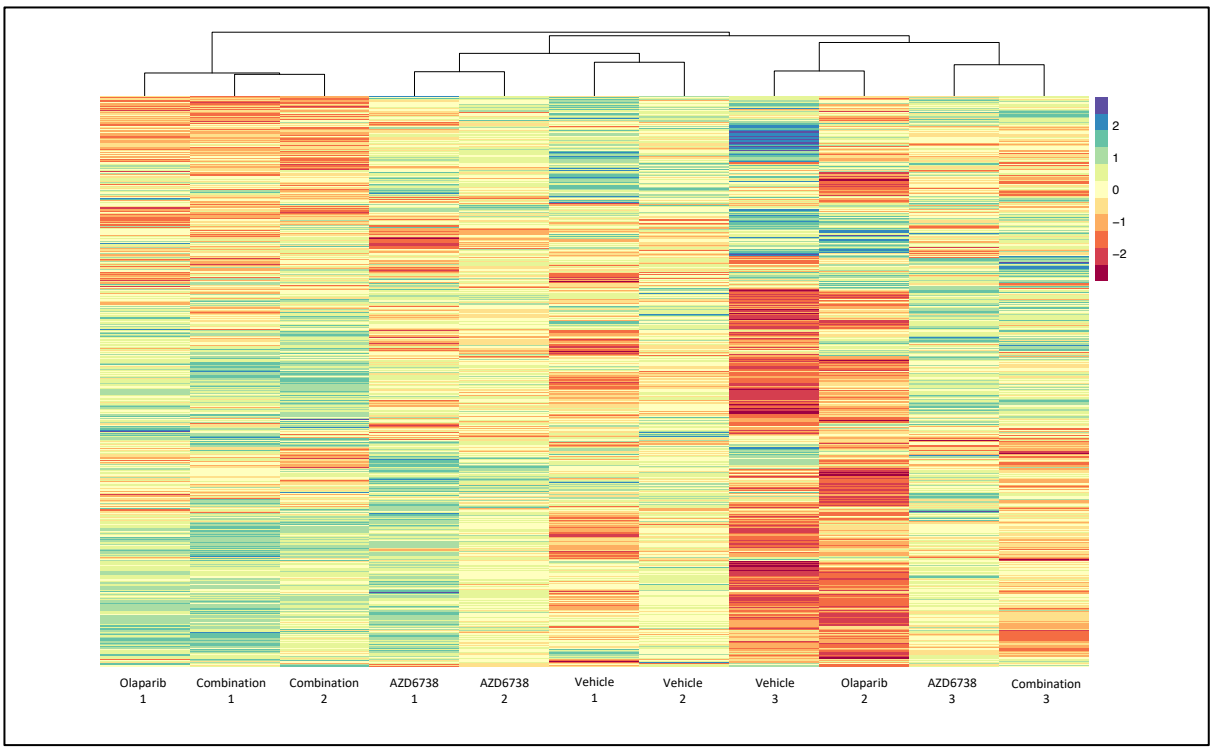

Figure 4.15: *Heatmap and dendrogram depicting the differential expression of proteins for each of the samples included in the full phosphoproteomic analysis, together with hierarchical clustering.* AZD6738; alternative name for ceralasertib.

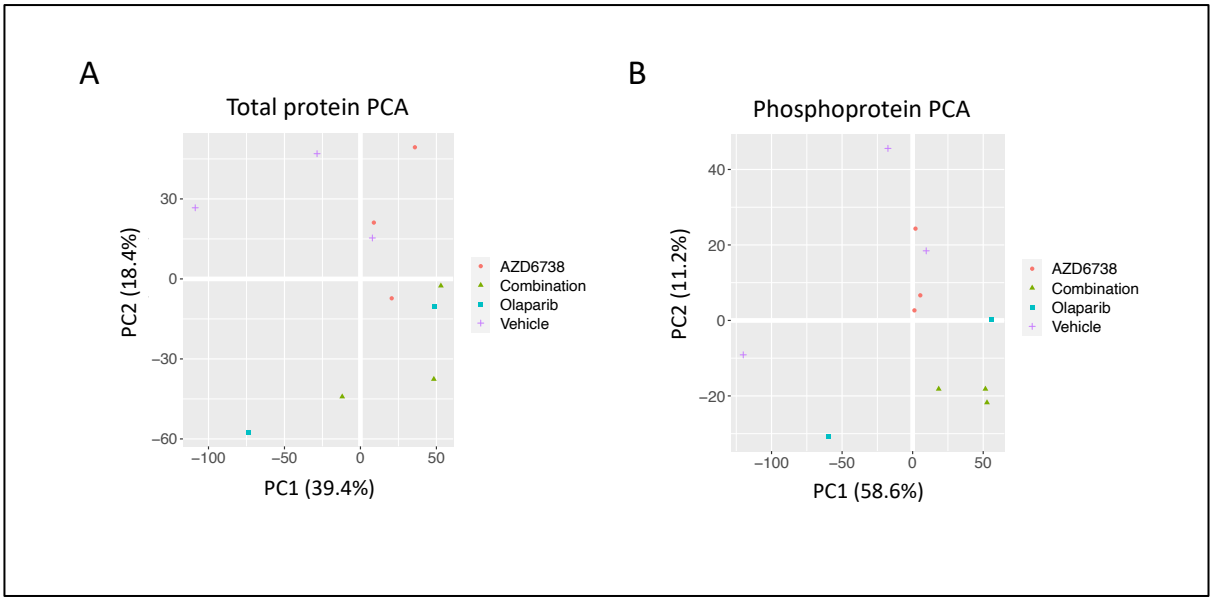

Figure 4.16: *Principal component analysis (PCA) plots demonstrating clustering of the proteome and phosphoproteome of tumours treated with ceralasertib (AZD6738) or combined olaparib and ceralasertib, but not in those treated with olaparib or vehicle.* A: Total protein PCA. B: Phosphoprotein PCA. Each point represents an individual tumour sample. AZD6738; alternative name for ceralasertib.

4.3.3 Combined PARP and ATR inhibition is well tolerated and results in positive disease outcomes in a preclinical trial using an immunocompetent GEMM of localised prostate cancer

4.3.3.1 Model characteristics and experimental cohort demographics

Having identified that combined PARPi and ATRi results in favourable outcomes in the PC-3 xenograft model of CRPC, the next step was to assess whether similar efficacy was observed in the setting of localised prostate cancer. The *PSA-Cre-ER$^{T2(+/-)}$; p53$^{fl/fl}$; Pten$^{fl/fl}$* model was chosen for the reasons outlined in Section 4.1. This model enables conditional depletion of *Trp53* and *Pten* tumour suppressor genes specifically within the prostatic epithelial cells, in part to recapitulate the PTEN and p53 loss of function in PC-3 cells and also to mirror clinical advanced prostate cancer in which co-alterations in both *PTEN* and *TP53* are common (Hamid et al., 2019). Furthermore, unlike the athymic nude mice used for the PC-3 subcutaneous xenograft model, the C57BL/6 mice used for the generation of the model retain immune system function, therefore enabling study of drug efficacy within the immunocompetent setting.

Given that the *PSA-Cre-ER$^{T2(+/-)}$; p53$^{fl/fl}$; Pten$^{fl/fl}$* model has not been extensively described in the literature it was important to firstly establish its histological characteristics prior to undertaking the full study. Given the recombination ability of PSA-Cre-ER^{T2} within each of the murine prostate lobes has been previously reported (Ratnacaram et al., 2008) and was again confirmed during the experiments outlined in Section 5.3.1, it was not repeated here. Three male mice with the *PSA-Cre-ER$^{T2(+/-)}$; p53$^{fl/fl}$; Pten$^{fl/fl}$* genotype underwent tamoxifen induction at eight weeks of age as described in Section 2.3.2.6. These mice were then terminated at 182 days following induction, their prostates fixed in formalin and H&E stained sections evaluated histologically. In contrast to the large, locally advanced tumours observed in mice with the *PB-Cre4 p53$^{fl/fl}$; Pten$^{fl/fl}$* genotype (Chen et al., 2005), *PSA-Cre-ER$^{T2(+/-)}$; p53$^{fl/fl}$; Pten$^{fl/fl}$* mice developed smaller tumours, predominantly involving the ventral lobes, as demonstrated in ***Figure 4.17***. This difference in phenotype is likely the result of the higher specificity and lower recombination efficiency of *PSA-Cre-ER^{T2}*, which is only expressed in prostatic epithelial cells, with the highest recombination efficiency in the luminal cells of the dorsolateral lobe (approximately 35%) (Ratnacaram et al., 2008). In contrast, PB-Cre4 is expressed in both luminal and basal epithelial cells, as well stromal cells and the gonads, and has a recombination efficiency of >95%, 50%, 10% and 5% in the lateral, ventral, dorsal and anterior prostate lobes respectively (Wu et al., 2001). Furthermore, PB-Cre4 is active throughout adult male life whereas *PSA-Cre-ER^{T2}* activity only occurs following induction with tamoxifen.

Histologically the prostate tumours of *PSA-Cre-ER$^{T2(+/-)}$; p53$^{fl/fl}$; Pten$^{fl/fl}$* mice comprised of high grade prostatic intraepithelial neoplasia (HG-PIN), with focal areas of invasion through the basement membrane and into surrounding stroma, termed microinvasive carcinoma, with 100% incidence (n=3/3). This is in keeping with a previous description by Parisotto et al. in which *PSA-Cre-ER$^{T2(+/-)}$; p53$^{fl/fl}$; Pten$^{fl/fl}$* mice developed tumours with a significantly higher mitotic index and loss of tissue architecture at the same timepoint when compared with wild-type controls (Parisotto et al., 2018). Despite recombination taking place in the luminal epithelial cells of each lobe, the dorsal, lateral and anterior prostate lobes appeared essentially histologically normal (***Figure 4.17***).

In confirming that *PSA-Cre-ER$^{T2(+/-)}$; p53$^{fl/fl}$; Pten$^{fl/fl}$* mice develop localised tumours at the 6 months post-tamoxifen induction timepoint, this model was then utilised for the transgenic in vivo preclinical trial to determine the effects of treatment with vehicle, olaparib (100 mg/kg), ceralasertib (25 mg/kg) and combined olaparib (100 mg/kg) and ceralasertib (25 mg/kg) for a single 21 day cycle. As such, male mice with the *PSA-Cre-ER$^{T2(+/-)}$; p53$^{fl/fl}$; Pten$^{fl/fl}$* genotype were induced with tamoxifen after reaching sexual maturity at 56 days and aged a further 169 days before being randomised to one of the four treatment groups (n=3-5 per treatment arm) outlined in ***Table 4.3***. Overall mean starting weight was 31.88 g (range 28.41 g to 36.32 g), with no difference between individual treatment groups, as shown in ***Figure 4.18***. Mice were subsequently treated according to the dosing schedule outlined in Section 2.3.3.3. Outcomes were again pre-determined prior to commencing the study. Safety outcomes were overall mortality and percentage weight loss compared with starting weight, as measured on the Monday, Wednesday and Friday of each treatment week and at the study endpoint. Primary efficacy outcome was prostate weight (total and individual lobes) at the time of dissection, represented as both an overall weight in mg and relative weight in percent.

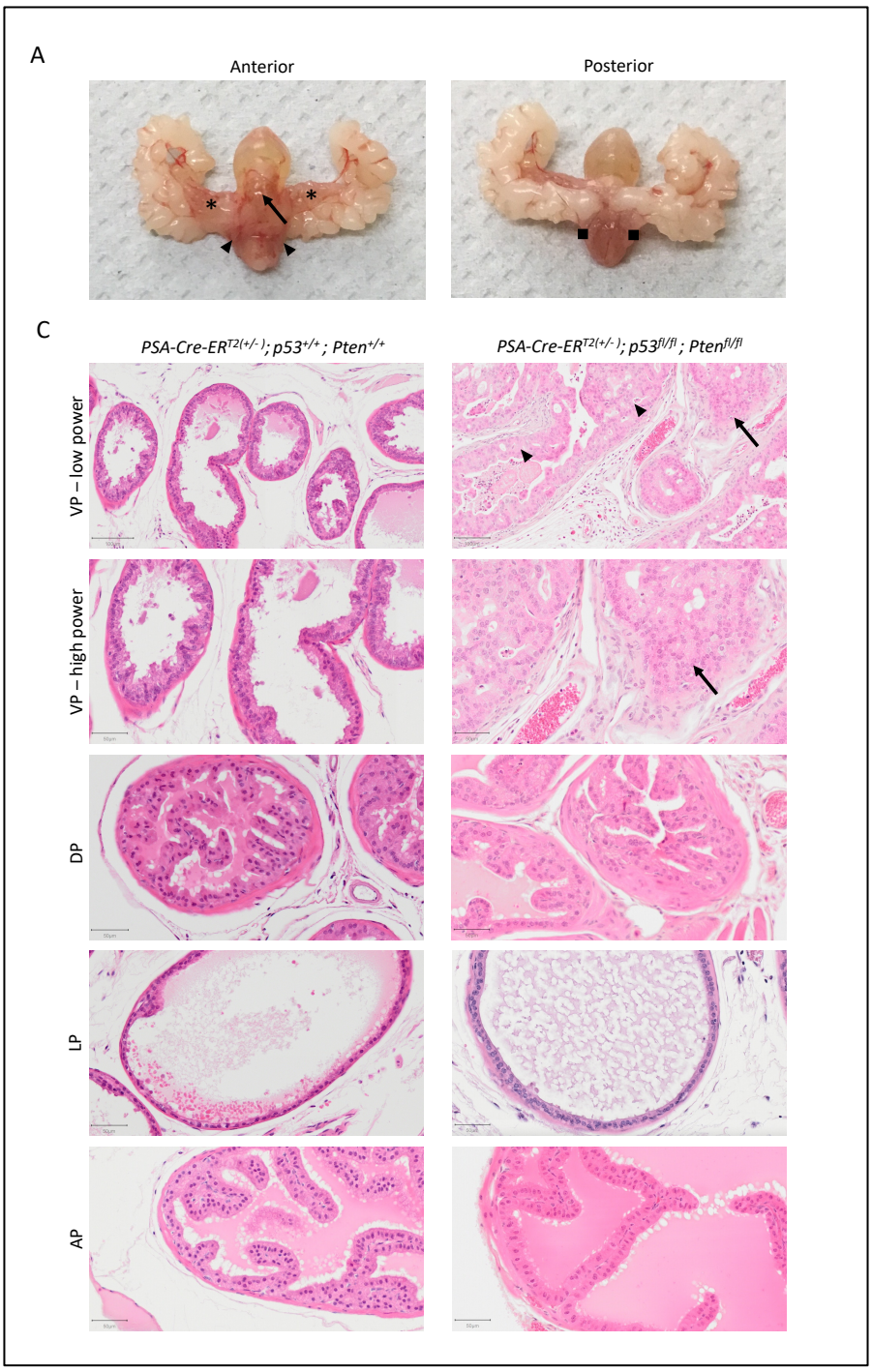

Figure 4.17: *Male PSA-Cre-ER$^{T2(+/-)}$; p53$^{fl/fl}$; Pten$^{fl/fl}$ mice that undergo induction with intraperitoneal injection of tamoxifen at 56 days of age develop localised prostate tumours within the ventral lobes comprising of high grade PIN and microinvasive carcinoma by 6 months.* A: Example image of the anterior and posterior aspects of the male genitourinary tract of a male *PSA-Cre-ER$^{T2(+/-)}$; p53$^{fl/fl}$; Pten$^{fl/fl}$* mouse demonstrating the macroscopic appearance of enlarged ventral prostate lobes (VP; arrow) and otherwise normal appearances of the anterior (AP; stars), lateral prostate lobes (LP; arrow heads) and dorsal prostate lobes (DL; squares). B: H&E stained sections of the individual lobes of a male *PSA-Cre-ER$^{T2(+/-)}$; p53$^{fl/fl}$; Pten$^{fl/fl}$* mouse at high power (scale bars 50 µm) compared with those of an aged match male *PSA-Cre-ER$^{T2(+/-)}$; p53$^{+/+}$; Pten$^{+/+}$* control (Wild Type control; WT). The ventral lobe is also displayed at low power (scale bars 50 µm) to show areas of abnormal glandular architecture characteristic of prostatic intraepithelial neoplasia (PIN; arrow heads) and microinvasive carcinoma (arrow).

Table 4.3: Allocation of mice to each treatment group in the *PSA-Cre-ER$^{T2(+/-)}$; p53$^{fl/fl}$; Pten$^{fl/fl}$* preclinical trial.

Group name	Treatment	Number of mice
Vehicle	Olaparib vehicle Ceralasertib vehicle	4
Olaparib	Olaparib 100 mg/kg Ceralasertib vehicle	3
Ceralasertib	Olaparib vehicle Ceralasertib 25 mg/kg	4
Combination	Olaparib 100 mg/kg Ceralasertib 25 mg/kg	5

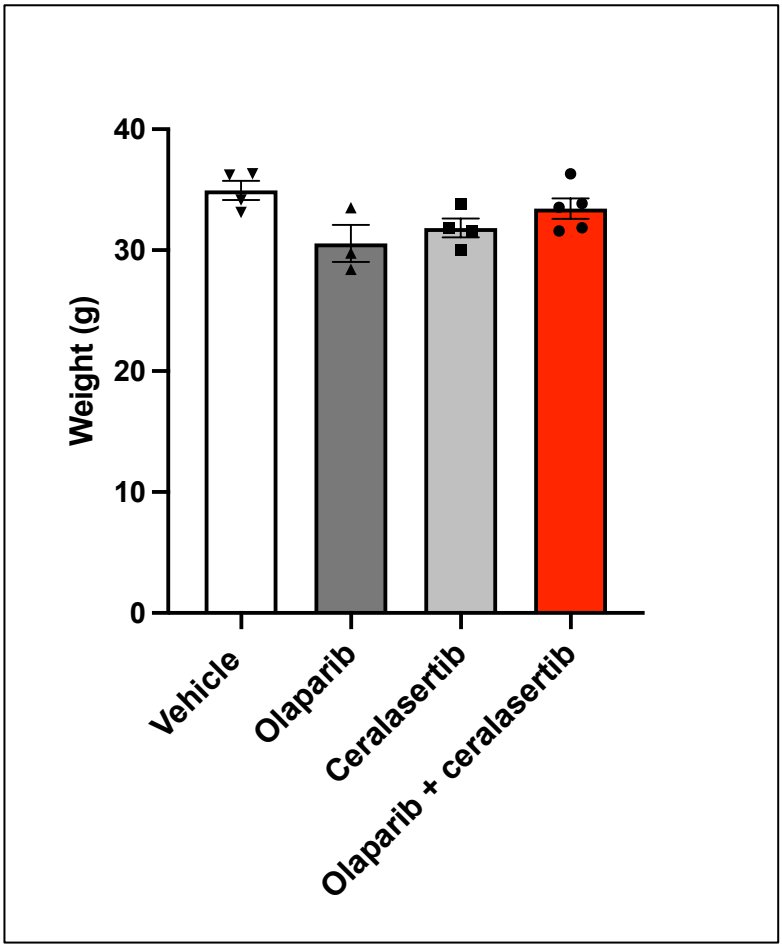

Figure 4.18: *Mean starting weight of experimental male PSA-Cre-ER$^{T2(+/-)}$; p53$^{fl/fl}$; Pten$^{fl/fl}$ mice according to treatment group.* Mouse numbers displayed as symbols. Error bars represent Standard Error of the mean. Statistical comparisons conducted using one-way ANOVA with Tukey correction for multiple comparisons, with no differences reaching the significance threshold.

4.3.3.2 Safety and tolerability

Treatment with olaparib and ceralasertib, alone and in combination was well tolerated throughout the study period. All mice experienced weight loss during the first 7 days, regardless of treatment group, most likely due to stress caused by increased handling and dosing, as demonstrated in ***Figure 4.19***. Upon initiation of once daily dosing from D8 onwards the majority maintained a stable weight until the D21 study endpoint. There were no significant differences between groups and no mice exhibited symptoms or signs suggestive of gastrointestinal or other organ system side effects during the study period. Collectively these data indicate that male transgenic mice on a C57BL/6 background are able to successfully tolerate olaparib and ceralasertib alone and in combination, with no evidence of severe side effects or significant weight loss over time.

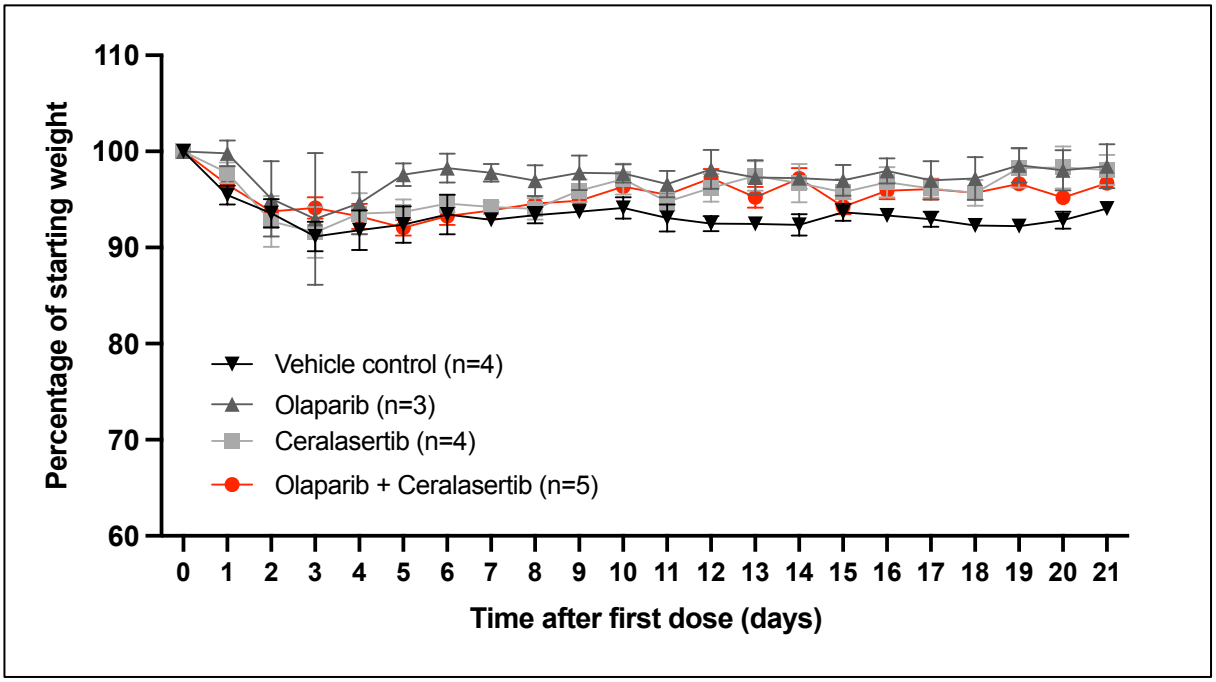

Figure 4.19: *Olaparib (100 mg/kg) or ceralasertib (25 mg/kg) alone or in combination does not significantly alter total body wight of PSA-Cre-ER$^{T2(+/-)}$; p53$^{fl/fl}$; Pten$^{fl/fl}$ experimental mice during 21 days treatment compared with vehicle treated controls.* Mean change in total body weight of experimental mice as measured at Day 0, stratified according to treatment received. Error bars represent Standard Error of the mean. Statistical significance calculated using one-way ANOVA with Tukey correction for multiple comparisons at each time point, with no differences reaching the significance threshold.

4.3.3.3 Efficacy

As the *PSA-Cre-ER$^{T2(+/-)}$; p53$^{fl/fl}$; Pten$^{fl/fl}$* model only results in the development of small tumours by the predetermined study timepoint, tumour volume and growth could not be quantified throughout the experiment and so the primary efficacy outcomes were total prostate and individual lobe weights at the D21 endpoint. Olaparib monotherapy and combined olaparib and ceralasertib reduced overall total prostate weight relative to vehicle treated controls, however these differences were less pronounced when adjusting for total body weight and failed to reach statistical significance (***Figure 4.20A)***. When comparing the weights of individual lobes, ceralasertib monotherapy resulted in a significant increase in overall VP weight (21.88 mg +/- 2.36 mg SEM) compared with vehicle treated controls (12.28 mg +/- 2.35 mg SEM; P=0.028), olaparib monotherapy (11.1 mg +/- 0.96 mg SEM; P=0.023) and combined olaparib and ceralasertib (9.66 mg +/- 1.81 mg SEM: P=0.004; ***Figure 4.20B)***, with a near identical trend seen for relative VP weight. On the contrary, treatment with ceralasertib either alone or in combination with olaparib led to a reduction in DLP weight compared with vehicle treated controls (6.25 mg +/- 0.86 mg SEM and 6.18 mg +/- 0.61 mg SEM versus 11.58 mg +/- 1.74 mg SEM; P=0.027 and P=0.015 respectively), again with a near identical trend seen for relative DLP weight. Finally, neither olaparib nor ceralasertib alone or in combination resulted in a significant change in overall or relative AP weight.

Although there was no significant difference in total prostate weight, these data demonstrate that ceralasertib, either alone or in combination with olaparib, is associated with a significant reduction in the weight of the DLP at the D21 timepoint. On the contrary, ceralasertib monotherapy also appears to be associated with a significant increase in the overall and relative weight of the VP at the D21 timepoint compared with the other treatment groups. This is an important finding given that tumour development was only identified within the VP during model characterisation, suggesting that whilst combined treatment appears to have no demonstratable effect on prostate mass, treatment with ceralasertib may in fact provide a proliferative advantage to cells of the VP. However, these data are limited by the low numbers of mice in each treatment group, together with the study being initiated whilst tumours were relatively small. Further trials involving larger numbers of mice at a later timepoint when tumours have become more established may therefore provide greater power to detect differences between groups.

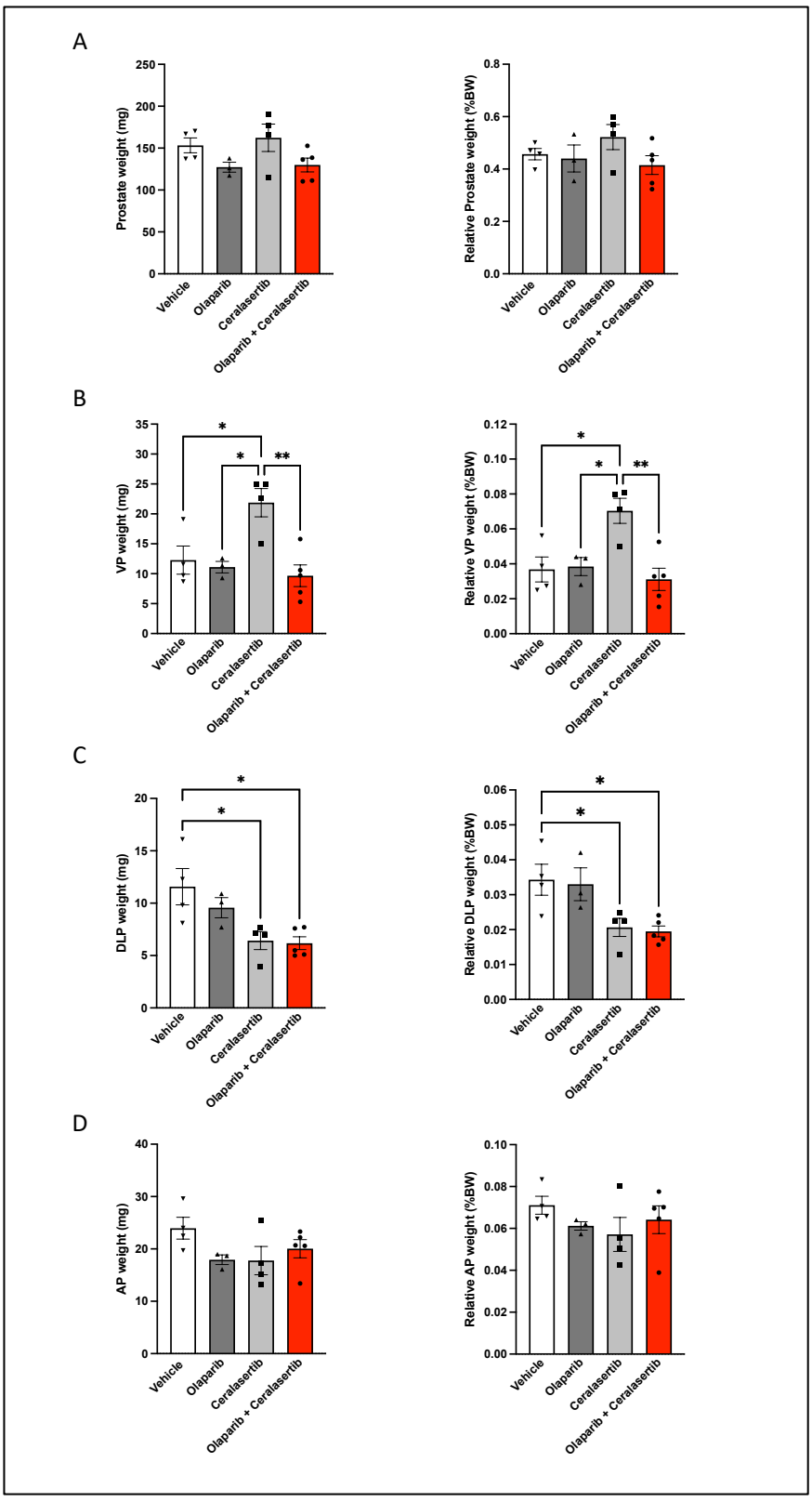

Figure 4.20: *Ceralasertib monotherapy (25 mg/kg) results in a significant increase in overall and relative VP weight following 21 days treatment compared with vehicle, olaparib monotherapy (100 mg/kg) and combined olaparib (100 mg/kg) and ceralasertib (25 mg/kg), whilst ceralasertib alone and in combination with olaparib results in a significant decrease in the overall and relative DP weight in PSA-Cre-ER$^{T2(+/-)}$; p53$^{fl/fl}$; Pten$^{fl/fl}$ mice*. A: Overall and relative total prostate weight. B-D: Total and relative weights of the VP (B), DP (C) and AP (D). Mouse numbers displayed as symbols. Error bars represent Standard Error of the mean. Statistical comparisons conducted using one-way ANOVA with Tukey correction for multiple comparisons. **: P ≤ 0.01, *: P ≤ 0.05.

To establish if tumour progression was impeded in response to treatment with olaparib or ceralasertib and investigate if the effects of treatment on proliferation and apoptosis observed in the PC-3 subcutaneous xenograft pre-clinical trial are mirrored in an immunocompetent setting, prostates of the *PSA-Cre-ER$^{T2(+/-)}$; p53$^{fl/fl}$; Pten$^{fl/fl}$* mice were evaluated histologically and using IHC for PCNA and CC-3 respectively. Due to issues during tissue processing and sectioning, not all sections included glands of each individual lobe and so only glands within tumours were assessed.

Figure 4.21A demonstrates representative low power H&E images of tumour glands from each treatment group, together with example PCNA and CC-3 stained IHC images at higher power. In vehicle treated tumours at the D21 timepoint, 23.2% (+/- 4.38% SEM) of glands demonstrated features of hyperplasia, 41.7% (+/-6.94% SEM) demonstrated PIN and 16.7% (+/- 2.78% SEM) demonstrated invasive carcinoma (***Figure 4.21B***). Treatment with combined olaparib and ceralasertib was associated with a significant reduction in the prevalence of microinvasive carcinoma (5.13% +/- 2.66% SEM) compared with vehicle treated controls (16.70% +/- 2.78%SEM; P=0.044), with no foci identified in one of the three tumours evaluated. Furthermore, combination treatment also resulted in a reduction in the prevalence of PIN and a corresponding increase in the prevalence of histologically normal glands compared with vehicle and both olaparib and ceralasertib monotherapy, although differences failed to reach statistical significance.

Given that glands demonstrating microinvasive carcinoma were not seen in all the evaluated tumours, proliferation and apoptosis were only assessed in glands demonstrating the pathological morphologies of hyperplasia and PIN in order to maintain statistical validity. The baseline proportion of proliferating cells in the hyperplastic glands of *PSA-Cre-ER$^{T2(+/-)}$; p53$^{fl/fl}$; Pten$^{fl/fl}$* mice treated with vehicle, as represented by mean PCNA index, was 2.91% (+/- 0.66% SEM), which is much lower than the 72.0% observed in the PC-3 subcutaneous xenograft tumours described in Section 4.3.2. Treatment with olaparib or ceralasertib either alone or in combination did not significantly alter this proportion, as shown in ***Figure 4.21C***. The proportion of cells undergoing apoptosis in hyperplastic glands of vehicle treated mice was even lower, as represented by mean CC-3 index of 0.518% (+/- 0.14% SEM). Similarly to PCNA index, treatment with olaparib or ceralasertib either alone or in combination did not alter the CC-3 index within this glandular phenotype (***Figure 4.21D***).

Unsurprisingly the proportion of proliferating cells within glands demonstrating PIN was higher than those with features of hyperplasia, as represented by a PCNA index of 9.83% (+/- 0.91% SEM) in vehicle treated tumours (***Figure 4.21C***). Whilst treatment with olaparib or ceralasertib monotherapy did not

significantly alter PCNA index compared with vehicle (9.79% +/- 0.65% SEM and 9.11% +/- 0.53% SEM respectively), combination therapy resulted in a highly significant reduction to 4.90% (+/- 0.92% SEM; P=0.008). Furthermore, this reduction was also significant when compared with olaparib monotherapy (P=0.009) and ceralasertib monotherapy (P=0.02), indicating that combination therapy is more effective than either agent alone at reducing proliferation within glands possessing a PIN phenotype. Similarly to hyperplastic glands, the proportion of cells undergoing apoptosis in PIN glands was very low, with no significant difference between treatment groups (***Figure 4.21D***).

Collectively these data provide some insight into effects of PARPi and ATRi in localised p53 and PTEN deficient prostate cancer in the immunocompetent setting. Whilst combined treatment was not associated with a reduction in the weight of the whole prostate compared with monotherapy or vehicle treated controls, it did result in a significant reduction in the proportion of tumour glands demonstrating invasive carcinoma at the D21 timepoint. Furthermore, the proportion of proliferating cells in glands demonstrating a PIN phenotype was significantly lower in those mice treated with combination therapy compared with both vehicle and either olaparib or ceralasertib alone. These data therefore suggest that through reducing the proliferation of cells in PIN lesions, combined PARPi and ATRi may reduce the rate of transformation to invasive carcinoma. However, there were no observed difference in the proportion of cells undergoing apoptosis between treatment groups at the D21 timepoint in either hyperplastic or PIN glands. This is similar to the observations in the PC-3 subcutaneous xenograft study and may be the result of the dosing regimen used relative to the timepoint at which tumours were evaluated. Again, ceralasertib was only given in combination with olaparib for the first 7 days of the treatment cycle whilst the analysed tissue was harvested after a further 14 days of olaparib alone. It is therefore possible that some of the biological effects of combination therapy may have occurred early in the treatment cycle and hence been missed by IHC characterisation at the D21 timepoint. Further in vivo preclinical trials with larger numbers of mice in each treatment cohort along with analysis at different timepoints are therefore required to fully characterise the effects of PARPi and ATRi in this particular model of localised prostate cancer.

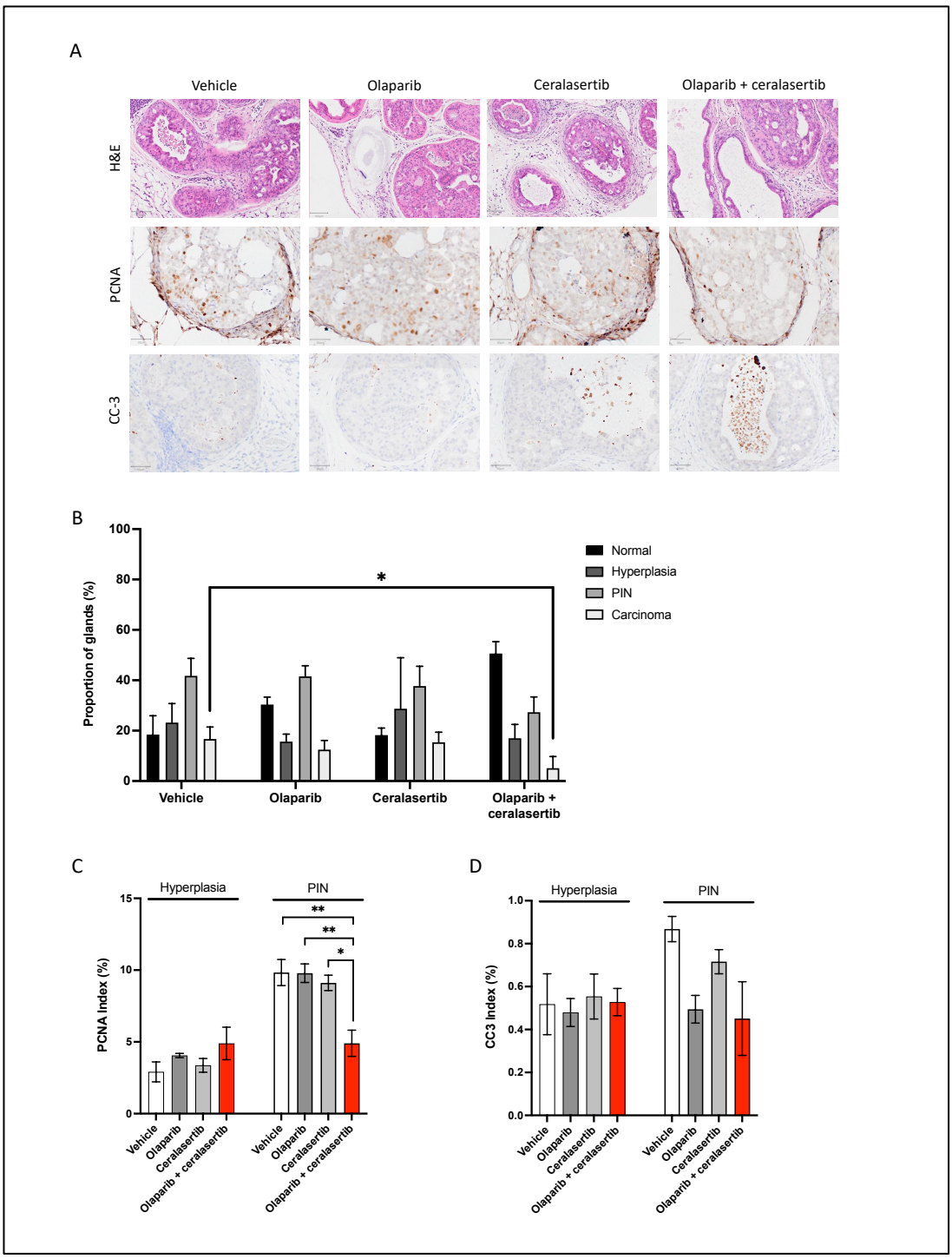

Figure 4.21: *Combined olaparib (100 mg/kg) and ceralasertib (25 mg/kg) treatment for 21 days results in a significant reduction in the prevalence of microinvasive carcinoma in the tumours of PSA-Cre-ER$^{T2(+/-)}$; p53$^{fl/fl}$; Pten$^{fl/fl}$ mice together with a reduction in proliferation within glands demonstrating PIN compared with those treated vehicle or either agent alone*. A: Representative low power H&E and high power IHC images of tumour glands stained for PCNA and CC-3 (brown cells). Scale bars represent 100 μm and 50 μm respectively. B: Bar chart illustrating the mean percentage of glands within each tumour demonstrating features of hyperplasia, intraepithelial neoplasia (PIN) and carcinoma. C: Bar chart demonstrating quantitation of PCNA within tumour glands with features of hyperplasia and PIN (expressed as the proportion of cells positive for PCNA; PCNA index). D: Bar chart demonstrating quantitation for CC-3 within tumour glands with features of hyperplasia or PIN (expressed as the proportion of cells positive for CC-3; CC-3 index). Three tumours evaluated per treatment group (n=3). Error bars represent Standard Error of the mean. Statistical comparisons conducted using one-way ANOVA with Tukey correction for multiple comparisons. **: $P \leq 0.01$, *: $P \leq 0.05$.

4.4 Discussion

The experiments in this chapter sought to determine the therapeutic effects of combined PARPi and ATRi in a variety of preclinical models of prostate cancer, beginning with the LN-NEPC-1 PDE of neuroendocrine metastatic CRPC. This model has only recently been developed by our laboratory group and therefore the exact genomic landscape of the lymph node metastasis from which it was derived is still under investigation. Whilst full genomic profiling is ongoing and hence the DDR status is unknown, basic characterisation has demonstrated it to be insensitive to ADT and both AR and PTEN negative, with only low levels of PSA expression (data not shown). Nevertheless, this model provides insight into the action of olaparib and ceralasertib in human CRPC tissue in which the original architecture and microenvironment is maintained. Importantly, optimisation prior to undertaking the drug study was performed to evaluate the proliferative capacity of cells within the model for comparison with those reported in the literature. The PCNA index of vehicle treated LN-NEPC-1 tissue at the 48 hour timepoint was 63.4%, which is considerably higher than the Ki67 proliferative index of 32.5% reported in PDE tissue at the same timepoint reported a previous study by Centenera et al. (Centenera et al., 2012). However, in their study the tumours used for PDE culture were taken from radical prostatectomy specimens and therefore reflect localised or locally advanced disease, rather than the advanced metastatic castrate resistant disease from which our PDE was derived. On the contrary, the proportion of cells undergoing apoptosis as measured using CC-3 in vehicle treated tissue was 8.7%, which is similar to the 8.9% in the LN-NEPC-1 study, hence indicating models to be comparable in terms of viability of control tissue after 48 hours culture.

Combined treatment with olaparib and ceralasertib for 48 hours resulted in a significant reduction in the proliferation of LN-NEPC-1 tumour cells and an increase in DNA DSBs compared with vehicle treated controls. These data therefore support the observations outlined in Chapter 3 in which 96 hours of combination therapy reduced proliferation and increased DNA damage in our panel of HR-proficient CRPC cells. However, in contrast to the in vitro data, although combined olaparib and ceralasertib increased apoptosis at the 48 hour timepoint to a greater extent than vehicle or either agent alone, there was no significant difference when compared with ceralasertib monotherapy. Whilst this therefore suggests that the addition of olaparib does not provide a significant benefit in terms of increasing cell death in this particular model, the exact reasons behind this are uncertain and it is possible that with further experimental repeats, subtle differences between groups may become more apparent.

Although no previous studies have reported the effects of combined PARPi and ATRi in a PDE model of CRPC, Schiewer et al., used a PDE established from a radical prostatectomy specimen to explore the biological effects of 48 hours PARPi with veliparib on AR function (Schiewer et al., 2012). PARPi treatment resulted in a significant decrease in total PAR within the tumour tissue relative to vehicle treated controls, together with a significant reduction in proliferation as measured using Ki67. Whilst 48 hours of olaparib monotherapy did result in a modest reduction in proliferation compared with vehicle treated controls as measured using PCNA in our study, this was not statistically significant and remained considerably higher than the levels reported by Schiewer et al. However, differences in origin of the PDE tissue, together with differences in the pharmacology and doses of veliparib and olaparib used make it difficult to draw meaningful comparisons. In addition, the DDR status of each model has not been established, which may also have influenced the response to treatment.

Perhaps the closest study for comparison is that reported by Neeb et al., in which the authors evaluated the effects of 6 days of combined PARPi and ATRi using olaparib (10 μM) and BAY1895344 (0.1 nM - 10 μM) in organoids derived from metastatic lymph node tissue of a patient with heavily pre-treated CRPC (Neeb et al., 2021). Despite loss of *ATM*, this model (termed CP50C) is wild-type for *TP53*, *PTEN* and *MYC*, with organoids being inherently resistant to olaparib monotherapy. However, organoids demonstrated sensitivity to ATRi in the nanomolar range, with additional benefit seen when in combination with olaparib, particularly at lower doses. Whilst there are significant differences in terms of methodology, tissue of origin and treatment doses/duration, this nevertheless provides corroborating evidence of the benefit of combined PARPi and ATRi in patient derived CRPC tissue.

Having demonstrated efficacy in the LN-NEPC-1 ex vivo model, experiments next sought to explore the effects of combined olaparib and ceralasertib in vivo through undertaking preclinical trials in models of CRPC and localised prostate cancer, as described in Section 4.1. In both studies olaparib and ceralasertib, alone and in combination, were well tolerated and not associated with any significant gastrointestinal or systemic side effects. Regardless of model, the majority of mice lost weight during the first 7 days of the 21 day treatment cycle, followed by either a plateau or weight gain in all but a small number of during the following 14 days, with no difference between treatment groups. These findings are in keeping with other preclinical studies in which this exact combination has been utilised in vivo and was well tolerated (Kim et al., 2016, Lloyd et al., 2020), as well as others in which different PAPRi and ATRi agents were used (Neeb et al., 2021). Furthermore, both olaparib and ceralasertib have entered clinical trials as single agents and in combination in patients with a range of solid cancers, including CRPC. Several trials have shown olaparib monotherapy to be well tolerated, with most

common adverse events being fatigue, anaemia and nausea (Mateo et al., 2015, Mateo et al., 2019, de Bono et al., 2020). Whilst ceralasertib monotherapy has been less widely studied, early phase trials have also shown this to be similarly well tolerated, with most common adverse effects again being fatigue, anaemia and nausea (Dillon et al., 2019). A number of early phase combination studies involving ceralasertib are underway, with Krebs et al. reporting the preliminary results of a phase I trial of ceralasertib in combination with olaparib or the anti-PD-L1 antibody durvalumab in patients with advanced solid cancers, including prostate (Krebs et al., 2018). Of the 45 patients treated with olaparib 100 - 300 mg twice daily continuously and ceralasertib 60 mg once daily to 240 mg twice daily for 5-14 days, the most common adverse effects were anaemia (15.5%), neutropenia (13.3%) and thrombocytopenia (11.1%), with the authors recommending the phase II dosing regimen to be a 28 day cycle comprising of ceralasertib 160 mg once daily for the first 7 seven days alongside olaparib 300 mg twice daily continuously.

The PC-3 xenograft preclinical trial reported in this thesis explored the in vivo therapeutic effects of combined olaparib and ceralasertib in a model of rapidly progressive CRPC. This identified that combination therapy results in superior control of tumour growth when compared with vehicle or either agent alone, with a highly significant reduction in tumour volume at the D18 short term timepoint. Additionally, although less pronounced, long term treatment involving a second cycle appeared to slow tumour growth compared with olaparib or ceralasertib alone, with two mice surviving at the D32 timepoint in the combination group compared with none in either monotherapy group. The most significant reduction in growth was seen within the first 14 days of the 21 day treatment cycle, with tumour volume appearing to increase more rapidly after this period. Similarly, the reintroduction of ceralasertib following commencement of the second treatment cycle in the long term cohort was able to reduce the rate of growth, albeit for a shorter period and to a lesser extent. Together this suggests that the maximum benefit of combination therapy was seen during the period in which both agents were given together, with tumour growth accelerating during periods of olaparib monotherapy to which previous experiments have confirmed PC-3 cells are inherently resistant. This would therefore suggest that a different treatment cycle involving a shorter period of olaparib monotherapy may provide greater efficacy in providing long term control of tumour growth.

However, Lloyd et al. have previously explored the use of different treatment cycles in the FaDu xenograft model, comparing continuous olaparib and either 3 days ceralasertib followed by 4 days off, 5 days ceralasertib followed by 9 days off or 7 days ceralasertib followed by 7 days off (Lloyd et al., 2020). Higher levels of toxicity were seen in the 7 day on and 7 day off cohort, indicating that the

benefits of any shortening of the 14 day olaparib monotherapy period would need to be carefully balanced against tolerability.

Given the significant reduction in growth of those tumours in the combination therapy group, further experiments were conducted to determine the underlying mechanisms responsible. Immunohistochemistry analysis at the D18 timepoint identified that combined olaparib and ceralasertib resulted in a highly significant reduction in the proliferation of tumour cells compared with vehicle and either agent alone, together with a modest increase in apoptosis compared with both vehicle and olaparib but not ceralasertib. Given that the absolute proportion of apoptotic cells was low (1.27% and 0.77% in combination and vehicle treated tumours respectively), it is therefore possible that the reduction in tumour growth was a result of reduced proliferation rather than cell death. However, it is also possible that cell death may have occurred via caspase independent mechanisms such as necroptosis, which may have been missed through use of CC-3 as the maker of apoptosis (Tait and Green, 2008). As in the in vitro experiments, treatment with olaparib resulted in an increase in both total CHK1 and p-CHK1 concentration compared with vehicle at the D18 timepoint. Similarly, this increase was reversed through combination with ceralasertib, again indicating that combination therapy is able to overcome the increased dependency on CHK1 signalling resulting from PARPi.

Additionally, the tumours of those mice treated with olaparib and ceralasertib were macroscopically paler and more translucent, with fewer vessels at the time of dissection than those treated with vehicle or either agent alone. When this was examined microscopically, only those tumours treated with combination therapy were found to have a significantly lower microvessel density compared with vehicle treated controls. Furthermore, microvessel diameter was also significantly smaller than in those treated with vehicle or either agent alone. Whilst this may be secondary to the smaller volume tumours requiring less blood supply, it may also indicate changes in angiogenesis within the PC-3 xenograft tumours in response to treatment.

Previous studies have explored the role of PARP1 in angiogenesis, with Tentori et al. identifying that pharmacological PARPi with GPI 15427 at non-cytotoxic concentrations reduced tube formation of HUV-ST endothelial cells and inhibited VEGF or PLGF induced migration in vitro (Tentori et al., 2007). Furthermore, in vivo studies involving injection of heaparin and VEGF impregnated matrigel plugs in the flanks of C57BL/6 mice demonstrated a reduction in macroscopic vessel formation and haemoglobin concentration, taken as surrogate markers of angiogenesis, when GPI 15427 was also

present. These findings have been confirmed by other authors (Rajesh et al., 2006), collectively indicating that PARP1 has a role in angiogenesis and hence its inhibition may provide an additional benefit when used in the treatment of solid cancers.

Similarly, previous studies have identified that both ATM and ATR are also involved in hypoxia driven angiogenesis. Shi et al. undertook a series of experiments exploring the role of seryl-tRNA synthetase (SeRS) in hypoxia, a transcriptional repressor of VEGFA that exerts its effects through its ability to bind to the VEGFA promoter and bring about histone deacetylase mediated epigenetic silencing (Shi et al., 2020). They found SeRS was inactivated in conditions of hypoxia through its phosphorylation by both ATM and ATR, enabling cMyc and HIF-1 mediated increases in VEGFA expression. Consequentially, inhibition of ATR either through siRNA mediated RNA interference or treatment with VE-821 significantly reduced hypoxia induced VEGFA induction. Collectively these studies indicate that both PARP and ATR play important roles in mediating angiogenesis, which may therefore explain the observed reduction in the presence of both macroscopic and microscopic blood vessels in those tumours treated with combined olaparib and ceralasertib, hence providing a potential mechanism for the observed reduction in tumour growth in vivo.

Whilst Gonzalez-Billalabeitia et al. have previously reported that 15 days treatment with olaparib (50 mg/kg daily) did not result in any change in the area of PC-3 xenograft tumours compared with vehicle (González-Billalabeitia et al., 2014), thereby validating our observation that such tumours are inherently insensitive to PARPi, no authors have directly reported the in vivo effects of combined olaparib and ceralasertib in this particular model of CRPC. Jette et al. undertook in vitro studies using these agents in PC-3 cells which had undergone CRISPR/Cas9 deletion of *ATM* (Jette et al., 2020). Interestingly they found that whilst 144 hours treatment with combined olaparib (1 μM) and ceralasertib (0.3 μM) only resulted in a small reduction in viability compared with vehicle treated controls in *ATM* wild-type cells, this effect was markedly increased in those that were *ATM* deficient, with benefits seen both in terms of reduced viability and increased apoptosis (Jette et al., 2020). However, whilst the olaparib dose was similar to that used in the in vitro experiments involving PC-3 cells reported in Section 3.3.2, the ceralasertib dose was considerably lower and the culture time longer which, together with the lack of further in vivo study, means it is difficult to directly compare results.

The small number of studies that evaluated the therapeutic effects of combined PARPi and ATRi in vitro (discussed previously in Section 3.4) also evaluated this combination approach in vivo using a

selection of solid tumour models, including prostate. In their study, Kim et al., tested the efficacy of combined olaparib (50 mg/kg once daily) and ceralasertib (25 mg/kg once daily) in an orthotopic PDX of *BRCA2* mutant ovarian cancer using a 7 day regimen comprising of continuous olaparib and ceralasertib for the first 3 days, followed by 4 days of olaparib monotherapy (Kim et al., 2016). Combined treatment resulted in a dramatic reduction in tumour volume compared with either agent alone, with complete regression seen in 57% of mice, indicating superior growth inhibition in this HR-deficient model. Similar to our findings, treatment with olaparib monotherapy resulted in an increase in p-CHK1, which was ameliorated by co-administration of ceralasertib. Likewise, Lloyd et al. assessed olaparib (50 mg/kg once daily) and ceralasertib (25 mg/kg once daily) alone and in combination in *ATM* deleted FaDu xenograft tumours using a variety of dosing regimens, with combined treatment resulting in greater tumour growth control (Lloyd et al., 2020). They went on to evaluate each agent alone and in combination in a panel of non-small cell lung cancer PXD models, with combination therapy resulting in superior tumour growth inhibition than treatment with either agent alone in both wild type and *ATM* deficient models, although significantly greater effects were seen in the latter, with complete tumour regression in the *ATM* deficient CTG-0828 model.

Finally, the study by Neeb et al. is the only example of an in vivo study conducted in the setting of CRPC (Neeb et al., 2021). Here the authors utilised a PDX model generated by the implantation of the aforementioned patient derived CP50C CRPC cells into castrated NSG mice. Treatment with olaparib (50 mg/kg) and (BAY1895344 30 mg/kg) using a 7 day regimen comprising of continuous olaparib and BAY1895344 for the first 3 days, followed by 4 days of olaparib monotherapy significantly reduced tumour growth compared with vehicle or either agent alone over the 56 day treatment period, indicating superior antitumour activity in the setting of *ATM* deficient CRPC. Collectively these studies corroborate our findings that combined PARPi and ATRi is effective at reducing growth of xenograft tumours in vivo. Whilst there are considerable differences in methodology, most were conducted in HR-deficient (most commonly *ATM* deficient) models, with significant benefits observed and even some examples of complete tumour regression. Given that our study demonstrated reduced growth of tumours comprising of HR-proficient PC-3 cells, it is possible that these effects could be further enhanced if ATM function were to be simultaneously depleted either genetically or through additional pharmacological inhibition.

The preclinical trial conducted using the *PSA-Cre-ER*$^{T2(+/-)}$*; p53*$^{fl/fl}$ *; Pten*$^{fl/fl}$ GEMM provided insight into the in vivo effects of combined PARPi and ATRi in earlier stage, localised prostate cancer in the immunocompetent setting. Characterisation of the model prior to commencement of the main study

confirmed that simultaneous loss of *Trp53* and *Pten* specifically within the prostatic epithelium resulted in development of a prostate cancer phenotype, although much less advanced than that of the better characterised *PB-Cre4 ; p53$^{fl/fl}$; Pten$^{fl/fl}$* model (Chen et al., 2005). The probable reasons for this are discussed in Section 4.3.3.1. Histologically the predominantly ventral tumours comprised of high grade prostatic intraepithelial neoplasia (HG-PIN), with focal areas of microinvasive carcinoma and were in keeping with the previous description in the literature (Parisotto et al., 2018).

Whilst a 21 day treatment cycle of combined olaparib and ceralasertib did not result in a significant change in either overall or relative prostate weight compared with vehicle or either agent alone, it was associated with a reduction in the proportion of proliferating cells within glands possessing a PIN phenotype at the D21 timepoint. Furthermore, combined olaparib and ceralasertib was the only treatment that led to a reduction in the proportion of tumour glands demonstrating microinvasive carcinoma. Together these results suggest that simultaneous PARPi and ATRi reduces the rate of transformation of PIN lesions to invasive carcinoma through a reduction in the proliferation of cells transformed by loss of p53 and PTEN function, thereby slowing tumour progression at an early stage of carcinogenesis.

To date no other study has compared the effects of these agents within a GEMM of early stage prostate cancer driven by loss of p53 and PTEN function. However, Gonzalez-Billalabeitia et al., previously investigated the effect of PARPi in prostate cancer with these genetic aberrations using the *PB-Cre4 ; p53$^{fl/fl}$; Pten$^{fl/fl}$* model (González-Billalabeitia et al., 2014). Depending on genotype, mice were treated with either vehicle, olaparib (50 mg/kg) or the PI3 kinase inhibitor BKM120 (30 mg/kg) for a duration of 1-2 weeks. Interestingly, olaparib treatment resulted in a significant increase in DNA damage as measured by γ-H2AX and apoptosis as measured using the TUNEL stain. However, whilst olaparib treatment also slightly reduced the proportion of glands demonstrating HG-PIN, this did not reach statistical significance, hence corroborating the finding that olaparib monotherapy did not alter the glandular phenotype within *PSA-Cre-ER$^{T2(+/-)}$; p53$^{fl/fl}$; Pten$^{fl/fl}$* tumours at the D21 timepoint.

It is probable that the reasons for the differing responses to combined olaparib and ceralasertib between PC-3 subcutaneous xenograft tumours and those arising in *PSA-Cre-ER$^{T2(+/-)}$; p53$^{fl/fl}$; Pten$^{fl/fl}$* mice are multifactorial, with limitations arising from the models used no doubt partially responsible, as discussed in Section 4.5. However, it is also possible that some of the differences are a result of genomic, pathobiological and histological differences between the models. PC-3 xenograft tumours comprised of clusters of immortalised human PC-3 CRPC cells, which are known to carry a number of

genetic aberrations in addition to *TP53* and *PTEN* loss, interspersed with stromal cells, vessels and immune infiltrate originating from the immunocompromised murine host. On the contrary, tumours in the *PSA-Cre-ER$^{T2(+/-)}$; p53$^{fl/fl}$; Pten$^{fl/fl}$* model comprised of glands containing transformed prostatic epithelial cells with only two specific gene alterations surrounded by reactive stroma, vessels and immune infiltrate originating from the immunocompetent host, with tumours representing a much earlier stage of disease. It is therefore plausible that these differences, such as the presence of additional genetic aberrations and associated oncogene induced replication stress in PC-3 cells, may have driven a higher level of inherent genomic instability that rendered them more susceptible to DDR targeted therapy. It is also possible that the higher proportion of proliferating cells within PC-3 xenograft tumours may have rendered them more susceptible to combined PARPi and ATRi, as only these proliferating cells would have aberrantly progressed through the cell cycle and undergone mitotic catastrophe as a result of treatment, as proposed in Section 3.4.

Additionally, the intact immune system of the experimental mice in the *PSA-Cre-ER$^{T2(+/-)}$; p53$^{fl/fl}$; Pten$^{fl/fl}$* model may have modulated the treatment response. There is emerging evidence to support the role of PARP enzymes in both the innate and adaptive immune system (Yélamos et al., 2020). For example, Moreno-Lama et al. recently utilised the *CD4* promoter to drive Cre recombinase expression specifically in T lymphocytes (*CD4-cre*) to specifically delete *Parp2* within these cells such that, when crossed with *Parp1* null mice, they were able to generate cohorts with T lymphocytes deficient in PARP1, PARP2 or both PARP1 and PARP2 (Moreno-Lama et al., 2020). Notably, growth of AT-3 breast cancer orthotopic xenograft tumours was reduced in those mice with PARP1 or PARP2 depleted T lymphocytes, but increased in those in which both PARP1 and PARP2 were depleted simultaneously. Whilst treatment with olaparib resulted in a significant decrease in tumour growth in AT-3 xenograft tumours generated in immunodeficient SCID mice, this was lost in AT-3 xenograft tumours generated in immunocompetent wild-type mice, suggesting that the antitumour effect of olaparib is blunted by an intact immune system. PARP1 and PARP2 also appear to play an important role in B cell homeostasis (Galindo-Campos et al., 2019), as well as the function of innate immune cells such as neutrophils, macrophages, dendritic cells and natural killer cells, all of which may also impact upon the tumour immune response following PARPi (Yélamos et al., 2020).

The ability to evade immune system is now a well-established hallmark of cancer, with the immune checkpoint signalling axis comprising of interactions between programmed death 1 (PD-1) and its ligand (PD-L1) enabling cancer cells to evade host cytotoxic immune cells within the tumour microenvironment (Freeman et al., 2000, Hanahan and Weinberg, 2011). As such, immune checkpoint

inhibitors aimed at reinstating the anti-tumour T lymphocyte response through blockade of PD-1 have shown efficacy in a number of different solid cancers (Esfahani et al., 2020). PARPi with both olaparib and talazoparib increased the total level of PD-L1, the ligand of PD-1, in both *BRCA* proficient and *BRCA* deficient triple negative breast cancer (TNBC) cell lines, as well as in orthotopic TNBC xenograft tumours treated with either olaparib or rucaparib for 3 weeks (Jiao et al., 2017). Of note, this increased PD-L1 expression correlated with resistance to T cell mediated cytotoxicity.

Whilst studies suggest that DNA damage and other DDR pathways also interact with the tumour immune response, the role of ATR remains to be fully elucidated (Mouw et al., 2017). However, Sun et al., identified that ATR depletion, either genetically using shRNA-mediated *ATR* knockdown or pharmacologically using VE-822, was able to overcome the increased PD-L1 expression induced by both ionising radiation or cisplatin in a range of cancer cell lines, including HeLa and U2OS (Sun et al., 2018). Furthermore, treatment with VE-822 and ceralasertib also induced PD-L1 downregulation in MDA-MB- 231 breast cancer cells, with additional experiments confirming that ATR inhibition sensitised cells to T lymphocyte mediated killing by destabilising PD-L1 and attenuating the PD-L1/PD-1 interaction. Whilst these experiments focussed on radiation and cisplatin induced PD-L1 expression, it is also possible that ATRi may be able to similarly overcome the aforementioned increases in expression seen following PARPi. Collectively these studies may therefore not only explain some of the observed differences in response between the in vivo models in this thesis, but may also provide another potential mechanism through which ATRi may enhance the antitumour effects of PARPi in immunocompetent cancers and hence explain the observed reduction in proliferation in PIN lesions and incidence of microinvasive carcinoma in combination treated *PSA-Cre-ER*$^{T2(+/-)}$*; p53*$^{fl/fl}$ *; Pten*$^{fl/fl}$ tumours.

4.5 Limitations

Some of the results reported in this chapter are again subject to limitations based on the experimental methods used. As with the in vitro studies, it is difficult to draw definitive conclusions regarding the effect of PARPi and ATRi on the phosphorylation and therefore activation of ATR due to the choice of antibody used for WB (discussed in Section 3.5). Likewise, the dosing schedule and timing of tissue harvest may have impacted upon the results of the mechanistic analysis. For example, in both the PC-3 xenograft and *PSA-Cre-ER$^{T2(+/-)}$; p53$^{fl/fl}$; Pten$^{fl/fl}$* preclinical trials, the doses and duration of olaparib and ceralasertib treatment within each 21 day treatment cycle were determined in collaboration with AstraZeneca on the basis of previous in vitro and in vivo studies (data not provided). In the case of combination therapy, olaparib and ceralasertib were given together for the first 7 days of treatment, followed by a 14 day period of olaparib monotherapy. By harvesting and analysing tissue at the D18 and D21 timepoints in each study respectively it is possible that some of the biological effects of combined PARPi and ATRi may have been missed, which could potentially explain why the cytotoxicity seen in our in vitro and ex vivo models were not recapitulated in vivo. Further preclinical trials involving additional cohorts that could be harvested and evaluated at earlier timepoints may therefore provide valuable additional insight into the mechanisms underlying the responses in each group.

Although WB and IHC were able to uncover some of the potential mechanisms responsible for the enhanced efficacy of combined olaparib and ceralasertib in the PC-3 xenograft preclinical trial, it was hoped that phosphoproteomic analysis would provide further insight into the pathways responsible. However, initial evaluation using hierarchical clustering and principle component analysis (PCA) identified a number of issues precluding full bioinformatic analysis. Firstly, one of the olaparib samples was found to have a significantly higher protein concentration than all others, despite this having been quantified prior to transport. As discussed in Section 4.3.2.4.4, the reasons for this are not certain but may have included contamination of the sample with non-homogenised tissue, or degradation during transport. This sample was therefore removed from subsequent analyses, which unfortunately undermined the statistical validity of any comparisons through reducing the sample number of the olaparib group to n=2. Furthermore, whilst PCA analysis demonstrated some clustering of samples from the same treatment groups, there appeared to be heterogeneity between individual samples. Again, the reasons for this are uncertain may have similarly been due to contamination of the sample with non-homogenised tissue, degradation during transport or due to individual tumour sections being taken from different regions of the parent tumour, perhaps leading to varying degrees of contamination with necrotic tissue content. On account of these issues full analysis was not undertaken, therefore meaning a subsequent repeat experiment involving a larger number of protein

samples taken from the same tumour regions in each treatment group is necessary in order to fully elucidate the key cell signalling pathways underpinning the observed treatment responses.

Finally, although some benefits were observed with combined olaparib and ceralasertib compared with vehicle and either agent alone in the GEMM preclinical trial, the model itself may have limited our ability to detect all but large differences between treatment groups on account of the small tumour size and short duration of treatment. Future trials performed using multiple treatment cycles in mice that have been aged to a later timepoint post induction may hence provide further insight into the effects of combined PARPi and ATRi in immunocompetent, p53 and PTEN deficient prostate cancer. Similarly, if we are to fully understand the potential benefits of this combination across the full spectrum of this diverse disease then further preclinical studies in models of other stages of prostate cancer must also be conducted, including those of metastases.

4.6 Conclusions and future work

In summary, the results outlined in this chapter demonstrate that combined PARPi and ATRi with olaparib and ceralasertib results in greater antitumour activity than vehicle or either agent alone in three methodologically distinct ex vivo/in vivo preclinical models of prostate cancer, with responses appearing to be greatest in those representing more advanced disease. Whilst these results support those of the in vitro experiments outlined in Chapter 3, further studies are needed to determine whether the hypothesised in vitro mechanism of synergy is also responsible for these in vivo effects. Furthermore, the observed reduction in macroscopic and microscopic vessels supplying PC-3 xenograft tumours indicates that some of the in vivo benefits may have been the result of complementary inhibitory effects of PARPi and ATRi on angiogenesis, therefore warranting further investigation. Likewise, emerging evidence suggests that ATRi may overcome some of the modulatory effects of PARPi in the tumour immune response, particularly immune checkpoint signalling involving PD-L1. Further studies are therefore also necessary to determine the role of PARP and ATR within the prostate cancer immune response to evaluate whether this may also provide a mechanism of synergy between PARPi and ATRi in this setting.

Whist other studies have found combined PARPi and ATRi to be more effective and even to induce tumour regression in models that are also *ATM* deficient, such aberrations are only present in 5.9-7.3% of CRPC tumours, therefore restricting the potential clinical benefits (Robinson et al., 2015, de Bono et al., 2020). Although these effects were also seen if ATM was pharmacologically inhibited

alongside PARP and ATR (Neeb et al., 2021), given the toxicity seen with combined PARPi and ATRi in early clinical studies (Krebs et al., 2018), together with the key functions of ATM in the DDR, it is likely that triple inhibition would result in intolerable toxicity and hence may not be clinically viable. However, experiments in this chapter have shown that combined PARPi and ATRi at clinically relevant doses is a potentially efficacious treatment option for *ATM* wild-type, HR-proficient prostate cancer, supporting its exploration in clinical trials. Indeed, a phase II trial exploring combined olaparib (300 mg twice daily for day 1-28 of a 28 day cycle) and ceralasertib (160 mg once daily for days 1-7 of a 28 day cycle) in men with both HR-proficient and deficient metastatic CRPC is currently recruiting (Reichert et al., 2020). The results of this trial, which aims to report in 2025, are eagerly awaited and will provide invaluable insight into whether the findings reported in this thesis translate into the clinical setting.

5 Delineating the mode of action of the PARP1 isoform in both normal prostate homeostasis and prostate cancer development and progression

5.1 Introduction

As discussed previously, PARP enzymes play a key role in a number of biological processes ranging from DNA damage repair and chromatin modulation to transcriptional regulation, inflammation and the cellular stress response (Schreiber et al., 2006, Slade et al., 2011, Hottiger, 2015, Gupte et al., 2017). Whilst least 17 isoforms have been identified, PARP1 is the most abundant and accounts for 85-90% of basal and stimulated PARP activity, followed by PARP2, which accounts for 5-15% (Bai, 2015, Dulaney et al., 2017). Although there is some overlap in function between PARP1 and PARP2 isoforms, particularly in terms of their role in the DDR, recent evidence suggests that they also have isoform specific functions, such as the independent roles of PARP2 in haematopoiesis, spermatogenesis and T cell development (Dantzer et al., 2006, Nicolas et al., 2010, Bai and Cantó, 2012, Farrés et al., 2013, Schiewer and Knudsen, 2014, Ali et al., 2016, Mateo et al., 2017).

GEMMs that enable the manipulation of gene function and/or expression are an invaluable tool for the study of proteins in both normal tissue homeostasis and a spectrum of disease states, including cancer (Vandamme, 2014). Unlike in vitro approaches in which genes can readily be knocked down or overexpressed at a cellular level, GEMMs also allow us to gain an appreciation of the effects of genetic alterations at a tissue and organism level, with preserved stromal and immune system interactions. Furthermore, these models also enable us to gain an appreciation of the natural history and progression of diseases, closely mimicking the clinical picture and providing a platform for the development and testing of therapeutics.

Some of our understanding of PARP1 and PARP2 biology has come through studies utilising GEMMs in which *Parp1* and *Parp2* genes have been disrupted, hence knocking down expression and enabling characterisation of protein function. Given that whole body knockout of *Parp1* and *Parp2* results in embryonic lethality in mice, the study of dual depletion in postnatal and adult life has not been possible using this approach (de Murcia et al., 2003). However, the discovery and development of Cre-LoxP recombination as a means of gene editing with both tissue and time specific control has revolutionised this field of research. Both *Parp1* and *Parp2* floxed alleles have been developed and utilised in conjunction with different Cre recombinase constructs to facilitate depletion of one or both isoforms in a host of different tissue and disease settings (Luo et al., 2017, Navarro et al., 2017).

Whilst the function of PARP enzymes in both normal and disease states has been extensively characterised (Bai, 2015), few authors have examined their role in either the normal adult prostate or during prostate cancer development and progression, with much of the preclinical evidence for use of PARPi in this setting being extrapolated from studies in other solid tumours (Deshmukh and Qiu, 2015). In one of only a handful of preclinical studies of PARP1 function in prostate cancer, Brenner et al. reported that PARP1 is required for ETS gene-mediated transcription and cell invasion, suggesting it may be necessary for progression of prostate cancers possessing the predominant oncogenic ETS gene fusion, *TMPRSS2:ERG* (Brenner et al., 2011). Additionally, Schiewer et al. found that pharmacological inhibition of PARP1 significantly reduced expression of well characterised prostate specific AR target genes, including *PSA* and *TMPRSS2*, with increased levels of auto PARylation and hence PARP1 activity in CRPC cells compared with hormone sensitive cells, implicating PARP1 in both AR function and disease progression (Schiewer et al., 2012). More recently, Asim et al. demonstrated that PARP activity is increased in prostate cancer tissue following ADT, supporting the link between AR and PARP function (Asim et al., 2017). Collectively these studies suggest that PARP plays a distinct role within the prostate, and hence research aimed at better understanding its biology in this setting may provide mechanistic insight into means of increasing the efficacy of PARPi in prostate cancer.

The experiments in this chapter therefore firstly sought to generate and characterise a GEMM for the study of PARP1 function in the normal adult prostate through the conditional depletion of PARP1 within prostatic epithelial cells using *PSA-Cre-ER*^{T2} in combination with the *Parp1* floxed allele. A second GEMM in which the *Parp1* floxed allele was also combined with *p53* and *Pten* floxed alleles was then generated to explore the role of PARP1 in the setting of p53 and PTEN deficient localised prostate cancer. Finally, given the emerging evidence supporting independent roles of PARP1 and PARP2, a series of in vitro experiments were undertaken to determine the effects of selective depletion of individual PARP isoforms using RNA interference in our panel of HR-proficient CRPC cells such to better understand the potential therapeutic effects of isoform specific PARP inhibitors.

5.2 Chapter aims

1. Delineate the role of PARP1 in normal adult mouse prostate tissue homeostasis in vivo.
2. Delineate the role of PARP1 in prostate cancer in vivo using a GEMM of localised disease.
3. Evaluate the biological effects of *PARP1* and *PARP2* knockdown using RNA interference in human CRPC cells in vitro.

5.3 Results

5.3.1 Delineating the role of PARP1 in normal adult mouse prostate tissue homeostasis in vivo

5.3.1.1 *PSA-Cre-ER^{T2} conditional Cre-LoxP targeting to deplete PARP1 in adult mouse prostate luminal epithelial cells reduces Parp1 mRNA transcript expression.*

To evaluate the role of PARP1 in the normal adult mouse prostate, cohorts of male *PSA-Cre-ER$^{T2(+/-)}$* mice harbouring wild-type (wt) *Parp1 (PSA-Cre-ER$^{T2(+/-)}$ Parp1$^{+/+}$* genotype), heterozygous *Parp1* floxed allele *(PSA-Cre-ER$^{T2(+/-)}$ Parp1$^{+/fl}$)* or homozygous *Parp1* floxed alleles *(PSA-Cre-ER$^{T2(+/-)}$ Parp1$^{fl/fl}$* genotype) were generated as outlined in Section 2.3.2. Mice underwent induction with intraperitoneal injection of tamoxifen at 56 days of age (+/- 7 days) and were subsequently aged to either 100 days (+/- 7 days; short term end point, n=6) or 300 days (+/- 7 days; long term end point, n=8-12) post-induction, before being terminated and prostate tissue characterised using histology and IHC. A further age matched cohort of *PSA-Cre-ER$^{T2(+/-)}$ Parp1$^{fl/fl}$* mice did not undergo tamoxifen induction and served as an uninduced control (356 days +/- 7, n = 4). The full details of each cohort and the numbers of mice in each are outlined in ***Table 5.1***.

Table 5.1: Cohort overview for experimental mice used to delineate the role of PARP1 during normal adult mouse prostate homeostasis.

Genotype	Cohort endpoint post induction (age at termination)	Number of mice
PSA-Cre-ER$^{T2(+/-)}$ Parp1$^{+/+}$	100 days (156 +/- 7 days)	6
PSA-Cre-ER$^{T2(+/-)}$ Parp1$^{fl/fl}$	100 days (156 +/- 7 days)	6
PSA-Cre-ER$^{T2(+/-)}$ Parp1$^{+/+}$	300 days (356 +/- 7 days)	12
PSA-Cre-ER$^{T2(+/-)}$ Parp1$^{+/fl}$	300 days (356 +/- 7 days)	8
PSA-Cre-ER$^{T2(+/-)}$ Parp1$^{fl/fl}$	300 days (356 +/- 7 days)	11
PSA-Cre-ER$^{T2(+/-)}$ Parp1$^{fl/fl}$ Uninduced	Not induced (356 +/- 7 days)	4

The *PSA-Cre-ER^{T2}* construct has previously been shown to induce recombination in all lobes of the murine prostate, with highest efficiency in the luminal epithelial cells of the DLP, in which recombination occurs in over 35% (Ratnacaram et al., 2008). To validate that PSA-Cre-ER^{T2} mediated recombination had occurred in experimental mice, *Parp1* floxed allele recombination events were analysed by PCR of gDNA extracted from individual prostate lobes of mice in each cohort harvested at the time of termination (n=3 per genotype) to detect *Parp1* wt, floxed and recombined alleles (***Figure 5.1***). Induction with tamoxifen led to *Parp1* recombination in all lobes of mice that possessed either one or two *Parp1* floxed alleles, but not in those with wild-type *Parp1* alleles. Furthermore, recombination was present at both the short and long term endpoints. Whilst there appears to be a weak band for the recombined allele in the anterior prostate of two mice in the *PSA-Cre-ER$^{T2(+/-)}$ Parp1$^{+/+}$* cohort, these are of much lower intensity and are most likely the result of sample contamination during the PCR reaction.

Having identified that recombination occurs within each of the prostate lobes, qRT-PCR was performed to determine if recombination of *Parp1* floxed alleles correlated with a reduction in *Parp1* mRNA expression. RNA was extracted from DLP lobes that were snap frozen in liquid nitrogen at the time of dissection and qRT-PCR performed to evaluate fold change in *Parp1* mRNA relative to that expressed in the DLP of *Parp1* wild-type mice, as described in Section 2.1.7. As shown in ***Figure 5.2***, recombination of both *Parp1* alleles significantly reduced expression relative to *Parp1* wild type (0.401-fold reduction; p=0.047), confirming that tamoxifen induction of mice with the *PSA-Cre-ER$^{T2(+/-)}$ Parp1$^{fl/fl}$* genotype results in conditional depletion of *Parp1* in luminal prostate epithelial cells that correlates with a reduction in *Parp1* mRNA expression of over 50%. Furthermore, given that this was a bulk RNA sample that included transcripts from basal and neuroendocrine cells together with those of the surrounding stroma in which *PSA-Cre-ER^{T2}* does not induce recombination, it would be anticipated that the degree of depletion within the epithelial cells themselves would be even greater.

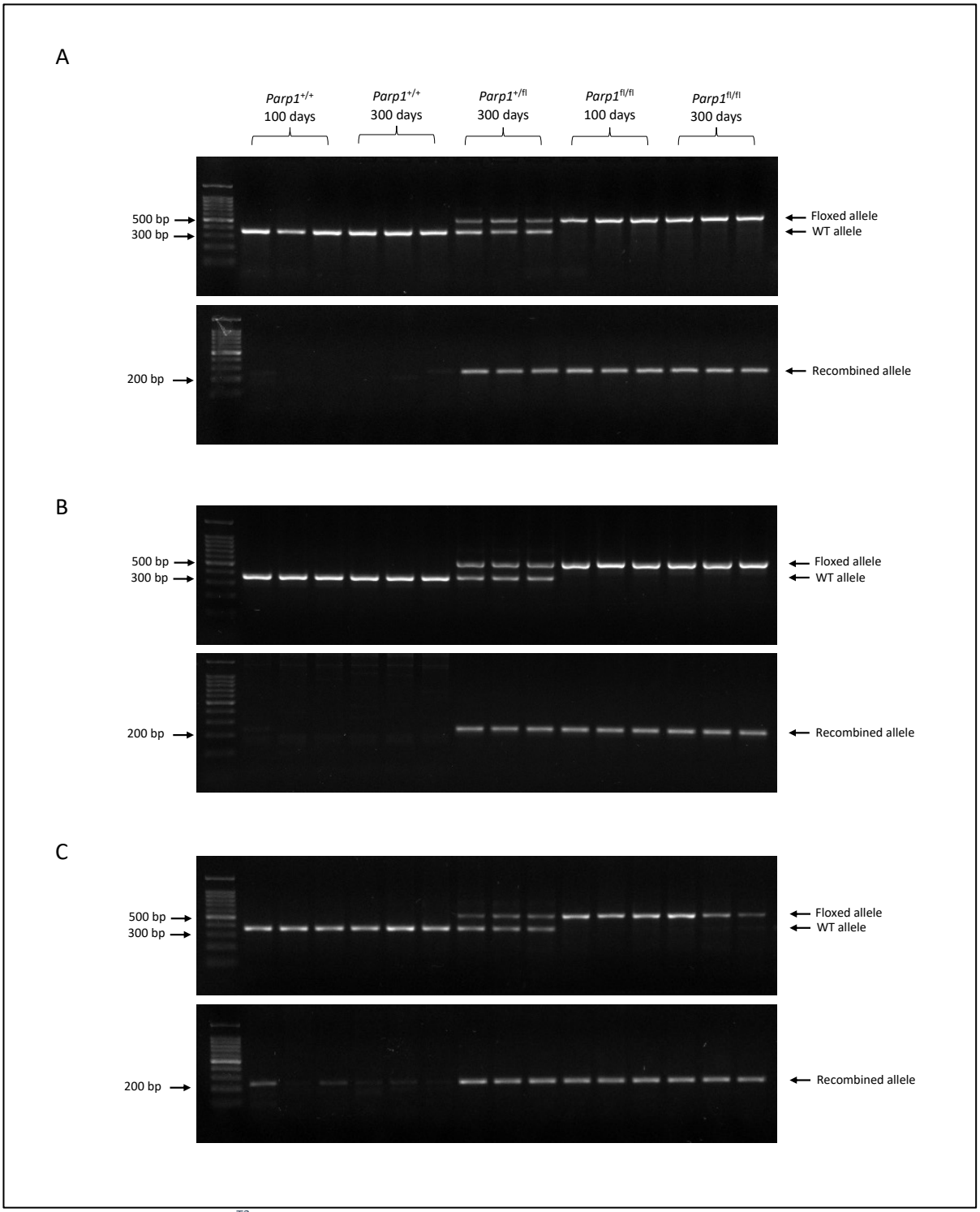

Figure 5.1: *The PSA-Cre-ER^{T2} transgene mediates recombination of Lox-P flanked Parp1 alleles in all lobes of the murine prostate following induction with intraperitoneal injection of tamoxifen.* Representative gel images demonstrating the presence of bands for WT (550 bp) and floxed *Parp1* (370 bp) in the ventral prostate (A), dorsolateral prostate (B) and anterior prostate (C) of each of the experimental cohorts indicated (n=3/genotype, top gel image), and the recombined *Parp1* allele (238 bp, bottom gel image), confirming that recombination has occurred. WT; wild type. bp; base pairs.

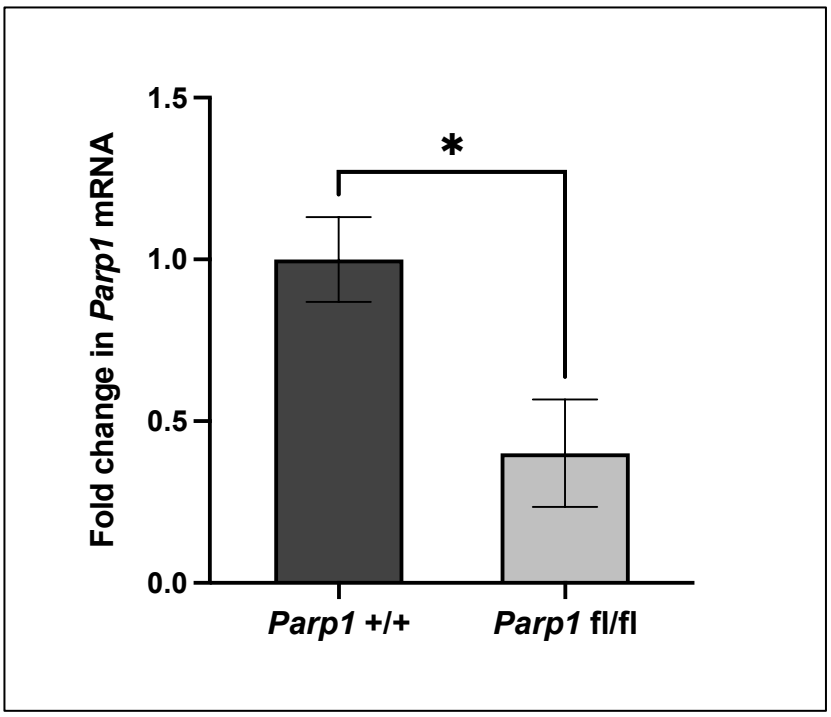

Figure 5.2: *PSACre-ER^{T2}-mediated recombination reduces Parp1 mRNA expression in dorsolateral (DLP) lobes of the mouse prostate.* Bar chart demonstrating fold change in *Parp1* mRNA transcript levels in the DLP lobes of *PSA-Cre-ER$^{T2(+/-)}$* positive mice that had undergone induction with intraperitoneal injection of tamoxifen at 8 weeks and aged to 300 days (+/- 7 days) post induction, as stratified according to *Parp1* genotype and determined using quantitative reverse transcription PCR. RNA extracted from DLP lobes of three mice per cohort (n=3) with three technical repeats per lobe. Error bars represent Standard Error of the mean. Statistical significance calculated using unpaired students t-test. * Symbols showing comparisons with *PSA-Cre-ER$^{T2(+/-)}$ Parp1$^{+/+}$* mice *: $P \leq 0.05$.

5.3.1.2 Conditional depletion of PARP1 within the prostatic epithelium does not significantly alter survival or overall body weight compared with Parp1 wild-type controls

Induction of recombination via daily intraperitoneal injection of 0.1 mg of tamoxifen for 5 consecutive days was well tolerated, with all cohort mice surviving to their allocated end points. The mean total body weights at the 300 day (+/- 7 days) post induction study endpoint for *PSA-Cre-ER$^{T2(+/-)}$ Parp1$^{+/+}$* , *PSA-Cre-ER$^{T2(+/-)}$ Parp1$^{+/fl}$ and PSA-Cre-ER$^{T2(+/-)}$ Parp1$^{fl/fl}$* experimental cohort mice were 37.1 g, 41.1 g and 43.5 g respectively (***Figure 5.3***). Although these data suggest that the presence of the *Parp1* floxed allele may be associated with an increase in total body weight, these differences did not reach statistical significance.

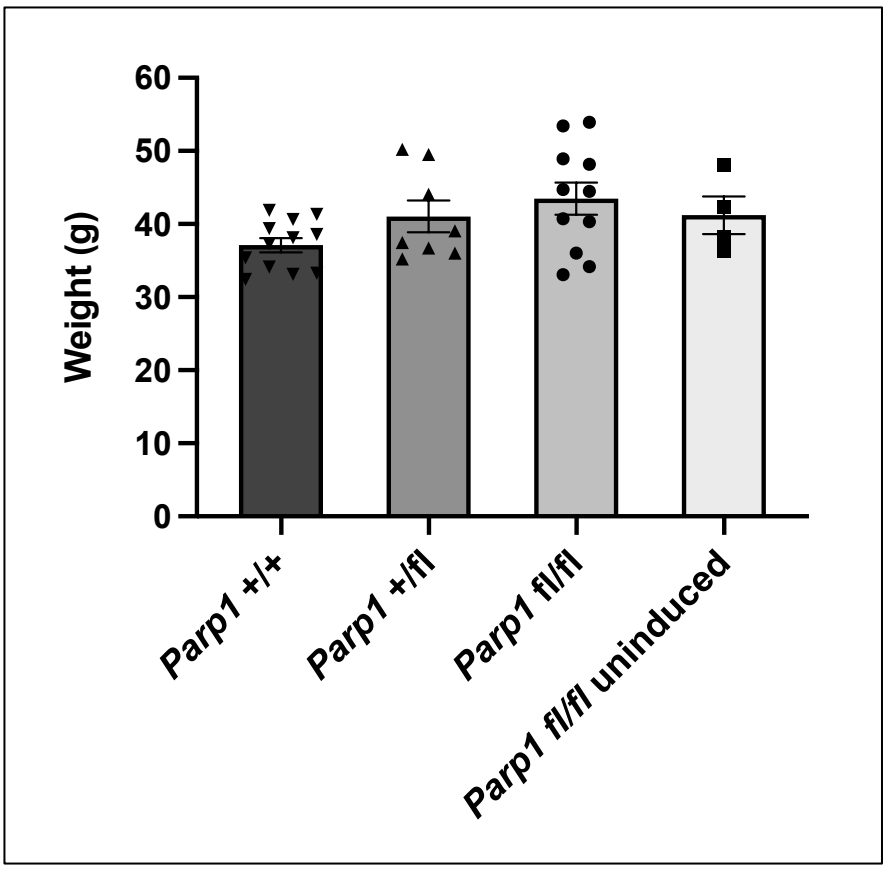

Figure 5.3: *Conditional depletion of PARP1 within the prostatic epithelium does not significantly alter overall body weight at 300 days following induction of recombination with intraperitoneal injection of tamoxifen.* Bar chart demonstrating final total body weight of mice at the 300 day post induction study endpoint. Individual mice represented as symbols. Error bars represent Standard Error of the mean. Statistical significance calculated using one-way ANOVA with Tukey correction for multiple comparisons, with no differences reaching the significance threshold. fl, floxed.

5.3.1.3 Conditional depletion of PARP1 within the prostatic epithelium results in variations in the weight of individual prostate lobes at both short and long term timepoints

To determine if PARP1 deficiency during normal adult prostate tissue homeostasis effects prostate growth, the weight of the total prostate and individual prostate lobes were compared for *PSA-Cre-ER$^{T2(+/-)}$* mice expressing either *Parp1$^{+/+}$*, *Parp1$^{+/fl}$* or *Parp1$^{fl/fl}$* alleles at 100 days and 300 days post-induction. Whilst there was no difference in total prostate weights between genotypes (overall or relative to total body mass) at 100 days, VP weight was statistically significantly higher in those of the *PSA-Cre-ER$^{T2(+/-)}$ Parp1$^{fl/fl}$* genotype compared to those of *PSA-Cre-ER$^{T2(+/-)}$ Parp1$^{+/+}$* mice (7.6 mg +/- 0.69 mg SEM versus 4.6 mg +/- 0.61 mg SEM, P = 0.031 and 0.024% +/- 0.0023% SEM versus 0.014% +/- 0.0022% SEM, P = 0.038, for overall and relative weights respectively; ***Figure 5.4***). A corresponding decrease was observed in overall and relative DLP weight, although the differences did not reach significance, whilst AP weight remained unchanged. These data therefore suggest that short term loss

of PARP1 function within the prostatic epithelium may result in impaired growth of the DLP alongside increased growth of the VP, whilst having no overall effect on total prostate weight.

Similar variation was observed at 300 days post induction. Interestingly, recombination of only one *Parp1* allele (*PSA-Cre-ER$^{T2(+/-)}$ Parp1$^{+/fl}$*) resulted in a decrease in overall total prostate weight compared with *PSA-Cre-ER$^{T2(+/-)}$ Parp1$^{+/+}$* mice (119.2 mg +/- 11.6 mg SEM versus 139.8 mg +/- 5.7 mg SEM). Recombination of both *Parp1* alleles (*PSA-Cre-ER$^{T2(+/-)}$ Parp1$^{fl/fl}$* mice) resulted in an increase (160.3 mg +/- 6.5 mg SEM), with the differences between this and the *PSA-Cre-ER$^{T2(+/-)}$ Parp1$^{+/fl}$* mice proving statistically significant (P=0.004). However, this trend was less pronounced when adjusting for body weight, with differences in relative prostate weight failing to reach significance. The opposite trend was observed in respect to the VP, with the overall and relative VP weight of *PSA-Cre-ER$^{T2(+/-)}$ Parp1$^{+/fl}$* mice being greater than that of *PSA-Cre-ER$^{T2(+/-)}$ Parp1$^{+/+}$* and *PSA-Cre-ER$^{T2(+/-)}$ Parp1$^{fl/f}$* mice, although these differences failed to reach significance. A corresponding decrease in overall and relative AP weight was seen in *PSA-Cre-ER$^{T2(+/-)}$ Parp1$^{+/fl}$* mice, although again this failed to reach significance. There was no discernible difference in overall or relative DLP weight between the difference genotypes.

Collectively these data indicate that alteration in PARP1 expression within the murine prostate is associated with time and lobe specific differences in growth as represented by weight. However, the magnitude of effect failed to reach statistical significance in all but a limited number of comparisons, thereby indicating the need for mechanistic evaluation to determine the effects of PARP1 loss at a cellular level.

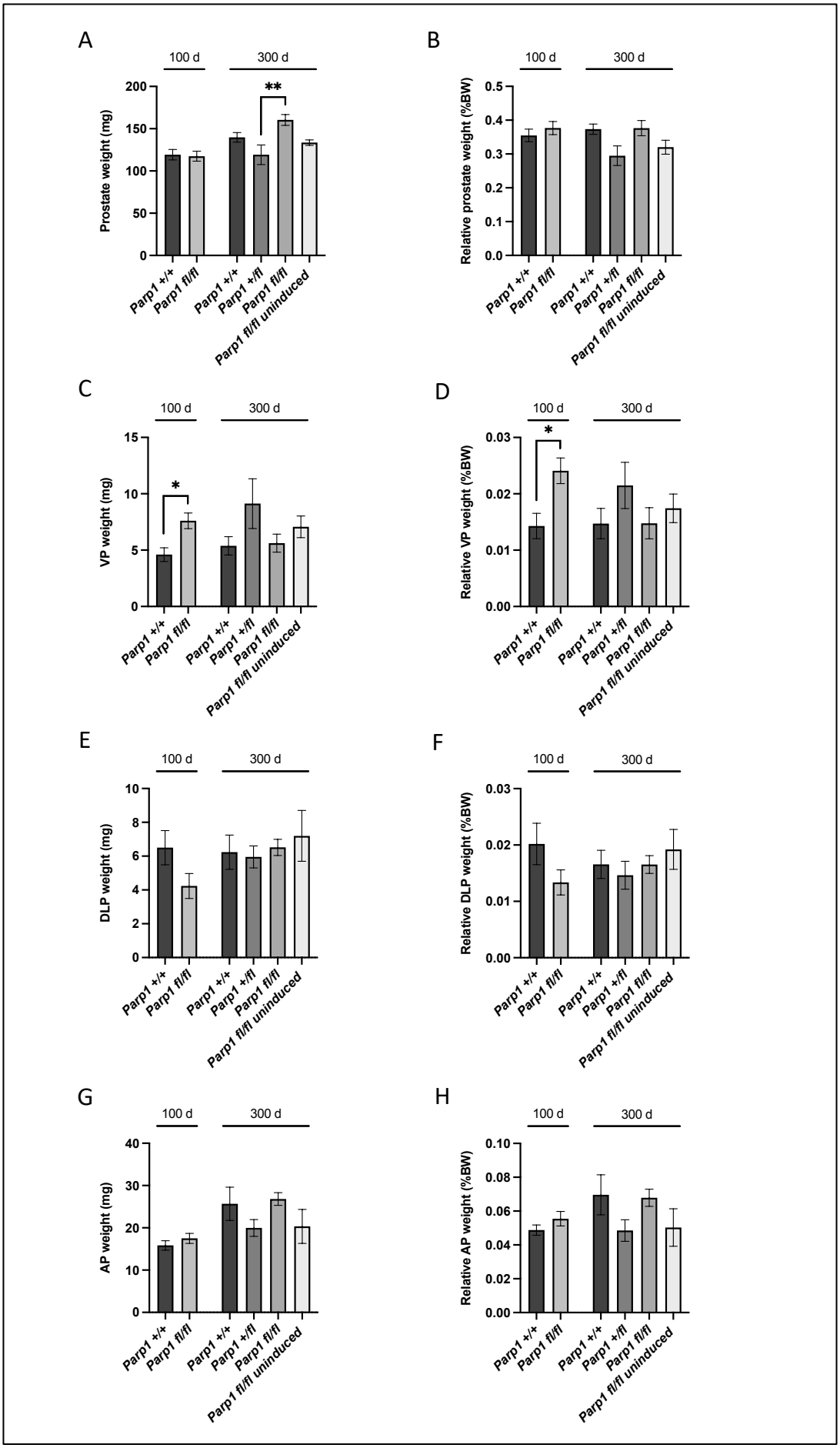
A
100 d
300 d
Prostate weight (mg)
200
150
100
50
0
**
Parp1 +/+
Parp1 fl/fl
Parp1 +/+
Parp1 +/fl
Parp1 fl/fl
Parp1 fl/fl uninduced
B
100 d
300 d
Relative prostate weight (%BW)
0.5
0.4
0.3
0.2
0.1
0.0
Parp1 +/+
Parp1 fl/fl
Parp1 +/+
Parp1 +/fl
Parp1 fl/fl
Parp1 fl/fl uninduced
C
100 d
300 d
VP weight (mg)
15
10
5
0
*
Parp1 +/+
Parp1 fl/fl
Parp1 +/+
Parp1 +/fl
Parp1 fl/fl
Parp1 fl/fl uninduced
D
100 d
300 d
Relative VP weight (%BW)
0.03
0.02
0.01
0.00
*
Parp1 +/+
Parp1 fl/fl
Parp1 +/+
Parp1 +/fl
Parp1 fl/fl
Parp1 fl/fl uninduced
E
100 d
300 d
DLP weight (mg)
10
8
6
4
2
0
Parp1 +/+
Parp1 fl/fl
Parp1 +/+
Parp1 +/fl
Parp1 fl/fl
Parp1 fl/fl uninduced
F
100 d
300 d
Relative DLP weight (%BW)
0.03
0.02
0.01
0.00
Parp1 +/+
Parp1 fl/fl
Parp1 +/+
Parp1 +/fl
Parp1 fl/fl
Parp1 fl/fl uninduced
G
100 d
300 d
AP weight (mg)
40
30
20
10
0
Parp1 +/+
Parp1 fl/fl
Parp1 +/+
Parp1 +/fl
Parp1 fl/fl
Parp1 fl/fl uninduced
H
100 d
300 d
Relative AP weight (%BW)
0.10
0.08
0.06
0.04
0.02
0.00
Parp1 +/+
Parp1 fl/fl
Parp1 +/+
Parp1 +/fl
Parp1 fl/fl
Parp1 fl/fl uninduced

Figure 5.4: *Conditional depletion of PARP1 in the prostatic epithelium results in variations in total prostate weight and individual lobe weight at 100 and 300 days following induction of recombination with intraperitoneal injection of tamoxifen.* A: Overall total prostate weight. B: Relative total prostate weight, calculated as overall prostate weight / total body weight x 100. C-H: Overall and relative VP, DLP and AP weights. Relative weight of each lobe calculated as individual lobe weight / total body weight x 100. *PSA-Cre-ER$^{T2(+/-)}$ Parp-1$^{+/fl}$*(100 d, n=3; 300 d, n=6); *PSA-Cre-ER$^{T2(+/-)}$ Parp-1$^{+/fl}$*(300 d, n=4); *PSA-Cre-ER$^{T2(+/-)}$ ER^{T2} Parp-1$^{fl/fl}$* (100 d, n=3; 300 d, n=6); *PSA-Cre-ER$^{T2(+/-)}$ Parp-1$^{fl/fl}$* uninduced (300 d, n=3). Error bars represent Standard Error of the mean. Statistical significance calculated using Student's t test (100 d) and one-way ANOVA with Tukey correction for multiple comparisons (300 d). **: P ≤ 0.01, *: P ≤ 0.05. fl, floxed; BW, total body weight.

5.3.1.4 Conditional depletion of PARP1 within the prostatic epithelium does not result in malignant transformation or alter the glandular architecture of individual prostate lobes at either 100 or 300 days following induction with intraperitoneal injection of tamoxifen

To determine the effect of PARP1 depletion on the growth and development of the murine prostate, the morphology of individual prostate lobes was firstly evaluated through assessment of glandular phenotype on H&E stained sections of each experimental cohort at low and high power (n=4-12 per genotype and timepoint). The total number of glands in each lobe was quantified and the proportion demonstrating features of each of the histological morphologies, including epithelial hyperplasia, prostatic intraepithelial neoplasia (PIN) and invasive carcinoma were calculated. Representative microscopy images of each lobe are illustrated in ***Figure 5.5***. Irrespective of genotype, no glands in any lobe demonstrated features of either hyperplasia, PIN or invasive carcinoma. Furthermore, there were no differences in glandular appearance between individual genotypes, collectively indicating that conditional depletion of PARP1 mediated by *PSA-Cre-ER^{T2}* does not result in either changes in glandular architecture or predispose to malignant transformation within the murine prostate at either the short or long term timepoints.

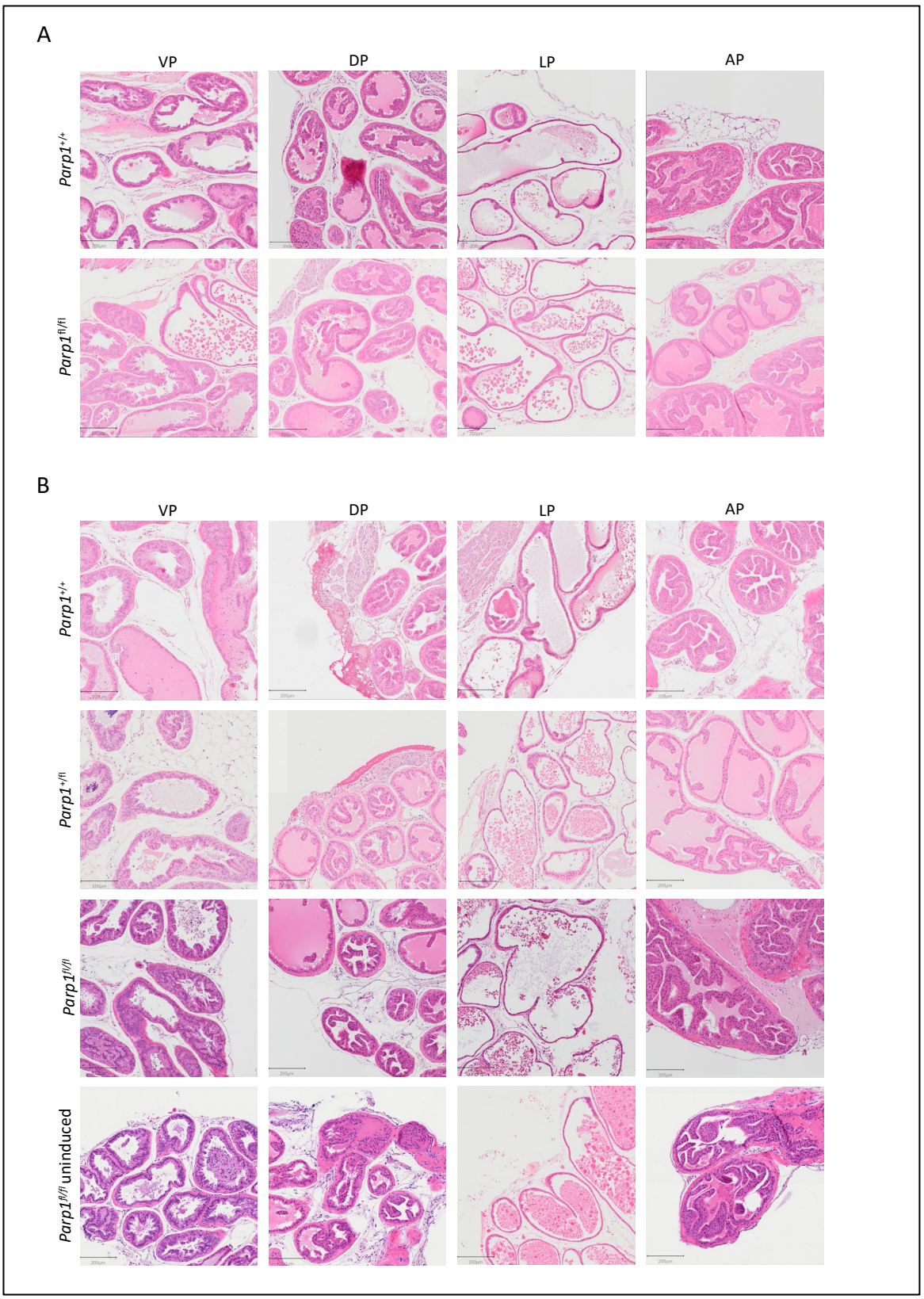

Figure 5.5: *Conditional depletion of PARP1 in the prostatic epithelium does not alter the histological appearances of the glands of individual prostate lobes at either 100 or 300 days post induction.* Representative light microscopy images demonstrating the histological glandular morphology within individual prostate lobes based on the extent of conditional knockout of *Parp1* within the prostatic epithelium. A: 100 day timepoint. B: 300 day timepoint. No glands demonstrated hyperplasia, prostatic intraepithelial neoplasia or invasive carcinoma. Scale bars represent 200µm. VP, ventral prostate; DP, dorsal prostate; LP, lateral prostate; AP, anterior prostate. fl, floxed.

5.3.1.5 *Conditional depletion of PARP1 within the prostatic epithelium does not alter the CK5 positive basal cell population within the glands of each prostate lobe at either 100 or 300 days following induction of recombination with intraperitoneal injection of tamoxifen*

To determine the effect of conditional depletion of PARP1 on the distribution of luminal and basal cells within individual glands of each prostate lobe, 4 μm sections of prostate taken from *PSA-Cre-ER$^{T2(+/-)}$ Parp1$^{+/+}$, Parp1$^{+/fl}$ and Parp1$^{fl/fl}$* mice at both the 100 and 300 day timepoints were stained for the basal and luminal cell markers CK5 and CK8 respectively using immunohistochemistry (n=3 per genotype and timepoint). Representative high power microscopy images of CK5 stained glands of each lobe are illustrated in ***Figure 5.6***. Quantitation of CK5-positive cells in *PSA-Cre-ER$^{T2(+/-)}$ Parp1$^{+/+}$* mice revealed the ventral lobe to have the lowest basal cell population in comparison to other lobes, as shown in ***Figure 5.7***. Whilst biallelic *Parp1* depletion appeared to increase the proportion of CK5-positive basal cells in the DP, LP and AP at the 100 day post induction timepoint, these differences failed to reach statistical significance and were no longer evident by the 300 day post induction timepoint, at which point no discernible trends were identified.

Formal quantitation of the proportion of luminal cells in each gland based on CK8 positivity was not possible due to the larger cytoplasmic area of the luminal cells overlying that of the smaller basal cells, preventing accurate determination of total glandular cell count. However, evaluation of sections at high power did not demonstrate any significant differences in appearance between genotypes or timepoints, as demonstrated in ***Figure 5.8***. Collectively these data therefore indicate that, despite a trend towards an increased proportion of CK5 positive cells in the DP, LP and AP associated with biallelic *Parp1* depletion in the short term, long term depletion does not appear to significantly alter the distribution of basal and luminal cell populations within any prostate lobe, suggesting that PARP1 does not play an important role in epithelial cell differentiation. However, further work utilising a different methodological approach such as immunofluorescence using antibodies for both basal and luminal markers simultaneously is needed to fully quantitate the different cell populations and calculate the ratios between each.

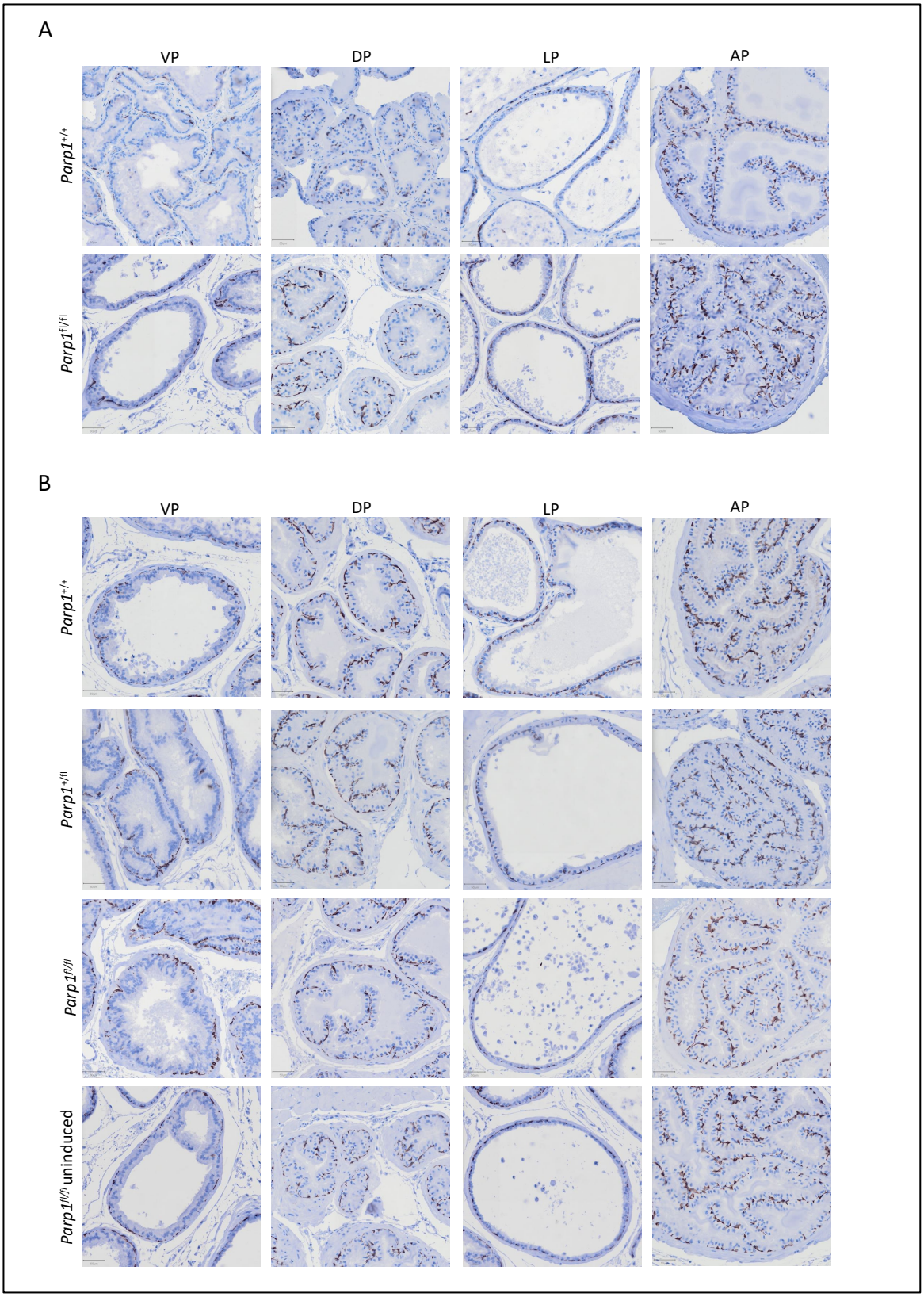

Figure 5.6: *Conditional depletion of PARP1 in the prostatic epithelium does not alter the proportion of CK5 positive basal cells in the glands of individual prostate lobes at either 100 or 300 days post induction.* Representative high power light microscopy images of tissue stained for CK5 using immunohistochemistry demonstrating the distribution and proportion of CK5 positive basal cells (brown stained cells) within individual glands of each prostate lobe based on the extent of conditional knockout of *Parp1* within the prostatic epithelium. A: 100 day timepoint. B: 300 day timepoint. Scale bars represent 50 µm. VP, ventral prostate; DP, dorsal prostate; LP, lateral prostate; AP, anterior prostate. fl, floxed.

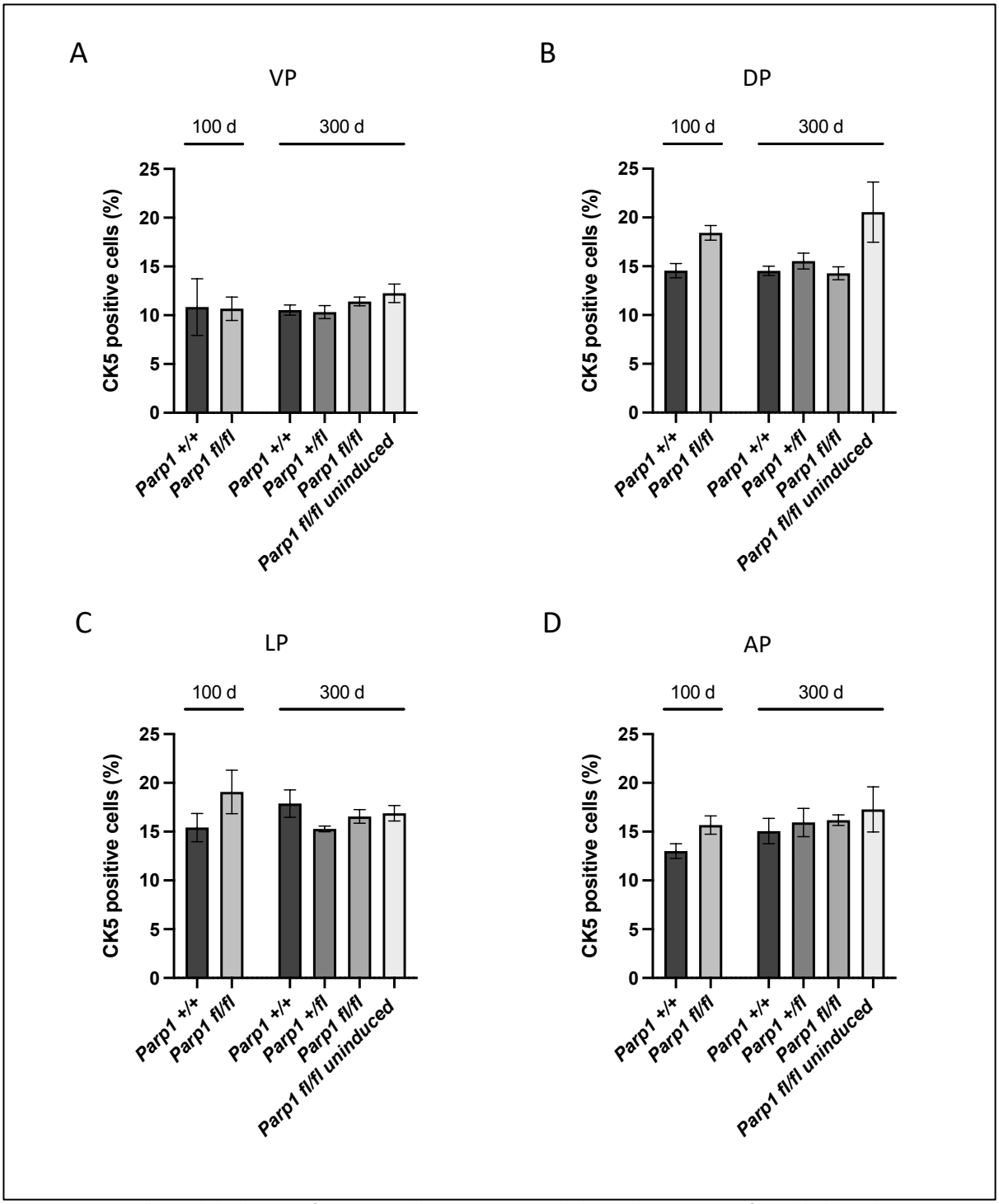

Figure 5.7: *Conditional depletion of PARP1 in the prostatic epithelium does not significantly alter the proportion of CK5 positive basal cells in the glands of individual prostate lobes at either 100 or 300 days post induction.* Bar charts demonstrating the mean percentage of CK5 positive basal cells per gland within each of the individual prostate lobes as stratified according to genotype and timepoint. A: Ventral prostate lobe (VP). B: Dorsal prostate lobe (DP). C: Lateral prostate lobe (LP). D: Anterior prostate lobe (AP). Glands of the ventral lobe demonstrated the lowest proportion of basal cells compared with other lobes, with no significant difference in the proportion or distribution observed between different genotypes or timepoints. Three mice per genotype (n=3), with quantification performed using at least 1000 cells of representative glands of each lobe per mouse. Error bars represent Standard Error of the mean. Statistical significance calculated using one-way ANOVA with Tukey correction for multiple comparisons, with no differences reaching the significance threshold.

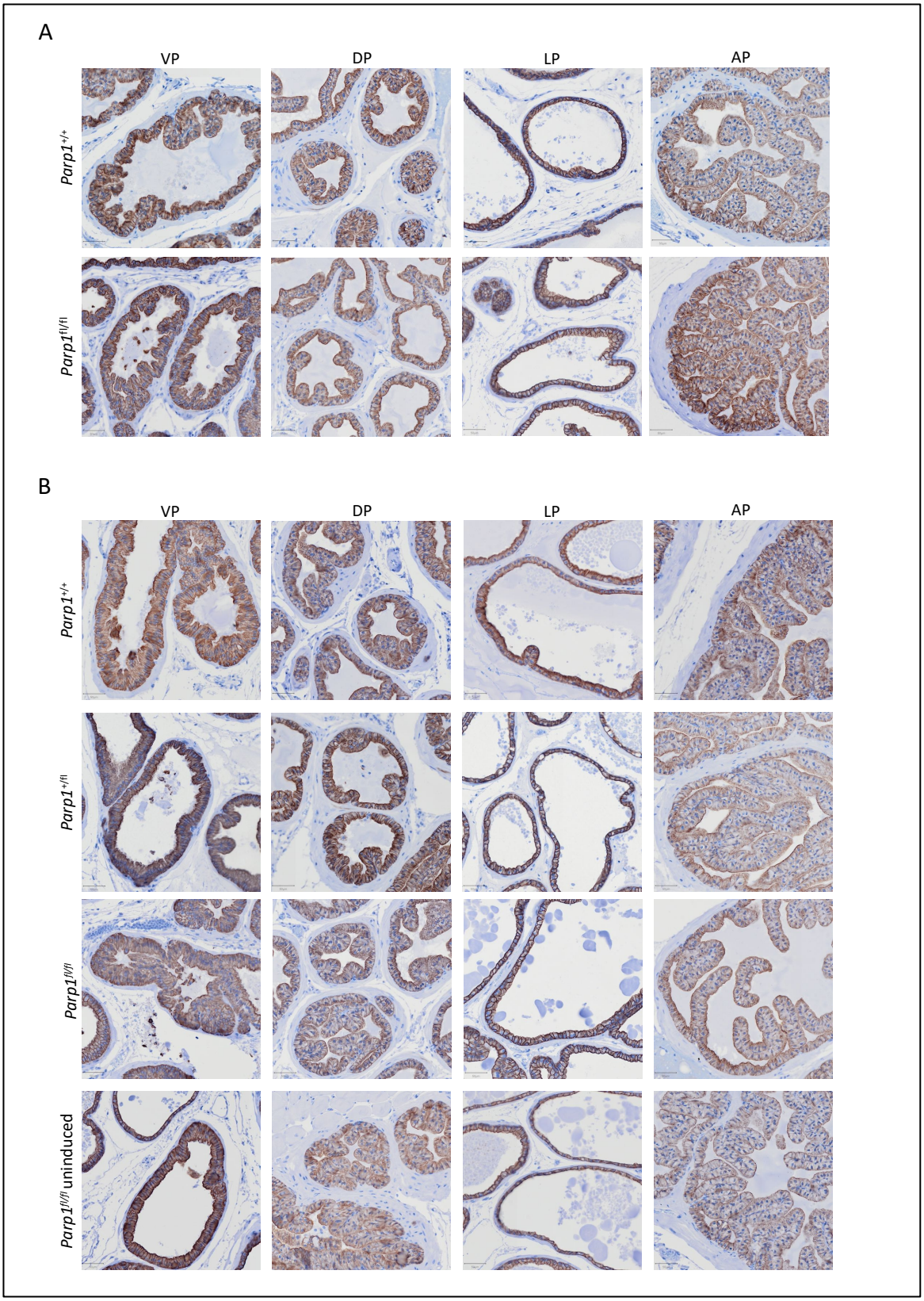

Figure 5.8: *Conditional depletion of PARP1 in the prostatic epithelium does not alter the proportion of CK8 positive luminal cells in the glands of individual prostate lobes at either 100 or 300 days post induction.* Representative high power light microscopy images of tissue stained for CK5 using immunohistochemistry demonstrating the distribution and proportion of CK8 positive basal cells (brown stained cells) within individual glands of each prostate lobe based on the extent of conditional knockout of *Parp1* within the prostatic epithelium. A: 100 day timepoint. B: 300 day timepoint. Scale bars represent 50 µm. VP, ventral prostate; DP, dorsal prostate; LP, lateral prostate; AP, anterior prostate. fl, floxed.

5.3.1.6 *Depletion of PARP1 within the prostatic epithelium increases the level of cellular proliferation in anterior prostate at both 100 and 300 days following induction of recombination with intraperitoneal injection of tamoxifen*

To further confirm that PARP1 is not essential for the maintenance of normal adult mouse prostate tissue homeostasis, immunohistochemistry was used to evaluate the number of cells undergoing proliferation in the glands of each lobe. As such, 4 μm sections of prostate were stained for proliferating cell nuclear antigen (PCNA) using immunohistochemistry as previously described (n=3 mice per genotype and timepoint). The number of PCNA positive cells per gland was quantitated and then divided by the total number of cells per gland to give the PCNA index, with a minimum of 1000 cells counted per lobe.

Representative microscopy images of PCNA stained sections of each lobe and each genotype are shown in ***Figure 5.9***. Quantitation of PCNA positive cells revealed that irrespective of genotype or timepoint, the PCNA index was highest in glands of the VP (2.31-3.59%) and AP lobes (1.24%-3.08%), with lower levels seen in those of the DP (1.20-1.74%) and LP (0.99-1.45%) lobes, as illustrated in ***Figure 5.10***. Interestingly, these levels of proliferation were much lower than observed previously in the PC-3 subcutaneous xenograft tumours (72.0%), and the PIN glands of *PSA-Cre-ER*$^{T2(+/-)}$ and *p53*$^{fl/fl}$ *; Pten*$^{fl/fl}$ model of localised prostate cancer (9.83%), indicating that the baseline level of proliferation in normal prostatic epithelium that has not been transformed by tumourigenic genetic alteration is low. The proportion of PCNA positive cells in glands of the anterior lobe was greatest in *PSA-Cre-ER*$^{T2(+/-)}$ *Parp1*$^{fl/fl}$ mice when compared with *PSA-Cre-ER*$^{T2(+/-)}$ *Parp1*$^{+/+}$ controls at both the 100 day short term timepoint (1.765 +/- 0.07% SEM versus 1.24% +/- 0.06% SEM; P=0.001) and the 300 day long term timepoint (3.08% +/- 0.32% SEM versus 1.66% +/- 0.09% SEM; P=0.042). A similar trend was also observed in the VP at the 100 day timepoint, although this failed to reach significance and was no longer evident by the 300 day post induction timepoint, at which point no discernible differences were identified. There were no differences in the proportion of PCNA positive cells in glands of the DP or LP between the genotypes at either timepoint.

Finally, to determine whether conditional depletion of PARP1 resulted in an increase in the number of cells undergoing apoptosis within each of the lobes, 4 μM sections were also stained for the apoptotic marker cleaved caspase-3 (CC-3; n=3 per genotype and timepoint). However, the positive cell numbers were negligible in each of the lobes and there was no visual difference between each genotype at either timepoint, so formal quantitation was not performed. Collectively, these data demonstrate that, when compared with wild-type controls, biallelic depletion of *Parp1* appears to result in an increase in the proliferation of cells within the glands of the VP in the short term and the

glands of the AP in both the short and long term, although comparisons were only statistically significant with respect to the AP and were not associated with any changes in apoptosis. The loss of PARP1 function therefore appears to have some impact on the proliferative capacity of prostatic epithelial cells in both a time and lobe specific manner.

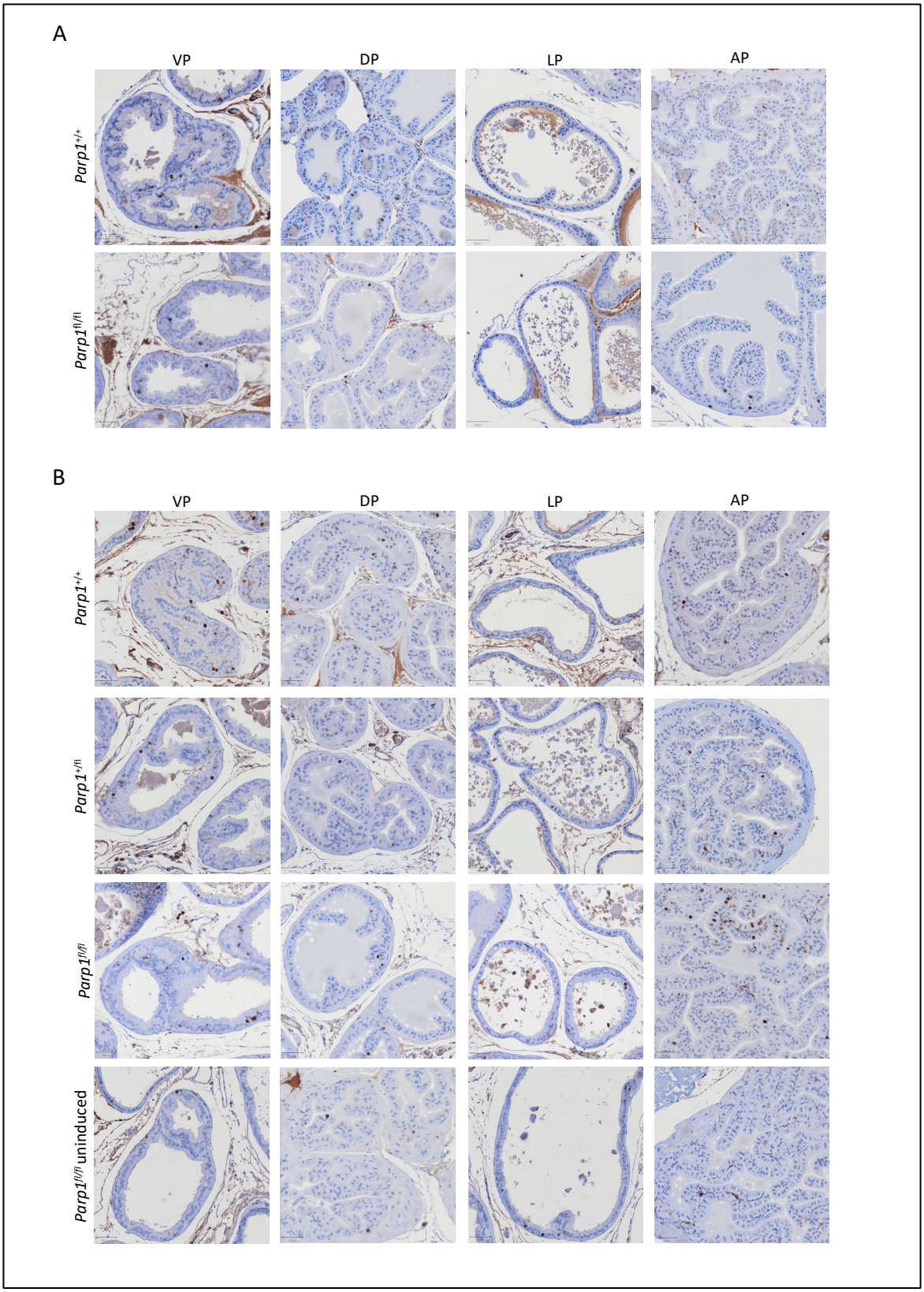

Figure 5.9: *Conditional depletion of PARP1 in the prostatic epithelium increases the proportion of PCNA positive proliferating cells in the anterior prostate lobe compared with wild-type controls at both 100 and 300 days post induction.* Representative high power light microscopy images of tissue stained for PCNA using immunohistochemistry to demonstrate the distribution and proportion of PCNA positive proliferating cells (brown stained cells) within individual glands of each prostate lobe based on the extent of conditional knockout of *Parp1* within the prostatic epithelium. A: 100 day timepoint. B: 300 day timepoint. Scale bars represent 50 µm. VP, ventral prostate; DP, dorsal prostate; LP, lateral prostate; AP, anterior prostate. fl, floxed.

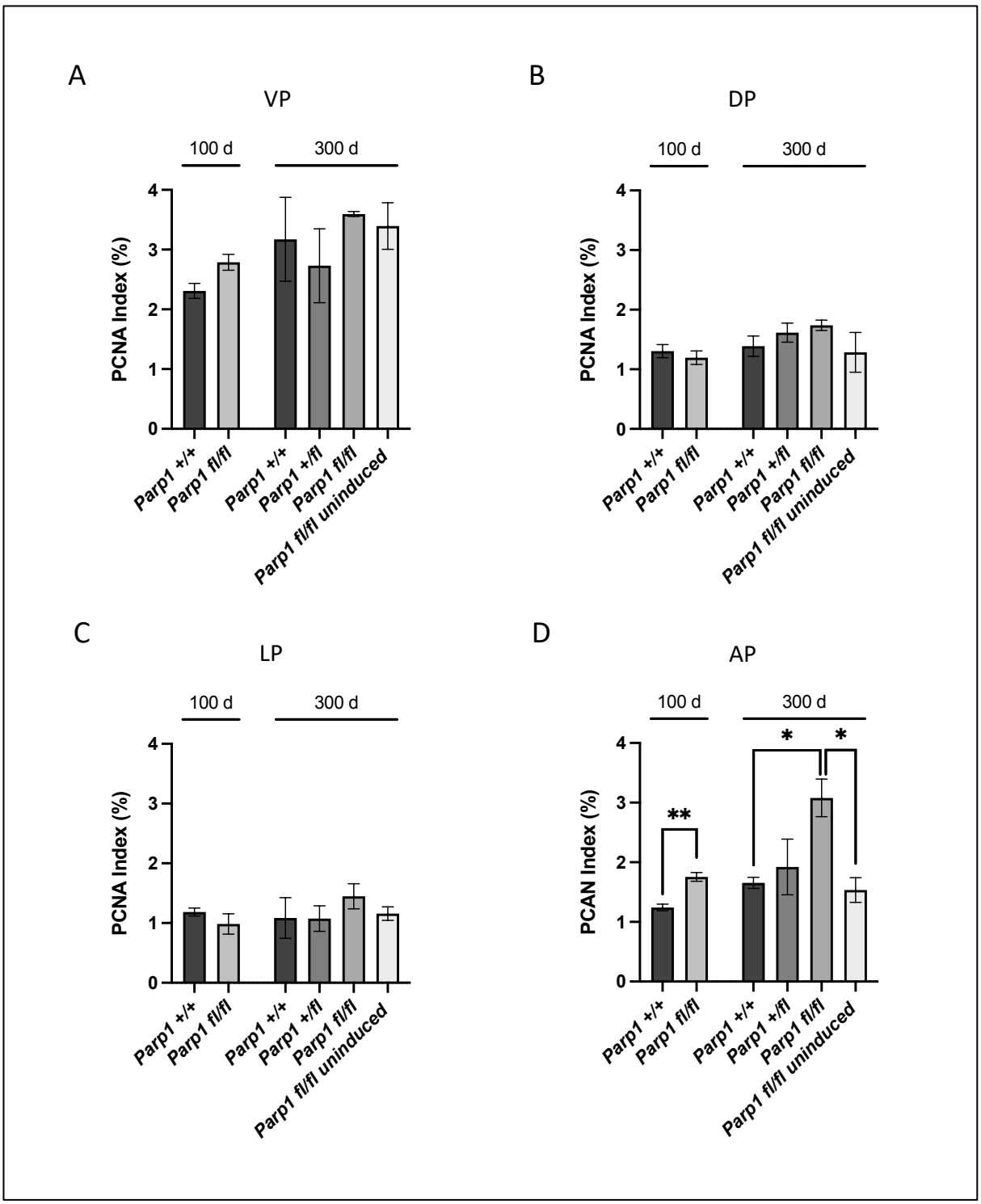

Figure 5.10: *Conditional depletion of PARP1 in the prostatic epithelium increases the proportion of PCNA positive proliferating cells in the anterior prostate lobe compared with wild-type controls at both 100 and 300 days post induction.* Bar charts demonstrating the mean percentage of PCNA positive basal cells per gland (termed PCNA index) within each of the individual prostate lobes as stratified according to genotype and timepoint. A: Ventral prostate lobe (VP). B: Dorsal prostate lobe (DP). C: Lateral prostate lobe (LP). D: Anterior prostate lobe (AP). Three mice per genotype (n=3), with quantification performed using at least 1000 cells of representative glands of each lobe per mouse. Error bars represent Standard Error of the mean. Statistical significance calculated using one-way ANOVA with Tukey correction for multiple comparisons. **: $P \leq 0.01$, *: $P \leq 0.05$. fl, floxed;

5.3.2 Delineating the role of PARP1 in prostate cancer in vivo using a GEMM of localised disease

5.3.2.1 Tamoxifen induction of mice co-expressing PSA-Cre-ER^{T2}, p53 floxed alleles, Pten floxed alleles and the Parp1 floxed allele results in successful recombination within localised prostate tumours

Having characterised the role of PARP1 within the normal adult prostate, the next series of experiments sought to determine its role in prostate cancer. A conditional transgenic approach was again utilised in which the Cre-LoxP recombination system was used to selectively delete *Parp1* alleles within the prostatic epithelial cells of male mice in combination with simultaneous deletion of the *Trp53* and *Pten* tumour suppressor genes. As discussed in Section 4.3.3, prior characterisation of *PSA-Cre-ER$^{T2(+/-)}$; p53$^{fl/fl}$; Pten$^{fl/fl}$* mice at 6 months following induction of recombination with intraperitoneal injection of tamoxifen demonstrated development of small localised tumours, predominantly involving the ventral lobes and comprising of PIN, with focal areas of microinvasive carcinoma (***Figure 4.17***). In order to enable tumours to progress to a greater extent and hence explore the role of PARP1 in more locally advanced disease, mice were aged to a later timepoint of 7.5 months (210 days) post induction. To generate experimental cohorts, *PSA-Cre-ER$^{T2(+/-)}$; p53$^{fl/fl}$; Pten$^{fl/fl}$* mice were bred with *Parp1$^{fl/fl}$* mice, and progeny intercrossed to produce *PSA-Cre-ER$^{T2(+/-)}$; p53$^{fl/fl}$; Pten$^{fl/fl}$* mice expressing either *Parp1$^{+/+}$*, *Parp1$^{+/fl}$* and *Parp1$^{fl/fl}$* as outlined in ***Table 5.2***. Mice subsequently underwent induction with intraperitoneal injection of tamoxifen at 56 days as described in Section 2.3.2.6 and were aged to 210 days post-induction before being terminated and prostate tissue weighed and characterised by histology and IHC. Prior to undertaking analysis, gDNA was isolated from tumours and underwent PCR to reconfirm the genotype of each experimental animal and validate that recombination of the *Parp1* floxed allele occurred as expected (***Figure 5.11)***.

Table 5.2: *Cohort overview for experimental mice used to delineate the role of PARP1 using a GEMM of localised prostate cancer.*

Genotype	Cohort endpoint post induction (age at termination)	Number of mice
PSA-Cre-ER$^{T2(+/-)}$ Parp-1$^{+/+}$ p53$^{fl/fl}$ Pten$^{fl/fl}$	210 days (266 +/- 7 days)	7
PSA-Cre-ER$^{T2(+/-)}$ Parp-1$^{+/fl}$ p53$^{fl/fl}$ Pten$^{fl/fl}$	210 days (266 +/- 7 days)	4
PSA-Cre-ER$^{T2(+/-)}$ Parp-1$^{+/fl}$ p53$^{fl/fl}$ Pten$^{fl/fl}$	210 days (266 +/- 7 days)	4

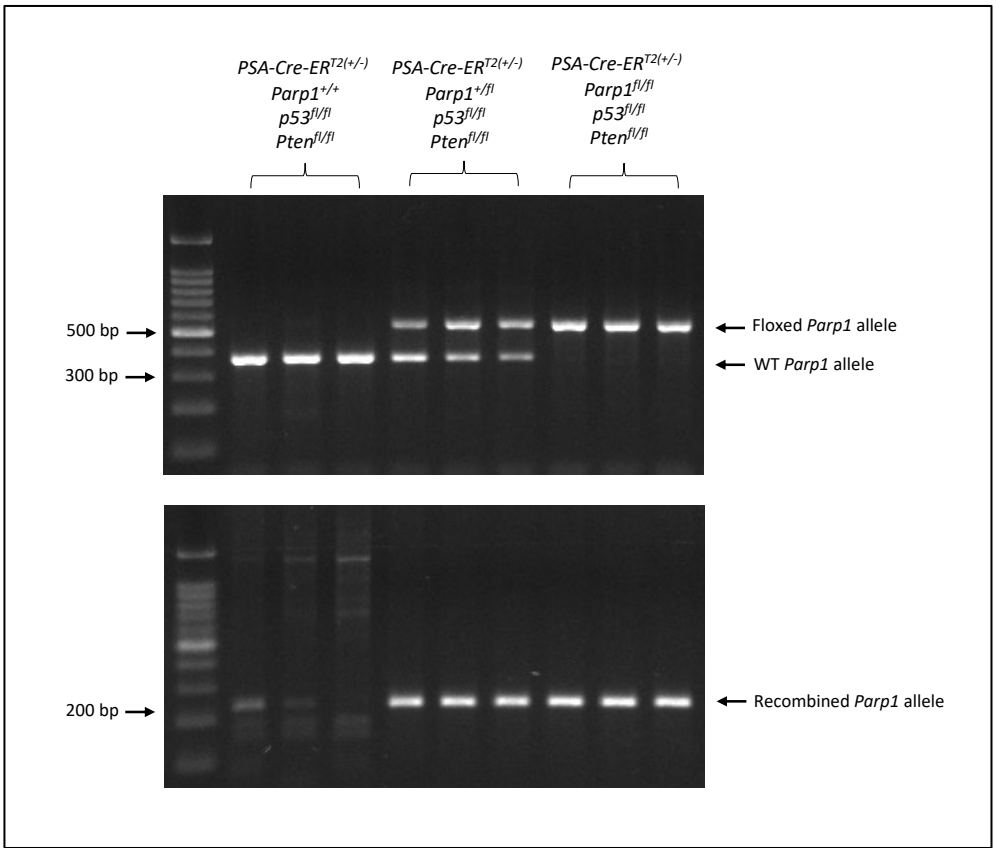

Figure 5.11: *PSA-Cre-ER^{T2} induces recombination of LoxP flanked Parp1 alleles in tumours arising in mice harbouring both LoxP flanked p53 and Pten alleles after intraperitoneal administration of tamoxifen at 56 days of age.* Representative gel images demonstrating the presence of bands for WT (550 bp) and floxed Parp1 (370 bp) in the tumours (above) in of each of the experimental cohorts (n=3 for each), with a further representative gel image (below) demonstrating the presence of a band representing the recombined Parp1 allele (238 bp), confirming that recombination has occurred. Prior confirmation of p53 and Pten genotype was also performed, data not shown. WT; wild type. Bp; base pairs.

5.3.2.2 *Conditional depletion of PARP1 within the prostatic epithelium of PSA-Cre-ER$^{T2(+/-)}$; p53$^{fl/fl}$; Pten$^{fl/fl}$ mice does not significantly alter survival or overall body weight compared with Parp1 wild-type controls.*

As with the conditional knockout model utilised in Section 5.3.1, induction of recombination via daily intraperitoneal injection of 0.1 mg of tamoxifen for 5 consecutive days was well tolerated. No experimental mice died within the study period, revealing that PARP1 depletion within the prostatic epithelium of *PSA-Cre-ER$^{T2(+/-)}$; p53$^{fl/fl}$; Pten$^{fl/fl}$* mice that are predisposed to localised prostate tumours does not impact on overall or disease specific mortality. Furthermore, this also confirms the that unlike simultaneous *p53* and *Pten* knockout driven by PB-Cre4, which results in disease specific mortality by 7 months of age (Chen et al., 2005), tumours of the *PSA-Cre-ER$^{T2(+/-)}$; p53$^{fl/fl}$; Pten$^{fl/fl}$* model are slower growing and did not result in the death of any mouse by the time point utilised in this study.

Figure 5.12 indicates total body weight at the study endpoint for each of the experimental cohorts. Interestingly the presence of the *Parp1* floxed allele again appeared to be associated with a small increase in total body weight, with mean weights of 34.9g, 37.3g and 36.9g for mice with the *PSA-Cre-ER$^{T2(+/-)}$; Parp1$^{+/+}$; p53$^{fl/fl}$; Pten$^{fl/fl}$*, *PSA-Cre-ER$^{T2(+/-)}$; Parp1$^{+/fl}$; p53$^{fl/fl}$; Pten$^{fl/fl}$ and PSA-Cre-ER$^{T2(+/-)}$; Parp-1$^{fl/fl}$; p53$^{fl/fl}$; Pten$^{fl/fl}$* genotypes respectively, although these differences did not reach statistical significance.

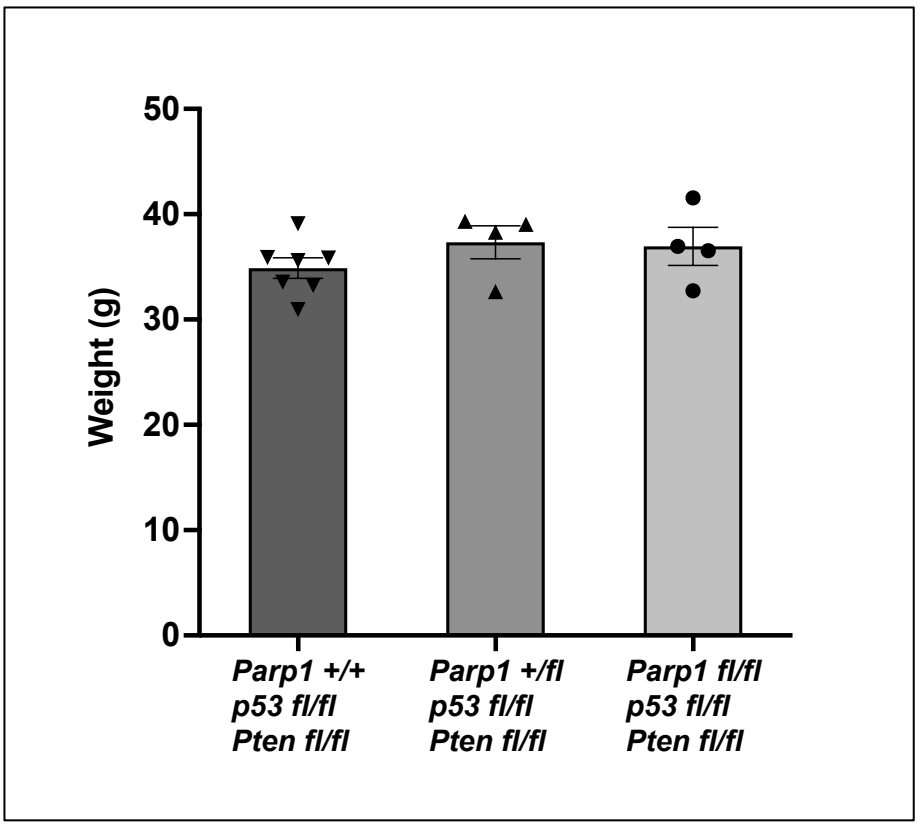

Figure 5.12: *Conditional depletion of PARP1 within the prostatic epithelium of PSA-Cre-ER$^{T2(+/-)}$; p53$^{fl/fl}$; Pten$^{fl/fl}$ mice does not significantly alter overall body weight at 210 days following induction of recombination with intraperitoneal injection of tamoxifen.* Bar chart demonstrating total body weight of mice at the study endpoint. Individual mice represented as symbols. Error bars represent Standard Error of the mean. Statistical significance calculated using one-way ANOVA with Tukey correction for multiple comparisons, with no differences reaching the significance threshold.

5.3.2.3 Conditional depletion of PARP1 within the prostatic epithelium of PSA-Cre-ER$^{T2(+/-)}$; p53$^{fl/fl}$; Pten$^{fl/fl}$ mice significantly reduces weight of the dorsolateral prostate at 210 days following induction of recombination with intraperitoneal injection of tamoxifen

To determine the role of PARP1 during localised prostate cancer growth in *PSA-Cre-ER$^{T2(+/-)}$; p53$^{fl/fl}$; Pten$^{fl/fl}$* mice, prostates of those expressing *Parp1$^{+/+}$*(n=7), *Parp1$^{+/fl}$* (n=4) and *Parp1$^{fl/fl}$* (n=4) alleles were dissected and weighed at 210 days post-induction and either fixed in formalin for subsequent IHC analysis or snap frozen in liquid nitrogen for further molecular analysis. The lobes of those prostates which were snap frozen were also first dissected individually and weighed to allow comparison of individual lobe weight between genotypes (n=4 per lobe for *Parp1$^{+/+}$,* n=3 per lobe for *Parp1$^{+/fl}$* and n=3 per lobe for *Parp1$^{fl/fl}$*). Weight values were represented as either overall weight, or relative weight calculated as a percentage of total body weight at the time of dissection.

There was no discernible difference in overall or relative total prostate weight between genotypes, as shown in ***Figure 5.13A***. There was also no difference in either overall or relative VP or AP weights

between cohorts (***Figure 5.13B*** and ***Figure 5.13D***). However, on the contrary, conditional knockout of either one or both *Parp1* alleles resulted in a highly significant reduction in overall weight of the DLP compared with *Parp1* wild-type controls (25.8mg +/- 0.34mg SEM for *PSA-Cre-ER*$^{T2(+/-)}$*; Parp1*$^{+/+}$*; p53*$^{fl/fl}$ *Pten*$^{fl/fl}$ versus 7.1mg +/- 2.4mg SEM for *PSA-Cre-ER*$^{T2(+/-)}$*; Parp1*$^{+/fl}$*; p53*$^{fl/fl}$; *Pten*$^{fl/fl}$ *(P<0.001)* and 6.2mg +/- 1.8mg SEM for *PSA-Cre-ER*$^{T2(+/-)}$*; Parp1*$^{fl/fl}$*; p53*$^{fl/fl}$; *Pten*$^{fl/fl}$ (P<0.001)), with a similar trend observed in DLP weight relative to total body weight (***Figure 5.13C***). These data therefore suggest that depletion of PARP1 within the prostatic epithelium alongside simultaneous depletion of p53 and PTEN results in impaired growth of the DLP but does not significantly alter the growth of either the VP or AP. Further histological and molecular evaluation was therefore warranted to determine the effects of PARP1 depletion at the cellular level.

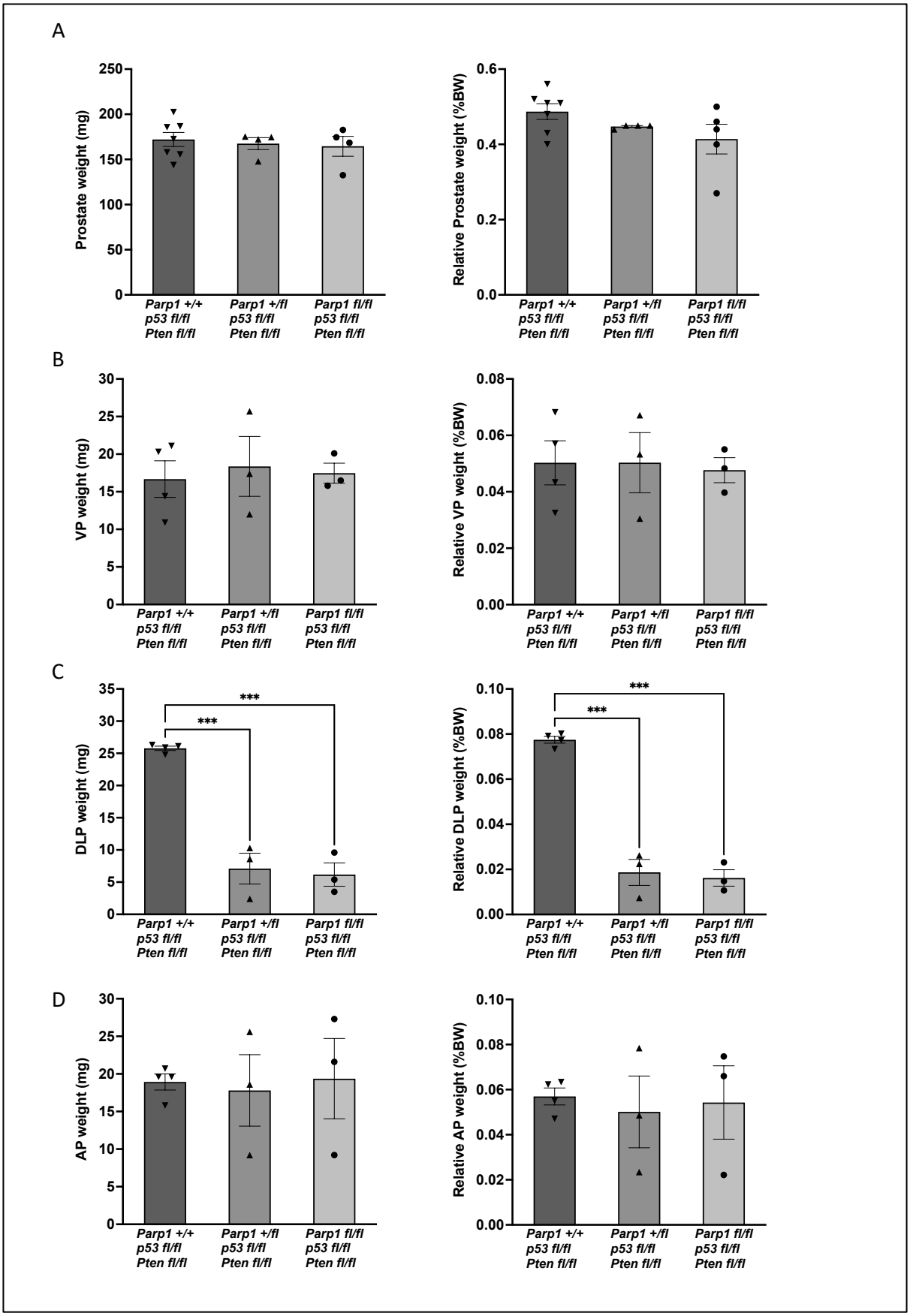
A
Prostate weight (mg)
250
200
150
100
50
0
Parp1 +/+ p53 fl/fl Pten fl/fl
Parp1 +/fl p53 fl/fl Pten fl/fl
Parp1 fl/fl p53 fl/fl Pten fl/fl
Relative Prostate weight (%BW)
0.6
0.4
0.2
0.0
B
VP weight (mg)
30
25
20
15
10
5
0
Relative VP weight (%BW)
0.08
0.06
0.04
0.02
0.00
C
DLP weight (mg)
35
30
25
20
15
10
5
0
***
***
Relative DLP weight (%BW)
0.10
0.08
0.06
0.04
0.02
0.00
D
AP weight (mg)
Relative AP weight (%BW)

Figure 5.13: *Simultaneous PARP1 depletion results in a significant reduction in the DLP weight of PSA-Cre-ER$^{T2(+/-)}$; p53$^{fl/fl}$; Pten$^{fl/fl}$ mice at 210 days following induction of recombination.* A: Overall total prostate weight and relative total prostate weight, calculated as overall prostate weight / total body weight x 100. B-D: Overall and relative VP, DLP and AP weights. Relative weight of each lobe calculated as individual lobe weight / total body weight x 100. Individual mice represented as symbols, with individual lobe weight only measured in those mice in each cohort allocated to snap freezing and subsequent molecular analysis. Error bars represent Standard Error of the mean. Statistical significance calculated using Student's t test. * symbols depicting statistical significance; ***: P ≤ 0.001. BW; total body weight.

5.3.2.4 Conditional depletion of PARP1 within the prostatic epithelium does not alter the histological morphology of glands within localised prostate tumours in PSA-Cre-ER$^{T2(+/-)}$; p53$^{fl/fl}$; Pten$^{fl/fl}$ mice

To determine the histopathological effect of PARP1 depletion on *PSA-Cre-ER$^{T2(+/-)}$; p53$^{fl/fl}$; Pten$^{fl/fl}$* tumour growth, H&E stained sections of tumour from each experimental cohort (n=4 per genotype) were evaluated using light microscopy, as shown in ***Figure 5.14A***. Due to issues during tissue processing and sectioning, not all sections included glands of each individual lobe and so only glands within tumours were assessed and compared.

Histopathological analysis of the glands within each tumour revealed that all mice developed both PIN and invasive carcinoma within the 210 day study period, regardless of *Parp1* genotype. PIN was the most common pathological morphology observed in control *PSA-Cre-ER$^{T2(+/-)}$; Parp1$^{+/+}$; p53$^{fl/fl}$ Pten$^{fl/fl}$* mice (51.0% prevalence), followed by epithelial hyperplasia (15.0%) and invasive carcinoma (11.6%; ***Figure 5.14B***). The conditional deletion of either one or both *Parp1* alleles did not significantly alter these proportions, thereby indicating that depletion of PARP1 alone has no impact on the proportion of glands progressing to PIN and invasive carcinoma following simultaneous depletion of p53 and PTEN at 210 days following recombination.

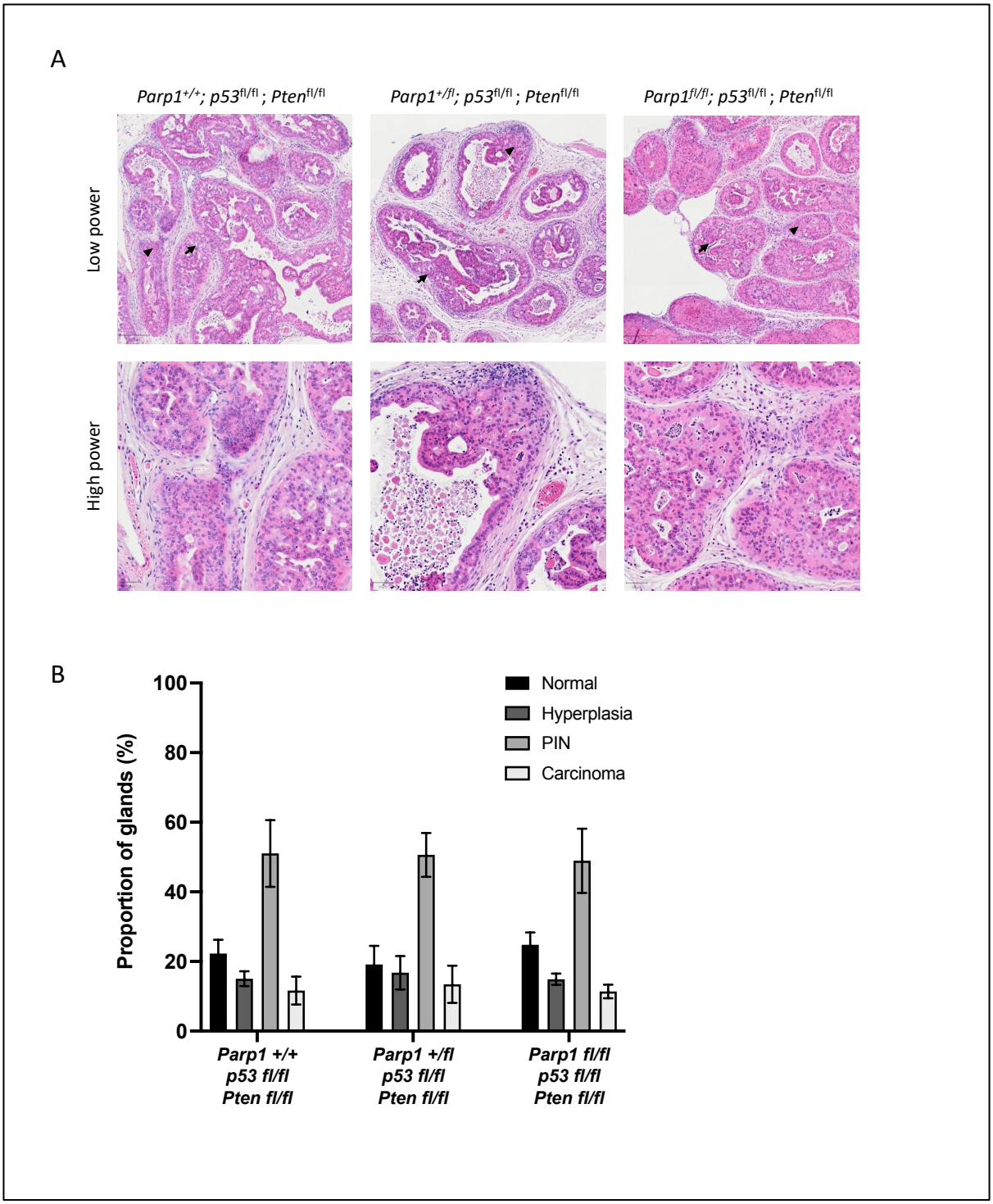

Figure 5.14: *Conditional depletion of PARP1 within the prostatic epithelium of localised prostate tumours developed by PSA-Cre-ER$^{T2(+/-)}$; p53$^{fl/fl}$; Pten$^{fl/fl}$ mice does not alter histological morphology of individual glands.* A: Representative low and high power light microscopy images demonstrating the histological glandular morphology within localised prostate tumours developed by *PSA-Cre-ER$^{T2(+/-)}$; p53$^{fl/fl}$; Pten$^{fl/fl}$* mice according to *Parp1* genotype. Multiple glands demonstrated prostatic intraepithelial neoplasia (PIN; black arrows), with a smaller proportion demonstrating microinvasive carcinoma (black arrow heads), together with surrounding reactive stroma. Scale bars represent 200 µm and 50 µm respectively. B: Bar chart demonstrating the distribution of glandular morphology within tumours of each genotype, with PIN being most common, followed by hyperplasia and invasive carcinoma. Four mice per genotype, with all glands of the tumour present on each H&E stained slide evaluated at high power. Error bars represent Standard Error of the mean. Statistical significance calculated using one-way ANOVA with Tukey correction for multiple comparisons, with no differences reaching the significance threshold.

5.3.2.5 *Conditional depletion of PARP1 within the prostatic epithelium does not alter the proportion of CK5 positive basal cells within individual glands of localised prostate tumours in PSA-Cre-ER$^{T2(+/-)}$; p53$^{fl/fl}$; Pten$^{fl/fl}$ mice*

To determine the effect of conditional depletion of PARP1 on the distribution of luminal and basal cells within individual glands of the localised prostate tumours of PSA-Cre-ER$^{T2(+/-)}$*; p53$^{fl/fl}$; Pten$^{fl/fl}$* mice, 4 μM sections of tumour tissue taken at the 210 day post-induction timepoint were stained for the basal and luminal cell markers CK5 and CK8 respectively using IHC. As in Section 5.3.1.5, CK8 staining overlapped adjacent basal cells, therefore rendering its use in the quantification of luminal cells inaccurate.

Representative low and high power microscopy images of CK5 and CK8 stained glands within the tumours of each genotype are illustrated in ***Figure 5.15A***. The majority of glands were surrounded by a single, non-continuous layer of CK5 positive basal cells, as was observed in Section 5.3.1.5. However, in areas of microinvasive carcinoma the basal cell layer was often significantly disrupted. This appearance was consistent throughout all genotypes, irrespective of *Parp1* genotype.

Quantitation of the proportion of CK5 positive basal cells per individual gland within tumours of each genotype was subsequently undertaken as previously described. A mean of 9.03% (+/- 0.74% SEM) of cells comprising tumour glands in *PSA-Cre-ER$^{T2(+/-)}$; Parp1$^{+/+}$; p53$^{fl/fl}$; Pten$^{fl/fl}$* mice were CK5 positive basal cells (***Figure 5.15B***), which is lower than that observed in each of the individual lobes of *Parp1* wild-type mice without co-existent p53 and PTEN depletion (***Figure 5.7***). This is most likely due to expansion of the luminal cell population in the transformed glands relative to the basal cell population as a result of reduced p53 and PTEN function. Additional loss of either one or both *Parp1* alleles did not significantly alter the proportion of CK5 positive basal cells (9.06% +/- 0.475 SEM and 9.94% +/- 0.27% SEM respectively), indicating that PARP1 depletion does not alter basal cell differentiation status in *PSA-Cre-ER$^{T2(+/-)}$; Parp1$^{+/+}$; p53$^{fl/fl}$; Pten$^{fl/fl}$* mice.

A

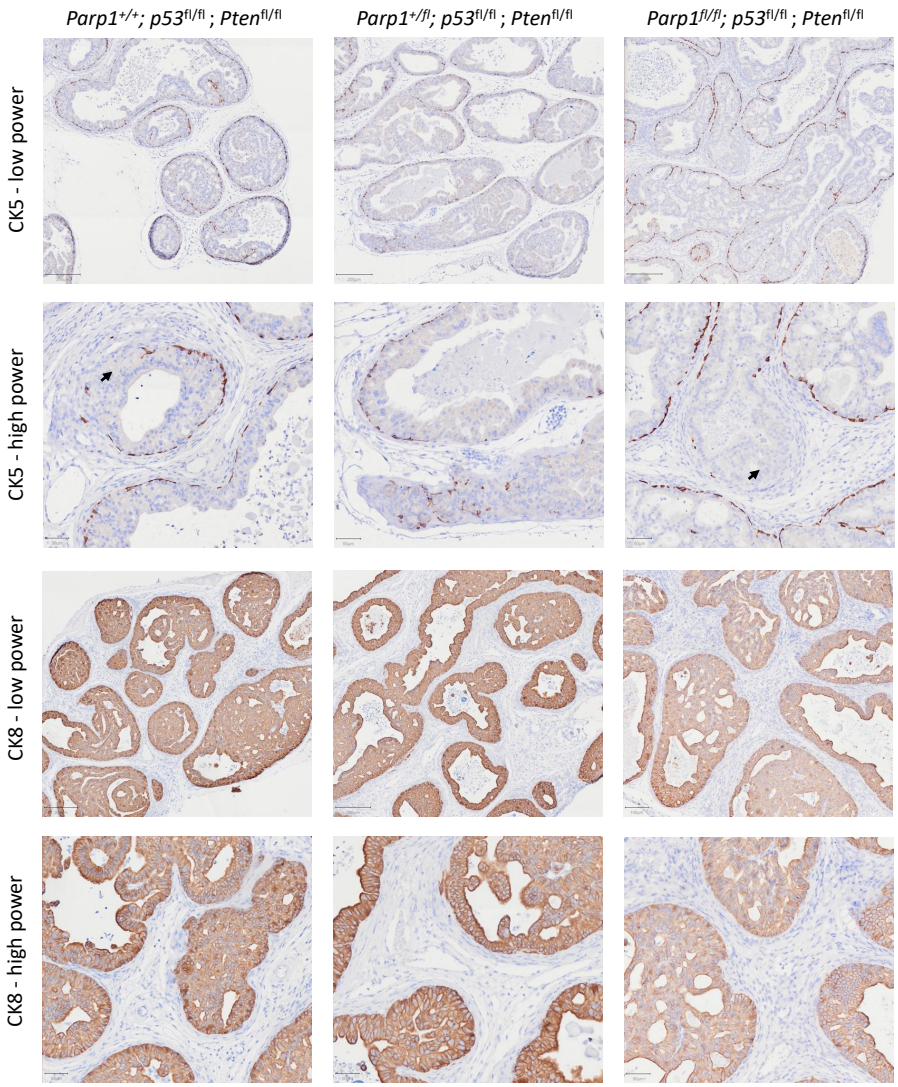
Parp1+/+; p53fl/fl ; Ptenfl/fl
Parp1+/fl; p53fl/fl ; Ptenfl/fl
Parp1fl/fl; p53fl/fl ; Ptenfl/fl
CK5 - low power
CK5 - high power
CK8 - low power
CK8 - high power

B

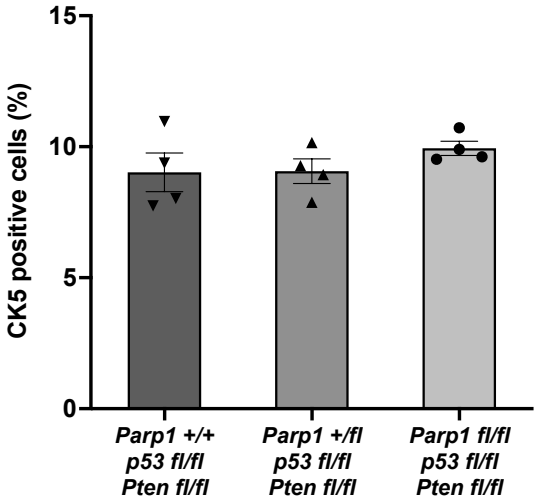
CK5 positive cells (%)
15
10
5
0
Parp1 +/+ p53 fl/fl Pten fl/fl
Parp1 +/fl p53 fl/fl Pten fl/fl
Parp1 fl/fl p53 fl/fl Pten fl/fl

Figure 5.15: *Conditional depletion of PARP1 within the prostatic epithelium does not result in a change in the proportion or distribution of CK5 positive basal cells within individual glands of localised prostate tumours developed by PSA-Cre-ER$^{T2(+/-)}$; p53$^{fl/fl}$; Pten$^{fl/fl}$ mice.* A: Representative light microscopy images at low and high power of tissue stained for CK5 and CK8 using immunohistochemistry to demonstrate the distribution of basal and luminal cells respectively. Basal cells were generally absent in areas of microinvasion (black arrows). Scale bars represent 200 µm and 50 µm respectively. B: Bar chart demonstrating the proportion of CK5 positive basal cells within individual glands of tumours according to *Parp1* genotype. Four mice per genotype, with quantification performed using at least 1000 cells of representative glands of each lobe per mouse. Error bars represent Standard Error of the mean. Statistical significance calculated using one-way ANOVA with Tukey correction for multiple comparisons, with no differences reaching the significance threshold.

5.3.2.6 Conditional depletion of PARP1 within the prostatic epithelium does not alter proliferation or apoptosis within individual glands of localised prostate tumours in PSA-Cre-ER$^{T2(+/-)}$; p53$^{fl/fl}$; Pten$^{fl/fl}$ mice

Given that 21 days of pharmacological PARP inhibition was not found to significantly alter the proportion of cells undergoing active proliferation or apoptosis in transformed glands of *PSA-Cre-ER$^{T2(+/-)}$; p53$^{fl/fl}$; Pten$^{fl/fl}$* mice in the preclinical study outlined in Section 4.3.3, experiments were conducted to determine whether long term depletion of PARP1 via conditional knockout of *Parp1* in the same transgenic model had a similar response, indicating this model is insensitive to PARP1 inhibition/loss. As such, 4 µM sections of tumour tissue from mice of each genotype taken at 210 day post-induction were stained for both PCNA and CC-3 using IHC (n=4 per genotype). Glands within each tumour underwent further analysis to quantify the total number of cells in each along with the number that were PCNA and CC-3 positive, enabling calculation of the PCNA and CC-3 indices as previously described.

Representative low and high power microscopy images of PCNA stained glands within the tumours of each genotype are illustrated in ***Figure 5.16A***, with the mean PCNA index of each demonstrated in ***Figure 5.16B***. The PCNA index of tumours from *PSA-Cre-ER$^{T2(+/-)}$; Parp1$^{+/+}$; p53$^{fl/fl}$; Pten$^{fl/fl}$* mice was 9.50% (+/- 0.74% SEM), which is similar to the 9.83% seen in PIN glands of vehicle treated *PSA-Cre-ER$^{T2(+/-)}$* and *p53$^{fl/fl}$; Pten$^{fl/fl}$* tumours in the aforementioned preclinical trial. The additional knockout of either one or both *Parp1* alleles had no effect on the number of PCNA positive cells in tumour glands (8.78% +/- 0.61% SEM and 9.96% +/- 1.0% SEM for *PSA-Cre-ER$^{T2(+/-)}$; Parp1$^{+/fl}$; p53$^{fl/fl}$ Pten$^{fl/fl}$* and *PSA-Cre-ER$^{T2(+/-)}$; Parp1$^{fl/fl}$; p53$^{fl/fl}$ Pten$^{fl/fl}$* mice respectively). Similarly to the preclinical trial, the mean proportion of cells undergoing apoptosis within individual glands of the tumours was very low, as represented by a CC-3 index of 0.618% (+/- 0.043% SEM) in *PSA-Cre-ER$^{T2(+/-)}$; Parp1$^{+/+}$; p53$^{fl/fl}$; Pten$^{fl/fl}$* mice (***Figure 5.17A***). As with PCNA, simultaneous knockout of either one or both *Parp1* alleles did not result in a significant increase in CC-3 positive cells in tumour glands, as demonstrated in ***Figure 5.17B***.

Collectively, these data confirm that sustained PARP1 depletion via a conditional transgenic approach has no effect on the proliferation or apoptosis of glands within localised prostate tumours of *PSA-Cre-ER$^{T2(+/-)}$; p53$^{fl/fl}$; Pten$^{fl/fl}$* mice, thereby corroborating the findings of the preclinical trial reported in Section 4.3.3.

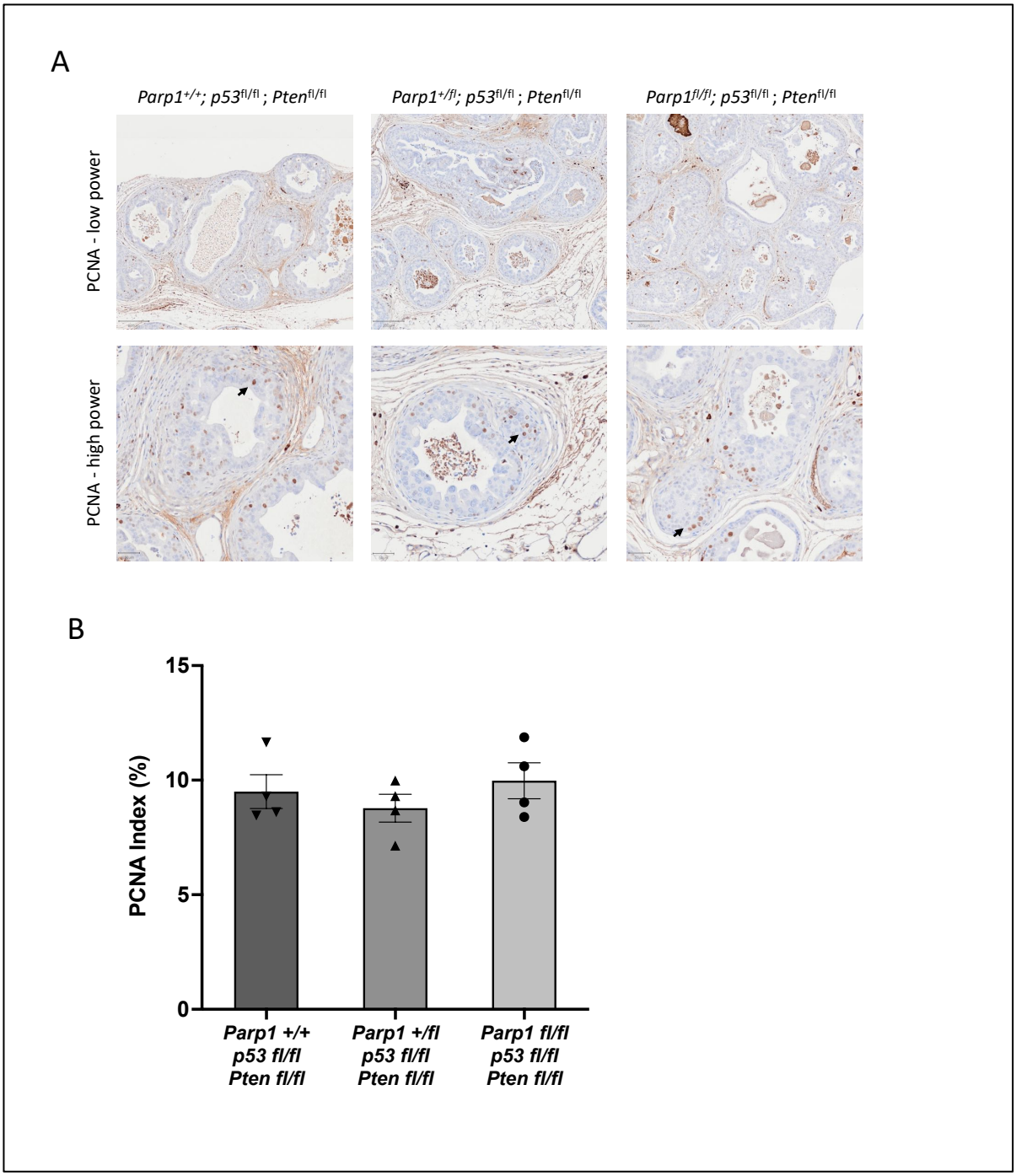

Figure 5.16: *Conditional depletion of PARP1 within the prostatic epithelium does not alter the proportion of cells undergoing proliferation within individual glands of localised prostate tumours developed by PSA-Cre-ER$^{T2(+/-)}$; p53$^{fl/fl}$; Pten$^{fl/fl}$ mice.* A: Representative light microscopy images at low and high power of tumour stained for PCNA using immunohistochemistry to demonstrate actively proliferating cells (black arrows) within individual tumour glands based on the extent of conditional knockout of *Parp1* within the prostatic epithelium. Scale bars represent 200µm and 50µm respectively. B: Bar chart demonstrating the proportion of PCNA positive cells within individual glands of the tumours (PCNA index) according to *Parp1* genotype, with no difference identified. Four mice per genotype, with quantification performed using at least 1000 cells of representative glands per mouse. Error bars represent Standard Error of the mean. Statistical significance calculated using one-way ANOVA with Tukey correction for multiple comparisons, with no differences reaching the significance threshold.

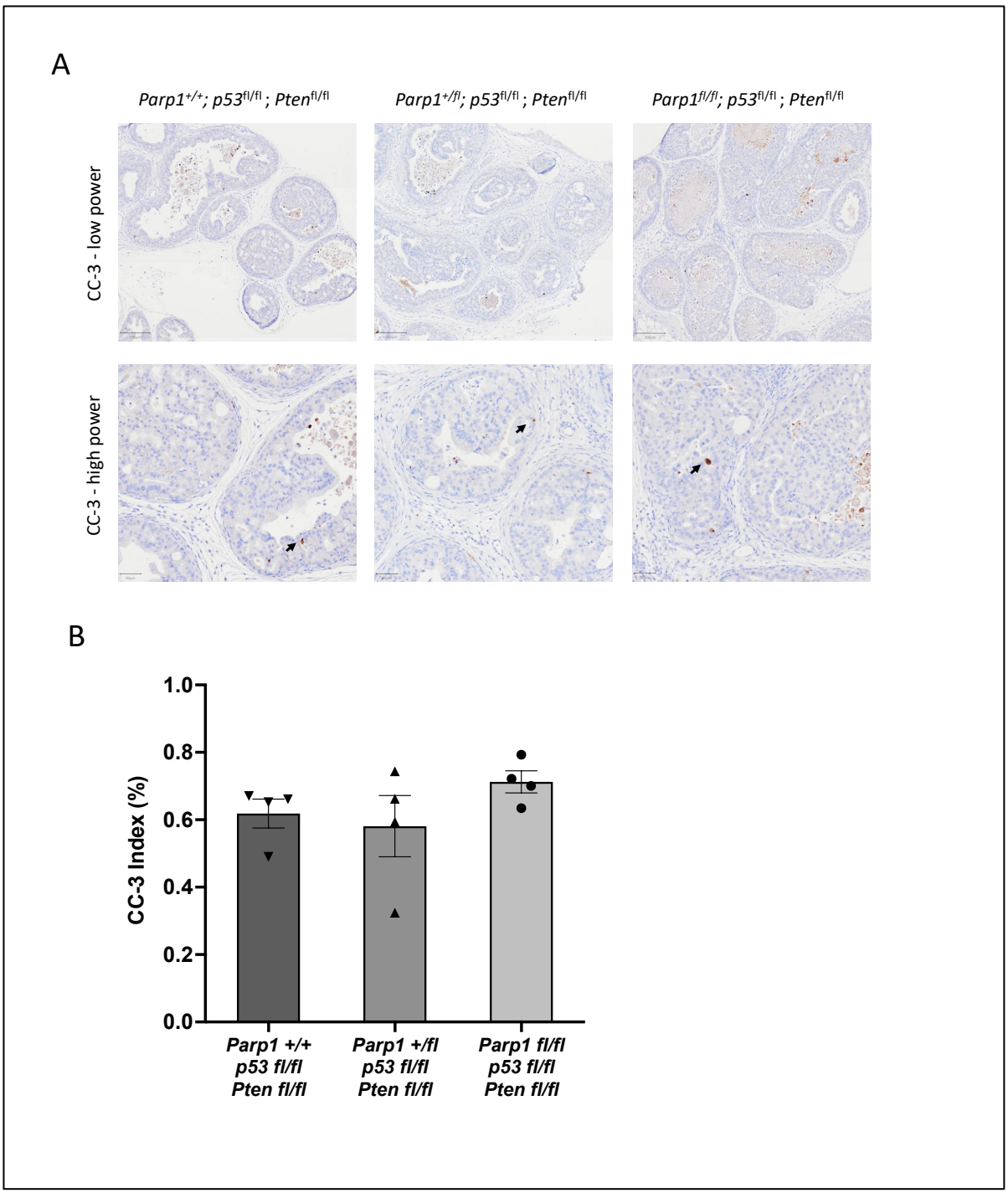

Figure 5.17: *Conditional depletion of PARP1 within the prostatic epithelium does not alter the proportion of cells undergoing apoptosis within individual glands of localised prostate tumours developed by PSA-Cre-ER$^{T2(+/-)}$; p53$^{fl/fl}$; Pten$^{fl/fl}$ mice.* A: Representative light microscopy images at low and high power of tumour stained for CC-3 using immunohistochemistry to demonstrate actively proliferating cells (black arrows) within individual tumour glands based on the extent of conditional knockout of *Parp1* within the prostatic epithelium. Scale bars represent 200µm and 50µm respectively. B: Bar chart demonstrating the proportion of CC-3 positive cells within individual glands of the tumours (CC-3 index) according to *Parp1* genotype, with no difference identified. Four mice per genotype, with quantification performed using at least 1000 cells of representative glands per mouse. Error bars represent Standard Error of the mean. Statistical significance calculated using one-way ANOVA with Tukey correction for multiple comparisons, with no differences reaching the significance threshold.

5.3.2.7 *Conditional depletion of PARP1 within the prostatic epithelium results in increased levels of CHK1 within localised prostate tumours of PSA-Cre-ER$^{T2(+/-)}$; p53$^{fl/fl}$; Pten$^{fl/fl}$ mice.*

Previous experiments in this thesis have identified that the phosphorylation of CHK1, the primary downstream effector of ATR, is increased in CRPC cells following 96 hours treatment with the PARP inhibitor olaparib at IC50 concentrations. Similarly, CHK1 phosphorylation was also increased in PC-3 xenograft tumours following 18 days treatment with olaparib (100 mg/kg), along with a highly significant increase in total CHK1 concentration. As such, experiments next sought to determine the effect of conditional genetic depletion of PARP1 on CHK1 signalling in the tumours of *PSA-Cre-ER$^{T2(+/-)}$; p53$^{fl/fl}$; Pten$^{fl/fl}$* mice at the 210 day timepoint. In order to be comparable with the previous studies involving the pharmacological inhibition of PARP1, only mice with biallelic *Parp1* deletion were included (*PSA-Cre-ER$^{T2(+/-)}$; Parp1$^{fl/fl}$; p53$^{fl/fl}$ Pten$^{fl/fl}$* genotype). Whole cell lysates were obtained from prostate tumour tissue that had been snap frozen in liquid nitrogen immediately following termination at the 210 day timepoint and total protein concentration determined. WB was undertaken for CHK1 and phospho-CHK1, with GAPDH as a loading control as described in Section 2.1.5. No signal was detected for phospho-CHK1 and unfortunately there was not sufficient time to optimise the assay, therefore restricting analysis to total CHK1 concentration only. Densitometry analysis was used to calculate total CHK1 concentration relative to the GAPDH loading control.

As demonstrated in ***Figure 5.18***, conditional deletion of both *Parp1* alleles (*PSA-Cre-ER$^{T2(+/-)}$; Parp1$^{fl/fl}$; p53$^{fl/fl}$ Pten$^{fl/fl}$* mice) resulted in a significant increase in total CHK1 protein levels compared with *PSA-Cre-ER$^{T2(+/-)}$; Parp1$^{+/+}$; p53$^{fl/fl}$ Pten$^{fl/fl}$* control mice, with a relative concentration value of 2.29 (+/- 0.57 SEM; P=0.046). These data therefore corroborate earlier observations and confirm that a reduction in PARP1 activity, be it through pharmacological inhibition or genetic depletion, increases CHK1 concentration in prostate cancer cells. Further experiments using a different antibody and/or conditions for phospho-CHK1 are required to determine whether phospho-CHK1 is augmented in a similar manner to CRPC cells (***Figure 3.5***) and PC-3 subcutaneous xenograft (***Figure 4.10***) tumours following treatment with olaparib.

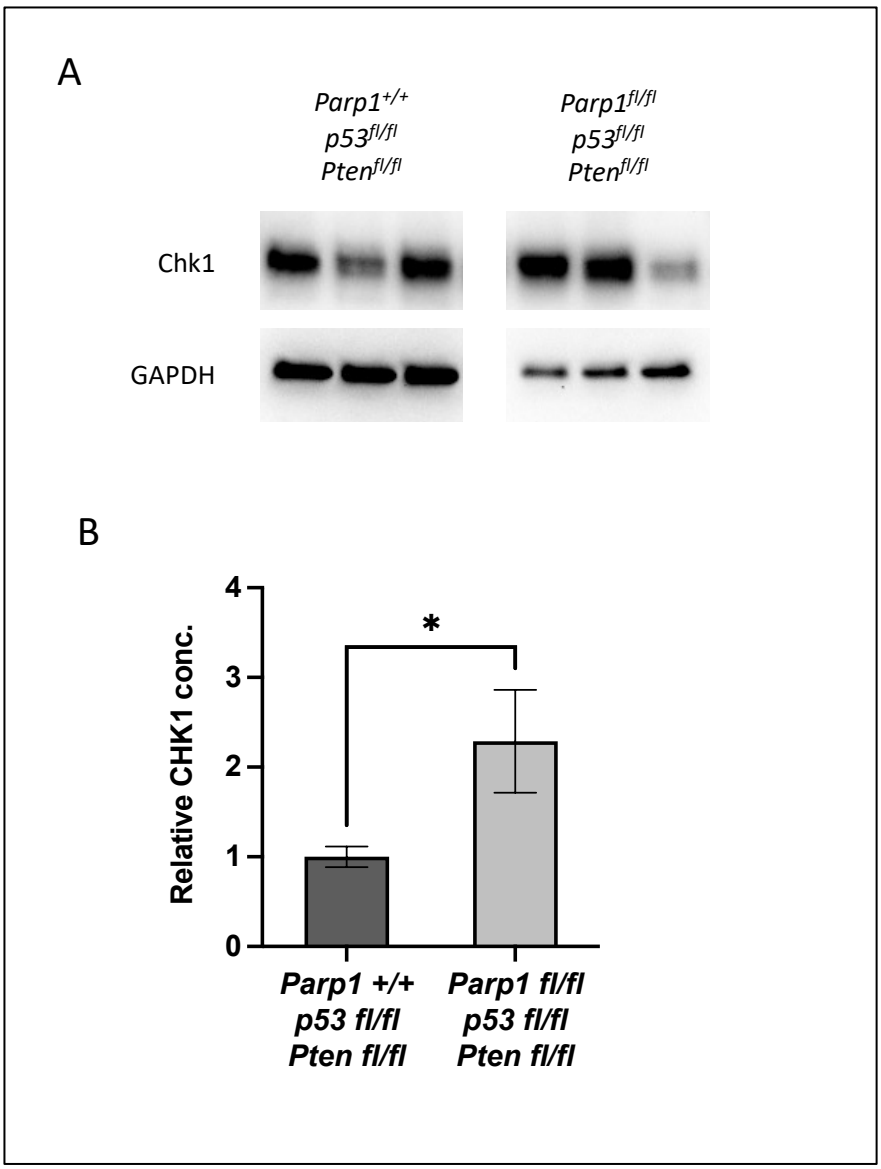

Figure 5.18: *Biallelic deletion of Parp1 increases total CHK1 protein levels in localised prostate tumours of PSA-Cre-ER$^{T2(+/-)}$; p53$^{fl/fl}$; Pten$^{fl/fl}$ mice at 210 days following induction compared with Parp1 wild type controls.* A: Representative Western Blots demonstrating CHK1 expression in tumour tissue harvested at the 210 day timepoint. B: Bar charts showing the concentration CHK1 relative to the GAPDH loading control, as assessed using densitometry (n=3 tumours per genotype). Error bars represent Standard Error of the mean. Statistical significance calculated using the unpaired Student's t-test. *: $P \leq 0.05$.

5.3.3 Evaluating the biological effects of *PARP1* and *PARP2* knockdown using RNA interference in human HR-proficient CRPC cells in vitro

5.3.3.1.1 Commercially available pooled siRNA successfully knocks down expression of *PARP1* and *PARP2* between 48 and 96 hours following transfection in HR-proficient CRPC cell lines in vitro

In order to study the differential biological effects of PARP1 and PARP2 isoforms in the setting of human prostate cancer, commercially available siRNA pools were used to transiently knock down the expression of both proteins (alone or simultaneously) in PC-3, DU-145 and 22Rv1 CRPC cells. A full description of the methodology used is given in Section 2.1.8. In brief, cells were incubated with a pool of four siRNA constructs targeted towards *PARP1* and/or *PARP2*, or with a pool of four non-targeting siRNA constructs, in serum free media containing Lipofectamine RNAiMAX transfection reagent. A pooled approach was utilised as this combines the weaker knock-down phenotypes of individual siRNA duplexes to create a more penetrant phenotype (Parsons et al., 2009). Protein level validation was then performed using WB to ensure adequate levels of knockdown prior to conducting additional functional assays within each of the cell lines. ***Figure 5.19*** demonstrates representative blots and changes in concentration of PARP1 and PARP2 in each cell line at 48 hours (***Figure 5.19A***) and 96 hours (***Figure 5.19B***) following siRNA transfection with either *PARP1* siRNA, *PARP2* siRNA or combined *PARP1* and *PARP2* siRNA, relative to non-targeting siRNA controls. The *PARP1* siRNA pool was highly effective at inducing knockdown of *PARP1*, reducing PARP1 protein levels to 20.6%, 7.3% and 9.2% of that of non-targeting siRNA treated controls in PC-3, DU-145 and 22Rv1 cells respectively at 48 hours post-transfection, with all differences proving statistically significant. This effect was sustained at 96 hours post-transfection, where PARP1 protein levels remained significantly decreased (6.5%, 10.7% and 10.6% relative to non-targeting siRNA control in PC-3, DU-145 and 22Rv1 cells respectively).

In comparison, the *PARP2* siRNA pool was less effective at inducing knockdown, with PARP2 protein levels reduced to 50.5%, 47.3% and 39.9% of that in non-targeting siRNA treated controls in PC-3, DU-145 and 22Rv1 cells respectively at 48 hours post-transfection, with all differences proving statistically significant. However, the level of knockdown again remained stable over the following 48 hours such that at 96 hours following transfection, PARP2 protein levels remained 44.2%, 27.0% and 55.3% of that of non-targeting siRNA treated controls in PC-3, DU-145 and 22Rv1 cells respectively. Likewise, simultaneous siRNA-mediated knockdown of *PARP1* and *PARP2* yielded similar levels of knockdown at both 48 and 98 hours, with all differences proving statistically significant in comparison to non-targeting siRNA treated controls at both timepoints.

Collectively these data indicate that the commercially available pool of siRNA targeted against *PARP1* provides significant levels of knockdown for the study of PARP1 biology between 48 and 96 hours following transfection (range: 79.4-93.5% reduction in protein concentration). Likewise, the pool of siRNA targeted against *PARP2* also provides significant levels of knockdown between the same timepoints, although to a lesser extent (range: 49.5-73.0% reduction in protein concentration). These differences must be taken into account when comparing results between PARP1 and PARP2 depletion in subsequent functional in vitro assays.

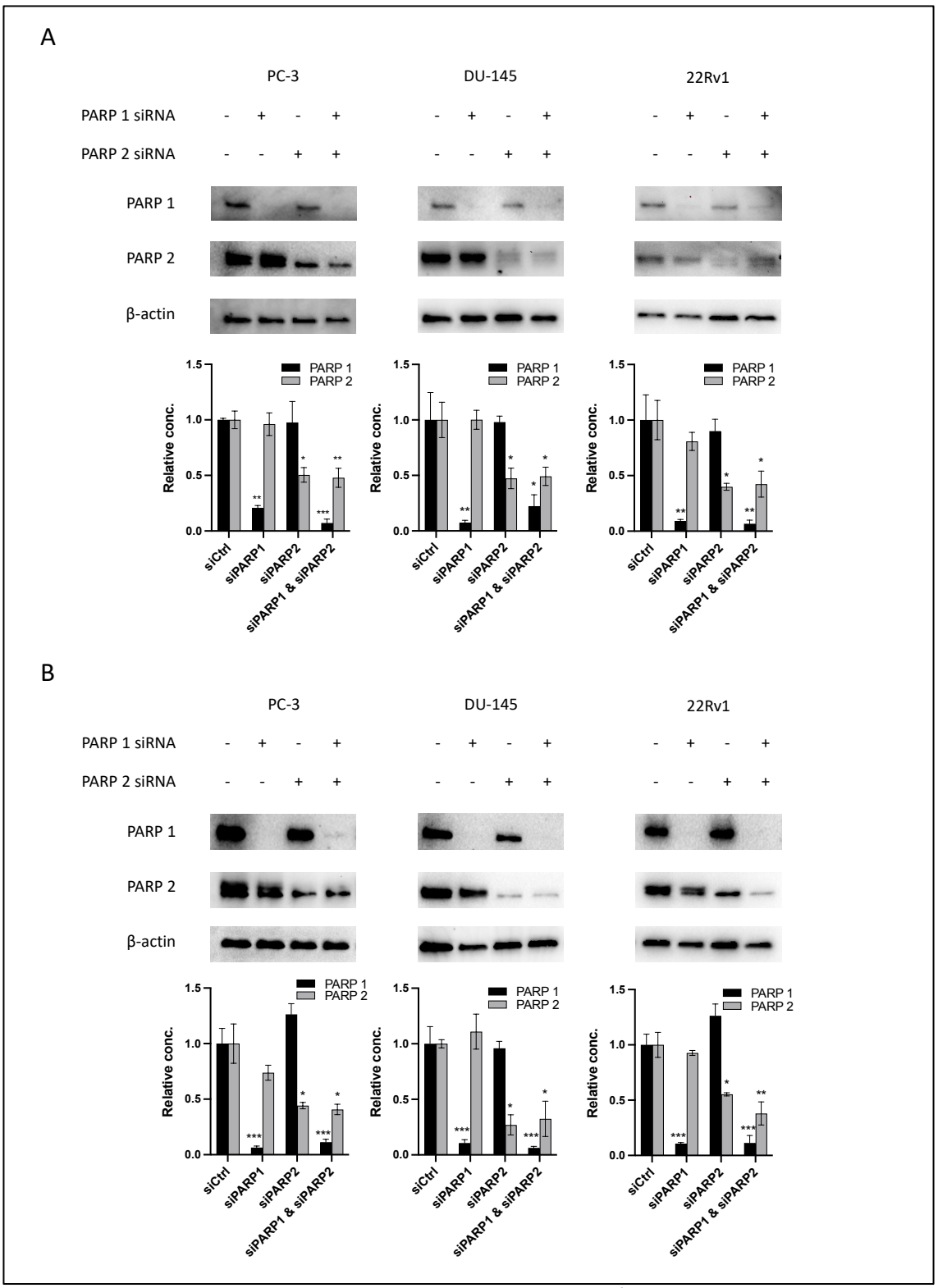

Figure 5.19: *Validation of siRNA-mediated knockdown of PARP1 and/or PARP2 in established human CRPC cell lines.* A: Representative Western Blots and densitometry bar charts demonstrating PARP1 and PARP2 protein levels in cells transfected with commercially available pools of siRNA targeting *PARP1* (siPARP1) and/or *PARP2* (siPARP2) relative to scrambled non-targeting siRNA (siCtrl) treated controls, as determined by densitometry analysis at 48 hours (A) and 96 hours (B) post-transfection. Densitometry data normalised to B-actin loading controls. Three independent repeats per cell line and time point (n=3), with three technical repeats per condition. Error bars represent Standard Error of the mean. Statistical significance calculated using one-way ANOVA with Tukey correction for multiple comparisons. * symbols depicting significance compared with siCtrl; **: $P \leq 0.001$, **: $P \leq 0.01$, *: $P \leq 0.05$.

5.3.3.1.2 siRNA mediated knockdown of *PARP1* but not *PARP2* significantly reduces proliferation of human CRPC cells in vitro

In order to determine the biological effects of *PARP1* and *PARP2* knockdown, CRPC cells were transfected with pools of siRNA targeted against *PARP1*, *PARP2* or *PARP1* and *PARP2* mRNA for 96 hours and cell viability assessed using the CellTitre Blue assay relative to non-targeting siRNA treated controls (***Figure 5.20A***). In PC-3 cells, knockdown of *PARP1* or *PARP2* resulted in a small but non-significant reduction in cell viability (0.806 +/- 0.095 SEM and 0.905 +/- 0.049 SEM respectively) relative to the control. Whilst *PARP1* and *PARP2* knockdown resulted in the greatest reduction in relative viability (0.788 +/- 0.055 SEM), the majority of cells remained viable, therefore mirroring the insensitivity of PC-3 cells to 96 hours treatment with olaparib (which is known to inhibit both PARP1 and PARP2 isoforms) and hence reflecting the overall insensitivity of this cell line to loss of PARP function.

In DU-145 cells, *PARP1* knockdown reduced cell viability relative to both *PARP2* knockdown and non-targeting siRNA treated controls (0.441 +/- 0.062 SEM versus 1.054 +/- 0.115 SEM, P=0.048 and 1.00 +/- 0.22 SEM, P= 0.071). Combined knockdown of *PARP1* and *PARP2* led to a smaller reduction in cell viability (0.583 +/- 0.087 SEM) when compared with *PARP1* knockdown alone, although this reduction was not statistically significant. Likewise, the same trend was observed in 22Rv1 cells, with *PARP1* and combined *PARP1* and *PARP2* knockdown resulting in similar reductions in viability (0.694 +/- 0.12 SEM and 0.640 +/- 0.056 SEM respectively), whilst *PARP2* knockdown alone again did not alter relative viability of the cells. These data collectively suggest that selective knockdown of *PARP1* may reduce the viability of HR-proficient CRPC cells whilst selective *PARP2* knockdown has little to no effect and does not clearly enhance the effect of simultaneous *PARP1* knockdown. However, variability between individual biological repeats limits our interpretation and therefore further experiments are required in order to determine whether differences between groups are truly significant.

To investigate whether the observed reduction in cell viability in response to selective *PARP1* knockdown correlates with reduced proliferation, cells underwent transfection and were then placed in the IncuCyte live cell imaging system and cell confluence measured every four hours between 48 – 96h post-transfection as described in Section 2.1.8.4. Cell confluence was normalised to the 48 hour timepoint to give relative confluence and plotted against time as a surrogate measure of cellular proliferation, as illustrated in ***Figure 5.20B***. In PC-3 and 22Rv1 cells, *PARP2* knockdown had little impact on proliferation, with the curves appearing almost identical to those of the non-targeting siRNA controls in each line. On the contrary, *PARP1* knockdown significantly reduced cell proliferation. Combined *PARP1* and *PARP2* knockdown mirrored the proliferation curve of *PARP1* knockdown alone,

indicating no additional effect conferred by *PARP2* knockdown. In DU-145 cells, *PARP2* knockdown actually appeared to provide a proliferative advantage, with relative confluence being higher than that of non-targeting siRNA treated controls at each time point (P=0.0002). Again, *PARP1* knockdown resulted in the greatest reduction in proliferation, with combined *PARP1* and *PARP2* knockdown resulting in a smaller but still significant reduction, presumably as a result of the observed proliferative advantage conferred by *PARP2* knockdown.

Collectively, these data indicate that PARP1 depletion has a greater impact on both viability and proliferation than PARP2 depletion in CRPC cells, and that simultaneous *PARP2* depletion does not appear to significantly enhance the effect of *PARP1* depletion alone.

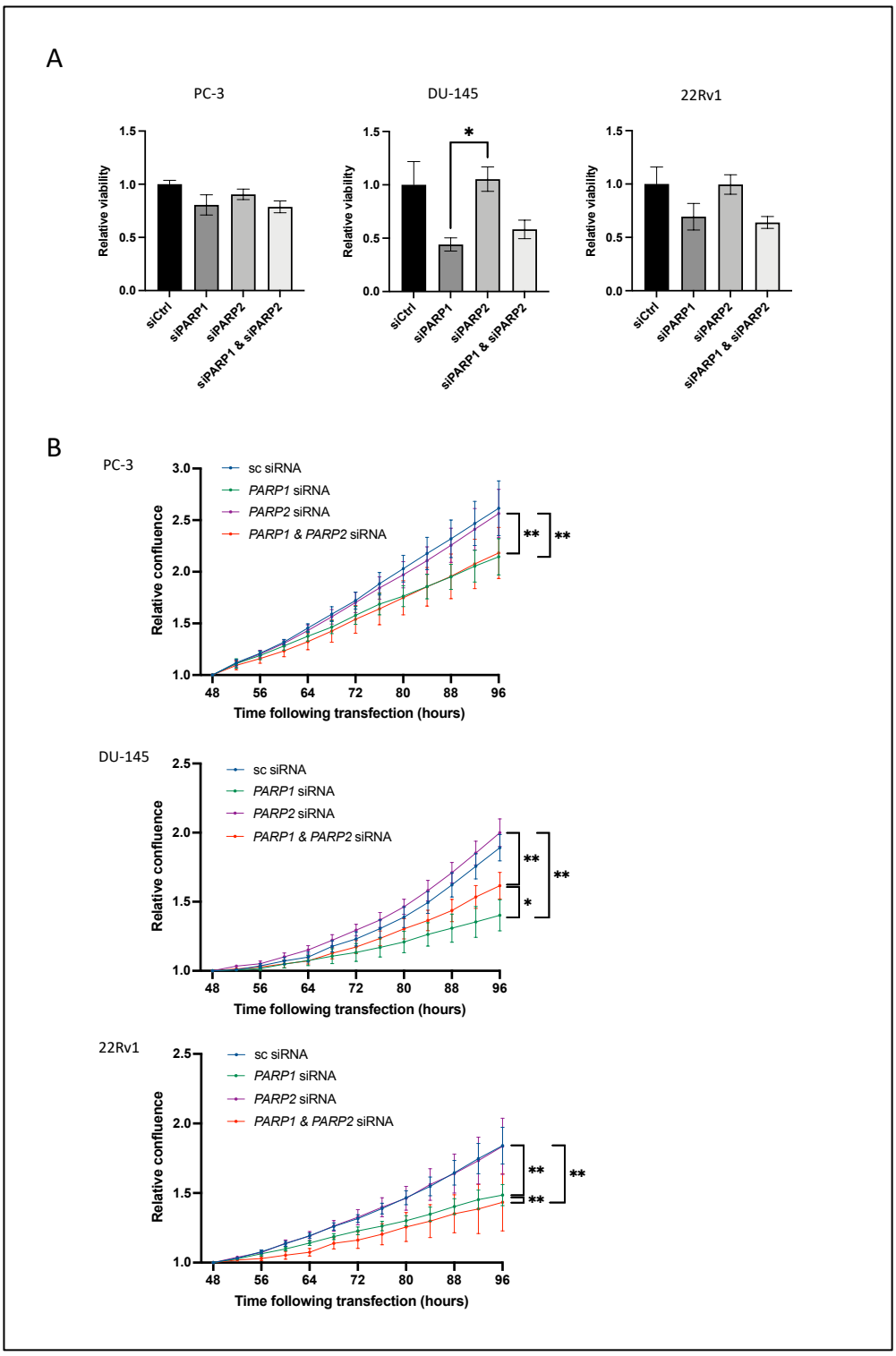

Figure 5.20: *siRNA mediated knockdown of PARP1 but not PARP2 results in a partial reduction in the viability and proliferation of CRPC cells in vitro between 48 and 96 hours following transfection.* A: Bar charts demonstrating the viability of cells of each line at 96 hours following transfection with commercially available siRNA pools targeting *PARP1* (siPARP1), *PARP2* (siPARP2) and both *PARP1* and *PARP2* (siPARP1 & siPARP2) mRNA relative to that of non-targeting siRNA (siCtrl) treated controls. B: Plots demonstrating the confluence of CRPC cells between 48 and 96 hours following transfection with commercially available siRNA pools targeting *PARP1*, *PARP2* and both *PARP1* and *PARP2* mRNA, normalised to that at the initial 48 hour timepoint. 3 independent repeats per cell line; error bars represent Standard Error of the mean. Statistical significance calculated using one-way ANOVA with Tukey correction for multiple comparisons.

5.4 Discussion

The experiments in this chapter firstly sought to characterise the effects of conditional genetic depletion of *PARP1* within the luminal epithelial cells of the normal prostate in adult male mice in both the short and long term. Following development of the GEMM, as described in Section 2.3.2, validation was undertaken which confirmed that intraperitoneal injection of tamoxifen induced recombination of the *Parp1* allele in each of the prostate lobes. This is consistent with the initial description of the PSA-Cre-ER^{T2} construct, in which recombination occurred in all lobes, with the highest recombination efficiency reported in the DLP (Ratnacaram et al., 2008). As such, the correlation between *Parp1* recombination and *Parp1* mRNA concentration within cells of the DLP was then assessed using qRT-PCR. This confirmed a reduction of over 50% in those mice with biallelic *Parp1* loss, which is likely to be an underestimate of the reduction in the prostatic epithelial cells specifically for the reasons outlined in Section 5.3.1.1. However, further experiments using mice harbouring a fluorescent reporter such as RFP or tdtomato constructs that have a LoxP-flanked STOP cassette preceding the gene to enable expression of the fluorescent gene upon recombination are needed to precisely quantify the degree of recombination specifically within this cell population.

Ageing of the experimental cohorts to the short and long term timepoints confirmed that PARP1 depletion specifically within the prostate has no effect on the health or overall survival of mice. Experiments were then performed to establish the impact on basic prostate homeostasis, starting with growth as assessed by means of total prostate weight and weight of individual lobes. Whilst biallelic *Parp1* deletion was associated with a significant increase in VP weight and a corresponding non-significant decrease in DLP weight at the 100 day timepoint, these differences were not apparent at 300 days. Subsequent experiments sought to determine the effects of conditional PARP1 depletion at a cellular level. Neither monoallelic or biallelic *Parp1* deletion was associated with a change in glandular morphology, with no evidence of hyperplasia, PIN or invasive carcinoma in any of the experimental mice, confirming that loss of PARP1 function alone is not sufficient to induce malignant transformation in the prostate. However, when further IHC characterisation was performed some differences between genotypes did emerge. Interestingly, biallelic *Parp1* deletion was associated with a trend towards an increased proportion of CK5 positive basal cells in the DP, LP and AP at the 100 day timepoint, although these differences failed to reach significance and were lost by 300 days as the prostate became more quiescent. Likewise, whilst the level of proliferation within individual glands was very low, biallelic *Parp1* deletion did appear to result in a significant increase in proliferation in glands of the AP at both 100 and 300 days, as well as a non-significant increase in glands of the VP at 100 days.

Whilst these findings collectively demonstrate that the conditional depletion of PARP1 within the prostatic epithelium using Cre-Lox recombination does not have any discernible effect on the overall health or survival of mice in either the short or long term, it does appear to result in time specific alterations in the weight of individual lobes which could not be explained by differences in glandular architecture. Furthermore, whilst biallelic deletion of *Parp1* does appear to result in changes in the proliferation of epithelial cells, again this does not account for the differences in weight given that the most significant increase was seen in the AP, for which there was no difference in weight when compared with *Parp1* wild-type controls. Overall, we can therefore conclude that although PARP1 is known to play a key role in several biological processes, its loss specifically within the murine prostate in the absence of significant DNA damage or cellular stress does not result in a significant change in phenotype and is therefore dispensable for the maintenance of normal adult prostate tissue homeostasis in mice.

Although numerous studies utilising both whole body knockout and organ specific *Parp1* deletion via Cre-LoxP recombination have sought to determine the role of PARP1 in a range of different biological processes, few other authors have explored the effects specifically within the prostatic epithelial cells of adult male mice. In one similar study, Pu et al. explored the effect of PARP1 functional loss in the prostate using *Parp1*$^{-/-}$ mice that lack functional PARP1 as a result of disruption of exon 2 of the *Parp1* gene (Wang et al., 1995, Pu et al., 2014). Similar to our findings, PARP1 functional loss did not alter the glandular morphology of the prostate or the number of apoptotic cells compared with wild-type controls when assessed via histopathological and IHC analysis respectively at 6 – 12 weeks of age (Pu et al., 2014). However, in contrast, the prostates of *Parp1*$^{-/-}$ mice had a lower normalised prostate weight and reduced proliferative capacity when assessed via IHC for Ki-67 compared with wild-type controls. Whilst this study both partially corroborates and contradicts the findings reported in this thesis, it is difficult to draw direct comparisons due differences in methodology. For example, Pu et al. performed their assessment at a much earlier timepoint, utilising a model in which all cells possessed PARP1 functional loss from birth, including those of the stroma and immune system. To what extent the observed differences are a direct result of loss of PARP1 activity within the epithelial cells is not known, hence the significance of the differences with those findings reported in this thesis is unclear.

Having determined that conditional PARP1 depletion in epithelial cells of the normal prostate is dispensable for maintenance of homeostasis, experiments next sought to determine its effect in the prostates of *PSA-Cre-ER*$^{T2(+/-)}$*; p53*$^{fl/fl}$*; Pten*$^{fl/fl}$ mice. This model, as described in Section 4.3.3.1, results in the development of localised, predominantly ventral tumours comprised of PIN with focal areas of

microinvasive carcinoma, hence enabling the study of PARP1 function in prostate cancer. Mice were aged to the later timepoint of 7.5 months (210 days) following induction to enable tumours to progress and hence represent slightly more advanced disease. Similar to the study in the normal prostate, conditional depletion of PARP1 had no effect on the health or overall survival of *PSA-Cre-ER$^{T2(+/-)}$; p53$^{fl/fl}$; Pten$^{fl/fl}$* mice. However, given that the model was one of localised disease which did not result in any deaths from prostate cancer during the 210 day post induction period, it is not possible to determine whether PARP1 depletion impacts upon disease specific survival on the basis of this experiment.

Whilst PARP1 depletion was not associated with alterations in overall prostate weight compared with *Parp1* wild-type controls, both monoallelic and biallelic deletion of *Parp1* was associated with a highly significant reduction in weight of the DLP. Interestingly this could not be explained by subsequent histopathological and IHC characterisation in which PARP1 depletion was not associated with any changes in the morphology of tumour glands, nor epithelial cell differentiation, proliferation, or apoptosis. These results differ from those in the normal prostate in which conditional depletion of PARP1 was associated with a significant increase in the proportion of proliferating cells in the AP at both 100 and 300 days following tamoxifen induction, suggesting that it may exert differing effects in both normal and disease states. As such, these findings suggest that loss of PARP1 activity alone is not sufficient to alter the turnover of prostatic epithelial cells through changes in either proliferation or apoptosis in conjunction with simultaneous *p53* and *Pten* deletion in the absence of additional mutational burden, significant DNA damage or cellular stress.

There is again a paucity of research exploring the role of PARP1 in prostate cancer using a GEMM approach. In the study by Pu et al., *Parp1$^{-/-}$* mice were crossed with transgenic adenocarcinoma of mouse prostate (TRAMP) mice, which are a well-established model of prostate cancer progression and metastases through expression of the T antigen oncoprotein (Gingrich et al., 1996, Pu et al., 2014). PARP1 functional loss was associated with a significant increase in tumour size and grade compared with controls, together with an increase and decrease in proliferation and apoptosis respectively (Pu et al., 2014). Further characterisation demonstrated that PARP1 functional loss led to reduced AR nuclear localisation and increased levels of transforming growth factor-β (TGF-β) and SMADS, leading the authors to conclude that loss of PARP1 function promotes tumourigenesis in vivo via TGF-β induced epithelial to mesenchymal transition (EMT). On the contrary, whilst the experiments in this thesis did not explore the impact of PARP1 depletion on AR signalling or EMT, it was found to have no effect on tumour growth or morphology, nor proliferation or apoptosis. However, as with the

conflicting findings reported in the normal prostate, these differences may again be due to differences in methodology, including the model used and timepoints at which analysis were performed, therefore rendering it difficult to draw direct comparisons.

The observation that biallelic deletion of *Parp1* does not affect the glandular morphology or proliferative capacity of cells within the prostates of *PSA-Cre-ER$^{T2(+/-)}$; p53$^{fl/fl}$; Pten$^{fl/fl}$* mice mirrors their lack of response to combined PARP1/2 inhibition with olaparib monotherapy in the preclinical trial reported in Section 4.3.3. However, given that *PSA-Cre-ER$^{T2(+/-)}$; p53$^{fl/fl}$; Pten$^{fl/fl}$* cells did respond to combined PARPi and ATRi, WB was undertaken to establish the effects of biallelic *Parp1* deletion on the expression and phosphorylation of CHK1 to determine whether this may provide insight into the mechanisms responsible. Biallelic *Parp1* deletion increased total CHK1 concentration compared with *Parp1* wild-type controls, thereby corroborating the earlier findings observed with olaparib monotherapy in our panel of CRPC cells in vitro (Section 3.3.1.4) and the PC-3 subcutaneous xenograft tumour cells in vivo (Section 4.3.2.3.4). Unfortunately, there was not sufficient time to optimise the WB to determine whether similar increases in p-CHK1 were observed with *Parp1* deletion. Nevertheless, these data provide evidence that loss of PARP1 activity within *PSA-Cre-ER$^{T2(+/-)}$; p53$^{fl/fl}$; Pten$^{fl/fl}$* prostate tumours increases expression of CHK1, thereby supporting the notion that increased efficacy of combined PARPi and ATRi in this model may be a result of similar mechanisms to those proposed in the CRPC cells in Section 3.4.

Given the emerging evidence of differential functions of PARP1 and PARP2, the final series of experiments in this chapter sought to determine the impact of PARP1 and PARP2 depletion in the panel of HR-proficient CRPC cells in vitro using siRNA to better determine their distinct roles in this setting. In all cell lines, PARP2 depletion resulted in no discernible change in viability compared with non-targeting siRNA treated controls, whilst PARP1 depletion resulted in a non-significant trend towards reduced viability. Similarly, PARP2 depletion had no effect on proliferation between 48 and 96 hours following transfection compared with non-targeting siRNA treated controls in both PC-3 and 22Rv1 cells, and actually appeared to result in an increase in proliferation in DU-145 cells. On the contrary, PARP1 depletion led to a highly significant reduction in proliferation in each of the cell lines, with combined PARP1 and PARP2 depletion resulting in either near identical proliferation curves to *PARP1* depletion alone or in the case of DU-145 cells, enhanced proliferation. Collectively, these findings indicate that each cell line was only partially sensitive to combined *PARP1* and *PARP2* knockdown, corroborating the results outlined in Section 3.3.1.1 in which the same HR-proficient CRPC cell lines demonstrated only partial sensitivity to olaparib, which targets both isoforms. Secondly,

these data suggest that inhibiting the activity of PARP2 alone has little impact on either the viability or proliferation of HR-proficient CRPC cells, and that simultaneous *PARP2* knockdown does not enhance the effect of *PARP1* knockdown.

Other studies have also explored the effects of selective knockdown of PARP1 expression in the setting of prostate cancer. Lai et al. used siRNA to reduce expression of *PARP1* in PC-3 cells and identified a reduction in migration and invasion in vitro compared with controls, as well as a reduction in PC-3 subcutaneous xenograft tumour growth over a 40 day study period (Lai et al., 2018). They also identified that PARP1 depletion increased markers of EMT in PC-3 cells both in vitro and in vivo, supporting the findings of Pu et al. in their *Parp1*$^{-/-}$ GEMM study (Pu et al., 2014). Unfortunately, this study did not include the depletion of PARP2 or combined PARP1 and PARP2 for comparison. On the contrary, Gui et al. explored the effect of PAPR1 and PARP2 depletion using both siRNA mediated knockdown in a panel of four prostate cancer cell lines together with CRISPR/Cas9 knockout in LNCaP cells (Gui et al., 2019). siRNA mediated depletion of PARP1 and PARP2 resulted in varying levels of growth inhibition in each cell line, with greater inhibitory effects in AR positive LNCaP and VCaP cells than AR negative PC-3 and DU-145 cells. Although combined PARP1 and PARP2 depletion was not analysed in this study, PARP1 or PARP2 depletion were comparable in terms of growth inhibition in all cells except VCaP, in which PARP2 depletion appeared to have the greater effect. Similarly, *PARP1* or *PARP2* deletion using CRISPR/Cas9 resulted in a significant reduction in growth rate of the LNCaP cells and completely diminished their ability to generate subcutaneous xenograft tumours, with no discernible differences between isoforms. Whilst some comparisons can be made with the results presented in this thesis, the commercially available pool of siRNA targeting *PARP2* resulted in a smaller degree of knockdown at the protein level compared to that targeting *PARP1*, and to a lesser extent than the *PARP2* siRNA constructs utilised by Gui et al. It is therefore possible that if different siRNA constructs with greater knockdown capabilities were used, there may have been equivalence between selective inhibition of the two isoforms.

Whilst these data suggest that inhibition of one isoform may provide equivalent effects to inhibition of both, we must be cautious when extrapolating the potential benefits of selective PARP1 or PARP2 inhibitors to the clinical setting. It is known that genetic depletion of PARP enzymes is less cytotoxic than their pharmacological inhibition, as the former only reduces catalytic activity through reduced levels of expression and does not lead to PARP trapping that is deemed a an important component of the mechanism of action of several PARPi (Murai et al., 2012). Furthermore, pharmacological inhibition occurs in all cells and therefore PARP inhibitors exert their effects not only upon the tumour

cells themselves, but also those involved in the microenvironment and immune system which may modulate response to treatment. For example, Moreno-Lama et al. have shown that deficiency of PARP1, PARP2 and both PARP1 and PARP2 exert differential effects on the intratumour immunological landscape, with single PARP isoform deficiency within T lymphocytes promoting an antitumour effect and dual deficiency favouring tumour growth (Moreno-Lama et al., 2020).

Studies have shown that PARPi induced synthetic lethality in BRCA mutant cells appears to be predominantly driven by PARP1 (Murai et al., 2012, Ronson et al., 2018). This, together with the fact that PARP2 is known to be essential in haematopoietic stem/progenitor cell survival (Farrés et al., 2013), has been taken to support the development of selective PARP1 inhibitors for use in the clinical setting with a view to enabling greater or equivalent efficacy without the severity of off target effects associated with current broad specificity compounds such as olaparib. One such PARP1 specific inhibitor, AZD5305, has recently been shown to reduce the growth of *BRCA* mutant triple-negative breast cancer PDX tumours with equivalence to olaparib whilst also reducing in vitro haematotoxicity, one of the significant adverse effects of PARPi in the clinical setting (Johannes et al., 2021). As such, this agent has recently entered into a Phase I clinical trial as both a monotherapy and in combination with paclitaxel, carboplatin and trastuzumab deruxtecan, in patients with advanced solid tumours, including prostate (NCT04644068).

5.5 Limitations

The results reported in this chapter are subject to limitations on account of both time constraints arising from the COVID-19 pandemic and the experimental methods used. The original aim was to utilise both *Parp1* and *Parp2* floxed constructs to study the differential effects of loss of each isoform in vivo using a GEMM approach. However, despite obtaining the *Parp2* floxed allele construct from collaborators just prior to the onset of the COVID-19 pandemic, experimental breeding pairs were separated in March 2020 and remained so for the duration of time during which the University was closed. Once breeding was recommenced in August 2020 there was not sufficient time remaining to generate and age the required experimental cohorts and therefore the *Parp2* floxed arm of the study was abandoned. However, breeding has subsequently continued and it is hoped that this work will be completed by another research student in the future.

Similarly, the interruption to breeding also meant that the experimental cohorts of the two transgenic models reached their timepoints close to the end of the project period. This left little time for

characterisation prior to my return to clinical practice, hence only permitting basic analysis of each model. It is therefore possible that conditional PARP1 depletion may have had effects on other physiological processes within the prostate, such as immune responses and angiogenesis, which we were unable to explore; thereby warranting further investigation. Furthermore, issues with paraffin embedding and sectioning of individual prostate lobes meant that not all slides contained tissue from each lobe, hence limiting the numbers characterised in the normal prostate GEMM study and restricting analysis to tumour tissue only in the prostate cancer GEMM study. Unfortunately, there was not sufficient time to overcome these issues through re-blocking the tissue and repeating the IHC within the project timeframe.

Finally, whilst the commercially available pool of siRNAs targeting *PARP1* was highly effective in inducing knockdown at the protein level, that targeting *PARP2* was less so, only achieving between 39.9 – 50.5% and 27.0 – 55.3% of control levels at 48 and 96 hours post transfection respectively. If similar differences were also confirmed at the mRNA level then it is possible that differences between effects of knockdown of each isoform may be an artefact of this discrepancy, rather than true differences in biological activity. As such, further experiments utilising a different pool of *PARP2* siRNA or an alternative gene editing approach such as CRISPR/Cas9 are required to make more accurate comparisons in the panel of HR-proficient CRPC cell lines.

5.6 Conclusions and future directions

In summary, the results outlined in this chapter demonstrate that although the genetic depletion of PARP1 within prostatic epithelial cells does result in some changes in the growth and proliferative capacity of individual lobes of the normal adult murine prostate, it does not alter the glandular phenotype or result in malignant transformation, hence indicating that PARP1 function is dispensable for the maintenance of normal tissue homeostasis in the absence of significant DNA damage or cellular stress. Furthermore, whilst PARP1 depletion also appears to reduce mass of the dorsal and lateral lobes in mice with simultaneous depletion of p53 and PTEN tumour suppressors, it does not result in differences in phenotype, epithelial cell differentiation, proliferation or apoptosis within tumour glands. Nevertheless, depletion of PARP1 within epithelial cells did increase expression of CHK1, therefore supporting the notion that the increased efficacy of combined PARPi and ATRi observed in *PSA-Cre-ER$^{T2(+/-)}$; p53$^{fl/fl}$; Pten$^{fl/fl}$* mice in the preclinical trial outlined in Section 4.3.3 may be a result of similar mechanisms to those proposed in the HR-proficient CRPC cells. Additional studies exploring this in more detail, together with more extensive characterisation of the effects of PARP1 depletion

in both GEMMs are required in order to better establish its impact on other key biological processes in which PARP enzymes are known to play a part.

Depletion of PARP1 using siRNA was superior to depletion of PARP2 in terms of reducing proliferation of a panel of HR-proficient CRPC cell lines. If this is confirmed in subsequent experiments utilising more effective *PARP2* siRNAs or alternative gene editing techniques, it suggests that selective PARP1 inhibitors could offer a means of reducing the potential haematological toxicity that may be encountered with combined PARP and ATR inhibition in patients with CRPC, thus increasing tolerability and/or enabling dose escalation to increase efficacy. Future work exploring the effects of selective PARP1 inhibition alone and in combination with ATRi in preclinical models such as those utilised in this thesis would therefore provide further insight into these potential benefits and help steer the direction of travel for PARPi/ATRi combination therapy as it enters into early phase clinical trials in CRPC.

6 Final discussion

Improvements in the detection, risk stratification and treatment of prostate cancer over recent decades have enabled an evolution in management of all stages of disease. In particular the contemporary outcomes of men presenting with localised disease are excellent, with only 17 of 1643 men in one landmark clinical trial dying from prostate cancer during 10 years of follow up (Hamdy et al., 2016). However, for those that go on to develop CRPC the estimated survival is only 14-22 months, mandating an ongoing search for more efficacious treatment options for this patient group (Kirby et al., 2011, James et al., 2015).

Advances in scientific and bioinformatic techniques have enabled a rapid and dramatic increase in our understanding of the molecular landscape and pathobiology of prostate cancer in recent years, paving the way for the identification and evaluation novel treatments. One area that has attracted considerable interest is that of DNA damage repair, with genomic studies identifying aberrations in genes encoding key proteins involved in homologous recombination in 22-28% of patients with CRPC, most commonly *BRCA2* and *ATM* (Robinson et al., 2015, de Bono et al., 2020). Several clinical trials have since demonstrated that PARP inhibitors are safe and effective in CRPC patients with these aberrations (Mateo et al., 2015, Mateo et al., 2019, de Bono et al., 2020, Hussain et al., 2020). However, subsequent analyses according to specific underlying gene aberration have shown that responses are poorer in those with *ATM* mutations than *BRCA2* mutations, prompting the search for means of increasing efficacy in this group (Abida et al., 2020, de Bono et al., 2020). A recent study published by Neeb et al. reported that combining PARPi with inhibition of another key DDR protein, ATR, was highly effective at controlling the growth of *ATM* deficient models of CRPC, corroborating the findings of similar preclinical studies exploring this combination in other *ATM* deficient solid cancers (Jette et al., 2020, Lloyd et al., 2020, Neeb et al., 2021). Nevertheless, given that such aberrations are only present in 5.9-7.3% of CRPC cases (Robinson et al., 2015, de Bono et al., 2020), the clinical application of such findings are potentially limited.

On the basis of a strong mechanistic rationale and evidence of synergy between PARPi and ATRi in other HR-proficient solid tumour models (Kim et al., 2016, Schoonen et al., 2019, Southgate et al., 2020), the experiments in Chapter 3 of this thesis firstly sought to determine whether this combination is effective in HR-proficient CRPC. Although the chosen panel of HR-proficient CRPC cells were inherently insensitive to PARPi monotherapy with olaparib in vitro, treatment did lead to an increase in DNA damage and an associated increase phosphorylation of the ATR downstream target CHK1, suggesting increased dependency on ATR-CHK1 signalling. Furthermore, whilst cells demonstrated

increased sensitivity to monotherapy with the ATRi ceralasertib, the combination of olaparib and ceralasertib at predetermined IC50 concentrations was synergistic and led to a significantly greater loss of viability than treatment with either agent alone. The results of subsequent experiments, together with those of similar studies reported in the literature, lead us to propose that synergy occurs as a result of PARPi preventing SSBs repair and resulting in PARP trapping at replication forks, leading to collapse and formation of DSBs. Under normal circumstances, ATR is activated in response to the resulting DNA damage and replication stress, in turn orchestrating several downstream processes including activation of CHK1 and cell cycle arrest at the G2-M checkpoint together with DSB repair via HR. However, if ATR function is pharmacologically inhibited with ceralasertib, this DNA damage continues to accumulate and, in the absence of CHK1 activation, cells aberrantly progress through the cell cycle and undergo apoptosis as a consequence of mitotic catastrophe. Further work is therefore needed to explore this hypothesis and better understand the exact mechanisms underlying the observed synergy.

To investigate the effects of combined PARPi and ATRi in vivo, preclinical trials were conducted using the PC-3 subcutaneous xenograft model of CRPC and the *PSA-Cre-ER*$^{T2(+/-)}$; *p53*$^{fl/fl}$; *Pten*$^{fl/fl}$ GEMM of *p53*, *Pten* deficient localised prostate cancer, as described in Chapter 4. In both studies, combined olaparib and ceralasertib treatment was well tolerated and more efficacious compared to monotherapy with either agent, although the effects were most pronounced in PC-3 subcutaneous xenograft tumours. As well as reducing proliferation of the PC-3 cells and increasing death by apoptosis, combined PARPi and ATRi reduced the macroscopic and microscopic vascularity of tumours compared with either agent alone. Given that previous studies have shown both PARP and ATR play important roles in angiogenesis it is possible that the antiangiogenic effects of combination therapy may contribute to the enhanced efficacy seen in this particular model, thereby warranting further investigation (Rajesh et al., 2006, Tentori et al., 2007, Shi et al., 2020). Similarly, previous research has also shown that PARP and ATR are involved in modulation of the tumour immune response (Jiao et al., 2017, Sun et al., 2018) which, although not explored in this thesis, may also contribute to treatment effects and therefore merits further investigation.

The effect of combined PARPi and ATRi was also explored using a recently developed ex vivo model generated from metastatic lymph node tissue of a heavily pre-treated patient with neuroendocrine variant CRPC. Similarly, combination therapy was the only treatment to result in reduced tumour cell proliferation and increased DNA damage when compared with vehicle. Neuroendocrine variant prostate cancer rarely occurs de novo and more commonly develops in patients with late stage disease in response to prolonged androgen deprivation therapy, with the incidence in CRPC patients

estimated to be 15-20% (Conteduca et al., 2019). This variant is typically characterised by the presence of visceral metastases and a low PSA, and is associated with poor survival outcomes (Conteduca et al., 2019). The finding that combined olaparib and ceralasertib is effective in this setting is of importance as it may offer a new avenue of treatment for this notoriously challenging variant.

The apparent efficacy of combined olaparib and ceralasertib across multiple models of HR-proficient prostate cancer in this thesis supports progression into early phase clinical trials exploring its role in this setting. Indeed, a phase II trial exploring combined olaparib (300 mg twice daily for day 1-28 of a 28 day cycle) and ceralasertib (160 mg once daily for days 1-7 of a 28 day cycle) in men with both HR-proficient and deficient metastatic CRPC is currently recruiting (Reichert et al., 2020). The results are eagerly awaited and will provide valuable insight into whether the observed findings translate into the clinical setting. Furthermore, this trial will also address the question of whether responses to combined PARPi and ATRi are greater in HR-proficient or HR-deficient disease, including the subgroup of patients with pre-existing aberrations in *ATM* in whom other preclinical studies have suggested it may be particularly efficacious (Neeb et al., 2021).

As well as having a potential role as combination therapy in men with CRPC that have already received a number of conventional treatments, different therapeutic strategies involving PARPi and ATRi could also be explored. For example, ATRi may provide a means of overcoming acquired resistance to PARPi that is known to develop after prolonged use in other HR-deficient cancers (Li et al., 2020). Numerous mechanisms underlying such resistance have been described, which are broadly divided into HR-dependent, for example through restoration of HR function via acquisition of secondary or reversion *BRCA* mutations, or HR-independent such as through upregulation of drug efflux pumps, PARP activity alteration and stabilisation of replication forks (Lord and Ashworth, 2013, D'Andrea, 2018, Li et al., 2020). As such, combination with ATRi may provide an avenue of restoring PARPi sensitivity in this setting. Indeed, a recent study by Kim et al. has shown that *BRCA* mutant ovarian cancer cells with acquired PARPi resistance through long term exposure to olaparib demonstrate higher basal levels of p-ATR and p-CHK1 compared with parental lines (Kim et al., 2020). This was overcome by ATRi with ceralasertib, which inhibited HR function and re-sensitised cells to PARPi in vitro, as well as in vivo in a selection of PARPi resistant PDX models of germline *BRCA1* and *BRCA2* mutant ovarian cancer (Kim et al., 2020). As the use of PARPi in HR-deficient CRPC is likely to become more widespread, it is probable that acquired PARPi resistance will also become a barrier to long term treatment in this setting. Further studies exploring the role of ATRi in models of HR-deficient CRPC that has developed

acquired PAPRi resistance are therefore warranted to explore this additional potentially promising avenue of therapy.

Previous preclinical studies have demonstrated that ADT acts to impair HR at the stage of DNA double strand end processing and that synthetic lethality is observed when PARPi and ADT are combined in vivo (Goodwin et al., 2013, Asim et al., 2017). This, together with the observation that PARP1 supports AR function, has prompted the evaluation of combined PARPi and ADT in men with mCRPC, with a recently published phase II trial of olaparib and abiraterone demonstrating significantly higher progression free survival compared with olaparib alone, regardless of the presence of HR defects (Schiewer et al., 2012, Clarke et al., 2018). Two further phase III trials are currently exploring this approach in men with mCRPC following primary failure of first line ADT; PROfound (NCT03732820) and MAGNITUDE (NCT03748641), with both reporting promising preliminary results (Chi et al., 2022, Saad et al., 2022). Furthermore, other trials are exploring the use of combined PARPi and ADT in the setting of metastatic castrate sensitive prostate cancer (mCSPC); Talapro-3 (NCT04821622) and AMPLITUDE (NCT04497844) (Rathkopf et al., 2021, Agarwal et al., 2022). If these studies confirm the earlier findings of Clarke et al. then it is possible that combined PARPi and ADT may have a role in men with both mCSPC and mCRPC.

Despite the novel antiandrogens abiraterone and enzalutamide demonstrating efficacy in men with mCRPC, 20-40% have primary resistance and exhibit no biochemical, radiological or clinical benefit whilst virtually all go on to develop secondary resistance (Boudadi and Antonarakis, 2016). Although not fully understood, a number of mechanisms by which this resistance occurs have been described, including upregulation of the AR, induction of AR splice variants, upregulation of cytochrome P450 17A1, activation of other oncogenic signalling pathways such as PI3K-Akt, and neuroendocrine transformation (Boudadi and Antonarakis, 2016). Although resistance to PARPi is acquired through different mechanisms (Lord and Ashworth, 2013, D'Andrea, 2018, Li et al., 2020), it is possible that durable responses to combined PARPi and ADT will not be possible due to acquisition of resistance to one or both of the agents involved during long term treatment. However, given that PARPi and ATRi was found to be efficacious in cells that were both castrate resistant and HR-proficient in this thesis, the addition of ATRi at the point when resistance occurs may offer a means of restoring efficacy, thereby warranting further exploration.

However, although ATRi may potentially be used to sensitise cells that have acquired resistance to PARPi when used as monotherapy or in combination with other agents such as abiraterone or

enzalutamide, not all tumours will be ATRi responsive and others may go on to acquire resistance following long term exposure. Unlike PARPi, for which there are clear biomarkers such as homozygous *BRCA2* deletion that indicate increased sensitivity, aberrations that correlate with response to ATRi have been less widely studied (Carreira et al., 2021). CRISPR-Cas9 and siRNA screening approaches have identified that loss of function of certain proteins involved in DNA repair and the cell cycle are associated with increased sensitivity, such as ATM, POLE3/4, ERCC1 and Coiled-coil domain-containing protein 6 (Mohni et al., 2014, Hustedt et al., 2019, Lloyd et al., 2021). Such studies have also identified proteins associated with resistance to ATRi, including Cyclin C, Cyclin-dependent kinase 8 and CDC25A (Ruiz et al., 2016, Lloyd et al., 2021). Whilst more research is needed in this area, it is possible that some resistance mechanisms may be shared with those responsible for acquired resistance to PARPi. For example, given that one of the proposed mechanisms of synergy between ATRi and PARPi is the ability of ATRi to inhibit DSB repair via HR, restoration of HR function in response to prolonged PARPi in a manner able to circumvent these inhibitory effects may also result in resistance to ATRi. Furthermore, non-HR related mechanisms such as drug efflux pumps may also apply to both agents. Therefore, whilst responses to combined PARPi and ATRi appear promising in the experiments presented in this thesis, it is possible that acquired resistance may provide a barrier to long term treatment. As such, further experiments exploring resistance to combination therapy and the mechanisms responsible will be essential for identifying those patients most likely to respond, as well as ways of overcoming these as and when they occur.

Given that a better understanding of PARP function within the prostate and prostate cancer may also identify ways with which to enhance responses to PARPi, the effects of conditional PARP1 depletion specifically within prostatic epithelial cells using Cre-LoxP recombination technology was explored in Chapter 5 of this thesis. Depletion of PARP1 did result in some changes in the growth and proliferative capacity of individual lobes of the normal adult murine prostate. However, it did not appear to alter the glandular phenotype or result in malignant transformation, hence indicating that PARP1 function is dispensable for the maintenance of normal homeostasis in the absence of significant DNA damage or cellular stress in the adult mouse. Furthermore, although PARP1 depletion also reduced growth of the dorsal and lateral lobes of *PSA-Cre-ER*$^{T2(+/-)}$*;* *p53*$^{fl/fl}$ *;* *Pten*$^{fl/fl}$ mice that develop localised, predominantly ventral prostate tumours, it did not result in differences in phenotype, epithelial cell differentiation, proliferation or apoptosis within tumour glands. Nevertheless, PARP1 depletion did increase expression of CHK1 in the tumour cells of this model, supporting the previous findings that PARP1 functional loss increases dependency on ATR-CHK1 signalling in prostate cancer.

Finally, to gain insight into the differential effects of PARP1 and PARP2 in CRPC, siRNA mediated genetic depletion was performed in the panel of HR-proficient CRPC cell lines. This identified that PARP1 depletion has a greater impact on both viability and proliferation than PARP2 depletion, and that simultaneous PARP1 and PARP2 depletion does not appear to significantly enhance the effect of PARP1 depletion alone. However, given that the knockdown efficiency of the *PARP2* siRNA used in these experiments was less than that of the *PARP1* siRNA, further experiments utilising different *PARP2* siRNA or an alternative gene editing approach such as CRISPR/Cas9 are needed. Nevertheless, other studies have shown that PARPi synthetic lethality in *BRCA* mutant cells appears to be predominantly driven by PARP1 (Murai et al., 2012, Ronson et al., 2018) which, together with the fact that PARP2 is essential in haematopoietic stem/progenitor cell survival (Farrés et al., 2013), has prompted development of selective PARP1 inhibitors, with one such agent currently being investigated in a phase I clinical trial (Johannes et al., 2021). If found to be safe and effective, selective PARP1 inhibitors could offer a means of reducing the haematological toxicity that has been observed in patients treated with combined PARP and ATR inhibition in early phase clinical trials, thus increasing tolerability and/or enabling dose escalation to increase efficacy.

Whilst the experiments in this were designed specifically to address each of the predefined aims, it is possible that some of the results may be subject to limitations based on the experimental methods used and time pressures resulting from the COVID-19 pandemic and associated restrictions on laboratory work. Specific limitations relating to each of the individual chapters are discussed in Sections 3.5, 4.5 and 5.5 respectively. Globally these can be divided into those related to dosing and time point selection, mechanistic evaluation at the protein level and the specific GEMMs utilised. With respect to the selection of drug concentrations used in the in vitro functional assays, dose response curves were firstly established based on cell viability at the 96 hour timepoint and the relative IC50 concentrations calculated (***Figures 3.1*** and ***3.7***). Although this approach enables comparisons between each of the individual cell lines, the IC50 concentrations may have differed if an alternative timepoint or endpoint were used. Furthermore, given the inherent insensitivity of the HR-proficient CRPC cells to PARPi in vitro, the relative IC50 concentration for olaparib was particularly high in the case of DU-145 cells (23.7 μM), thereby meaning some of the observed responses may have been the result of off-target effects. Whilst each of the concentrations used were within a range that is clinically achievable (Dillon et al., 2019, Pilla Reddy et al., 2019), one way of overcoming these issues would be to use a standard concentration of each of the agents across all of the cell lines and assays.

Similarly, the selection of timepoint for both the in vitro and in vivo experiments may have also impacted upon the results obtained. The chosen in vitro timepoint of 96 hours was based on previously published experiments exploring responses to PARPi in prostate cancer (Feiersinger et al., 2018). However, given that PARPi induced DNA damage accumulates over successive cell cycles, it is possible that different responses may have been observed if a later timepoint were utilised (Simoneau et al., 2021). The dosing schedules for the in vivo studies reported in Chapter 4 were chosen following discussion with AstraZeneca, the manufacturers of olaparib and ceralasertib. Whilst these were based previous in vitro and in vivo toxicity and efficacy studies (data not seen), mechanistic evaluation at the Day 18 and Day 21 timepoints in the PC-3 subcutaneous xenograft and GEMM preclinical trials respectively may have missed some of the effects of combined PARPi and ATRi on account of each agent only being given in combination for the first seven days of the treatment cycle. Further experiments utilising different timepoints may therefore provide additional and valuable insight into the mechanisms underlying responses to PARPi and ATRi both in vitro and in vivo.

Secondly, the mechanistic evaluation of responses to PARPi and ATRi in this thesis were predominantly based on results obtained through WB and IHC. Whilst these are standard and scientifically valid techniques for the assessment of protein expression, the use of WB to provide quantitative data is limited and may be subject to sources of error. To mitigate against this, densitometry was performed on blots obtained from three independent repeats and amalgamated to enable statistical analysis. However, in order to fully characterise the effects of treatment on protein concentration and post-translational modification, including interactions between different signalling pathways, lysates from PC-3 subcutaneous xenograft tumours were sent to collaborators in the University of Bristol for phosphoproteomic assessment. However, initial evaluation using hierarchical clustering and principle component analysis identified a number of issues precluding full bioinformatic analysis, as discussed in Section 4.5. A repeat experiment involving a larger number of protein samples taken from the same tumour regions in each treatment group is therefore necessary in order to fully elucidate the key cell signalling pathways underpinning the observed treatment responses.

Finally, the results of the GEMM studies may have been limited by both the choice of conditional knockout approach and timepoints utilised. Firstly, the *PSA-Cre-ER$^{T2(+/-)}$; p53$^{fl/fl}$; Pten$^{fl/fl}$* model was chosen for the reasons outlined in Section 4.1. Given that *PB-Cre4 p53$^{fl/fl}$; Pten$^{fl/fl}$* mice develop locally advanced tumours that are almost inevitably fatal by seven months of age (Chen et al., 2005), it was anticipated that *PSA-Cre-ER$^{T2(+/-)}$; p53$^{fl/fl}$; Pten$^{fl/fl}$* mice would also develop a similar tumours within the same timeframe. However, as discussed in Section 4.3.3, characterisation experiments conducted

prior to the preclinical trial demonstrated that *PSA-Cre-ER$^{T2(+/-)}$; p53$^{fl/fl}$; Pten$^{fl/fl}$* mice develop small localised tumours at six months following tamoxifen induction, predominantly involving the ventral lobes, as demonstrated in ***Figure 4.17***. This difference in phenotype is likely the result of the higher specificity and lower recombination efficiency of *PSA-Cre-ER^{T2}*, which is only expressed in prostatic epithelial cells following exposure to tamoxifen (Ratnacaram et al., 2008). Although combined PARPi and ATRi did result in favourable responses with respect to proliferation and prevalence of microinvasive carcinoma, further experiments utilising mice aged to a later timepoint prior to commencement of the preclinical trial may provide additional insight into treatment effects in larger, locally advanced tumours.

Similarly, the use of Cre-LoxP recombination with *PSA-Cre-ER^{T2}* to study the effects of PARP1 within the prostatic epithelium is associated with its own limitations. Given that recombination only occurs within epithelial cells, these models were unable to evaluate the effects of PARP1 loss within other cell types within the prostate, including those of the stroma or immune infiltrate, in which it may play an important biological role. Furthermore, it is difficult to draw direct comparisons between genetic depletion of PARP enzymes and their pharmacological inhibition, as the former only reduces catalytic activity through reduced levels of expression and does not lead to PARP trapping that is deemed a an important component of the mechanism of action of PARP inhibitors (Murai et al., 2012). However, the main limitations of the PARP function GEMM studies in this thesis are a lack of in-depth analysis and assessment of PARP2 loss, both of which are the result of the aforementioned restrictions on laboratory work as a consequence of the COVID-19 pandemic. Nevertheless, the *Parp2 floxed* allele has already been imported and breeding is now underway to generate cohorts with genetic depletion of PARP1, PARP2 and both PARP1 and PARP2. It is therefore hoped that more detailed analysis of the prostates of these mice will provide a better understanding of the effects of loss of both isoforms within the prostatic epithelium in both normal homeostasis and prostate cancer driven by simultaneous p53 and PTEN loss.

In conclusion, the results presented in this thesis provide evidence to support the ongoing investigation of combined PARP and ATR inhibition in the setting of HR-proficient CRPC. In doing so it is hoped that these findings may contribute to the development of safe and effective treatments that improve the clinical outcomes and quality of life of men with this lethal disease in whom options are currently limited.

7 References

Aaron, L., Franco, O.E. and Hayward, S.W. 2016. Review of prostate anatomy and embryology and the etiology of benign prostatic hyperplasia. *Urologic Clinics* 43(3), pp. 279-288.

Abate-Shen, C. and Shen, M.M. 2000. Molecular genetics of prostate cancer. *Genes and Development* 14(19), pp. 2410-2434.

Abeshouse, A., et al. 2015. The molecular taxonomy of primary prostate cancer. *Cell* 163(4), pp. 1011-1025.

Abida, W., et al. 2020. Non-BRCA DNA damage repair gene alterations and response to the PARP inhibitor rucaparib in metastatic castration-resistant prostate cancer: analysis from the phase II TRITON2 study. *Clinical Cancer Research* 26(11), pp. 2487-2496.

Abida, W., et al. 2019. Genomic correlates of clinical outcome in advanced prostate cancer. *Proceedings of the National Academy of Sciences* 116(23), pp. 11428-11436.

Abrahamsson, P. 1999. Neuroendocrine cells in tumour growth of the prostate. *Endocrine-Related Cancer* 6(4), pp. 503-519.

Adashek, J.J., Jain, R.K. and Zhang, J. 2019. Clinical development of PARP inhibitors in treating metastatic castration-resistant prostate cancer. *Cells* 8(8), pp. 860.

Agarwal, N., et al. 2022. Talapro-3: A phase 3, double-blind, randomized study of enzalutamide (ENZA) plus talazoparib (TALA) versus placebo plus enza in patients with DDR gene mutated metastatic castration-sensitive prostate cancer (mCSPC). *Journal of Clinical Oncology* 40(supplement 6), pp. 1.

Ahmed, H.U., et al. 2017. Diagnostic accuracy of multi-parametric MRI and TRUS biopsy in prostate cancer (PROMIS): a paired validating confirmatory study. *The lancet* 389(10071), pp. 815-822.

Albertsen, P.C., Hanley, J.A. and Fine, J. 2005. 20-year outcomes following conservative management of clinically localized prostate cancer. *Journal of the American Medical Association* 293(17), pp. 2095-2101.

Albertsen, P.C., Hanley, J.A., Gleason, D.F. and Barry, M.J. 1998. Competing risk analysis of men aged 55 to 74 years at diagnosis managed conservatively for clinically localized prostate cancer. *Journal of the American Medical Association* 280(11), pp. 975-980.

Albertsen, P.C., Moore, D.F., Shih, W., Lin, Y., Li, H. and Lu-Yao, G.L. 2011. Impact of comorbidity on survival among men with localized prostate cancer. *Journal of Clinical Oncology* 29(10), pp. 1335.

Ali, S.O., Khan, F.A., Galindo-Campos, M.A. and Yélamos, J. 2016. Understanding specific functions of PARP-2: new lessons for cancer therapy. *American Journal of Cancer Research* 6(9), pp. 1842.

Allott, E.H., Masko, E.M. and Freedland, S.J. 2013. Obesity and prostate cancer: weighing the evidence. *European Urology* 63(5), pp. 800-809.

Amory, J.K. and Bremner, W.J. 2003. Regulation of testicular function in men: implications for male hormonal contraceptive development. *The Journal of steroid biochemistry and molecular biology* 85(2-5), pp. 357-361.

Andriole, G.L., et al. 2010. Effect of dutasteride on the risk of prostate cancer. *New England Journal of Medicine* 362, pp. 1192-1202.

Armenia, J., et al. 2018. The long tail of oncogenic drivers in prostate cancer. *Nature Genetics* 50(5), pp. 645-651.

Asim, M., et al. 2017. Synthetic lethality between androgen receptor signalling and the PARP pathway in prostate cancer. *Nature Communications* 8(1), pp. 374.

Baca, S.C., et al. 2013. Punctuated evolution of prostate cancer genomes. *Cell* 153(3), pp. 666-677.

Bagnardi, V., Blangiardo, M., La Vecchia, C. and Corrao, G. 2001. A meta-analysis of alcohol drinking and cancer risk. *British Journal of Cancer* 85(11), pp. 1700-1705.

Bai, P. 2015. Biology of poly (ADP-ribose) polymerases: the factotums of cell maintenance. *Molecular cell* 58(6), pp. 947-958.

Bai, P. and Cantó, C. 2012. The role of PARP-1 and PARP-2 enzymes in metabolic regulation and disease. *Cell Metabolism* 16(3), pp. 290-295.

Balk, S.P., Ko, Y.-J. and Bubley, G.J. 2003. Biology of prostate-specific antigen. *Journal of Clinical Oncology* 21(2), pp. 383-391.

Banez, L.L., et al. 2007. Obesity-related plasma hemodilution and PSA concentration among men with prostate cancer. *Journal of the American Medical Association* 298(19), pp. 2275-2280.

Bankhead, P., et al. 2017. QuPath: Open source software for digital pathology image analysis. *Scientific reports* 7(1), pp. 1-7.

Barbieri, C.E., et al. 2012. Exome sequencing identifies recurrent SPOP, FOXA1 and MED12 mutations in prostate cancer. *Nature Genetics* 44(6), pp. 685-689.

Barentsz, J.O., et al. 2016. Synopsis of the PI-RADS v2 guidelines for multiparametric prostate magnetic resonance imaging and recommendations for use. *European Urology* 69(1), pp. 41-49.

Barnieh, F.M., Loadman, P.M. and Falconer, R.A. 2021. Progress towards a clinically-successful ATR inhibitor for cancer therapy. *Current Research in Pharmacology and Drug Discovery* 2, pp. 100017.

Barreto-Andrade, J.C., et al. 2011. Response of human prostate cancer cells and tumors to combining PARP inhibition with ionizing radiation. *Molecular Cancer Therapeutics* 10(7), pp. 1185-1193.

Barry, M.J., et al. 2001. Outcomes for men with clinically nonmetastatic prostate carcinoma managed with radical prostactectomy, external beam radiotherapy, or expectant management: a retrospective analysis. *Cancer* 91(12), pp. 2302-2314.

Barzell, W.E., Melamed, M.R., Cathcart, P., Moore, C.M., Ahmed, H.U. and Emberton, M. 2012. Identifying candidates for active surveillance: an evaluation of the repeat biopsy strategy for men with favorable risk prostate cancer. *The Journal of urology* 188(3), pp. 762-768.

Baskar, R., Dai, J., Wenlong, N., Yeo, R. and Yeoh, K.-W. 2014. Biological response of cancer cells to radiation treatment. *Frontiers in Molecular Biosciences* 1, pp. 24.

Beer, T.M., et al. 2014. Enzalutamide in metastatic prostate cancer before chemotherapy. *New England Journal of Medicine* 371(5), pp. 424-433.

Benafif, S., Kote-Jarai, Z. and Eeles, R.A. 2018. A review of prostate cancer genome-wide association studies (GWAS). *Cancer Epidemiology and Prevention Biomarkers* 27(8), pp. 845-857.

Berg, K.D., Thomsen, F.B., Mikkelsen, M.K., Ingimarsdóttir, I.J., Hansen, R.B., Kejs, A.M.T. and Brasso, K. 2017. Improved survival for patients with de novo metastatic prostate cancer in the last 20 years. *European Journal of Cancer* 72, pp. 20-27.

Bill-Axelson, A., et al. 2018. Radical prostatectomy or watchful waiting in prostate cancer—29-year follow-up. *New England Journal of Medicine* 379(24), pp. 2319-2329.

Bladou, F., Vessella, R.L., Buhler, K.R., Ellis, W.J., True, L.D. and Lange, P.H. 1996. Cell proliferation and apoptosis during prostatic tumor xenograft involution and regrowth after castration. *International Journal of Cancer* 67(6), pp. 785-790.

Bolla, M., et al. 2009. Duration of androgen suppression in the treatment of prostate cancer. *New England Journal of Medicine* 360(24), pp. 2516-2527.

Boorjian, S.A., Karnes, R.J., Rangel, L.J., Bergstralh, E.J. and Blute, M.L. 2008. Mayo Clinic validation of the D'amico risk group classification for predicting survival following radical prostatectomy. *The Journal of urology* 179(4), pp. 1354-1361.

Bostwick, D.G., Shan, A., Qian, J., Darson, M., Maihle, N.J., Jenkins, R.B. and Cheng, L. 1998. Independent origin of multiple foci of prostatic intraepithelial neoplasia: comparison with matched foci of prostate carcinoma. *Cancer: Interdisciplinary International Journal of the American Cancer Society* 83(9), pp. 1995-2002.

Boudadi, K. and Antonarakis, E.S. 2016. Resistance to novel antiandrogen therapies in metastatic castration-resistant prostate cancer. *Clinical Medicine Insights: Oncology* 10, pp. 34534.

Brandt, A., Bermejo, J.L., Sundquist, J. and Hemminki, K. 2010. Age-specific risk of incident prostate cancer and risk of death from prostate cancer defined by the number of affected family members. *European Urology* 58(2), pp. 275-280.

Bratan, F., et al. 2013. Influence of imaging and histological factors on prostate cancer detection and localisation on multiparametric MRI: a prospective study. *European Radiology* 23(7), pp. 2019-2029.

Brenner, J.C., et al. 2011. Mechanistic rationale for inhibition of poly (ADP-ribose) polymerase in ETS gene fusion-positive prostate cancer. *Cancer Cell* 19(5), pp. 664-678.

Breslow, N., et al. 1977. Latent carcinoma of prostate at autopsy in seven areas. Collaborative study organized by the International Agency for Research on Cancer, Lyons, France. *International Journal of Cancer* 20(5), pp. 680-688.

Brewster, D., Fraser, L., Harris, V. and Black, R. 2000. Rising incidence of prostate cancer in Scotland: increased risk or increased detection? *British Journal of Urology International* 85(4), pp. 463-473.

Brierley, J.D., Gospodarowicz, M.K. and Wittekind, C. (2017). *TNM classification of malignant tumours*: John Wiley & Sons.

Bruinsma, S.M., et al. 2017. Expert consensus document: Semantics in active surveillance for men with localized prostate cancer—results of a modified Delphi consensus procedure. *Nature Reviews Urology* 14(5), pp. 312.

Bryant, H.E., et al. 2005. Specific killing of BRCA2-deficient tumours with inhibitors of poly (ADP-ribose) polymerase. *Nature* 434(7035), pp. 913-917.

Butler, L.M., Wang, R., Wong, A.S., Koh, W.-P. and Mimi, C.Y. 2009. Cigarette smoking and risk of prostate cancer among Singapore Chinese. *Cancer Causes and Control* 20(10), pp. 1967-1974.

Cancer Research UK. (2018). *Prostate cancer statistics* [*online*]. Available at: https://www.cancerresearchuk.org/health-professional/cancer-statistics/statistics-by-cancer-type/prostate-cancer#heading-Zero [Accessed 9 February 2022 2022].

Cao, Y. and Ma, J. 2011. Body mass index, prostate cancer–specific mortality, and biochemical recurrence: a systematic review and meta-analysis. *Cancer Prevention Research* 4(4), pp. 486-501.

Carreira, S., et al. 2021. Biomarkers Associating with PARP Inhibitor Benefit in Prostate Cancer in the TOPARP-B TrialPredictive Biomarkers for PARP Inhibition in Prostate Cancer. *Cancer discovery* 11(11), pp. 2812-2827.

Carvalhal, G.F., Smith, D.S., Mager, D.E., Ramos, C. and Catalona, W.J. 1999. Digital rectal examination for detecting prostate cancer at prostate specific antigen levels of 4 ng./ml. or less. *The Journal of Urology* 161(3), pp. 835-839.

Castro, E., et al. 2015. Effect of BRCA mutations on metastatic relapse and cause-specific survival after radical treatment for localised prostate cancer. *European Urology* 68(2), pp. 186-193.

Castro, E., et al. 2013. Germline BRCA mutations are associated with higher risk of nodal involvement, distant metastasis, and poor survival outcomes in prostate cancer. *Journal of Clinical Oncology* 31(14), pp. 1748-1757.

Ceccaldi, R., Rondinelli, B. and D'Andrea, A.D. 2016. Repair pathway choices and consequences at the double-strand break. *Trends in Cell Biology* 26(1), pp. 52-64.

Centenera, M.M., et al. 2012. Evidence for efficacy of new Hsp90 inhibitors revealed by ex vivo culture of human prostate tumors. *Clinical Cancer Research* 18(13), pp. 3562-3570.

Cerami, E., et al. 2012. The cBio cancer genomics portal: an open platform for exploring multidimensional cancer genomics data. *Cancer Discovery* 2(5), pp. 401-404.

Cerveira, N., Ribeiro, F.R., Peixoto, A., Costa, V., Henrique, R., Jerónimo, C. and Teixeira, M.R. 2006. TMPRSS2-ERG gene fusion causing ERG overexpression precedes chromosome copy number changes in prostate carcinomas and paired HGPIN lesions. *Neoplasia* 8(10), pp. 826.

Chan, J.M., Gann, P.H. and Giovannucci, E.L. 2005. Role of diet in prostate cancer development and progression. *Journal of Clinical Oncology* 23(32), pp. 8152-8160.

Chen, H., et al. 2003. RNASEL mutations in hereditary prostate cancer. *Journal of Medical Genetics* 40(3), pp. e21-e21.

Chen, Z., et al. 2005. Crucial role of p53-dependent cellular senescence in suppression of Pten-deficient tumorigenesis. *Nature* 436(7051), pp. 725.

Chi, K.N., et al. 2022. Phase 3 MAGNITUDE study: First results of niraparib (NIRA) with abiraterone acetate and prednisone (AAP) as first-line therapy in patients (pts) with metastatic castration-resistant prostate cancer (mCRPC) with and without homologous recombination repair (HRR) gene alterations. *Journal of Clinical Oncology* 40(supplement 6), pp. 1.

Chodak, G. and Warren, K. 2006. Watchful waiting for prostate cancer: a review article. *Prostate Cancer and Prostatic Diseases* 9(1), pp. 25-29.

Choi, J.-H., Lindsey-Boltz, L.A., Kemp, M., Mason, A.C., Wold, M.S. and Sancar, A. 2010. Reconstitution of RPA-covered single-stranded DNA-activated ATR-Chk1 signaling. *Proceedings of the National Academy of Sciences* 107(31), pp. 13660-13665.

Chu, L.W., Ritchey, J., Devesa, S.S., Quraishi, S.M., Zhang, H. and Hsing, A.W. 2011. Prostate cancer incidence rates in Africa. *Prostate cancer* 2011.

Chua, C.W., et al. 2014. Single luminal epithelial progenitors can generate prostate organoids in culture. *Nature Cell Biology* 16(10), pp. 951-961.

Clarke, N., et al. 2018. Olaparib combined with abiraterone in patients with metastatic castration-resistant prostate cancer: a randomised, double-blind, placebo-controlled, phase 2 trial. *The Lancet Oncology* 19(7), pp. 975-986.

Cohen, M.S., et al. 2008. Comparing the Gleason prostate biopsy and Gleason prostatectomy grading system: the Lahey Clinic Medical Center experience and an international meta-analysis. *European Urology* 54(2), pp. 371-381.

Collins, A.R. 2004. The comet assay for DNA damage and repair. *Molecular biotechnology* 26(3), pp. 249-261.

Collins, A.T., Habib, F.K., Maitland, N.J. and Neal, D.E. 2001. Identification and isolation of human prostate epithelial stem cells based on α2β1-integrin expression. *Journal of Cell Science* 114(21), pp. 3865-3872.

Conteduca, V., et al. 2019. Clinical features of neuroendocrine prostate cancer. *European Journal of Cancer* 121, pp. 7-18.

Cox, A., Jefferies, M. and Persad, R. 2019. Prostate Structure and Function. *Blandy's Urology*, pp. 509-521.

Cunningham, D. and You, Z. 2015. In vitro and in vivo model systems used in prostate cancer research. *Journal of biological methods* 2(1), pp. 17.

D'amico, A.V., et al. 1998. Biochemical outcome after radical prostatectomy, external beam radiation therapy, or interstitial radiation therapy for clinically localized prostate cancer. *Journal of the American Medical Association* 280(11), pp. 969-974.

D'Andrea, A.D. 2018. Mechanisms of PARP inhibitor sensitivity and resistance. *DNA repair* 71, pp. 172-176.

Dana, H., et al. 2017. Molecular mechanisms and biological functions of siRNA. *International journal of biomedical science* 13(2), pp. 48.

Dantzer, F., et al. 2006. Poly (ADP-ribose) polymerase-2 contributes to the fidelity of male meiosis I and spermiogenesis. *Proceedings of the National Academy of Sciences* 103(40), pp. 14854-14859.

Darzynkiewicz, Z. 2011. Redundancy in response to DNA damage: The key to protection of genome integrity Comment on: Ciznadija D, et al. Cell Cycle 2011; 10:2714-23. *Cell Cycle* 10(20), pp. 3425-3425.

Daugherty, M.D., Young, J.M., Kerns, J.A. and Malik, H.S. 2014. Rapid evolution of PARP genes suggests a broad role for ADP-ribosylation in host-virus conflicts. *PLoS Genetics* 10(5), pp. e1004403.

Davis, A.J. and Chen, D.J. 2013. DNA double strand break repair via non-homologous end-joining. *Translational cancer research* 2(3), pp. 130.

De Bono, J., et al. 2020. Olaparib for metastatic castration-resistant prostate cancer. *New England Journal of Medicine* 382(22), pp. 2091-2102.

De Bono, J.S., et al. 2011. Abiraterone and increased survival in metastatic prostate cancer. *New England Journal of Medicine* 364(21), pp. 1995-2005.

De Murcia, J.M., et al. 2003. Functional interaction between PARP-1 and PARP-2 in chromosome stability and embryonic development in mouse. *The EMBO journal* 22(9), pp. 2255-2263.

Dehm, S.M. and Tindall, D.J. 2006. Molecular regulation of androgen action in prostate cancer. *Journal of Cellular Biochemistry* 99(2), pp. 333-344.

DeMarzo, A.M., Nelson, W.G., Isaacs, W.B. and Epstein, J.I. 2003. Pathological and molecular aspects of prostate cancer. *The Lancet* 361(9361), pp. 955-964.

Denham, J.W., et al. 2011. Short-term neoadjuvant androgen deprivation and radiotherapy for locally advanced prostate cancer: 10-year data from the TROG 96.01 randomised trial. *The Lancet Oncology* 12(5), pp. 451-459.

DeRose, Y.S., et al. 2011. Tumor grafts derived from women with breast cancer authentically reflect tumor pathology, growth, metastasis and disease outcomes. *Nature Medicine* 17(11), pp. 1514-1520.

Deshmukh, D. and Qiu, Y. 2015. Role of PARP-1 in prostate cancer. *American journal of clinical and experimental urology* 3(1), pp. 1.

Dillon, M., et al. 2019. A phase I study of ATR inhibitor, AZD6738, as monotherapy in advanced solid tumours (PATRIOT part A, B). *Annals of Oncology* 30, pp. v165-v166.

Downer, M.K., et al. 2019. Alcohol intake and risk of lethal prostate cancer in the Health Professionals Follow-Up Study. *Journal of Clinical Oncology* 37(17), pp. 1499-1511.

Dulaney, C., Marcrom, S., Stanley, J. and Yang, E.S. 2017. Poly (ADP-ribose) polymerase activity and inhibition in cancer. Seminars in cell & developmental biology, Elsevier.

Egevad, L., Granfors, T., Karlberg, L., Bergh, A. and Stattin, P. 2002. Prognostic value of the Gleason score in prostate cancer. *British Journal of Urology International* 89(6), pp. 538-542.

Endogenous Hormones and Prostate Cancer Collaborative Group. 2008. Endogenous sex hormones and prostate cancer: a collaborative analysis of 18 prospective studies. *Journal of the National Cancer Institute* 100(3), pp. 170-183.

Epstein, J.I., Allsbrook Jr, W.C., Amin, M.B., Egevad, L.L. and Committee, I.G. 2005. The 2005 International Society of Urological Pathology (ISUP) consensus conference on Gleason grading of prostatic carcinoma. *The American journal of surgical pathology* 29(9), pp. 1228-1242.

Epstein, J.I., Egevad, L., Amin, M.B., Delahunt, B., Srigley, J.R. and Humphrey, P.A. 2016a. The 2014 International Society of Urological Pathology (ISUP) consensus conference on Gleason grading of prostatic carcinoma. *The American journal of surgical pathology* 40(2), pp. 244-252.

Epstein, J.I., Partin, A.W., Sauvageot, J. and Walsh, P.C. 1996. Prediction of progression following radical prostatectomy: a multivariate analysis of 721 men with long-term follow-up. *The American journal of surgical pathology* 20(3), pp. 286-292.

Epstein, J.I., Pizov, G. and Walsh, P.C. 1993. Correlation of pathologic findings with progression after radical retropubic prostatectomy. *Cancer* 71(11), pp. 3582-3593.

Epstein, J.I., et al. 2016b. A contemporary prostate cancer grading system: a validated alternative to the Gleason score. *European Urology* 69(3), pp. 428-435.

Esfahani, K., Roudaia, L., Buhlaiga, N.a., Del Rincon, S., Papneja, N. and Miller, W. 2020. A review of cancer immunotherapy: from the past, to the present, to the future. *Current Oncology* 27(s2), pp. 87-97.

Euhus, D.M., Hudd, C., Laregina, M.C. and Johnson, F.E. 1986. Tumor measurement in the nude mouse. *Journal of Surgical Oncology* 31(4), pp. 229-234.

Fang, Y. and Eglen, R.M. 2017. Three-dimensional cell cultures in drug discovery and development. *Slas discovery: Advancing Life Sciences R&D* 22(5), pp. 456-472.

Farashi, S., Kryza, T., Clements, J. and Batra, J. 2019. Post-GWAS in prostate cancer: from genetic association to biological contribution. *Nature Reviews Cancer* 19(1), pp. 46-59.

Farmer, H., et al. 2005. Targeting the DNA repair defect in BRCA mutant cells as a therapeutic strategy. *Nature* 434(7035), pp. 917.

Farrés, J., et al. 2013. Parp-2 is required to maintain hematopoiesis following sublethal γ-irradiation in mice. *Blood, The Journal of the American Society of Hematology* 122(1), pp. 44-54.

Fearon, E.R. and Vogelstein, B. 1990. A genetic model for colorectal tumorigenesis. *Cell* 61(5), pp. 759-767.

Feiersinger, G.E., et al. 2018. Olaparib is effective in combination with, and as maintenance therapy after, first-line endocrine therapy in prostate cancer cells. *Molecular oncology* 12(4), pp. 561-576.

Fernández-Balsells, M.M., et al. 2010. Adverse effects of testosterone therapy in adult men: a systematic review and meta-analysis. *The Journal of Clinical Endocrinology & Metabolism* 95(6), pp. 2560-2575.

Foerster, B., et al. 2018. Association of smoking status with recurrence, metastasis, and mortality among patients with localized prostate cancer undergoing prostatectomy or radiotherapy: a systematic review and meta-analysis. *JAMA oncology* 4(7), pp. 953-961.

Fong, P.C., et al. 2009. Inhibition of poly (ADP-ribose) polymerase in tumors from BRCA mutation carriers. *New England Journal of Medicine* 361(2), pp. 123-134.

Fontanini, G., et al. 1997. Neoangiogenesis and p53 protein in lung cancer: their prognostic role and their relation with vascular endothelial growth factor (VEGF) expression. *British journal of cancer* 75(9), pp. 1295-1301.

Foo, K.T. 2017. Pathophysiology of clinical benign prostatic hyperplasia. *Asian Journal of Urology* 4(3), pp. 152-157.

Foote, K.M., et al. 2018. Discovery and characterization of AZD6738, a potent inhibitor of ataxia telangiectasia mutated and Rad3 related (ATR) kinase with application as an anticancer agent. *Journal of Medicinal Chemistry* 61(22), pp. 9889-9907.

Fosså, S.D., et al. 2016. Ten-and 15-yr prostate cancer-specific mortality in patients with nonmetastatic locally advanced or aggressive intermediate prostate cancer, randomized to lifelong endocrine treatment alone or combined with radiotherapy: final results of the Scandinavian Prostate Cancer Group-7. *European Urology* 70(4), pp. 684-691.

Foulds, L. 1954. The experimental study of tumor progression: a review. *Cancer Research* 14(5), pp. 327-339.

Franken, N.A., Rodermond, H.M., Stap, J., Haveman, J. and Van Bree, C. 2006. Clonogenic assay of cells in vitro. *Nature Protocols* 1(5), pp. 2315.

Fraser, M., et al. 2017. Genomic hallmarks of localized, non-indolent prostate cancer. *Nature* 541(7637), pp. 359-364.

Freedland, S.J., Aronson, W.J., Kane, C.J., Presti Jr, J.C., Amling, C.L., Elashoff, D. and Terris, M.K. 2004. Impact of obesity on biochemical control after radical prostatectomy for clinically localized prostate cancer: a report by the Shared Equal Access Regional Cancer Hospital database study group. *Journal of Clinical Oncology* 22(3), pp. 446-453.

Freeman, G.J., et al. 2000. Engagement of the PD-1 immunoinhibitory receptor by a novel B7 family member leads to negative regulation of lymphocyte activation. *The Journal of Experimental Medicine* 192(7), pp. 1027-1034.

Fujita, K. and Nonomura, N. 2019. Role of androgen receptor in prostate cancer: a review. *The World Journal of Men's Health* 37(3), pp. 288-295.

Galindo-Campos, M.A., et al. 2019. Coordinated signals from the DNA repair enzymes PARP-1 and PARP-2 promotes B-cell development and function. *Cell Death & Differentiation* 26(12), pp. 2667-2681.

Gallagher, D.J., et al. 2010. Germline BRCA mutations denote a clinicopathologic subset of prostate cancer. *Clinical Cancer Research* 16(7), pp. 2115-2121.

Gandaglia, G., et al. 2021. Epidemiology and prevention of prostate cancer. *European Urology Oncology* 4(6), pp. 877-892.

Gandhi, J., et al. 2018. The molecular biology of prostate cancer: current understanding and clinical implications. *Prostate Cancer and Prostatic Diseases* 21(1), pp. 22-36.

Gangoda, L., et al. 2012. Cre transgene results in global attenuation of the cAMP/PKA pathway. *Cell Death & Disease* 3(8), pp. e365-e365.

Gani, C., Coackley, C., Kumareswaran, R., Schütze, C., Krause, M., Zafarana, G. and Bristow, R.G. 2015. In vivo studies of the PARP inhibitor, AZD-2281, in combination with fractionated radiotherapy: An exploration of the therapeutic ratio. *Radiotherapy and Oncology* 116(3), pp. 486-494.

Gao, J., et al. 2013. Integrative analysis of complex cancer genomics and clinical profiles using the cBioPortal. *Science Signaling* 6(269), pp. pl1-pl1.

Garinis, G.A., Van der Horst, G.T., Vijg, J. and Hoeijmakers, J.H. 2008. DNA damage and ageing: new-age ideas for an age-old problem. *Nature Cell Biology* 10(11), pp. 1241.

Gayet, M., van der Aa, A., Beerlage, H.P., Schrier, B.P., Mulders, P.F. and Wijkstra, H. 2016. The value of magnetic resonance imaging and ultrasonography (MRI/US)-fusion biopsy platforms in prostate cancer detection: a systematic review. *British Journal of Urology International* 117(3), pp. 392-400.

Gerber, G.S., et al. 1997. Results of radical prostatectomy in men with locally advanced prostate cancer: multi-institutional pooled analysis. *European Urology* 32, pp. 385-390.

Gerhauser, C., et al. 2018. Molecular evolution of early-onset prostate cancer identifies molecular risk markers and clinical trajectories. *Cancer Cell* 34(6), pp. 996-1011. e1018.

Gerstenbluth, R.E., Seftel, A.D., Hampel, N., Oefelein, M.G. and Resnick, M.I. 2002. The accuracy of the increased prostate specific antigen level (greater than or equal to 20 ng./ml.) in predicting prostate cancer: is biopsy always required? *The Journal of Urology* 168(5), pp. 1990-1993.

Gillet, J.-P., Varma, S. and Gottesman, M.M. 2013. The clinical relevance of cancer cell lines. *Journal of the National Cancer Institute* 105(7), pp. 452-458.

Gingrich, J.R., et al. 1996. Metastatic prostate cancer in a transgenic mouse. *Cancer research* 56(18), pp. 4096-4102.

Giovannucci, E., Liu, Y., Platz, E.A., Stampfer, M.J. and Willett, W.C. 2007. Risk factors for prostate cancer incidence and progression in the health professionals follow-up study. *International Journal of Cancer* 121(7), pp. 1571-1578.

Gleason, D.F. 1966. Classification of prostatic carcinomas. *Cancer Chemotherapy Reports* 50, pp. 125-128.

Gnanapragasam, V., Bratt, O., Muir, K., Lee, L., Huang, H., Stattin, P. and Lophatananon, A. 2018. The Cambridge Prognostic Groups for improved prediction of disease mortality at diagnosis in primary non-metastatic prostate cancer: a validation study. *BMC medicine* 16(1), pp. 1-10.

Gong, Z., Kristal, A.R., Schenk, J.M., Tangen, C.M., Goodman, P.J. and Thompson, I.M. 2009. Alcohol consumption, finasteride, and prostate cancer risk: results from the Prostate Cancer Prevention Trial. *Cancer: Interdisciplinary International Journal of the American Cancer Society* 115(16), pp. 3661-3669.

González-Billalabeitia, E., et al. 2014. Vulnerabilities of PTEN–TP53-deficient prostate cancers to compound PARP–PI3K inhibition. *Cancer discovery* 4(8), pp. 896-904.

Goodwin, J.F., et al. 2013. A hormone–DNA repair circuit governs the response to genotoxic insult. *Cancer discovery* 3(11), pp. 1254-1271.

Gosselaar, C., Roobol, M.J., Roemeling, S. and Schröder, F.H. 2008. The role of the digital rectal examination in subsequent screening visits in the European randomized study of screening for prostate cancer (ERSPC), Rotterdam. *European Urology* 54(3), pp. 581-588.

Grasso, C.S., et al. 2012. The mutational landscape of lethal castration-resistant prostate cancer. *Nature* 487(7406), pp. 239-243.

Gui, B., et al. 2019. Selective targeting of PARP-2 inhibits androgen receptor signaling and prostate cancer growth through disruption of FOXA1 function. *Proceedings of the National Academy of Sciences* 116(29), pp. 14573-14582.

Gunn, A. and Stark, J.M. 2012. I-SceI-based assays to examine distinct repair outcomes of mammalian chromosomal double strand breaks. *DNA repair protocols* 920, pp. 379-391.

Guo, L.-H., et al. 2015. Comparison between ultrasound guided transperineal and transrectal prostate biopsy: a prospective, randomized, and controlled trial. *Scientific Reports* 5, pp. 16089.

Gupte, R., Liu, Z. and Kraus, W.L. 2017. PARPs and ADP-ribosylation: recent advances linking molecular functions to biological outcomes. *Genes and Development* 31(2), pp. 101-126.

Haince, J.-F., McDonald, D., Rodrigue, A., Déry, U., Masson, J.-Y., Hendzel, M.J. and Poirier, G.G. 2008. PARP1-dependent kinetics of recruitment of MRE11 and NBS1 proteins to multiple DNA damage sites. *Journal of Biological Chemistry* 283(2), pp. 1197-1208.

Hamdy, F.C., et al. 2016. 10-year outcomes after monitoring, surgery, or radiotherapy for localized prostate cancer. *New England Journal of Medicine* 375(15), pp. 1415-1424.

Hamid, A.A., et al. 2019. Compound genomic alterations of TP53, PTEN, and RB1 tumor suppressors in localized and metastatic prostate cancer. *European Urology* 76(1), pp. 89-97.

Hammond, G.L., Avvakumov, G.V. and Muller, Y.A. 2003. Structure/function analyses of human sex hormone-binding globulin: effects of zinc on steroid-binding specificity. *The Journal of steroid biochemistry and molecular biology* 85(2-5), pp. 195-200.

Hampel, H., et al. 2005. Screening for the Lynch syndrome (hereditary nonpolyposis colorectal cancer). *New England Journal of Medicine* 352(18), pp. 1851-1860.

Han, S., et al. 2013. Targeted radiosensitization of ETS fusion-positive prostate cancer through PARP1 inhibition. *Neoplasia* 15(10), pp. 1207-1217.

Hanahan, D. and Weinberg, R.A. 2000. The hallmarks of cancer. *Cell* 100(1), pp. 57-70.

Hanahan, D. and Weinberg, R.A. 2011. Hallmarks of cancer: the next generation. *Cell* 144(5), pp. 646-674.

Haynes, B., Murai, J. and Lee, J.-M. 2018. Restored replication fork stabilization, a mechanism of PARP inhibitor resistance, can be overcome by cell cycle checkpoint inhibition. *Cancer Treatment Reviews* 71, pp. 1-7.

Hieronymus, H., et al. 2014. Copy number alteration burden predicts prostate cancer relapse. *Proceedings of the National Academy of Sciences* 111(30), pp. 11139-11144.

Ho, T., et al. 2014. Smoking and risk of low-and high-grade prostate cancer: results from the REDUCE study. *Clinical Cancer Research* 20(20), pp. 5331-5338.

Hoeijmakers, J.H.J. 2001. Genome maintenance mechanisms for preventing cancer. *Nature* 411(6835), pp. 366-374.

Hoeijmakers, J.H.J. 2009. DNA Damage, Aging, and Cancer. (vol 361, pg 1475, 2009). *New England Journal of Medicine* 361(19), pp. 1914-1914.

Hoejmakers, J., et al. 2006. DNA damage repair, cancer, ageing and life span extension. *Hormone Research* 65, pp. 1-1.

Hoffmann, B., Lange, T., Labitzky, V., Riecken, K., Wree, A., Schumacher, U. and Wedemann, G. 2020. The initial engraftment of tumor cells is critical for the future growth pattern: a mathematical study based on simulations and animal experiments. *BMC cancer* 20, pp. 1-14.

Horton, J.K., Stefanick, D.F., Kedar, P.S. and Wilson, S.H. 2007. ATR signaling mediates an S-phase checkpoint after inhibition of poly (ADP-ribose) polymerase activity. *DNA repair* 6(6), pp. 742-750.

Horton, J.K., Stefanick, D.F., Naron, J.M., Kedar, P.S. and Wilson, S.H. 2005. Poly (ADP-ribose) polymerase activity prevents signaling pathways for cell cycle arrest after DNA methylating agent exposure. *Journal of Biological Chemistry* 280(16), pp. 15773-15785.

Hottiger, M.O. 2015. Nuclear ADP-ribosylation and its role in chromatin plasticity, cell differentiation, and epigenetics. *Annual Review of Biochemistry* 84, pp. 227-263.

Hsing, A.W., Tsao, L. and Devesa, S.S. 2000. International trends and patterns of prostate cancer incidence and mortality. *International Journal of Cancer* 85(1), pp. 60-67.

Hu, Y., et al. 2012. A biopsy simulation study to assess the accuracy of several transrectal ultrasonography (TRUS)-biopsy strategies compared with template prostate mapping biopsies in patients who have undergone radical prostatectomy. *British Journal of Urology International* 110(6), pp. 812-820.

Huang, Y., Cheng, C., Zhang, C., Zhang, Y., Chen, M., Strand, D.W. and Jiang, M. 2016. Advances in prostate cancer research models: From transgenic mice to tumor xenografting models. *Asian Journal of Urology* 3(2), pp. 64-74.

Hudson, D.L., Guy, A.T., Fry, P., O'Hare, M.J., Watt, F.M. and Masters, J.R. 2001. Epithelial cell differentiation pathways in the human prostate: identification of intermediate phenotypes by keratin expression. *Journal of Histochemistry and Cytochemistry* 49(2), pp. 271-278.

Huertas, P. 2010. DNA resection in eukaryotes: deciding how to fix the break. *Nature Structural and Molecular Biology* 17(1), pp. 11-16.

Huggins, C. and Hodges, C.V. 1941. Studies on prostatic cancer. *Cancer Research* 1, pp. 297.

Huntoon, C.J., Flatten, K.S., Hendrickson, A.E.W., Huehls, A.M., Sutor, S.L., Kaufmann, S.H. and Karnitz, L.M. 2013. ATR inhibition broadly sensitizes ovarian cancer cells to chemotherapy independent of BRCA status. *Cancer Research* 73(12), pp. 3683-3691.

Hussain, M., et al. 2020. Survival with olaparib in metastatic castration-resistant prostate cancer. *New England Journal of Medicine* 383(24), pp. 2345-2357.

Hustedt, N., et al. 2019. A consensus set of genetic vulnerabilities to ATR inhibition. *Open biology* 9(9), pp. 190156.

Ianevski, A., He, L., Aittokallio, T. and Tang, J. 2017. SynergyFinder: a web application for analyzing drug combination dose–response matrix data. *Bioinformatics* 33(15), pp. 2413-2415.

Ilic, D., et al. 2018. Prostate cancer screening with prostate-specific antigen (PSA) test: a systematic review and meta-analysis. *British Journal of Medicine* 362, pp. 3519.

Indra, A.K., Warot, X., Brocard, J., Bornert, J.-M., Xiao, J.-H., Chambon, P. and Metzger, D. 1999. Temporally-controlled site-specific mutagenesis in the basal layer of the epidermis: comparison of the recombinase activity of the tamoxifen-inducible Cre-ERT and Cre-ERT2 recombinases. *Nucleic Acids Research* 27(22), pp. 4324-4327.

Islami, F., Moreira, D.M., Boffetta, P. and Freedland, S.J. 2014. A systematic review and meta-analysis of tobacco use and prostate cancer mortality and incidence in prospective cohort studies. *European Urology* 66(6), pp. 1054-1064.

James, N.D., et al. 2017. Abiraterone for prostate cancer not previously treated with hormone therapy. *New England Journal of Medicine* 377(4), pp. 338-351.

James, N.D., et al. 2015. Survival with newly diagnosed metastatic prostate cancer in the "docetaxel era": data from 917 patients in the control arm of the STAMPEDE trial (MRC PR08, CRUK/06/019). *European Urology* 67(6), pp. 1028-1038.

James, N.D., et al. 2016. Addition of docetaxel, zoledronic acid, or both to first-line long-term hormone therapy in prostate cancer (STAMPEDE): survival results from an adaptive, multiarm, multistage, platform randomised controlled trial. *The Lancet* 387(10024), pp. 1163-1177.

Jang, T.L., et al. 2018. Comparative effectiveness of radical prostatectomy with adjuvant radiotherapy versus radiotherapy plus androgen deprivation therapy for men with advanced prostate cancer. *Cancer* 124(20), pp. 4010-4022.

Jette, N.R., et al. 2020. ATM-deficient lung, prostate and pancreatic cancer cells are acutely sensitive to the combination of olaparib and the ATR inhibitor AZD6738. *Genome Instability & Disease* 1(4), pp. 197-205.

Jiao, S., et al. 2017. PARP inhibitor upregulates PD-L1 expression and enhances cancer-associated immunosuppression. *Clinical Cancer Research* 23(14), pp. 3711-3720.

Johannes, J.W., et al. 2021. Discovery of 5-{4-[(7-Ethyl-6-oxo-5, 6-dihydro-1, 5-naphthyridin-3-yl) methyl] piperazin-1-yl}-N-methylpyridine-2-carboxamide (AZD5305): A PARP1–DNA Trapper with High Selectivity for PARP1 over PARP2 and Other PARPs. *Journal of Medicinal Chemistry* 64(19), pp. 14498-14512.

Jonkers, J., Meuwissen, R., van der Gulden, H., Peterse, H., van der Valk, M. and Berns, A. 2001. Synergistic tumor suppressor activity of BRCA2 and p53 in a conditional mouse model for breast cancer. *Nature Genetics* 29(4), pp. 418-425.

Jung, D.C., Lee, H.J., Seo, J.W., Park, S.Y., Lee, S.J., Lee, J.H. and Kim, I.H. 2012. Diffusion-weighted imaging of a prostate cancer xenograft model seen on a 7 Tesla animal MR scanner: comparison of ADC values and pathologic findings. *Korean Journal of Radiology* 13(1), pp. 82-89.

Kaighn, M., Narayan, K.S., Ohnuki, Y., Lechner, J. and Jones, L. 1979. Establishment and characterization of a human prostatic carcinoma cell line (PC-3). *Investigative Urology* 17(1), pp. 16-23.

Kantoff, P.W., et al. 2010. Sipuleucel-T immunotherapy for castration-resistant prostate cancer. *New England Journal of Medicine* 363(5), pp. 411-422.

Karthaus, W.R., et al. 2014. Identification of multipotent luminal progenitor cells in human prostate organoid cultures. *Cell* 159(1), pp. 163-175.

Kasivisvanathan, V., et al. 2018. MRI-targeted or standard biopsy for prostate-cancer diagnosis. *New England Journal of Medicine* 378(19), pp. 1767-1777.

Kaufman, B., et al. 2015. Olaparib monotherapy in patients with advanced cancer and a germline BRCA1/2 mutation. *Journal of clinical oncology* 33(3), pp. 244.

Ke, X.-S., et al. 2009. Genome-wide profiling of histone h3 lysine 4 and lysine 27 trimethylation reveals an epigenetic signature in prostate carcinogenesis. *PLoS ONE* 4(3), pp. 4687.

Kenfield, S.A., Stampfer, M.J., Chan, J.M. and Giovannucci, E. 2011. Smoking and prostate cancer survival and recurrence. *Journal of the American Medical Association* 305(24), pp. 2548-2555.

Khan, M.A., Partin, A.W., Mangold, L.A., Epstein, J.I. and Walsh, P.C. 2003. Probability of biochemical recurrence by analysis of pathologic stage, Gleason score, and margin status for localized prostate cancer. *Urology* 62(5), pp. 866-871.

Kiciński, M., Vangronsveld, J. and Nawrot, T.S. 2011. An epidemiological reappraisal of the familial aggregation of prostate cancer: a meta-analysis. *PLoS ONE* 6(10), pp. 27130.

Kim, H., et al. 2016. Targeting the ATR/CHK1 axis with PARP inhibition results in tumor regression in BRCA-mutant ovarian cancer models. *Clinical Cancer Research* 23(12), pp, 3097-3108.

Kim, H., Kim, M., Im, S.-K. and Fang, S. 2018. Mouse Cre-LoxP system: general principles to determine tissue-specific roles of target genes. *Laboratory Animal Research* 34(4), pp. 147-159.

Kim, H., et al. 2020. Combining PARP with ATR inhibition overcomes PARP inhibitor and platinum resistance in ovarian cancer models. *Nature Communications* 11(1), pp. 1-16.

Kirby, M., Hirst, C. and Crawford, E. 2011. Characterising the castration-resistant prostate cancer population: a systematic review. *International Journal of Clinical Practice* 65(11), pp. 1180-1192.

Klotz, L., et al. 2015. Long-term follow-up of a large active surveillance cohort of patients with prostate cancer. *Journal of Clinical Oncology* 33(3), pp. 272-277.

Knoblaugh, S.E., True, L., Tretiakova, M. and Hukkanen, R.R. 2018. Male reproductive system. *Comparative Anatomy and Histology*. Elsevier. 335-363.

Kolonel, L.N., Altshuler, D. and Henderson, B.E. 2004. The multiethnic cohort study: exploring genes, lifestyle and cancer risk. *Nature Reviews Cancer* 4(7), pp. 519-527.

Kote-Jarai, Z., et al. 2011. BRCA2 is a moderate penetrance gene contributing to young-onset prostate cancer: implications for genetic testing in prostate cancer patients. *British Journal of Cancer* 105(8), pp. 1230-1234.

Krebs, M.G., et al. 2018. Phase I study of AZD6738, an inhibitor of ataxia telangiectasia Rad3-related (ATR), in combination with olaparib or durvalumab in patients (pts) with advanced solid cancers. *Cancer Research* 78, pp. 13.

Krejci, L., Altmannova, V., Spirek, M. and Zhao, X. 2012. Homologous recombination and its regulation. *Nucleic Acids Research* 40(13), pp. 5795-5818.

Krishnakumar, R. and Kraus, W.L. 2010. The PARP side of the nucleus: molecular actions, physiological outcomes, and clinical targets. *Molecular Cell* 39(1), pp. 8-24.

Krokan, H.E. and Bjoras, M. 2013. Base Excision Repair. *Cold Spring Harbor Perspectives in Biology* 5(4).

Kumar, A., et al. 2016. Substantial interindividual and limited intraindividual genomic diversity among tumors from men with metastatic prostate cancer. *Nature Medicine* 22(4), pp. 369.

Kvåle, R., et al. 2007. Interpreting trends in prostate cancer incidence and mortality in the five Nordic countries. *Journal of the National Cancer Institute* 99(24), pp. 1881-1887.

Kwok, M., et al. 2015. Synthetic lethality in chronic lymphocytic leukaemia with DNA damage response defects by targeting the ATR pathway. *The Lancet* 385, pp. S58.

Kyprianou, N., English, H.F. and Isaacs, J.T. 1990. Programmed cell death during regression of PC-82 human prostate cancer following androgen ablation. *Cancer Research* 50(12), pp. 3748-3753.

Lai, Y., et al. 2018. PARP1-siRNA suppresses human prostate cancer cell growth and progression. *Oncology Reports* 39(4), pp. 1901-1909.

Lamont, K.R. and Tindall, D.J. (2010). Androgen regulation of gene expression. *Advances in Cancer Research*. Elsevier. 137-162.

Lancaster, M.A. and Knoblich, J.A. 2014. Organogenesis in a dish: modeling development and disease using organoid technologies. *Science* 345(6194), pp. 1247125.

Lans, H. and Vermeulen, W. 2015. Tissue specific response to DNA damage: C. elegans as role model. *DNA Repair* 32, pp. 141-148.

Lau, A., et al. 2015. Pre-clinical efficacy of the ATR inhibitor AZD6738 in combination with the PARP inhibitor olaparib. *Molecular Targets and Cancer Therapeutics* 15(12), pp. 60.

Lavin, M.F. 2008. Ataxia-telangiectasia: from a rare disorder to a paradigm for cell signalling and cancer. *Nature reviews Molecular cell biology* 9(10), pp. 759-769.

Le, J.D., et al. 2015. Multifocality and prostate cancer detection by multiparametric magnetic resonance imaging: correlation with whole-mount histopathology. *European Urology* 67(3), pp. 569-576.

Ledermann, J., et al. 2012. Olaparib maintenance therapy in platinum-sensitive relapsed ovarian cancer. *New England Journal of Medicine* 366(15), pp. 1382-1392.

Ledermann, J., et al. 2014. Olaparib maintenance therapy in patients with platinum-sensitive relapsed serous ovarian cancer: a preplanned retrospective analysis of outcomes by BRCA status in a randomised phase 2 trial. *The Lancet Oncology* 15(8), pp. 852-861.

Lee, J.-H. and Paull, T.T. 2005. ATM activation by DNA double-strand breaks through the Mre11-Rad50-Nbs1 complex. *Science* 308(5721), pp. 551-554.

Lehmann, B.D., McCubrey, J.A., Jefferson, H.S., Paine, M.S., Chappell, W.H. and Terrian, D.M. 2007. A dominant role for p53-dependent cellular senescence in radiosensitization of human prostate cancer cells. *Cell cycle* 6(5), pp. 595-605.

Leongamornlert, D., et al. 2012. Germline BRCA1 mutations increase prostate cancer risk. *British Journal of Cancer* 106(10), pp. 1697-1701.

Li, H., Liu, Z.-Y., Wu, N., Chen, Y.-C., Cheng, Q. and Wang, J. 2020. PARP inhibitor resistance: the underlying mechanisms and clinical implications. *Molecular Cancer* 19(1), pp. 1-16.

Li, J.J. and Shen, M.M. 2019. Prostate stem cells and cancer stem cells. *Cold Spring Harbor Perspectives in Medicine* 9(6), pp. 030395.

Li, X. and Heyer, W.-D. 2008. Homologous recombination in DNA repair and DNA damage tolerance. *Cell Research* 18(1), pp. 99-113.

Lichtenstein, P., et al. 2000. Environmental and heritable factors in the causation of cancer—analyses of cohorts of twins from Sweden, Denmark, and Finland. *New England Journal of Medicine* 343(2), pp. 78-85.

Lilja, H. 1985. A kallikrein-like serine protease in prostatic fluid cleaves the predominant seminal vesicle protein. *The Journal of Clinical Investigation* 76(5), pp. 1899-1903.

Liu, W., et al. 2009. Copy number analysis indicates monoclonal origin of lethal metastatic prostate cancer. *Nature Medicine* 15(5), pp. 559.

Liu, Z.-g. and Jiao, D. 2020. Necroptosis, tumor necrosis and tumorigenesis. *Cell Stress* 4(1), pp. 1.

Livak, K.J. and Schmittgen, T.D. 2001. Analysis of relative gene expression data using real-time quantitative PCR and the 2− ΔΔCT method. *Methods* 25(4), pp. 402-408.

Lloyd, R.L., et al. 2021. Loss of Cyclin C or CDK8 provides ATR inhibitor resistance by suppressing transcription-associated replication stress. *Nucleic Acids Research* 49(15), pp. 8665-8683.

Lloyd, R.L., et al. 2020. Combined PARP and ATR inhibition potentiates genome instability and cell death in ATM-deficient cancer cells. *Oncogene* 39(25), pp. 4869-4883.

Loblaw, D.A., et al. 2007. Initial hormonal management of androgen-sensitive metastatic, recurrent, or progressive prostate cancer: 2006 update of an American Society of Clinical Oncology practice guideline. *Journal of Clinical Oncology* 25(12), pp. 1596-1605.

Löbrich, M., et al. 2010. γH2AX foci analysis for monitoring DNA double-strand break repair: strengths, limitations and optimization. *Cell cycle* 9(4), pp. 662-669.

Loggini, B., et al. 2003. CD34 microvessel density and VEGF expression in basal and squamous cell carcinoma. *Pathology-Research and Practice* 199(11), pp. 705-712.

Lord, C.J. and Ashworth, A. 2013. Mechanisms of resistance to therapies targeting BRCA-mutant cancers. *Nature medicine* 19(11), pp. 1381-1388.

Lord, C.J. and Ashworth, A. 2017. PARP inhibitors: the first synthetic lethal targeted therapy. *Science* 355(6330), pp. 1152-1158.

Lord, C.J., Tutt, A.N. and Ashworth, A. 2015. Synthetic lethality and cancer therapy: lessons learned from the development of PARP inhibitors. *Annual Review of Medicine* 66, pp. 455-470.

Lowsley, O.S. 1912. The development of the human prostate gland with reference to the development of other structures at the neck of the urinary bladder. *American Journal of Anatomy* 13(3), pp. 299-349.

Lozano, R., Castro, E., Aragón, I.M., Cendón, Y., Cattrini, C., López-Casas, P.P. and Olmos, D. 2021. Genetic aberrations in DNA repair pathways: A cornerstone of precision oncology in prostate cancer. *British Journal of Cancer* 124(3), pp. 552-563.

Luo, X., et al. 2017. PARP-1 controls the adipogenic transcriptional program by PARylating C/EBPβ and modulating its transcriptional activity. *Molecular Cell* 65(2), pp. 260-271.

Mabjeesh, N.J., Lidawi, G., Chen, J., German, L. and Matzkin, H. 2012. High detection rate of significant prostate tumours in anterior zones using transperineal ultrasound-guided template saturation biopsy. *British Journal of Urology International* 110(7), pp. 993-997.

MacInnis, R.J. and English, D.R. 2006. Body size and composition and prostate cancer risk: systematic review and meta-regression analysis. *Cancer Causes and Control* 17(8), pp. 989-1003.

Macintosh, C.A., Stower, M., Reid, N. and Maitland, N.J. 1998. Precise microdissection of human prostate cancers reveals genotypic heterogeneity. *Cancer Research* 58(1), pp. 23-28.

Mah, L., El-Osta, A. and Karagiannis, T. 2010. γH2AX: a sensitive molecular marker of DNA damage and repair. *Leukemia* 24(4), pp. 679-686.

Maréchal, A. and Zou, L. 2013. DNA damage sensing by the ATM and ATR kinases. *Cold Spring Harbor Perspectives in Biology* 5(9), pp. 012716.

Mason, M.D., et al. 2015. Final report of the intergroup randomized study of combined androgen-deprivation therapy plus radiotherapy versus androgen-deprivation therapy alone in locally advanced prostate cancer. *Journal of Clinical Oncology* 33(19), pp. 2143.

Mateo, J., et al. 2017. DNA repair in prostate cancer: biology and clinical implications. *European Urology* 71(3), pp. 417-425.

Mateo, J., et al. 2015. DNA-repair defects and olaparib in metastatic prostate cancer. *New England Journal of Medicine* 2015(373), pp. 1697-1708.

Mateo, J., et al. 2019. Olaparib in patients with metastatic castration resistant prostate cancer with DNA repair gene aberrations (TOPARP-B): a multicentre, open label, randomised, phase 2 trial. *Lancet Oncology* 21(1), pp. 162-174.

Mayya, V. and Han, D.K. 2009. Phosphoproteomics by mass spectrometry: insights, implications, applications and limitations. *Expert Review of Proteomics* 6(6), pp. 605-618.

McCabe, N., et al. 2006. Deficiency in the repair of DNA damage by homologous recombination and sensitivity to poly (ADP-ribose) polymerase inhibition. *Cancer Research* 66(16), pp. 8109-8115.

McLeod, D.G., Iversen, P., See, W.A., Morris, T., Armstrong, J., Wirth, M.P. and Group, C.E.P.C.T. 2006. Bicalutamide 150 mg plus standard care vs standard care alone for early prostate cancer. *British Journal of Urology International* 97(2), pp. 247-254.

McNeal, J.E. 1968. Regional morphology and pathology of the prostate. *American Journal of Clinical Pathology* 49(3), pp. 347-357.

McNeal, J.E. 1981. The zonal anatomy of the prostate. *The prostate* 2(1), pp. 35-49.

McNeal, J.E. 1988. Normal histology of the prostate. *The American Journal of Surgical pathology* 12(8), pp. 619-633.

McNeal, J.E., Redwine, E.A., Freiha, F.S. and Stamey, T.A. 1988. Zonal distribution of prostatic adenocarcinoma. Correlation with histologic pattern and direction of spread. *The American journal of surgical pathology* 12(12), pp. 897-906.

McNeal, J.E., Villers, A.A., Redwine, E.A., Freiha, F.S. and Stamey, T.A. 1990. Histologic differentiation, cancer volume, and pelvic lymph node metastasis in adenocarcinoma of the prostate. *Cancer* 66(6), pp. 1225-1233.

Mellinger, G.T., Gleason, D. and Bailar III, J. 1967. The histology and prognosis of prostatic cancer. *The Journal of Urology* 97(2), pp. 331-337.

Menyhart, O., Harami-Papp, H., Sukumar, S., Schaefer, R., Magnani, L., de Barrios, O. and Győrffy, B. 2016. Guidelines for the selection of functional assays to evaluate the hallmarks of cancer. *Biochimica et Biophysica Acta (BBA)-Reviews on Cancer* 1866(2), pp. 300-319.

Messing, E.M., et al. 2006. Immediate versus deferred androgen deprivation treatment in patients with node-positive prostate cancer after radical prostatectomy and pelvic lymphadenectomy. *The Lancet Oncology* 7(6), pp. 472-479.

Metzger, D., Li, M. and Chambon, P. 2005. Targeted somatic mutagenesis in the mouse epidermis. *Methods in Molecular Biology* 289*,* pp. 329-340.

Millender, L.E., Aubin, M., Pouliot, J., Shinohara, K. and Roach III, M. 2004. Daily electronic portal imaging for morbidly obese men undergoing radiotherapy for localized prostate cancer. *International Journal of Radiation Oncology* 59(1), pp. 6-10.

Mistry, M., Parkin, D., Ahmad, A.S. and Sasieni, P. 2011. Cancer incidence in the United Kingdom: projections to the year 2030. *British Journal of Cancer* 105(11), pp. 1795-1803.

Mitra, A., et al. 2008. Prostate cancer in male BRCA1 and BRCA2 mutation carriers has a more aggressive phenotype. *British Journal of Cancer* 98(2), pp. 502.

Moad, M., et al. 2017. Multipotent basal stem cells, maintained in localized proximal niches, support directed long-ranging epithelial flows in human prostates. *Cell Reports* 20(7), pp. 1609-1622.

Mohni, K.N., Kavanaugh, G.M. and Cortez, D. 2014. ATR Pathway Inhibition Is Synthetically Lethal in Cancer Cells with ERCC1 Deficiency ATR Inhibition Is Synthetic Lethal with Loss of ERCC1. *Cancer Research* 74(10), pp. 2835-2845.

Moreno-Lama, L., et al. 2020. Coordinated signals from PARP-1 and PARP-2 are required to establish a proper T cell immune response to breast tumors in mice. *Oncogene* 39(13), pp. 2835-2843.

Mottet, N., et al. 2017. EAU-ESTRO-SIOG guidelines on prostate cancer. Part 1: screening, diagnosis, and local treatment with curative intent. *European Urology* 71(4), pp. 618-629.

Mouw, K.W., Goldberg, M.S., Konstantinopoulos, P.A. and D'Andrea, A.D. 2017. DNA damage and repair biomarkers of immunotherapy response. *Cancer Discovery* 7(7), pp. 675-693.

Mucci, L.A., et al. 2016. Familial risk and heritability of cancer among twins in Nordic countries. *Journal of the American Medical Association* 315(1), pp. 68-76.

Murai, J., et al. 2014. Stereospecific PARP trapping by BMN 673 and comparison with olaparib and rucaparib. *Molecular Cancer Therapeutics* 13(2), pp. 433-443.

Murai, J., et al. 2012. Trapping of PARP1 and PARP2 by clinical PARP inhibitors. *Cancer Research* 72(21), pp. 5588-5599.

Murphy, A.B., et al. 2013. Smoking and prostate cancer in a multi-ethnic sample. *The Prostate* 73(14), pp. 1518-1528.

Na, R., et al. 2017. Germline mutations in ATM and BRCA1/2 distinguish risk for lethal and indolent prostate cancer and are associated with early age at death. *European Urology* 71(5), pp. 740-747.

Nam, E.A. and Cortez, D. 2011. ATR signalling: more than meeting at the fork. *Biochemical Journal* 436(3), pp. 527-536.

Nam, E.A., Zhao, R., Glick, G.G., Bansbach, C.E., Friedman, D.B. and Cortez, D. 2011. Thr-1989 phosphorylation is a marker of active ataxia telangiectasia-mutated and Rad3-related (ATR) kinase. *Journal of Biological Chemistry* 286(33), pp. 28707-28714.

National Cancer Institute: Surveillance Epidemiology and End Results Programme. 2018. SEER Cancer Statistics Review 1975-2015. Available at: www.seer.cancer.gov/archive/csr/1975_2015/. [Accessed 10 February 2019].

National Institute for Health and Care Excellence. 2021. Prostate cancer: diagnosis and management [NG131]. Available at: www.nice.org.uk/guidance/ng131. [Accessed 1 March 2022].

National Prostate Cancer Audit. 2021. Annual Report 2020: results of the NPCA prospective audit in England and Wales for men diagnosed from 1 April 2018 to 31 March 2019. Available at: www.ncpa.org.uk/reports/npca-annual-report-2020. [Accessed 1 March 2022].

Navarro, J., et al. 2017. PARP-1/PARP-2 double deficiency in mouse T cells results in faulty immune responses and T lymphomas. *Scientific Reports* 7, pp. 41962.

Neeb, A., et al. 2021. Advanced prostate cancer with ATM loss: PARP and ATR inhibitors. *European Urology* 79(2), pp. 200-211.

Nicolas, L., et al. 2010. Loss of poly (ADP-ribose) polymerase-2 leads to rapid development of spontaneous T-cell lymphomas in p53-deficient mice. *Oncogene* 29(19), pp. 2877-2883.

Noda, D., et al. 2006. ELAC2, a putative prostate cancer susceptibility gene product, potentiates TGF-β/Smad-induced growth arrest of prostate cells. *Oncogene* 25(41), pp. 5591-5600.

O'Driscoll, M., Ruiz-Perez, V.L., Woods, C.G., Jeggo, P.A. and Goodship, J.A. 2003. A splicing mutation affecting expression of ataxia–telangiectasia and Rad3–related protein (ATR) results in Seckel syndrome. *Nature Genetics* 33(4), pp. 497-501.

O'Connor, M.J. 2015. Targeting the DNA damage response in cancer. *Molecular Cell* 60(4), pp. 547-560.

Okotie, O.T., Roehl, K.A., Han, M., Loeb, S., Gashti, S.N. and Catalona, W.J. 2007. Characteristics of prostate cancer detected by digital rectal examination only. *Urology* 70(6), pp. 1117-1120.

Packer, J.R. and Maitland, N.J. 2016. The molecular and cellular origin of human prostate cancer. *Biochimica et Biophysica Acta (BBA)-Molecular Cell Research* 1863(6), pp. 1238-1260.

Page, E.C., et al. 2019. Interim results from the IMPACT study: evidence for prostate-specific antigen screening in BRCA2 mutation carriers. *European Urology* 76(6), pp. 831-842.

Paju, A., Bjartell, A., Zhang, W.-M., Nordling, S., Borgström, A., Hansson, J. and Stenman, U.-H. 2000. Expression and characterization of trypsinogen produced in the human male genital tract. *The American Journal of Pathology* 157(6), pp. 2011-2021.

Palma, J.P., et al. 2009. ABT-888 confers broad in vivo activity in combination with temozolomide in diverse tumors. *Clinical Cancer Research* 15(23), pp. 1078-0432.

Papa, A. and Pandolfi, P.P. 2019. The PTEN–PI3K Axis in Cancer. *Biomolecules* 9(4), pp. 153.

Parisotto, M., et al. 2018. PTEN deletion in luminal cells of mature prostate induces replication stress and senescence in vivo. *Journal of Experimental Medicine* 215(6), pp. 1749-1763.

Parker, A., et al. 2013a. Obese men have more advanced and more aggressive prostate cancer at time of surgery than non-obese men after adjusting for screening PSA level and age: results from two independent nested case–control studies. *Prostate Cancer and Prostatic Diseases* 16(4), pp. 352-356.

Parker, C., et al. 2013b. Alpha emitter radium-223 and survival in metastatic prostate cancer. *New England Journal of Medicine* 369(3), pp. 213-223.

Parker, C.C., et al. 2020. Timing of radiotherapy after radical prostatectomy (RADICALS-RT): a randomised, controlled phase 3 trial. *The Lancet* 396(10260), pp. 1413-1421.

Parker, C.C., et al. 2018. Radiotherapy to the primary tumour for newly diagnosed, metastatic prostate cancer (STAMPEDE): a randomised controlled phase 3 trial. *The Lancet* 392(10162), pp. 2353-2366.

Parsons, B.D., Schindler, A., Evans, D.H. and Foley, E. 2009. A direct phenotypic comparison of siRNA pools and multiple individual duplexes in a functional assay. *PloS ONE* 4(12), pp. 8471.

Paull, T.T. 2015. Mechanisms of ATM activation. *Annual Review of Biochemistry* 84, pp. 711-738.

Pearl, L.H., Schierz, A.C., Ward, S.E., Al-Lazikani, B. and Pearl, F.M. 2015. Therapeutic opportunities within the DNA damage response. *Nature Reviews Cancer* 15(3), pp. 166.

Pilla Reddy, V., Bui, K., Scarfe, G., Zhou, D. and Learoyd, M. 2019. Physiologically based pharmacokinetic modeling for olaparib dosing recommendations: bridging formulations, drug interactions, and patient populations. *Clinical Pharmacology & Therapeutics* 105(1), pp. 229-241.

Pommier, Y., O'Connor, M.J. and de Bono, J. 2016. Laying a trap to kill cancer cells: PARP inhibitors and their mechanisms of action. *Science Translational Medicine* 8(362), pp. 17.

Popp, H.D., Brendel, S., Hofmann, W.-K. and Fabarius, A. 2017. Immunofluorescence Microscopy of γH2AX and 53BP1 for Analyzing the Formation and Repair of DNA Double-strand Breaks. *Journal of Visualized Experiments* 3(129), pp. 56617.

Powley, I.R., et al. 2020. Patient-derived explants (PDEs) as a powerful preclinical platform for anti-cancer drug and biomarker discovery. *British Journal of Cancer*, pp. 1-10.

Price, D. 1963. Comparative aspects of development and structure in the prostate. *National Cancer Institute Monograph* 12, pp. 1-27.

Pritchard, C.C., et al. 2016. Inherited DNA-repair gene mutations in men with metastatic prostate cancer. *New England Journal of Medicine* 2016(375), pp. 443-453.

Pu, H., Horbinski, C., Hensley, P.J., Matuszak, E.A., Atkinson, T. and Kyprianou, N. 2014. PARP-1 regulates epithelial–mesenchymal transition (EMT) in prostate tumorigenesis. *Carcinogenesis* 35(11), pp. 2592-2601.

Purnell, M.R. and Whish, W. 1980. Novel inhibitors of poly (ADP-ribose) synthetase. *Biochemical Journal* 185(3), pp. 775.

Quaresma, M., Coleman, M.P. and Rachet, B. 2015. 40-year trends in an index of survival for all cancers combined and survival adjusted for age and sex for each cancer in England and Wales, 1971–2011: a population-based study. *The Lancet* 385(9974), pp. 1206-1218.

Rae, C. and Mairs, R.J. 2017. Evaluation of the radiosensitizing potency of chemotherapeutic agents in prostate cancer cells. *International Journal of Radiation Biology* 93(2), pp. 194-203.

Rafiei, S., et al. 2020. ATM loss confers greater sensitivity to ATR inhibition than PARP inhibition in prostate cancer. *Cancer Research* 80(11), pp. 2094-2100.

Rajesh, M., Mukhopadhyay, P., Godlewski, G., Bátkai, S., Haskó, G., Liaudet, L. and Pacher, P. 2006. Poly (ADP-ribose) polymerase inhibition decreases angiogenesis. *Biochemical and biophysical research communications* 350(4), pp. 1056-1062.

Rathkopf, D.E., et al. 2021. AMPLITUDE: A study of niraparib in combination with abiraterone acetate plus prednisone (AAP) versus AAP for the treatment of patients with deleterious germline or somatic homologous recombination repair (HRR) gene-altered metastatic castration-sensitive prostate cancer (mCSPC). *Journal of Clinical Oncology* 39(supplement 6), pp. 1.

Ratnacaram, C.K., Teletin, M., Jiang, M., Meng, X., Chambon, P. and Metzger, D. 2008. Temporally controlled ablation of PTEN in adult mouse prostate epithelium generates a model of invasive prostatic adenocarcinoma. *Proceedings of the National Academy of Sciences* 105(7), pp. 2521-2526.

Rawla, P. 2019. Epidemiology of prostate cancer. *World Journal of Oncology* 10(2), pp. 63.

Rea, D., et al. 2016. Mouse models in prostate cancer translational research: from xenograft to PDX. *BioMed Research International* 2016.

Reaper, P.M., et al. 2011. Selective killing of ATM-or p53-deficient cancer cells through inhibition of ATR. *Nature Chemical Biology* 7(7), pp. 428-430.

Reichert, Z.R., Daignault, S., Teply, B.A., Devitt, M.E. and Heath, E.I. (2020). Targeting resistant prostate cancer with ATR and PARP inhibition (TRAP trial): A phase II study. *Journal of Clinical Oncology* 38(6), pp. 254.

Ren, S., et al. 2018. Whole-genome and transcriptome sequencing of prostate cancer identify new genetic alterations driving disease progression. *European Urology* 73(3), pp. 322-339.

Richardson, G.D., Robson, C.N., Lang, S.H., Neal, D.E., Maitland, N.J. and Collins, A.T. 2004. CD133, a novel marker for human prostatic epithelial stem cells. *Journal of Cell Science* 117(16), pp. 3539-3545.

Richie, J.P., et al. 1993. Effect of patient age on early detection of prostate cancer with serum prostate-specific antigen and digital rectal examination. *Urology* 42(4), pp. 365-374.

Risbridger, G.P. and Taylor, R.A. 2016. Patient-derived prostate cancer: from basic science to the clinic. *Hormones and Cancer* 7(4), pp. 236-240.

Risbridger, G.P., Toivanen, R. and Taylor, R.A. 2018. Preclinical models of prostate cancer: patient-derived xenografts, organoids, and other explant models. *Cold Spring Harbor Perspectives in Medicine* 8(8), pp. 030536.

Roberts, M. and Jarvi, K. 2009. Steps in the investigation and management of low semen volume in the infertile man. *Canadian Urological Association Journal* 3(6), pp. 479.

Robinson, D., et al. 2015. Integrative clinical genomics of advanced prostate cancer. *Cell* 161(5), pp. 1215-1228.

Rohrmann, S., Genkinger, J.M., Burke, A., Helzlsouer, K.J., Comstock, G.W., Alberg, A.J. and Platz, E.A. 2007. Smoking and risk of fatal prostate cancer in a prospective US study. *Urology* 69(4), pp. 721-725.

Rökman, A., et al. 2002. Germline alterations of the RNASEL gene, a candidate HPC1 gene at 1q25, in patients and families with prostate cancer. *The American Journal of Human Genetics* 70(5), pp. 1299-1304.

Ronson, G.E., et al. 2018. PARP1 and PARP2 stabilise replication forks at base excision repair intermediates through Fbh1-dependent Rad51 regulation. *Nature Communications* 9(1), pp. 1-12.

Rose, M., Burgess, J.T., O'Byrne, K., Richard, D.J. and Bolderson, E. 2020. PARP inhibitors: clinical relevance, mechanisms of action and tumor resistance. *Frontiers in Cell and Developmental Biology*, pp. 879.

Rouleau, M., Patel, A., Hendzel, M.J., Kaufmann, S.H. and Poirier, G.G. 2010. PARP inhibition: PARP1 and beyond. *Nature Reviews Cancer* 10(4), pp. 293-301.

Rubin, M.A. 2012. ETS rearrangements in prostate cancer. *Asian Journal of Andrology* 14(3), pp. 393.

Ruiz, S., Mayor-Ruiz, C., Lafarga, V., Murga, M., Vega-Sendino, M., Ortega, S. and Fernandez-Capetillo, O. 2016. A genome-wide CRISPR screen identifies CDC25A as a determinant of sensitivity to ATR inhibitors. *Molecular Cell* 62(2), pp. 307-313.

Rundle, S., Bradbury, A., Drew, Y. and Curtin, N.J. 2017. Targeting the ATR-CHK1 Axis in Cancer Therapy. *Cancers* 9(5), pp. 41.

Ryan, C.J., et al. 2015. Abiraterone acetate plus prednisone versus placebo plus prednisone in chemotherapy-naive men with metastatic castration-resistant prostate cancer (COU-AA-302): final overall survival analysis of a randomised, double-blind, placebo-controlled phase 3 study. *The Lancet Oncology* 16(2), pp. 152-160.

Saad, F., et al. 2022. PROpel: Phase III trial of olaparib (ola) and abiraterone (abi) versus placebo (pbo) and abi as first-line (1L) therapy for patients (pts) with metastatic castration-resistant prostate cancer (mCRPC). *Journal of Clinical Oncology* 40(supplement 6), pp. 1.

Saad, F., Bögemann, M., Suzuki, K. and Shore, N. 2021. Treatment of nonmetastatic castration-resistant prostate cancer: focus on second-generation androgen receptor inhibitors. *Prostate Cancer and Prostatic Diseases* 24(2), pp. 323-334.

Sánchez-Chapado, M., Olmedilla, G., Cabeza, M., Donat, E. and Ruiz, A. 2003. Prevalence of prostate cancer and prostatic intraepithelial neoplasia in Caucasian Mediterranean males: an autopsy study. *The Prostate* 54(3), pp. 238-247.

Schally, A.V., et al. 1971. Isolation and properties of the FSH and LH-releasing hormone. *Biochemical and Biophysical Research Communications* 43(2), pp. 393-399.

Scher, H.I., et al. 2012. Increased survival with enzalutamide in prostate cancer after chemotherapy. *New England Journal of Medicine* 367(13), pp. 1187-1197.

Schiewer, M.J., et al. 2012. Dual roles of PARP-1 promote cancer growth and progression. *Cancer Discovery* 2(12), pp. 1134-1149.

Schiewer, M.J. and Knudsen, K.E. 2014. Transcriptional roles of PARP-1 in cancer. *Molecular Cancer Research* 12(8), pp. 1069-1080.

Schmitt, A., et al. 2017. ATM deficiency is associated with sensitivity to PARP1-and ATR inhibitors in lung adenocarcinoma. *Cancer Research* 77(11), pp. 3040-3056.

Schoonen, P.M., Kok, Y.P., Wierenga, E., Bakker, B., Foijer, F., Spierings, D.C. and van Vugt, M.A. 2019. Premature mitotic entry induced by ATR inhibition potentiates olaparib inhibition-mediated genomic instability, inflammatory signaling, and cytotoxicity in BRCA2-deficient cancer cells. *Molecular Oncology* 13(11), pp. 2422-2440.

Schreiber, V., Dantzer, F., Ame, J.-C. and De Murcia, G. 2006. Poly (ADP-ribose): novel functions for an old molecule. *Nature Reviews Molecular Cell Biology* 7(7), pp. 517.

Schröder, F.H., et al. 2014. The European randomized study of screening for prostate cancer–prostate cancer mortality at 13 years of follow-up. *The Lancet* 384(9959), pp. 2027.

Schulte, R.T., Wood, D.P., Daignault, S., Shah, R.B. and Wei, J.T. 2008. Utility of extended pattern prostate biopsies for tumor localization: pathologic correlations after radical prostatectomy. *Cancer: Interdisciplinary International Journal of the American Cancer Society* 113(7), pp. 1559-1565.

Schumacher, F.R., et al. 2018. Association analyses of more than 140,000 men identify 63 new prostate cancer susceptibility loci. *Nature Genetics* 50(7), pp. 928.

Sciarra, A., et al. 2016. A meta-analysis and systematic review of randomized controlled trials with degarelix versus gonadotropin-releasing hormone agonists for advanced prostate cancer. *Medicine* 95(27), pp. 3845.

Sebaugh, J. 2011. Guidelines for accurate EC50/IC50 estimation. *Pharmaceutical Statistics* 10(2), pp. 128-134.

Seluanov, A., Mao, Z. and Gorbunova, V. 2010. Analysis of DNA double-strand break (DSB) repair in mammalian cells. *JoVE (Journal of Visualized Experiments)*(43), pp. e2002.

Senturk, E. and Manfredi, J.J. (2013). p53 and cell cycle effects after DNA damage. *p53 Protocols*. Springer. 49-61.

Shappell, S.B., et al. 2004. Prostate pathology of genetically engineered mice: definitions and classification. The consensus report from the Bar Harbor meeting of the Mouse Models of Human Cancer Consortium Prostate Pathology Committee. *Cancer Research* 64(6), pp. 2270-2305.

Shen, M.M. and Abate-Shen, C. 2007. Pten inactivation and the emergence of androgen-independent prostate cancer. *Cancer Research* 67(14), pp. 6535-6538.

Shen, M.M. and Abate-Shen, C. 2010. Molecular genetics of prostate cancer: new prospects for old challenges. *Genes and Development* 24(18), pp. 1967-2000.

Shi, Y., Liu, Z., Zhang, Q., Vallee, I., Mo, Z., Kishi, S. and Yang, X.-L. 2020. Phosphorylation of seryl-tRNA synthetase by ATM/ATR is essential for hypoxia-induced angiogenesis. *PLoS Biology* 18(12), pp. 3000991.

Siddiqui, M.M., et al. 2013. Magnetic resonance imaging/ultrasound–fusion biopsy significantly upgrades prostate cancer versus systematic 12-core transrectal ultrasound biopsy. *European Urology* 64(5), pp. 713-719.

Siddiqui, M.M., et al. 2015. Comparison of MR/ultrasound fusion–guided biopsy with ultrasound-guided biopsy for the diagnosis of prostate cancer. *Journal of the American Medical Association* 313(4), pp. 390-397.

Simoneau, A., Xiong, R. and Zou, L. 2021. The trans cell cycle effects of PARP inhibitors underlie their selectivity toward BRCA1/2-deficient cells. *Genes & Development* 35(17-18), pp. 1271-1289.

Sinnott, M., Falzarano, S.M., Hernandez, A.V., Jones, J.S., Klein, E.A., Zhou, M. and Magi-Galluzzi, C. 2012. Discrepancy in prostate cancer localization between biopsy and prostatectomy specimens in patients with unilateral positive biopsy: implications for focal therapy. *The Prostate* 72(11), pp. 1179-1186.

Slade, D., et al. 2011. The structure and catalytic mechanism of a poly (ADP-ribose) glycohydrolase. *Nature* 477(7366), pp. 616.

Sooriakumaran, P. 2017. Testing radical prostatectomy in men with prostate cancer and oligometastases to the bone: a randomized controlled feasibility trial. *British Journal of Urology International* 120(5), pp. 8-20.

Soos, G., Tsakiris, I., Szanto, J., Turzo, C., Haas, P.G. and Dezso, B. 2005. The prevalence of prostate carcinoma and its precursor in Hungary: an autopsy study. *European Urology* 48(5), pp. 739-744.

Southgate, H.E., Chen, L., Tweddle, D.A. and Curtin, N.J. 2020. ATR inhibition potentiates PARP inhibitor cytotoxicity in high risk neuroblastoma cell lines by multiple mechanisms. *Cancers* 12(5), pp. 1095.

Sramkoski, R.M., et al. 1999. A new human prostate carcinoma cell line, 22Rv1. *In Vitro Cellular & Developmental Biology-Animal* 35(7), pp. 403-409.

Stamey, T.A., Yang, N., Hay, A.R., McNeal, J.E., Freiha, F.S. and Redwine, E. 1987. Prostate-specific antigen as a serum marker for adenocarcinoma of the prostate. *New England Journal of Medicine* 317(15), pp. 909-916.

Stone, K.R., Mickey, D.D., Wunderli, H., Mickey, G.H. and Paulson, D.F. 1978. Isolation of a human prostate carcinoma cell line (DU 145). *International Journal of Cancer* 21(3), pp. 274-281.

Sun, L.-L., et al. 2018. Inhibition of ATR downregulates PD-L1 and sensitizes tumor cells to T cell-mediated killing. *American Journal of Cancer Research* 8(7), pp. 1307.

Suzuki, A., et al. 2001. T cell-specific loss of Pten leads to defects in central and peripheral tolerance. *Immunity* 14(5), pp. 523-534.

Sweeney, C.J., et al. 2015. Chemohormonal therapy in metastatic hormone-sensitive prostate cancer. *New England Journal of Medicine* 373(8), pp. 737-746.

Tait, S.W. and Green, D.R. 2008. Caspase-independent cell death: leaving the set without the final cut. *Oncogene* 27(50), pp. 6452-6461.

Tang, B., et al. 2017. Smoking increased the risk of prostate cancer with grade group≥ 4 and intraductal carcinoma in a prospective biopsy cohort. *The Prostate* 77(9), pp. 984-989.

Tangen, C.M., Faulkner, J.R., Crawford, E.D., Thompson, I.M., Hirano, D., Eisenberger, M. and Hussain, M. 2003. Ten-year survival in patients with metastatic prostate cancer. *Clinical Prostate Cancer* 2(1), pp. 41-45.

Tannock, I.F., et al. 2004. Docetaxel plus prednisone or mitoxantrone plus prednisone for advanced prostate cancer. *New England Journal of Medicine* 351(15), pp. 1502-1512.

Tavtigian, S.V., et al. 2001. A candidate prostate cancer susceptibility gene at chromosome 17p. *Nature Genetics* 27(2), pp. 172-180.

Tentori, L., et al. 2007. Poly (ADP-ribose) polymerase (PARP) inhibition or PARP-1 gene deletion reduces angiogenesis. *European Journal of Cancer* 43(14), pp. 2124-2133.

Theoret, M.R., Ning, Y.-M., Zhang, J.J., Justice, R., Keegan, P. and Pazdur, R. 2011. The risks and benefits of 5α-reductase inhibitors for prostate-cancer prevention. *New England Journal of Medicine* 365(2), pp. 97-99.

Thompson, I.M., et al. 2003. The influence of finasteride on the development of prostate cancer. *New England Journal of Medicine* 349(3), pp. 215-224.

Thompson, I.M., et al. 2004. Prevalence of prostate cancer among men with a prostate-specific antigen level≤ 4.0 ng per milliliter. *New England Journal of Medicine* 350(22), pp. 2239-2246.

Thomsen, F.B., Brasso, K., Klotz, L.H., Røder, M.A., Berg, K.D. and Iversen, P. 2014. Active surveillance for clinically localized prostate cancer—A systematic review. *Journal of Surgical Oncology* 109(8), pp. 830-835.

Toivanen, R. and Shen, M.M. 2017. Prostate organogenesis: tissue induction, hormonal regulation and cell type specification. *Development* 144(8), pp. 1382-1398.

Tomayko, M.M. and Reynolds, C.P. 1989. Determination of subcutaneous tumor size in athymic (nude) mice. *Cancer Chemotherapy and Pharmacology* 24(3), pp. 148-154.

Tomlins, S.A., et al. 2005. Recurrent fusion of TMPRSS2 and ETS transcription factor genes in prostate cancer. *Science* 310(5748), pp. 644-648.

Tronche, F., Casanova, E., Turiault, M., Sahly, I. and Kellendonk, C. 2002. When reverse genetics meets physiology: the use of site-specific recombinases in mice. *FEBS Letters* 529(1), pp. 116-121.

Turnham, D.J., Bullock, N., Dass, M.S., Staffurth, J.N. and Pearson, H.B. 2020. The PTEN conundrum: how to target PTEN-deficient prostate cancer. *Cells* 9(11), pp. 2342.

Vakifahmetoglu, H., Olsson, M. and Zhivotovsky, B. 2008. Death through a tragedy: mitotic catastrophe. *Cell Death & Differentiation* 15(7), pp. 1153-1162.

Van Bokhoven, A., et al. 2003. Molecular characterization of human prostate carcinoma cell lines. *The Prostate* 57(3), pp. 205-225.

Vandamme, T.F. 2014. Use of rodents as models of human diseases. *Journal of Pharmacy & Bioallied Sciences* 6(1), pp. 2.

Vanneste, B.G., Van Limbergen, E.J., van Lin, E.N., van Roermund, J.G. and Lambin, P. 2016. Prostate cancer radiation therapy: what do clinicians have to know? *BioMed Research International* 2016, pp. 6829875.

Verhagen, A.P., Ramaekers, F.C., Aalders, T.W., Schaafsma, H.E., Debruyne, F.M. and Schalken, J.A. 1992. Colocalization of basal and luminal cell-type cytokeratins in human prostate cancer. *Cancer Research* 52(22), pp. 6182-6187.

Verze, P., Cai, T. and Lorenzetti, S. 2016. The role of the prostate in male fertility, health and disease. *Nature Reviews Urology* 13(7), pp. 379.

Wang, Y., Hayward, S.W., Cao, M., Thayer, K.A. and Cunha, G.R. 2001. Cell differentiation lineage in the prostate. *Differentiation* 68(4-5), pp. 270-279.

Wang, Z.-Q., Auer, B., Stingl, L., Berghammer, H., Haidacher, D., Schweiger, M. and Wagner, E.F. 1995. Mice lacking ADPRT and poly (ADP-ribosyl) ation develop normally but are susceptible to skin disease. *Genes & development* 9(5), pp. 509-520.

Ward, J.F., Slezak, J.M., Blute, M.L., Bergstralh, E.J. and Zincke, H. 2005. Radical prostatectomy for clinically advanced (cT3) prostate cancer since the advent of prostate-specific antigen testing: 15-year outcome. *British Journal of Urology International* 95(6), pp. 751-756.

Watson, P.A., Arora, V.K. and Sawyers, C.L. 2015. Emerging mechanisms of resistance to androgen receptor inhibitors in prostate cancer. *Nature Reviews Cancer* 15(12), pp. 701-711.

Webber, M.M., Bello, D. and Quader, S. 1996. Immortalized and tumorigenic adult human prostatic epithelial cell lines: Characteristics and applications part I. Cell markers and immortalized nontumorigenic cell lines. *The Prostate* 29(6), pp. 386-394.

Weidner, N., Semple, J.P., Welch, W.R. and Folkman, J. 1991. Tumor angiogenesis and metastasis—correlation in invasive breast carcinoma. *New England Journal of Medicine* 324(1), pp. 1-8.

Weinreb, J.C., et al. 2016. PI-RADS prostate imaging–reporting and data system: 2015, version 2. *European Urology* 69(1), pp. 16-40.

Wilt, T.J., et al. 2017. Follow-up of prostatectomy versus observation for early prostate cancer. *New England Journal of Medicine* 377(2), pp. 132-142.

Wolf, A.M., et al. 2010. American Cancer Society guideline for the early detection of prostate cancer: update 2010. *CA: A Cancer Journal for Clinicians* 60(2), pp. 70-98.

Wu, I. and Modlin, C.S. 2012. Disparities in prostate cancer in African American men: what primary care physicians can do. *Cleveland Clinic Journal of Medicine* 79(5), pp. 313-320.

Wu, M., Wang, X., Mcgregor, N., Pienta, K. and Zhang, J. 2014. Dynamic regulation of Rad51 by E2F1 and p53 in prostate cancer cells upon drug induced DNA damage under hypoxia. *Molecular Pharmacology*, pp. mol. 113.090688.

Wu, X., Gong, S., Roy-Burman, P., Lee, P. and Culig, Z. 2013. Current mouse and cell models in prostate cancer research. *Endocrine-related Cancer* 20(4), pp. 155-170.

Wu, X., et al. 2001. Generation of a prostate epithelial cell-specific Cre transgenic mouse model for tissue-specific gene ablation. *Mechanisms of Development* 101(1-2), pp. 61-69.

Xie, Q., Liu, Y., Cai, T., Horton, C., Stefanson, J. and Wang, Z.A. 2017. Dissecting cell-type-specific roles of androgen receptor in prostate homeostasis and regeneration through lineage tracing. *Nature Communications* 8, pp. 14284.

Yélamos, J., Moreno-Lama, L., Jimeno, J. and Ali, S.O. 2020. Immunomodulatory roles of PARP-1 and PARP-2: impact on PARP-centered cancer therapies. *Cancers* 12(2), pp. 392.

Zhang, Y. and Hunter, T. 2014. Roles of Chk1 in cell biology and cancer therapy. *International Journal of Cancer* 134(5), pp. 1013-1023.

Ziadeh, T. and Kourie, H.R. 2021. Poly (ADP-ribose) polymerase inhibitors in prostate cancer: a cornerstone in precision oncology. *Pharmacogenomics* 22(18), pp. 1237-1250.